

## Copyright Undertaking

This thesis is protected by copyright, with all rights reserved.

**By reading and using the thesis, the reader understands and agrees to the following terms:**

1. The reader will abide by the rules and legal ordinances governing copyright regarding the use of the thesis.
2. The reader will use the thesis for the purpose of research or private study only and not for distribution or further reproduction or any other purpose.
3. The reader agrees to indemnify and hold the University harmless from and against any loss, damage, cost, liability or expenses arising from copyright infringement or unauthorized usage.

### IMPORTANT

If you have reasons to believe that any materials in this thesis are deemed not suitable to be distributed in this form, or a copyright owner having difficulty with the material being included in our database, please contact [lbsys@polyu.edu.hk](mailto:lbsys@polyu.edu.hk) providing details. The Library will look into your claim and consider taking remedial action upon receipt of the written requests.

**FLUID EFFECTS ON THE INTERACTION OF WAVES WITH  
ROCK JOINTS**

**YANG HUI**

**PhD**

**The Hong Kong Polytechnic University**

**2022**

The Hong Kong Polytechnic University  
Department of Civil and Environmental Engineering

Fluid effects on the interaction of waves with rock joints

YANG Hui

A thesis submitted in partial fulfillment of the requirements for the  
degree of Doctor of Philosophy

June 2021

## **CERTIFICATE OF ORIGINALITY**

I hereby declare that this thesis is my own work and that, to the best of my knowledge and belief, it reproduces no material previously published or written, nor material that has been accepted for the award of any other degree or diploma, except where due acknowledgement has been made in the text.

\_\_\_\_\_ (Signed)

\_\_\_\_\_ YANG Hui \_\_\_\_\_ (Name of student)



*For my beloved parents,*

*LIANG Jun-hui and YANG Yong-qin*

# ABSTRACT

Rock joints are ubiquitous in the Earth's crust, providing main conduits and spaces for flow, transportation, migration, and storage of fluids. The existence of fluids could have important influences on mechanical, hydraulic, thermodynamic, and seismic behaviours of rock joints. Understanding the role of fluids in the interaction of waves with rock joints is of great interest to seismologists, geoscientists, mining engineers and so on. This thesis research aims to determine the fluid effects on the interaction of waves with individual rock joints at the laboratory scale under different test conditions. To this end, an ultrasonic test system in the laboratory was developed and applied for the investigation of the low-intensity wave behaviours across individual rock joints containing fluids. On the other hand, a steel SHPB test configuration was established for the study of the high-intensity stress wave responses of single fluid-filled rock joints. The main contents and results of this thesis research are summarised as follows.

Substantial ultrasonic tests were conducted on various water-saturated clay-rich rock joints using the self-designed ultrasonic test configuration, aiming to determine the effects of water on low-intensity wave attributes of individual clay-rich rock joints. The test results show that the water saturation dependent wave responses of single clay-rich rock joints are strongly affected by the wave mode and the clay mineralogical components. Particularly, for P-wave propagation across single rock joints filled with the kaolinite-dominant gouge, the increasing water saturation enhances wave velocity and attenuation while an opposite trend is found as P-wave passing through the joint filled with the bentonite-dominant gouge. On the other hand, for the propagation of S-waves, an approximately nonlinear decrease trend is observed for the wave velocity while a concave trend (down first and then up) is revealed for wave energy attenuation with the water saturation degree regardless of the clay mineralogical components. Moreover, it is observed that, for both P- and S-waves, the wave velocity and attenuation across the clay-rich rock joint increase with the dominant frequency of incident waves. The above-mentioned findings could be interpreted through a combination of the local flow mechanism, the clay hydration and the wave theories relating to individual rock joints.

The self-developed ultrasonic test system was adopted to carry out acoustic measurements on single fluid-filled rock joints to investigate low-intensity compressional wave propagation and attenuation through individual fluid-filled rock joints. The test results indicate that wave behaviours across single fluid-filled rock joints are strongly affected by the composition and

volume fraction of filling fluids, the joint orientation, and the thermal condition. Specifically, filling water results in faster wave propagation and more wave transmission compared to light oils. In most circumstances, increasing liquid content in a single-liquid filled joint enhances wave velocity and wave energy transmission. For dual-liquid filled rock joints, both wave velocity and wave transmission increase with increasing water content. Regarding the effects of joint orientation, for vertical single-liquid filled joints, wave velocity and wave transmission drastically increase with rising liquid content. By comparison, for horizontal single-liquid filled joints, the liquid content could only dominate wave propagation and attenuation when it exceeds a critical value. With respect to the thermal effect, it is found that a higher temperature results in faster wave velocity and more wave energy transmission through the water-filled rock joint. By contrast, the increasing temperature causes decreases in the wave velocity and wave energy transmission for the light oil-filled joint. The lab-scale results could be attributed to the fluid stiffening and viscous friction of the joint induced by the discrepancies in compressibility and viscosity of various fluids.

The self-established SHPB test system was employed to perform dynamic impacting tests on single fluid-filled rock joints, with the aim of understanding the interaction of high-intensity waves with individual fluid-filled rock joints. Based on the laboratory data, the dynamic mechanical properties, energy evolution characteristics and wave responses of rock specimens with single fluid-filled rock joints were analysed and elaborated. The test results reveal that the smaller joint thickness and the larger joint contact area result in the stiffer joint regardless of the fluid filling condition, causing less wave attenuation and reflection. With respect to the role of filling fluid, the increasing filling liquid content leads to an increase in the joint stiffness, reducing wave attenuation across the joint for most of the scenarios considered. More specifically, for rock joints filled with low-viscosity liquids, wave energy transmission monotonically increases with the filling liquid content. For rock joints filled with high-viscosity liquids, wave energy transmission firstly decreases as liquid content increases from 0% to 25% while it increases with liquid content rising from 25% to 100%. The experimental findings could be well explained by the wave-induced fluid flow and fluid stiffening effect. More importantly, the high-speed camera images provide the evidence for the role of the wave-induced fluid flow in the wave attenuation caused by the fluid-filled rock joints.

The findings in this thesis may not only shed a light on the fluid effects on the interaction of waves and rock joints at a laboratory scale, but also could serve as a guide to interpret seismic wave phenomena relating to fluid-saturated rock discontinuities encountered in many natural

and human-made activities. Moreover, these lab-scale results could make contributions to the validation of the existing theories and provide more insights into the development and improvement of theoretical models in the field of the interplay between stress waves and rock discontinuities.

Keywords: rock joint; fluid; wave behaviour; mechanical behaviour; the ultrasonic test; the SHPB test

## ACKNOWLEDGEMENTS

First and foremost, I would like to express the sincerest gratitude to my supervisor, Dr. DUAN Huan-feng, for his enormous support, continuous encouragement and inspirational supervision throughout my graduate education. He is always willing to share my happiness of the research gains and give me unwavering trust as well as tolerance at the upset time. His vast knowledge in fluid acoustics and dynamics has given me a valuable guidance to the experimental design, data processing and analysis as well as academic paper writing in my research. His infectious enthusiasm and innovative mindset have created a positive research atmosphere for me and other fellow students in our group. Without his immense patience and dedication to my research, I would not have the chance to reach a higher level of education. Most importantly, his rigorous attitudes and creative thinking towards academic research set a high-level standard for me to follow on the road to be a well-qualified researcher. I look forward to more collaborations with him in my upcoming research career. Also, I sincerely thank my co-supervisors, Professors YIN Jian-hua (The Hong Kong Polytechnic University) and ZHAO Jian (Monash University), for their invaluable advice, guidance and encouragement through my graduate study.

My earnest thanks must go to Professor ZHU Jian-bo (Shenzhen University) for his heartfelt guidance, creative ideas and useful discussions during all the stages of my research. I am indebted to him for awarding me the opportunity to pursue this research when I just finished my undergraduate study without any experience in scientific research. His advanced insights into rock dynamics and wave theories have offered the grounding of my understanding of wave propagation and attenuation across rock joints. I am really lucky to have him as a mentor who is available any time when I need help and advice. I have benefited tremendously from his suggestions on my research work and career development.

I am very grateful to Prof. Derek ELSWORTH (Pennsylvania State University) and Prof. LI Jian-chun (Southeast University) for serving on my doctoral committee, reviewing my thesis, as well as providing constructive suggestions and criticisms on my research work. I have benefited tremendously from their critical insights into my research work and their kind encouragement for me. Also, I would like to thank Prof. CHAU Kwok-wing (The Hong Kong Polytechnic University) for serving as the chair of my thesis committee and taking charge of my oral examination.

I really appreciate the help from my colleagues at the Hong Kong Polytechnic University: Dr. ZHOU Tao, Dr. LIAO Zhi-yi, Dr. HAN Dong-ya, Dr. FENG Wei-qiang, Dr. CHE Tong-chuan, Dr. LI Fei, Dr. LI Hua, Dr. WEN Yong, Ms. LI Fang-jin, Mr. CHEN Xing-yu, Mr. PAN Bin and Mr. ZHANG Zi-xin. Particularly, I want to extend my appreciation to the senior technician in the Rock Mechanics Laboratory, Mr. LEUNG Kwok-man, for his friendship to me and continuous assistance with my laboratory work. He was very accessible and resourceful whenever I sought help on my experiments.

I wish to thank my friends for making my PhD life a more fulfilling and enjoyable experience: Ms. HE Hao, Ms. LI Xiao-ying, Ms. CAO Rui-jun, Ms. LI Yashi, Ms. HUANG Lin, Ms. CHEN Sha-yu, Ms. ZHENG Yu-jiao, Ms. LIU Zi-ran, Ms. LI Ying-yuan, Ms. WANG Man-li, Mr. LI Jian, Mr. LIN Guan, Mr. TIE Yu and Mr. HUANG Chun-ying.

Finally, I owe the deepest appreciation to my parents, Mr. LIANG Jun-hui and Mrs. YANG Yong-qin, for their eternal and unconditional love and support throughout my life. The thesis is especially dedicated to my beloved dad, who had struggled against the advanced oesophageal cancer and multiple system atrophy over the past two years. He always offered me unconditional love and support in my graduate study even when he was suffering from the serious illness. His positive attitude and great perseverance maintained through the adversity will continue to encourage me to overcome the obstacles in the rest of my life.

# CONTENTS

Abstract.....	I
Acknowledgements.....	IV
Contents .....	VI
List of Figures .....	XIII
List of Tables .....	XX
List of Symbols and Abbreviations.....	XXI
CHAPTER 1 Introduction .....	1
1.1 Research background and significance.....	1
1.2 Research objectives and scope of the thesis .....	5
1.3 Structure of the thesis.....	6
CHAPTER 2 Literature review .....	9
2.1 Review on theoretical models for describing wave behaviours across individual rock joints.....	9
2.1.1 The displacement discontinuity models.....	10
2.1.2 The layered medium models .....	17
2.2 Review on laboratory investigations into wave behaviours across individual rock joints .....	20
2.2.1 Laboratory investigations using the ultrasonic technique.....	21
2.2.1.1 Fundamental knowledge of the ultrasonic technique.....	21
2.2.1.2 Studies of wave propagation across rock joints without considering stress effects .....	22
2.2.1.3 Studies of wave behaviours across rock joints considering stress effects .....	23
2.2.2 Laboratory investigations using the resonant column techniques .....	27
2.2.2.1 Fundamental knowledge of the resonant column technique.....	27
2.2.2.2 Studies of wave propagation across rock joints using the QSRC apparatus....	30
2.2.2.3 Studies of wave propagation across rock joints using the RCA .....	31

2.2.3 Laboratory investigations using the split Hopkinson pressure bar technique.....	32
2.2.3.1 Fundamental knowledge of the split Hopkinson pressure bar technique .....	32
2.2.3.2 Studies of stress wave propagation through unfilled rock joints using the SHPB technique .....	34
2.2.3.3 Studies of stress wave propagation through filled rock joints using the SHPB technique .....	36
2.2.3.4 Extended studies on the interaction of rock joints and waves using the modified SHPB techniques .....	38
2.3 Existing research gap and concluding remarks.....	39
CHAPTER 3 Research methodologies.....	41
3.1 The ultrasonic pulse-transmission (UPT) test.....	41
3.1.1 Experimental system and calibration .....	41
3.1.1.1 The UPT test set-up and apparatuses .....	41
3.1.1.2 Calibration of the UPT test system .....	43
3.1.2 Data processing methods .....	44
3.1.2.1 Calculation of wave velocities .....	44
3.1.2.2 Calculation of transmission ratio .....	46
3.1.2.3 Calculation of frequency spectra .....	47
3.1.2.4 Calculation of attenuation quality factor.....	48
3.1.2.5 Time-frequency analysis.....	49
3.2 The Split Hopkinson pressure bar (SHPB) test.....	50
3.2.1 Experimental system and calibration .....	50
3.2.1.1 The SHPB test set-up and apparatuses.....	50
3.2.1.2 Pulse shaping .....	53
3.2.1.3 Calibrations of the SHPB test system .....	54
3.2.2 Data processing methods .....	55
3.2.2.1 Pre-processing of the original signals .....	55
3.2.2.2 Stress-strain relations .....	56



3.2.2.3 Specific joint normal stiffness .....	57
3.2.2.4 Energy evolution characteristics .....	58
3.2.2.5 Transmission and reflection coefficients .....	59
3.2.2.6 Seismic attenuation quality factor.....	60
3.2.2.7 Frequency spectra .....	60
3.3 Concluding remarks .....	61
CHAPTER 4 Fluid effects on low-intensity wave behaviours across individual clay-rich rock joints	62
4.1 Introduction.....	62
4.2 Experimental procedure .....	63
4.2.1 Specimen description .....	63
4.2.1.1 Filling clay-rich gouge specimens .....	63
4.2.1.2 Rock specimens .....	65
4.2.2 Test programme .....	67
4.2.2.1 The amplitude sweep tests for measuring rheological properties of clay-rich soil specimens.....	67
4.2.2.2 The UPT tests for determining wave attributes of individual clay-rich soil-filled rock joints.....	68
4.3 Experimental results and analysis .....	69
4.3.1 Rheological properties of infill clay-rich soil specimens .....	69
4.3.2 P-wave attributes of single rock joints filled with wet clay-rich soils.....	71
4.3.2.1 P-wave velocity.....	71
4.3.2.2 P-wave transmission ratio .....	74
4.3.2.3 Time-frequency-energy distribution of P-waves .....	76
4.3.3 S-wave attributes of single rock joints filled with wet clay-rich soils.....	82
4.3.2.1 S-wave velocity.....	82
4.3.2.2 S-wave transmission ratio .....	84
4.3.2.3 Time-frequency-energy distribution of S-waves .....	85

4.4 Discussion .....	93
4.4.1 The discrepancies in P-wave behaviours across single kaolinite- and bentonite-filled rock joints.....	93
4.4.2 The discrepancies in S-wave behaviours across single kaolinite- and bentonite-filled rock joints.....	95
4.4.3 The comparison between P- and S-wave behaviours across single clay-rich soil-filled rock joints .....	97
4.4.4 The physical mechanisms lying behind wave behaviours across single clay-rich soil-filled joints .....	98
4.5 Concluding remarks .....	99
CHAPTER 5 Fluid effect on low-intensity wave behaviours across individual fluid-filled rock joints	103
5.1 Introduction.....	103
5.2 Experimental procedure .....	104
5.2.1 Specimen description .....	104
5.2.1.1 Infill fluid specimens .....	104
5.2.1.2 Rock specimens .....	104
5.2.2 Test programme .....	106
5.2.2.1 The UPT tests for determining the influences of joint parameters .....	106
5.2.2.2 The UPT tests for determining the influences of temperature .....	108
5.3 Results and analysis .....	108
5.3.1 Typical transmitted waveforms.....	108
5.3.1.1 Transmitted waveforms for fluid-filled rock joints with different fluid compositions and spatial orientation.....	108
5.3.1.2 Transmitted waveforms for fluid-filled rock joints under different thermal conditions.....	110
5.3.2 Effects of fluid type and composition on wave behaviours across single fluid-filled rock joints.....	111
5.3.2.1 Wave velocity .....	111

5.3.2.2 Transmission ratio.....	114
5.3.2.3 Frequency spectra .....	117
5.3.2.4 $Q$ value.....	121
5.3.3 Effects of joint orientation on wave behaviours across single fluid-filled rock joints .....	124
5.3.3.1 Wave velocity .....	124
5.3.3.2 Transmission ratio.....	125
5.3.3.3 Frequency spectra .....	126
5.3.3.4 $Q$ value.....	127
5.3.4 Effects of temperature on wave behaviours across single fluid-filled rock joints .....	127
5.3.4.1 Wave velocity .....	127
5.3.4.2 Transmission ratio.....	128
5.3.4.3 Frequency spectra .....	129
5.3.4.4 $Q$ value.....	130
5.4 Discussion.....	131
5.4.1 Comparison with previous studies of fluid effects on wave propagation in fluid-saturated rock masses.....	131
5.4.2 Comparison with previous studies of thermal effects on wave propagation in fluids and fluid-saturated geomaterials .....	132
5.4.3 Interpretation from acoustics in fluids .....	134
5.4.4 Influences of the incident wave frequency .....	136
5.5 Concluding remarks.....	140
CHAPTER 6 Fluid effects on the high-intensity stress wave BEHAVIOURS ACROSS individual fluid-filled rock joints.....	142
6.1 Introduction.....	142
6.2 Experimental procedure.....	143
6.2.1 Specimen description.....	143

6.2.1.1 Rock specimens .....	143
6.2.1.2 Filling fluid specimens.....	147
6.2.2 Test programme .....	148
6.2.2.1 The SHPB tests on single water-filled rock joints .....	148
6.2.2.2 The SHPB tests on single rock joints filled with viscous liquids .....	148
6.3 Results and analysis .....	149
6.3.1 The interaction of stress waves with single fluid-filled rock joints .....	149
6.3.1.1 Typical signals recorded by the strain gauges .....	149
6.3.1.2 Stress-deformation relations of single fluid-filled rock joints .....	152
6.3.1.3 Specific stiffnesses of single fluid-filled rock joints.....	157
6.3.1.4 Energy evolution characteristics of the rock specimens with single fluid-filled joints.....	159
6.3.1.5 Transmission and reflection coefficients for the rock specimens with single fluid-filled joints .....	164
6.3.1.6 Seismic attenuation factor for the rock specimens with single fluid-filled joints .....	168
6.3.1.7 Frequency spectra for the rock specimens with single fluid-filled joints .....	170
6.3.2 The effects of the fluid viscosity on the interaction of stress waves with single fluid-filled rock joints .....	174
6.3.2.1 The influence of fluid viscosity on the specific normal stiffness of single fluid-filled rock joints .....	175
6.3.2.2 The influence of fluid viscosity on transmission and reflection coefficients for the rock specimens with single fluid-filled joints .....	177
6.3.2.3 The influence of fluid viscosity on seismic quality factor for the rock specimens with single fluid-filled joints.....	179
6.3.3 High-speed images for the dynamic responses of single fluid-filled rock joints under the passage of the high-intensity stress waves .....	180
6.4 Discussion .....	186

6.4.1 Discussion on the possible mechanisms lying behind the laboratory observations .....	186
6.4.2 Comparison with the findings of the low-intensity wave behaviours across single fluid-filled rock joints .....	189
6.5 Concluding remarks .....	190
CHAPTER 7 Summary and future work .....	193
7.1 Summary of the thesis work .....	193
7.2 Future work .....	197
References .....	200

# LIST OF FIGURES

Figure 1.1 Overview of the research subjects of wave propagation in rock masses (modified after Zhao et al. (1999)).	2
Figure 1.2 Some examples for the fluid-saturated rock joints presented in nature and practical engineering: (a). The conceptual model of groundwater flow at the south spring study area, Coles Hill, Virginia (adopted from Gannon et al., 2012); (b). the conceptual model of fluid migration in Loiano, Italy (adopted from Del Sole et al., 2020); (c). the conceptual model for the geology of the fractured basement reservoir in the Lancaster field (adopted from Holdsworth et al., 2020); (d). the conceptual depiction of groundwater movement in the aquifers of the Appalachian Plateaus (adopted from Panel, 2016); (e). the conceptual model of the marine environment during deposition of the first extensive SEDEX bed (M3) in the Foss deposit of the Scotland Grampian region (adopted from Moles et al., 2015).	4
Figure 1.3 The framework for the organization of the main body of the thesis.	8
Figure 2.1 Transmitted, reflected and converted components of waves at the rock joint (i.e., a displacement discontinuity) for incident (a) P-wave, (b) SV-wave, and (c) SH-wave (modified from Pyrak-Nolte et al. (1990)).	10
Figure 2.2 Typical experimental setup for studying wave behaviours across rock joints subjected to mix-mode loadings: (a). single-direct-shear configuration (modified from Hedayat et al., 2014), (b) double-direct-shear configuration (modified from Kenigsberg et al., 2019).	25
Figure 2.3 The schematic and Lagrangian wave propagation diagram of a conventional SHPB system (modified after Zhang (2014)).	33
Figure 3.1 The self-established ultrasonic pulse-transmission test system used in this research: (a). the schematic of the test system, (b). the laboratory photograph of the test system.	42
Figure 3.2 The waveforms of transmitted pulses obtained from the calibration tests on the aluminium specimen using two ultrasonic transducer pairs for generating (a). 1-MHz P-waves and (b). 1-MHz S-waves.	43
Figure 3.3 Illustration of determining the travel time and peak-to-peak amplitude of the first arrival pulses based on laboratory data for: (a). P-waves and (b). S-waves.	46
Figure 3.4 The examples for the demonstration of isolating first arrival pulses using the appropriate tapers.	47

Figure 3.5 The self-established split Hopkinson pressure bar test system used in this research: (a). the schematic of the test system, (b). the laboratory photograph of the test system. ....	52
Figure 3.6 The selection of an appropriate pulse shaper: (a). the shaped incident pulses produced by different shapers, (b). the pulse shaper used in this study. Herein, $t$ and $d$ represent the thickness and diameter of the copper disc, respectively, and $m$ is the weight of the plasticine. ....	53
Figure 3.7 The verification of the stress equilibrium of the self-designed SHPB test system by conducting calibration tests on: (a) an intact rock specimen, (b) a typical jointed rock specimen used in this experiment. Note that the Inc. Stress, Ref. Stress and Tra. Stress denote the incident, reflected and transmitted stress waves, respectively, and (Inc. + Ref.) Stress represents the sum of incident and reflected stress waves.....	54
Figure 3.8 The noise elimination of a typical original signal obtained from the SHPB test using the Kalman filter: (a) a typical original signal, (b) the denoised signal, and (c) the comparison between the original and denoised pulses.....	55
Figure 3.9 The post-processing of the denoised signals to ascertain the stress and strain in the tested rock specimen: (a). the denoised signals collected from a SHPB test; (b). the stress equilibrium check; (c). the time histories of stress and strain; (d) the stress-strain curve.....	56
Figure 3.10 The energy evolution characteristics of a typical jointed rock sample in the SHPB test: (a) the time history curves of the incident, transmitted and reflected wave energy, and (b) the time history curve of the absorption energy.....	58
Figure 4.1 The grain-size distribution curves for clayey soils used in this study.....	64
Figure 4.2 The gabbro rock used in the study: (a). The jointed and intact rock specimens; (b) the representative microphotograph of gabbro. ....	66
Figure 4.3 The Modular Compact Rheometer with a parallel-plate system for conducting amplitude sweep tests .....	67
Figure 4.4 The shear moduli and viscosities of kaolinite specimens (a), (c) and bentonite specimens (b), (d) measured by the amplitude sweep tests. Herein, $S_r$ denotes the degree of water saturation of clay-rich specimens.....	70
Figure 4.5 P-wave velocity across rock samples with single: (a). kaolinite-filled joints, (b) Bentonite-filled joints. Herein, $V_{RP-0.1}$ and $V_{RP-1}$ represent P-wave velocities across the entire rock specimen for 0.1-MHz and 1-MHz incident waves, respectively; $V_{JP-0.1}$ and $V_{JP-1}$ denote P-wave velocities across the clay-rich joint for 0.1-MHz and 1-MHz incident waves, respectively. ....	72

Figure 4.6 P-wave transmission ratio across rock samples with single: (a). kaolinite-filled joints, (b) Bentonite-filled joints. Herein, $T_{RP-0.1}$ and $T_{RP-1}$ represent transmission ratios across the rock specimen for 0.1-MHz and 1-MHz incident P-waves, respectively. ....	74
Figure 4.7 Time-frequency maps for transmitted 0.1-MHz P-waves across individual rock joints filled with kaolinite at different saturation degrees. Herein, $S_r$ denotes the degree of water saturation of clay-rich specimens.....	78
Figure 4.8 Time-frequency maps for transmitted 1-MHz P-waves across individual rock joints filled with kaolinite at different saturation degrees. Herein, $S_r$ denotes the degree of water saturation of clay-rich specimens.....	79
Figure 4.9 Time-frequency maps for transmitted 0.1-MHz P-waves across individual rock joints filled with bentonite at different saturation degrees. Herein, $S_r$ denotes the degree of water saturation of clay-rich specimens.....	80
Figure 4.10 Time-frequency maps for transmitted 1-MHz P-waves across individual rock joints filled with bentonite with different saturation degrees. Herein, $S_r$ denotes the degree of water saturation of clay-rich specimens.....	81
Figure 4.11 S-wave velocity across rock samples with single: (a). kaolinite-filled joints, (b) Bentonite-filled joints. Herein, $V_{RS-0.25}$ , $V_{RS-0.5}$ and $V_{RS-1}$ represent S-wave velocities across the entire rock specimen for 0.25-MHz, 0.5-MHz and 1-MHz incident waves, respectively; $V_{JS-0.25}$ , $V_{JS-0.5}$ and $V_{JS-1}$ represent S-wave velocities across the clay-rich joint for 0.25-MHz, 0.5-MHz and 1-MHz incident waves, respectively. ....	82
Figure 4.12 S-wave transmission ratio across rock samples with single: (a). kaolinite-filled joints, (b) Bentonite-filled joints. Herein, $T_{RS-0.25}$ , $T_{RS-0.5}$ and $T_{RS-1}$ represent transmission ratios across the rock specimen for 0.25-MHz, 0.5-MHz and 1-MHz incident S-waves, respectively. ....	84
Figure 4.13 Time-frequency maps for transmitted 0.25-MHz S-waves across individual rock joints filled with kaolinite at different saturation degrees. Herein, $S_r$ denotes the degree of water saturation of clay-rich specimens.....	86
Figure 4.14 Time-frequency maps for transmitted 0.5-MHz S-waves across individual rock joints filled with kaolinite at different saturation degrees. Herein, $S_r$ denotes the degree of water saturation of clay-rich specimens.....	87
Figure 4.15 Time-frequency maps for transmitted 1-MHz S-waves across individual rock joints filled with kaolinite at different saturation degrees. Herein, $S_r$ denotes the degree of water saturation of clay-rich specimens.....	88



Figure 4.16 Time-frequency maps for transmitted 0.25-MHz S-waves across individual rock joints filled with bentonite at different saturation degrees. Herein, $S_r$ denotes the degree of water saturation of clay-rich specimens.....	89
Figure 4.17 Time-frequency maps for transmitted 0.5-MHz S-waves across individual rock joints filled with bentonite at different saturation degrees. Herein, $S_r$ denotes the degree of water saturation of clay-rich specimens.....	90
Figure 4.18 Time-frequency maps for transmitted 1-MHz S-waves across individual rock joints filled with bentonite at different saturation degrees. ....	91
Figure 5.1 Materials used in this study: (a) Light oils, (b) Gabbro rock specimens.....	104
Figure 5.2 Selected transmitted waveforms for P-waves propagation through rock samples with single-liquid filled joints: 100-kHz input waves across (a) vertical and (b) horizontal joints; 1-MHz input waves across (c) vertical and (d) horizontal joints. ....	109
Figure 5.3 Selected transmitted waveforms for P-waves propagation through rock samples with dual-liquid filled joints: 100-kHz input waves through (a) vertical and (b) horizontal joints; 1-MHz input waves through (c) vertical and (d) horizontal joints.....	110
Figure 5.4 The typical waveforms of transmitted pulses through jointed rock samples with: (a) single water-filled joints; and (b) single M68-filled joints under different thermal conditions. ....	111
Figure 5.5 The average wave velocities in single-liquid filled rock joints and corresponding jointed rock samples: (a) and (b) For 100-kHz and 1-MHz incident P-waves across vertical joints, respectively; (c) and (d) for 100-kHz and 1-MHz incident P-waves across horizontal joints, respectively. Herein, R and J represent the rock sample and joint, respectively. ....	112
Figure 5.6 The average wave velocities in dual-liquid filled rock joints and corresponding jointed rock samples: (a) and (b) For 100-kHz and 1-MHz incident P-waves across vertical joints, respectively; (c) and (d) for 100-kHz and 1-MHz incident P-waves across horizontal joints, respectively. Herein, R and J represent the rock sample and joint, respectively. ....	113
Figure 5.7 Transmission ratios for rock samples with single-liquid filled rock joints: (a) and (b) For 100-kHz and 1-MHz incident P-waves across vertical joints, respectively; (c) and (d) for 100-kHz and 1-MHz incident P-waves across horizontal joints, respectively. ....	114
Figure 5.8 Transmission ratios for rock samples with dual-liquid filled rock joints: (a) and (b) For 100-kHz and 1-MHz incident P-waves across vertical joints, respectively; (c) and (d) for 100-kHz and 1-MHz incident P-waves across horizontal joints, respectively. ....	116
Figure 5.9 Frequency spectra of transmitted waves through rock samples with different liquid volume content in single-liquid filled joints: 100-kHz P-waves across (a) vertical and (b)	

horizontal joints; 1-MHz P-waves across (c) vertical and (d) horizontal joints. Note that the single-liquid filled joint is filled with one kind of liquids among water, BL10 and M68. For water- filled joints, $P\_L$ represents volume content of water; for BL10-filled joints, $P\_L$ stands for volume content of BL10; for M68-filled joints, $P\_L$ refers to volume content of M68. . . . .	117
Figure 5.10 Frequency spectra of transmitted waves through rock samples with dual-liquid filled joints: 100-kHz input waves through (a) vertical and (b) horizontal joints; 1-MHz input waves through (c) vertical and (d) horizontal joints. Note that the dual-liquid filled joint is fully filled with two kinds of liquids among water, BL10 and M68. $P\_L$ represents volume contents of water while $P\_O$ refers to volume contents of light oil (BL10 or M68). . . . .	120
Figure 5.11 Attenuation quality factor $Q$ of rock samples with single-liquid filled rock joints versus liquid content in rock joint: (a) and (b) for 100-kHz and 1-MHz incident P-waves across vertical joints, respectively; (c) and (d) for 100-kHz and 1-MHz incident P-waves across horizontal joints, respectively. . . . .	122
Figure 5.12 Attenuation quality factor $Q$ of rock samples with dual-liquid filled rock joints vs water content in rock joint: (a) and (b) for 100-kHz and 1-MHz incident P-waves across vertical joints, respectively; (c) and (d) for 100-kHz and 1-MHz incident P-waves across horizontal joints, respectively. . . . .	123
Figure 5.13 Wave velocities versus temperature for: (a) water-filled joint and the corresponding jointed rock sample; and (b) M68-filled joint and the corresponding jointed rock sample. Wave speed of water ( $V_{\text{water}}$ ) measured by Wilson (1959) and wave speed of one kind of light oil ( $V_{\text{oil}}$ ) measured by Wang and Nur (1991) are also presented in the figure. . . . .	128
Figure 5.14 Transmission ratios versus temperature for rock samples with different individual fluid-filled joints. $T_{R\_W}$ and $T_{R\_M68}$ represent transmission ratios across rock samples with single water-filled and M68-filled joints, respectively. . . . .	129
Figure 5.15 Thermal effect on spectral contents of waves transmitted through jointed rock samples with: (a) single water-filled joints; and (b) single M68-filled joints. . . . .	129
Figure 5.16 The $Q$ values versus temperature for rock samples with different individual fluid-filled joints. $Q_{R\_W}$ and $Q_{R\_M68}$ represent attenuation quality factors across rock samples with single water-filled and M68-filled joints, respectively. . . . .	130
Figure 5.17 Time-frequency maps for 100-kHz P-waves transmitted through air-water filled rock joints with different water contents: (a) - (e) vertical rock joints, (f) - (j) horizontal joints. Herein, $P\_W$ stands for water volume content in the joint. . . . .	138

Figure 5.18 Time-frequency maps for 1-MHz P-waves transmitted through air-water filled rock joints with different water contents: (a) - (e) vertical rock joints, (f) - (j) horizontal joints. Herein, $P\_W$ stands for water volume content in the joint .....	139
Figure 6.1 The illustration of a typical jointed rock specimen used in this experiment. ....	145
Figure 6.2 The rock cylinders with single rough surface used in this experiment, which were mainly divided into four groups: (a) Group GA, (b) Group GB, (b) Group GC and (b) Group GD according to the geometrical properties of the rough surface. ....	145
Figure 6.3 Typical waveforms obtained from the SHPB tests for various jointed rock specimens (a) GA-I-S1, (b) GA-II-S1, (c) GA-III-S1, (d) GB-I-S1, (e) GB-II-S1, (f) GB-III-S1, (g) GC-I-S1, (h) GC-II-S1, (i) GC-III-S1 under different filling conditions. Note that the black and red curves represent the signals recorded by the strain gauges mounted on the incident and transmitted bars, respectively. Besides, $P\_W$ stands for the filling water volume content in the rock joint. ....	151
Figure 6.4 The typical stress-deformation curves of single fluid-filled rock joints for different test cases: the effects of water content within the joint. ....	152
Figure 6.5 The typical stress-deformation curves of single fluid-filled rock joints for different test cases: the effects of the joint thickness. ....	154
Figure 6.6 The typical stress-deformation curves of single fluid-filled rock joints for different test cases: the effects of the JMC. ....	155
Figure 6.7 The calculated joint normal specific stiffness of individual fluid-filled rock joints: (a) - (c) for the effects of the water content within the joint, (d) - (f) for the effects of the joint thickness, and (g) - (i) for the effects of the JMC. ....	157
Figure 6.8 The representative energy-time history curves for the tested rock specimens with single fluid-filled joints at an approximately identical JMC of 0.443: (a)-(e) for the joint thickness of 2 mm, (f)-(j) for the joint thickness of 4 mm, (k)-(o) for the joint thickness of 6 mm. ....	162
Figure 6.9 The representative energy-time history curves for the tested rock specimens with single fluid-filled joints at an approximately identical joint thickness of 4 mm: (a)-(e) for JMC of 0.255, (f)-(j) for the JMC of 0.443, (k)-(o) for the JMC of 0.505. ....	163
Figure 6.10 The calculated transmission and reflection coefficients for various fluid-filled rock joints: the effects of the water content within the joint. ....	164
Figure 6.11 The calculated transmission and reflection coefficients for various fluid-filled rock joints: the effects of the joint thickness. ....	166

Figure 6.12 The calculated transmission and reflection coefficients for various fluid-filled rock joints: the effects of the JMC. ....	167
Figure 6.13 The calculated seismic attenuation factor $Q$ for the tested rock specimens with various single fluid-filled rock joints: (a) - (c) for the effects of the water content within the joint, (d) - (f) for the effects of the joint thickness, and (g) - (i) for the effects of the JMC..	170
Figure 6.14 The frequency spectra of the incident (SA_I), transmitted (SA_T) and reflected waves (SA_R) for the tested rock specimens with single fluid-filled joints at an approximately identical JMC of 0.443: (a)-(e) for the joint thickness of 2 mm, (f)-(j) for the joint thickness of 4 mm, (k)-(o) for the joint thickness of 6 mm. ....	172
Figure 6.15 The frequency spectra of the incident (SA_I), transmitted (SA_T) and reflected waves (SA_R) for the tested rock specimens with single fluid-filled joints at an approximately identical joint thickness of 4 mm: (a)-(e) for JMC of 0.255, (f)-(j) for the JMC of 0.443, (k)-(o) for the JMC of 0.505.....	173
Figure 6.16 The normalized variation in the specific stiffness of single fluid-filled rock joints as functions of (a) the liquid content and (b) the viscosity of filling liquid, respectively. ....	176
Figure 6.17 The normalized variation in the transmission and reflection coefficients for single fluid-filled rock joints as functions of (a), (b) the liquid content and (c), (d) the viscosity of filling liquid, respectively. ....	177
Figure 6.18 The normalized variation in the seismic attenuation quality for single fluid-filled rock joints as functions of (a) the liquid content and (b) the viscosity of filling liquid, respectively. ....	179
Figure 6.19 The selected high-speed images for the single fluid-filled rock joints at an approximately identical JMC of 0.443 under the impact loading: the effects of the joint thickness.....	182
Figure 6.20 The selected high-speed images for the single fluid-filled rock joints at an approximately identical JMC of 0.443 during the passage of the high-intensity stress waves: the effects of the joint thickness.....	183
Figure 6.21 The selected high-speed images for individual rock joints filled with different viscous liquids.....	185

## LIST OF TABLES

Table 3.1 The results of the error analysis on waveforms obtained from the calibration of UPT test system using different transducer pairs. ....	44
Table 4.1 Some basic properties of clayey soils used in the study .....	64
Table 4.2 The information about the prepared clay-rich soil specimens used in the study .....	65
Table 4.3 Physical and mechanical properties of rock specimens used in the study .....	66
Table 4.4 The pre-setting parameters for the amplitude sweep tests conducted in this study .....	68
Table 4.5 The information about waves generated by ultrasonic transducers and transmitted waves across the intact rock specimen in this study .....	69
Table 5.1 Properties of filling fluids at room temperature (about 20 °C) .....	105
Table 5.2 Kinematic viscosities of water and M68 (light oil) at different temperatures .....	105
Table 5.3 Horizontal and vertical fluid-filled joints under different filling conditions tested in this study .....	107
Table 5.4 Rock joints filled with fluid (water or M68) at different temperatures .....	108
Table 5.5 Maximum amplitudes of frequency spectra for transmitted waves through rock samples with different fluid-filled joints.....	121
Table 6.1 The parameters for all jointed rock specimens used in this experiment.....	146
Table 6.2 The summary of filling fluid specimens used in this study .....	147
Table 6.3 The summary of test conditions for fluid-filled rock joints used in this part .....	149

# LIST OF SYMBOLS AND ABBREVIATIONS

$A$	Cross-sectional area
$A_t, A_i$	The peak-to-peak amplitudes of initial wave transmitted through the jointed rock sample and the intact rock sample, respectively
$A(f)$	Acceleration function
$D$	Damping ratio
$D_t$	The outer diameter of the tube
$e_t$	The wall thickness of the tube
$E$	Young's modulus of material
$E_t$	The elastic modulus of the tube
$f$	Wave frequency
$ G^* $	Complex shear modulus of soil specimen
$I, I_0$	Mass polar moments of inertia for the tested sample and driving plate, respectively
$K_{F1}, K_{F2}$	Bulk moduli of fluids in the rock joint
$K_{liq}, K_{air}$	Bulk moduli of the liquid and air, respectively
$l_s, l_j$	The lengths of rock specimen and rock joint, respectively
$L, l$	Length of the tested sample
$L_j, L_j$	The length of the rock matrix and the rock joint, respectively
$m$	Mass of the tested sample
$P_L, P_W, P_O$	Volume contents of liquid, water and light oil in the joint, respectively
$Q, Q_{sei}$	Attenuation quality factor
$Q_{R\_Water}, Q_{R\_BL10}, Q_{R\_M68}$	$Q$ values of rock samples containing water-filled, BL10-filled and M68-filled joints, respectively
$Q_{R\_WB}, Q_{R\_WM}$	$Q$ values of rock samples containing water-BL10 filled and water-M68 filled joints, respectively
$R_e$	Reflected coefficient obtained from stress wave energy

$SA\_I, SA\_T, SA\_R$	The frequency spectra of the incident, transmitted and reflected waves for the tested rock specimens
$S_r$	Saturation degree of soil specimens
$t$	The travel time of wave through the rock specimen
$t_a$	The measured arrival time of wave through the rock specimen
$t_d$	The delay time
$t_r, t_j$	The travel time of waves across the rock matrix and the rock joint, respectively
$T_e$	Transmission coefficient obtained from stress wave energy
$T_{R\_Water}, T_{R\_BL10}, T_{R\_M68}$	Transmission ratio of rock samples containing water-filled, BL10-filled and M68-filled joints, respectively
$T_{R\_WB}, T_{R\_WM}$	Transmission ratio of rock samples containing water-BL10 filled and water-M68 filled joints, respectively
$T_{RP-0.1}, T_{RP-1}$	Transmission ratio across the jointed rock specimen for P-waves at the central frequencies of 0.1 and 1MHz, respectively
$T_{RS-0.25}, T_{RS-0.5}, T_{RS-1}$	Transmission ratio across the jointed rock specimen for S-waves at the central frequencies of 0.25, 0.5 and 1MHz, respectively
$u_x, u_y, u_z$	Displacements of the joint along the x-, y- and z-axis, respectively
$\Delta u_R, \Delta u_J, \Delta u$	Deformation of the host rock matrix, the rock joint and the jointed rock specimen, respectively
$V_P, V_S$	Wave velocity for P- and S-waves, respectively
$V_{JP-0.1}, V_{JP-1}$	Wave velocity across the rock joint for P-waves at the central frequencies of 0.1 and 1 MHz, respectively
$V_{JS-0.25}, V_{JS-0.5}, V_{JS-1}$	Wave velocity across the rock joint for S-waves at the central frequencies of 0.25, 0.5 and 1 MHz, respectively
$V_{J\_Water}, V_{J\_BL10}, V_{J\_M68}$	Wave velocities across water-filled, BL10-filled and M68-filled joints, respectively

$V_{J\_WB}, V_{J\_WM}$	Wave velocities across water-BL10 filled and water-M68 filled joints, respectively
$V_{RP-0.1}, V_{RP-1}$	Wave velocity across the jointed rock specimen for P-waves at the central frequencies of 0.1 and 1 MHz, respectively
$V_{RS-0.25}, V_{RS-0.5}, V_{RS-1}$	Wave velocity across the jointed rock specimen for S-waves at the central frequencies of 0.25, 0.5 and 1 MHz, respectively
$V_{R\_Water}, V_{R\_BL10}, V_{R\_M68}$	Wave velocities of rock samples containing water-filled, BL10-filled and M68-filled joints, respectively
$V_{R\_WB}, V_{R\_WM}$	Wave velocities of rock samples containing water-BL10 filled and water-M68 filled joints, respectively
$W_A$	The absorbed energy
$W_I, W_T, W_R$	The energy of the incident, transmitted and reflected waves, respectively
$\Delta W$	The dissipated energy
$Z_P, Z_S$	Seismic impedances for P- and S-waves, respectively
$\alpha$	Attenuation coefficient
$\theta_A, \theta_B$	Incident and transmitted angles for P-wave
$\phi_A, \phi_B$	Reflected and transmitted angles for S-waves
$\phi_{F1}, \phi_{F2}$	Volume fractions of fluids in the joint
$\sigma_x, \sigma_y, \sigma_z$	Stresses applied to the joint along the x-, y- and z-axis, respectively
$\sigma_{\Delta u_J/2}$	The compressive stress at the value of joint closure equalling to $\Delta u_J / 2$
$\varepsilon_{In}, \varepsilon_{Tr}, \varepsilon_{Re}$	The incident, transmitted and reflected strain waves obtained from the SHPB test, respectively
$\eta$	Dynamic viscosity
$\eta_{F1}, \eta_{F2}$	Dynamic viscosities of fluids in the rock joint
$\eta_x, \eta_z, \eta_y$	The joint specific viscosity along the x-, y- and z-axis, respectively



$ \eta^* $	Complex viscosity of soil specimen
$\kappa_x, \kappa_y, \kappa_z$	The joint specific stiffness along the x-, y- and z-axis, respectively
$\kappa_x$	Joint specific normal stiffness
$\rho$	Density of material
$\rho_{F1}, \rho_{F2}$	Densities of fluids in the rock joint
$\rho_{liq}, \rho_{air}$	Densities of liquid and air, respectively
$\nu$	Poisson's ratio
$\omega$	Wave angular frequency
BL10	Shell Morlina S2 BL10 light oil
CSD	Controlled shear deformation
CSS	Controlled shear stress
CWT	Continuous-wavelet transform
CYM	Continuously yielding model
DDM	Displacement discontinuity model
DDT	Displacement discontinuity theory
DSDM	Displacement and stress discontinuity model
DVDM	Displacement and velocity discontinuity model
FB-WIFF	Fracture-to-background wave-induced fluid flow
FF-WIFF	Fracture-to-fracture wave-induced fluid flow
FFT	Fast Fourier transform
fps	Frames per second
FRC	Fracture roughness coefficient
IFD	Image fractal dimension
IW_P	Incident P-wave
IW_SH	Incident SH-wave
IW_SV	Incident SV-wave
JMC	Joint matching coefficient
JRC	Joint roughness coefficient
LMT	Layered medium theory
LVE	Linear viscoelastic
M68	Shell Tellus S2 M68 light oil

MOC	Method of characteristics
NDT	Non-destructive testing
PC	Personal computer
QSRC	Quasi-static resonant column
RCA	Resonant column apparatus
RW_P	Reflected P-wave
RW_SH	Reflected SH-wave
RW_SV	Reflected SV-wave
SHPB	Split Hopkinson pressure bar
SHRB	Split Hopkinson rock bar
SSP	Split shear plates
SVI	Sound velocity index
TDRM	Time-domain recursive method
TLIM	Thin-layer interface model
TTL	Transistor-transistor-logic
TW_P	Transmitted P-wave
TW_SH	Transmitted SH-wave
TW_SV	Transmitted SV-wave
UPT	Ultrasonic pulse-transmission
WIFF	Wave-induced fluid flow

# CHAPTER 1 INTRODUCTION

## 1.1 Research background and significance

Rock discontinuities on all scales from micro-cracks and pores to joints and fractures to bedding planes and tectonic faults are pervasive in the Earth's crust (John, 1969), where the joints, fractures and faults are generally termed as rock joints (Cook, 1992). Rock joints, which may be closed, open or filled with various materials, such as calcite, dolomite, gypsum, quartz sand, clay, water, gas, oil and magma (Jaeger et al., 2009), play a dominant role in mechanical, hydraulic, thermal and wave characteristics of rock masses (Bandis et al., 1983, Barton et al., 1985, Pollard and Aydin, 1988, Cook, 1992, Zhao and Brown, 1992, Pyrak-Nolte, 1996, Zimmerman and Bodvarsson, 1996, Elsworth et al., 2016). The knowledge concerning the interaction of waves with rock joints is of great interest to geology, hydrogeology, seismology, geo-thermal engineering, mining engineering, petroleum engineering, tunneling engineering and so on.

In practice, waves have been a popular and efficient tool to image and map the subsurface because of the sensitivity of wave velocities, amplitudes, spectral contents to rock joints. To be specific, a number of geophysical methods, e.g., ultrasonic imaging (at  $10^6$  Hz frequency range), sonic wellbore logging (at several  $10^4$  Hz frequency) and vertical seismic profiling (below 200 Hz), have been well developed and widely applied to detect, monitor and characterize rock joints in practical applications (Rienstra and Hirschberg, 2004, Brossier et al., 2009, Montone and Mariucci, 2015). Therefore, the understanding of wave behaviours across rock joints could serve as a guidance to the interpretation of seismic data obtained from the acoustic-based field tests. It should be mentioned that waves generated by those geophysical techniques commonly take very low energy that is insufficient to exert significant deformation and destruction on rock joints.

Furthermore, waves are commonly encountered in many natural events (e.g., earthquakes, crustal movements, fault reactivation and volcanic eruption) and human-made activities (e.g., rock bursts, percussive drilling, engineering blasting and explosion). In particular, the waves associated with dynamic stresses often carry high-intensity energy responsible for the evident deformations of rock joints (e.g., opening, closing and slippery displacements) as well as severe damage to surrounding rock masses, underground construction, ground infrastructures, etc (Cai, 2001, Berta, 1994). In light of that, understanding the interaction of high-intensity stress waves

and rock joints is crucial for the design and implementation of protective projects, monitoring and even predicting hazardous activities, as well as assessing and detecting the stability and damages of rock masses (Barla et al., 2010).

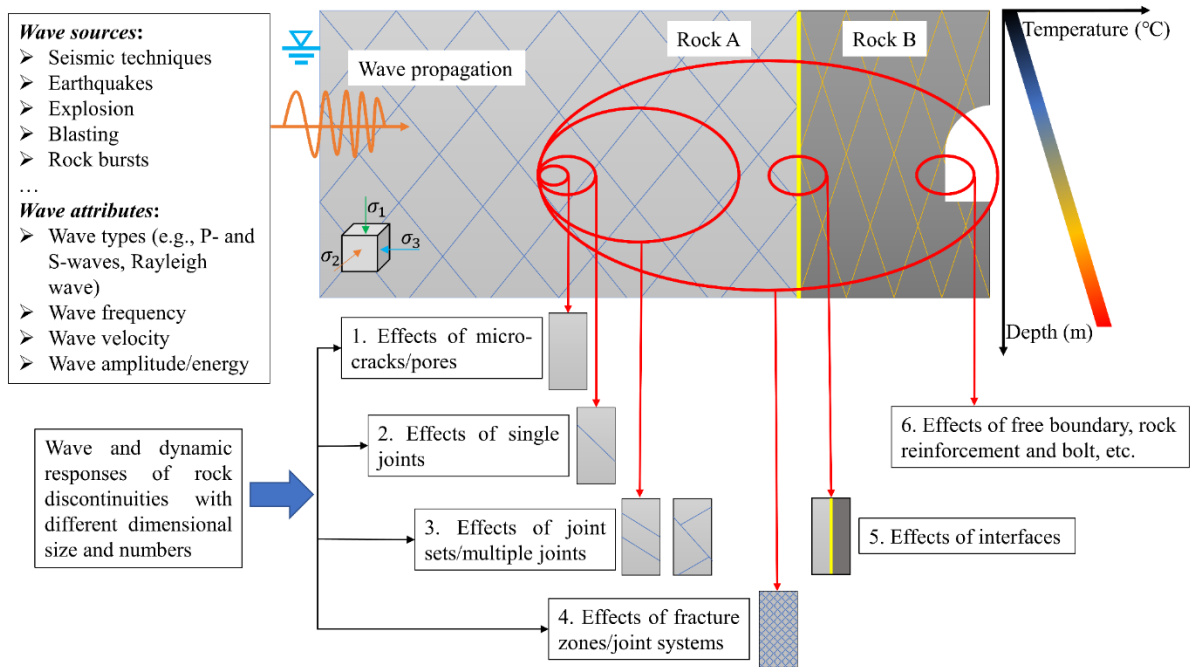


Figure 1.1 Overview of the research subjects of wave propagation in rock masses (modified after Zhao et al. (1999)).

From the academic perspective, the research issues relating to wave propagation in rock masses can be summarised as: ① the effects of micro-cracks and pores on wave and dynamic responses of rock masses; ② the interaction of individual rock joints and waves; ③ the interaction of waves and multiple joints as well as joint sets; ④ the interaction of waves and fracture zones as well as joint systems; ⑤ the interaction of waves and interfaces between different rock materials; ⑥ the influences of free boundaries and rock constructions on wave and dynamic responses of rock masses, as illustrated in Figure 1.1 (Zhao et al., 1999). Accordingly, it can be concluded that understanding the interaction of waves with rock joints is utmost to establish a comprehensive body of knowledge of wave propagation in rock masses.

In view of the above-mentioned great practical and scientific importance, the interaction of waves with rock joints has been a subject of active research for decades (Pyrak-Nolte, 1988, Hopkins, 1991, Nakagawa, 1998, Zhao, 2004, Resende, 2010, Zhu, 2011, Hedayat, 2013). Given that the knowledge concerning the wave attributes of single rock joints provides the essential insights for understanding the effects of multiple joints and joint systems on wave

propagation in rock masses (Cook, 1992), substantial theoretical and experimental studies have been conducted to determine the interaction of waves with individual rock joints (Suarez-Rivera et al., 1992, Roy and Pyrak-Nolte, 1997, Zhao and Cai, 2001, Ju et al., 2007, Li et al., 2010, Wu et al., 2014). The general conclusion from these efforts is that single rock joints could cause a diminution in wave energy, a shift in phase velocity and a change in frequency contents, whilst the propagating waves may lead to nonlinear deformations (e.g., the frictional slip and closure of aperture) and even damage of the joint (e.g., the crushing of asperities or infilling materials) (Schoenberg, 1980, Pyrak-Nolte et al., 1990, Li et al., 2014). Moreover, it is found that the interplay between waves and individual rock joints is strongly affected by various parameters, including the joint parameters (e.g., joint roughness, joint thickness and joint orientation), filling conditions (e.g., the mineralogical components and humidity of filling materials), environmental factors (e.g., stress states and temperature) and wave characteristics (e.g., the wave mode, amplitude and dominant frequency) (Li et al., 2011, Li et al., 2017).

Geological observations recognize that rock joints provide the main conduits and space for fluid flow, transport, migration, and storage, producing abundant fluid-saturated rock joints in natural and practical activities (see some examples presented in Figure 1.2). In this context, the role of fluid in the interaction of waves with individual rock joints has been an important hotspot for its conceptual and practical significance in the Earth, environmental and engineering sciences. To the best of our knowledge, many theoretical and numerical investigations have been conducted to determine the fluid effects on the interaction of waves with single rock joints, where mainly two scenarios are considered in view of the hydrological properties of the host rock. One situation is to regard the fluid-saturated joint as being embedded within the homogenous, impermeable, and elastic host rock (Schoenberg, 1980, Fehler, 1982, Pyrak-Nolte et al., 1990, Liu et al., 2000, Zhu et al., 2011, Li et al., 2013, Oelke et al., 2013). In this respect, the viscous coupling together with the viscous frictional loss are induced by the saturating fluids. Correspondingly, the filling fluid stiffens the joint while it causes more energy dissipation due to the viscous friction. The other more realistic scenario is to consider the fluid-saturated rock joint as being embedded in a porous and permeable host rock (Nakagawa and Schoenberg, 2007, Rubino et al., 2015, Barbosa et al., 2016, Barbosa et al., 2017, Nakagawa et al., 2019). In this situation, the Biot's theory of poro-elasticity is adopted to account for the influence of possible fluid exchange between the joint and the host rock. The wave-induced fluid flow (WIFF) caused by the high compressibility is thought to be the principal reason for the significant wave dissipation and velocity dispersion. It is also found

that the WIFF effect is frequency dependent, which is more evident at low frequencies below the characteristic transition frequency determined by the ratio of the diffusion length and the host rock thickness.

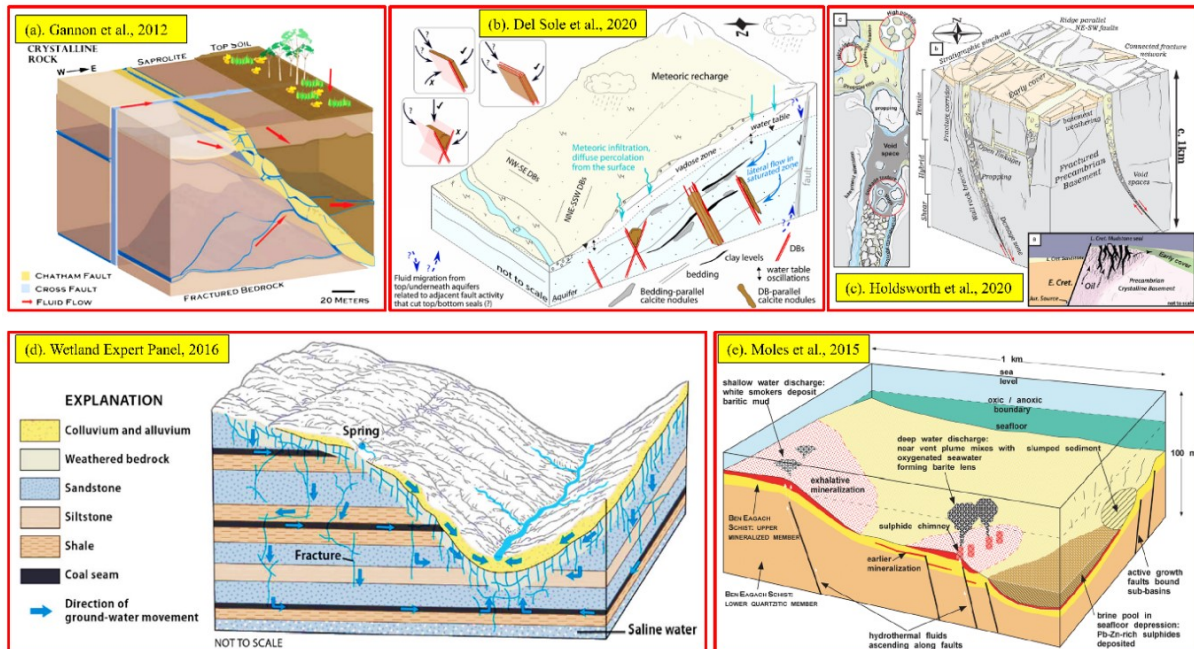


Figure 1.2 Some examples for the fluid-saturated rock joints presented in nature and practical engineering: (a). The conceptual model of groundwater flow at the south spring study area, Coles Hill, Virginia (adopted from Gannon et al., 2012); (b). the conceptual model of fluid migration in Loiano, Italy (adopted from Del Sole et al., 2020); (c). the conceptual model for the geology of the fractured basement reservoir in the Lancaster field (adopted from Holdsworth et al., 2020); (d). the conceptual depiction of groundwater movement in the aquifers of the Appalachian Plateaus (adopted from Panel, 2016); (e). the conceptual model of the marine environment during deposition of the first extensive SEDEX bed (M3) in the Foss deposit of the Scotland Grampian region (adopted from Moles et al., 2015).

Despite the progress made on the theoretical and numerical levels, the laboratory-based understanding of the fluid effects the interaction of waves with individual rock joints is still at its infancy. Particularly, the existing experimental studies mainly concentrate on the rock joints filled with water-saturated soils/gouges consisting predominantly of granular materials (i.e., quartz sand) (Li et al., 2010, Wu and Zhao, 2015, Huang et al., 2018), which point out that the water-dependence of wave behaviours across individual rock joints are related to the layer thickness, the particle size distributions and the mineralogical compositions of the infillings. However, the fluid effects on wave responses of individual rock joints filled with clayey

materials remain enigmatic due to the lack of laboratory documents. On the other hand, there is lacking laboratory investigations into the interaction of waves with the rock joints filled with fluids solely. Although the limited laboratory documents have revealed that the presence of fluids enhances wave transmission yet reduces wave reflection across single fluid-filled rock joints (Pyrak-Nolte et al., 1990, Place et al., 2016, Huang et al., 2020), the effects of various filling fluid parameters (e.g., the content, compositions and spatial distribution of filling fluids) have not been systematically and quantitatively studied in the laboratory.

We can conclude from the above brief literature review that there are still many key issues remaining to be addressed to gain a deeper understanding of the fluid effects on the interaction of waves with individual rock joints at laboratory scale. As a matter of fact, the laboratory test results could be used not only to validate the existing theoretical models but also to complete the body of knowledge of wave behaviours across individual rock joints. In this context, this research is motivated to provide more insights for the knowledge concerning the role of fluids in the interaction between waves and individual rock joints based on massive laboratory tests.

## 1.2 Research objectives and scope of the thesis

The thesis research aims to determine the fluid effects on the interaction of waves with individual rock joints at the laboratory scale. Within the research scope, three primary objectives of this research are summarised as follows,

**1) *To determine the fluid effects on low-intensity wave responses of individual clay-rich rock joints.***

How the water saturation of filling clay-rich gouge affects low-intensity wave behaviours across single rock joint will be investigated by conducting ultrasonic tests in the laboratory. Meanwhile, the influences of the wave mode, the dominant wave frequency, and the mineralogical composition of filling gouge on the water saturation-dependent wave attributes will be systematically examined and clarified.

**2) *To explore the fluid effects on low-intensity wave propagation and attenuation across individual fluid-filled rock joints.***

The low-intensity wave responses of single fluid-filled rock joints will be measured using the ultrasonic technique at the laboratory scale. The relationships between wave attributes and the components, contents, and spatial distribution of filling fluids will be quantitatively



analysed based on the experimental results. Furthermore, the thermal effects on fluid-dependent wave characteristics of single fluid-filled rock joints will be briefly studied via the ultrasonic measurements.

**3) *To ascertain the fluid effects on the interaction of high-intensity stress waves with individual fluid-filled rock joints.***

A series of dynamic impacting tests will be performed on single fluid-filled rock joints via a self-established steel SHPB bar system, aiming to quantitatively determine the effects of the joint thickness, the joint contact area, the content and viscosity of filling fluids on the dynamic mechanical properties, the energy evolution characteristics as well as the high-intensity stress wave responses of single fluid-filled rock joints. The dynamic responses of single fluid-filled rock joints will be recorded using the high-speed photography, with the aim of obtaining additional insights for the role of fluids in the interaction of high-intensity stress waves with individual fluid-filled rock joints.

### 1.3 Structure of the thesis

This thesis is comprised of seven chapters. The organization of the main body of this thesis is illustrated in Figure 1.3. Following the introduction of the research background and specific objectives in this chapter (**Chapter 1**), **Chapter 2** presents a state-of-the-art review of the interaction of waves and individual rock joints from the theoretical and experimental perspectives.

**Chapter 3** covers a comprehensive description of the experimental techniques and the corresponding data processing methods employed in this research. Firstly, a well-established test configuration for conducting ultrasonic pulse-transmission tests is described in detail, followed by an illustration of the typical methods for processing the ultrasonic test data to evaluate wave velocity, frequency spectra, wave attenuation and time-frequency maps. Then, an introduction of a self-designed steel SHPB test system is presented, together with a thorough demonstration of the representative data processing approaches for evaluating the dynamic mechanical and wave characteristics through the collected strain signals in SHPB tests.

**Chapter 4** is devoted to the study of fluid effects on the low-amplitude wave behaviours across single clay-rich rock joints. The experimental procedure for performing ultrasonic pulse-transmission tests on individual water-saturated clay-rich rock joints is presented in detail. According to the laboratory results, the correlations between water saturation and wave



attributes (e.g., wave velocity, transmission ratio and frequency contents) are quantitatively analysed. Furthermore, the effects of the wave mode, the dominant wave frequency, and the mineralogical components of infill gouge on the water saturation dependence of wave characteristics are clarified. The physical mechanism lying behind the observed wave behaviours are discussed from the perspective of a combination of the clay hydration, the local flow effect and the wave scattering at the interface.

**Chapter 5** deals with the investigation into the low-amplitude wave attributes of individual fluid-filled rock joints. The detailed experimental programme of conducting ultrasonic pulse-transmission measurements on individual fluid-filled rock joints is described. The obtained test results are analysed to quantitatively illuminate the influences of the composition, content and spatial distribution of filling fluids on wave responses of single fluid-filled rock joints. Furthermore, the thermal effects on wave behaviours across individual fluid-filled joints are briefly clarified based on the ultrasonic measurements on water- and oil-filled rock joints under different temperature conditions. The possible mechanisms responsible for the observed wave responses of single fluid-filled rock joints are discussed in view of the acoustics and thermodynamics in fluids and the wave theories relating to individual rock joints.

**Chapter 6** is dedicated to the study of the interaction of individual fluid-filled rock joints with the high-amplitude stress waves induced by the dynamic impacting. The experimental procedure for carrying out the SHPB tests on single fluid-filled rock joints is illustrated. Based on the SHPB test results, the effects of the joint thickness, the joint contact area as well as the content and viscosity of filling fluids on the dynamic mechanical properties, energy evolution characteristics and wave attributes of single fluid-filled rock joints are quantitatively determined. Furthermore, the high-speed images are used to identify the visual dynamic responses of individual fluid-filled rock joints during the passage of the high-intensity stress waves. A discussion about the underlying physical mechanisms for the experimental findings is presented based on the stiffening effect, the global flow effect, the mesoscopic wave-induced fluid flow effect as well as the wave theories relating to individual rock joints.

**Chapter 7** summarizes the main findings and conclusions obtained from all experiments included in this research. Additionally, the applications and limitations of the current work are discussed. The recommendations for possible future research are provided as well.

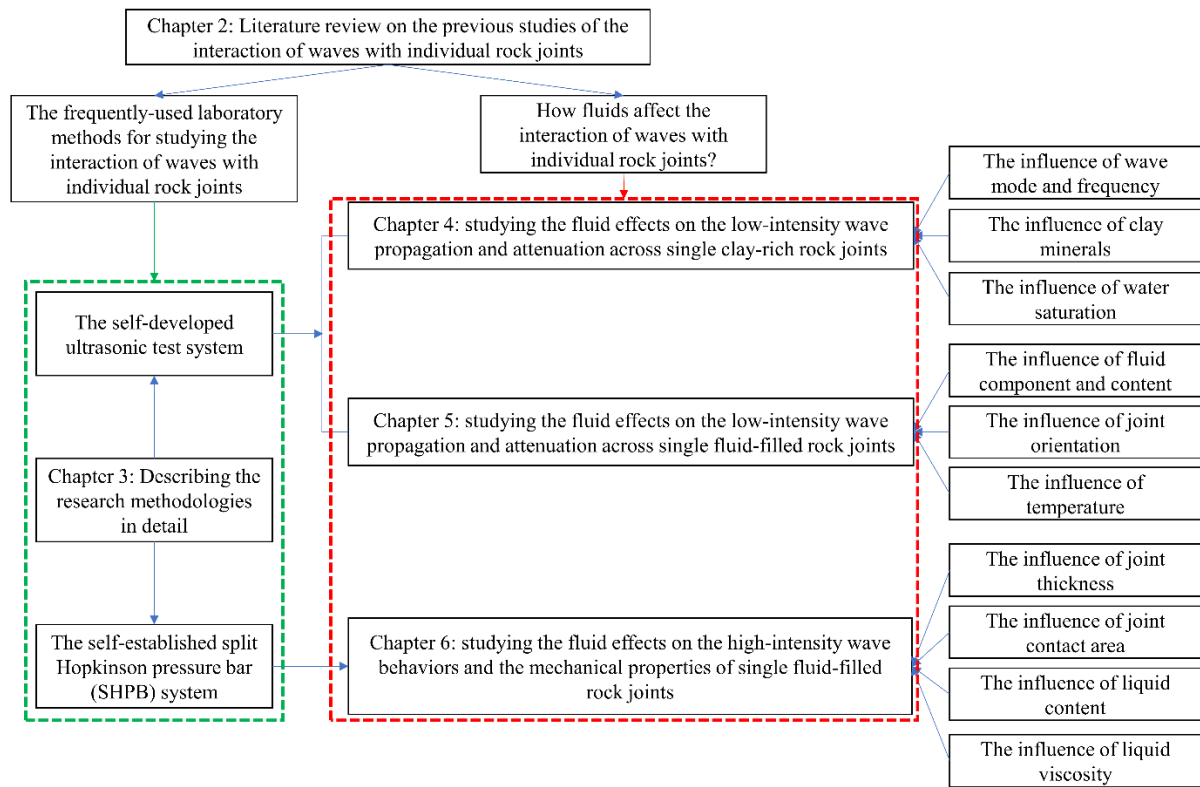


Figure 1.3 The framework for the organization of the main body of the thesis.

## CHAPTER 2 LITERATURE REVIEW

The focus of this chapter is on the review the state-of-the-art knowledge of the interaction of waves with individual rock joints from the theoretical and experimental perspectives. In section 2.1, an overview of the theoretical models for describing wave propagation and attenuation across individual rock joints are emphasized. In section 2.2, previous laboratory studies of wave responses of individual rock joints are briefly reviewed. Based on the literature review presented in former two sections, the research gaps in the interaction of seismic waves and individual rock joints are discussed in section 2.3.

It should be mentioned that the overview in this chapter only focuses on the interaction of plane waves with sparsely distributed rock joints. Plane waves are generally categorised into the compressional wave and shear wave. The compressional wave (i.e., P-wave) is a longitudinal pulse with the direction of propagation parallel to that of particle motions, while the shear wave (i.e., S-wave) propagates in the direction perpendicular to the plane of particle motion. Moreover, shear waves associated with particle motions in the plane of incidence is termed as the SV-wave while those associated with particle motions perpendicular to the incident plane is regarded as the SH-wave. Though this part could be incomplete because there is a great deal of previous studies on the interaction of plane waves and individual rock joints, the main trace of the development and advance in this research subject has been reviewed.

### 2.1 Review on theoretical models for describing wave behaviours across individual rock joints

This section provides an overview of theoretical models for describing wave behaviors across individual rock joints. In the existing studies, there are mainly two theories, the displacement discontinuity theory (DDT) and layered medium theory (LMT), applied to model wave propagation and attenuation across individual rock joints. Theoretically speaking, the DDT is only valid for the rock joint that with thickness much smaller than the incident wavelength, while the applicability of LMT is independent on the relationship between the joint aperture and wavelength. With the combination of those two theories and different constitutive relationships of the joint deformational behaviours, a series of models have been established and developed to characterize wave attributes of individual rock joints. The development and advances of some representative theoretical models have been briefly demonstrated in this

section. Furthermore, the characteristics, applicability and limitations of those models are to some extent discussed.

### 2.1.1 The displacement discontinuity models

The displacement discontinuity theory (DDT), also known as the linear slip theory or non-weld interface theory, was originally proposed by Mindlin (1960) to study wave behaviours across the non-welded interface between two homogenous, isotropic and linear elastic spaces half-spaces. In this theory, the joint is physically modelled as a displacement discontinuity at the interface between two elastic half-spaces, which is mathematically represented as boundary conditions for wave equations. More specifically, the boundary conditions of a displacement discontinuity are assumed to be that the stress remains continuous while the displacement is discontinuous as waves impinge upon the joint. Based on the displacement discontinuity theory, a series of displacement discontinuity models (DDMs) have been established to describe wave responses to individual rock joints with linear or nonlinear deformational behaviours.

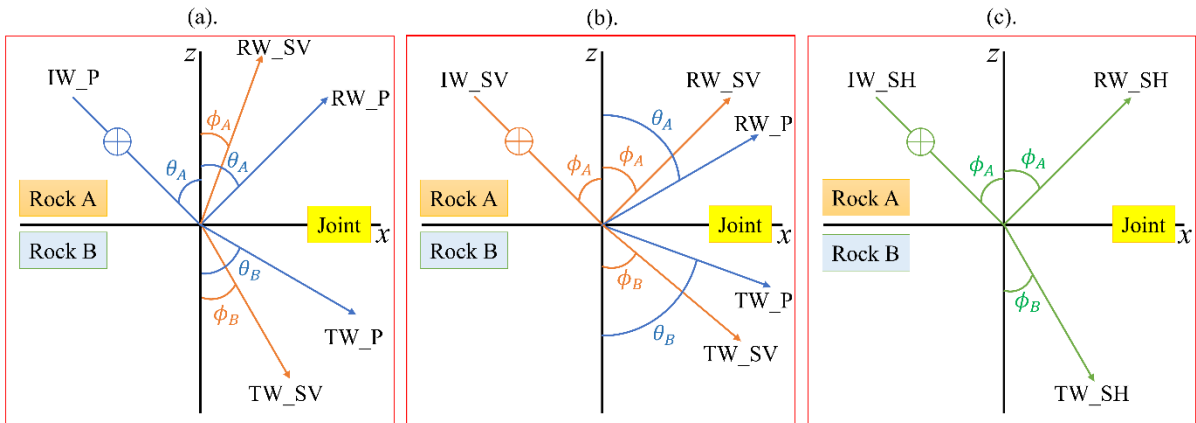


Figure 2.1 Transmitted, reflected and converted components of waves at the rock joint (i.e., a displacement discontinuity) for incident (a) P-wave, (b) SV-wave, and (c) SH-wave (modified from Pyrak-Nolte et al. (1990)).

The DDT was firstly adopted by Pyrak-Nolte and her colleagues (1987, 1988, 1990) to theoretically analyse wave behaviours across single rock joints with linear stress-deformation relationships. In their work, the complete solutions of wave transmission and reflection coefficients for arbitrary incidence of P, SH and SV waves upon single dry and fluid-filled rock joints were obtained, which were to some extent consistent with the full solutions derived by Schoenberg (1980). Different from Schoenberg (1980), they defined the joint specific stiffness

as the ratio of the applied stress to the average displacement it produces (i.e., the inverse of the joint compliance) to correlate the stresses and discontinuity in displacements.

When plane waves impinge on a rock joint, the transmission, reflection and conversion may occur at the interface, as shown in Figure 2.1. Assuming the joint between two dissimilar rock materials lies in the XOY plane (see Figure 2.1), the boundary conditions for the P wave or SV wave propagation across a linearly elastic rock joint are expressed as (Pyrak-Nolte et al., 1990)

$$u_z^A - u_z^B = \frac{\sigma_z}{\kappa_z} \quad \text{Equation 2.1}$$

$$u_x^A - u_x^B = \frac{\sigma_x}{\kappa_x} \quad \text{Equation 2.2}$$

$$\sigma_z = \sigma_z^A = \sigma_z^B \quad \text{Equation 2.3}$$

$$\sigma_x = \sigma_x^A = \sigma_x^B \quad \text{Equation 2.4}$$

where  $u_A$  and  $u_B$  are displacements on the two sides of the joint,  $\sigma_x$  and  $\sigma_z$  are stresses applied to the joint along the x-axis and z-axis, respectively,  $\kappa_z$  and  $\kappa_x$  are the normal and shear joint specific stiffnesses, respectively. On the other hand, the boundary conditions for an incident SH wave across an elastic rock joint are (Pyrak-Nolte et al., 1990)

$$u_y^A - u_y^B = \frac{\sigma_y}{\kappa_y} \quad \text{Equation 2.5}$$

$$\sigma_y = \sigma_y^A = \sigma_y^B \quad \text{Equation 2.6}$$

where  $\sigma_y$  and  $\kappa_y$  are the uniaxial stress and the shear specific stiffness of the joint in the y-axis direction, respectively. Substituting the assumed solutions of two-dimensional wave equations into those boundary conditions (Equations 2.3-2.8), Pyrak - Nolte et al. (1990) derived the general solutions for the P, SV and SH waves incidence upon the elastic rock joint from a free angle. According to Pyrak-Nolte et al. (1990), for waves normal incidence to the joint between two half-spaces made of the same rock material, the transmission and reflection coefficients for P, SV and SH waves can be determined by

$$T_p(\omega) = \frac{2(\kappa_z / Z_p)}{-i\omega + 2(\kappa_z / Z_p)} \quad \text{Equation 2.7}$$

$$R_p(\omega) = \frac{i\omega}{-i\omega + 2(\kappa_z / Z_p)} \quad \text{Equation 2.8}$$

$$T_{SV}(\omega) = \frac{2(\kappa_x / Z_s)}{-i\omega + 2(\kappa_x / Z_s)} \quad \text{Equation 2.9}$$

$$R_{SV}(\omega) = \frac{-i\omega}{-i\omega + 2(\kappa_x / Z_s)} \quad \text{Equation 2.10}$$

$$T_{SH}(\omega) = \frac{2(\kappa_y / Z_s)}{-i\omega + 2(\kappa_y / Z_s)} \quad \text{Equation 2.11}$$

$$R_{SH}(\omega) = \frac{-i\omega}{-i\omega + 2(\kappa_y / Z_s)} \quad \text{Equation 2.12}$$

where  $\omega$  denotes the angular frequency of the wave,  $Z_p$  and  $Z_s$  are seismic impedances (i.e., the product of the density and wave phase velocity) of the background rock for P and S waves, respectively.

The capability of above-mentioned solutions for describing wave behaviours across a linear rock joint was validated by the comparison of theoretical predictions with experimental results obtained from ultrasonic tests on dry rock joints (Pyrak-Nolte et al., 1990). It should be mentioned that those solutions were obtained based on the assumption of harmonic wave propagation across single rock joint. Based on the linear DDM and the conservation of momentum at the wave fronts, Li and Ma (2010) deduced the wave equations for the interaction of a linear elastic rock joint with plane waves (i.e., P and SV waves) at free incident angles. In that study, the DDM was extended to characterize the effects of an elastic rock joint on propagation of waves with any possible waveforms.

The above-mentioned elastic DDM is incapable of analysing wave propagation across single wet rock joints because that the presence of liquid in a rock joint may introduce the viscous coupling and increase the joint specific stiffness. Considering the viscous effect caused by the filling liquid, Schoenberg (1980) derived a solution for the elastic wave propagation across a viscous interface, where the role of joint stiffness was neglected. Furthermore, Pyrak-Nolte et al. (1990) established a displacement and velocity discontinuity model (DVDM) by integrating the linear rheologic models (i.e., the Kelvin and Maxwell models) into the DDM to analyse wave behaviours across single wet rock joints, where the effects of fluid induced variations in

joint specific stiffness and viscosity were taken into consideration. In the DVDMM, the boundary conditions for an incident P wave or SV wave are

$$\kappa_z(u_z^A - u_z^B) + \eta_z(\dot{u}_z^A - \dot{u}_z^B) = \sigma_z \quad (\text{for the Kelvin model})$$

*Equation 2.13*

$$\kappa_x(u_x^A - u_x^B) + \eta_x(\dot{u}_x^A - \dot{u}_x^B) = \sigma_x \quad (\text{for the Kelvin model})$$

*Equation 2.14*

$$\dot{u}_z^A - \dot{u}_z^B = \dot{\sigma}_z / \kappa_z + \sigma_z / \eta_z \quad (\text{for the Maxwell model})$$

*Equation 2.15*

$$\dot{u}_x^A - \dot{u}_x^B = \dot{\sigma}_x / \kappa_x + \sigma_x / \eta_x \quad (\text{for the Maxwell model})$$

*Equation 2.16*

$$\sigma_z = \sigma_z^A = \sigma_z^B \quad \text{Equation 2.17}$$

$$\sigma_x = \sigma_x^A = \sigma_x^B \quad \text{Equation 2.18}$$

For the incidence of an SH wave, the boundary conditions are

$$\kappa_y(u_y^A - u_y^B) + \eta_y(\dot{u}_y^A - \dot{u}_y^B) = \sigma_y \quad (\text{for the Kelvin model})$$

*Equation 2.19*

$$\dot{u}_y^A - \dot{u}_y^B = \dot{\sigma}_y / \kappa_y + \sigma_y / \eta_y \quad (\text{for the Maxwell model})$$

*Equation 2.20*

$$\sigma_y = \sigma_y^A = \sigma_y^B \quad \text{Equation 2.21}$$

where  $\eta$  denotes the joint specific viscosity with the unit of Pa·s/m. Based on those boundary conditions, Pyrak-Nolte et al. (1990) derived the full analytical solutions for plane waves arbitrarily impinging upon a single liquid-filled rock joint. Particularly, for the normal incidence of P, SV and SH waves, the transmission and reflection coefficients across a liquid saturated rock joint can be given by

$$T_p(\omega) = \frac{2(\kappa_z - i\omega\eta_z)}{-i\omega + 2(\kappa_z / Z_p)} \quad (\text{for the Kelvin model})$$

Equation 2.22

$$T_p(\omega) = \frac{(1 + Z_p/2\eta_z) + (i\omega Z_p/2\kappa_z)}{(1 + Z_p/2\eta_z)^2 + (\omega Z_p/2\kappa_z)^2} \quad (\text{for the Maxwell model})$$

Equation 2.23

$$R_p(\omega) = \frac{-i\omega Z_p}{2\kappa_z - i\omega(2\eta_z + Z_p)} \quad (\text{for the Kelvin model})$$

Equation 2.24

$$R_p(\omega) = \frac{(-Z_p/2\eta_z)(1 + Z_p/2\eta_z) + (\omega Z_p/2\kappa_z)(i - \omega Z_p/2\kappa_z)}{(1 + Z_p/2\eta_z)^2 + (\omega Z_p/2\kappa_z)^2}$$

(for the Maxwell model) Equation 2.25

$$T_{sv}(\omega) = \frac{2(\kappa_x - i\omega\eta_x)}{2\kappa_x - i\omega(2\eta_x + Z_s)} \quad (\text{for the Kelvin model})$$

Equation 2.26

$$T_{sv}(\omega) = \frac{(1 + Z_s/2\eta_x) + (i\omega Z_p/2\kappa_x)}{(1 + Z_s/2\eta_x)^2 + (\omega Z_s/2\kappa_x)^2} \quad (\text{for the Maxwell model})$$

Equation 2.27

$$R_{sv}(\omega) = \frac{-i\omega Z_s}{2\kappa_x - i\omega(2\eta_x + Z_s)} \quad (\text{for the Kelvin model})$$

Equation 2.28

$$R_{sv}(\omega) = \frac{(Z_s/2\eta_x)(1 + Z_s/2\eta_x) + (\omega Z_s/2\kappa_x)(-i + \omega Z_s/2\kappa_x)}{(1 + Z_s/2\eta_x)^2 + (\omega Z_s/2\kappa_x)^2}$$

(for the Maxwell model) Equation 2.29

$$T_{sh}(\omega) = \frac{2(\kappa_y - i\omega\eta_y)}{2\kappa_y - i\omega(2\eta_y + Z_s)} \quad (\text{for the Kelvin model})$$

Equation 2.30



$$T_{SH}(\omega) = \frac{(1 + Z_s/2\eta_y) + (i\omega Z_s/2\kappa_y)}{(1 + Z_s/2\eta_y)^2 + (\omega Z_s/2\kappa_y)^2} \quad (\text{for the Maxwell model})$$

*Equation 2.31*

$$R_{SV}(\omega) = \frac{-i\omega Z_s}{2\kappa_y - i\omega(2\eta_y + Z_s)} \quad (\text{for the Kelvin model})$$

*Equation 2.32*

$$R_{SH}(\omega) = \frac{(Z_s/2\eta_y)(1 + Z_s/2\eta_y) + (\omega Z_s/2\kappa_y)(-i + \omega Z_s/2\kappa_y)}{(1 + Z_s/2\eta_y)^2 + (\omega Z_s/2\kappa_y)^2}$$

(for the Maxwell model) *Equation 2.33*

The applicability of the above-mentioned linear DDMs for characterizing the wave behaviours across single rock joints have been confirmed by a series of ultrasonic tests on artificial and natural rock joints at the laboratory scale (Myer et al., 1990, Pyrak-Nolte et al., 1990, Roy and Pyrak-Nolte, 1995, Gu et al., 1996). However, those linear elastic DDMs are incapable of modelling wave propagation across rock joints with nonlinear deformational behaviours induced by the closure of voids, the nonlinear deformation of asperities and the frictional slip of the joint. It has been found that the complete deformational behaviours of rock joints are nonlinear in most circumstances (Goodman, 1989). In this regard, considerable efforts have been devoted to developing nonlinear DDMs for the analysis of wave propagation across rock joints with nonlinear deformational behaviours.

Based on the friction boundary conditions, Miller (1977, 1978) proposed a nonlinear DDM to analyse normally incident plane harmonic shear waves propagation across a frictional joint between two semi-infinite elastic media. He deduced the approximate solutions of the effective transmission, reflection, and absorption coefficients with the help of the equivalent linearization method. The accuracy of the presented nonlinear DDM was validated by the comparison of approximate and exact solutions in a numerical case of a Coulomb friction boundary plane between two identical elastic media. His work showed that the transmission of wave relied on the ratio of incident S-wave amplitude to the characteristic frictional shear stress associated with the nonlinear DDM.

Zhao and Cai (2001) established a nonlinear DDM to study normally incident P-wave propagation across a dry joint with nonlinear normal deformational behaviour, where the

Barton-Bandis (B-B) model was adopted to describe the nonlinear normal deformation of rock joint. Using the method of characteristics (MOC), they solved the one-dimensional wave equation and derived numerical solutions of the particle velocities in wave fields as well as the coefficients of transmission and reflection. The comparison of numerical results between the established DDM and linear DDM indicated that, when P-wave normally incident upon the nonlinear deformable joint rather than the linear deformable joint, less wave energy attenuation occurs, and wave modes at higher frequencies are involved in transmitted pulses.

Based on the dynamic stress-strain relation obtained from a series of SHPB tests on single artificial sand-filled rock joints, Li et al. (2010) presented a nonlinear DDM to analyse normally incident P-wave propagation across single filled rock joints. The MOC was employed to analytically solve the one-dimensional wave equation for P-wave normal incidence upon single filled rock joints. The effectiveness of the proposed nonlinear DDM was confirmed by the comparison between analytical and experimental results. However, the shear deformation of joint was overlooked in their study.

By introducing the Coulomb-slip model to describe the slippery behaviour of joint, Li et al. (2011a) presented a nonlinear DDM to analyse P- and S-wave propagation across a slippery rock joint. In their study, wave equations for arbitrarily incident P- and S-waves upon a rock joint were derived based on the principle of conservation of momentum. The established DDM was validated by the numerical simulation of the interaction of stochastic seismic waves and a slippery rock joint. The numerical results showed that the incident P-wave is seldom affected by the slippery rock joint while the incident S-wave is obviously controlled by the slippery property of joint. After then, Li et al. (2011b) improved their nonlinear DDM by adopting the B-B model to describe the nonlinear normal deformation of joint. The enhanced nonlinear DDM could be used to analyse obliquely incident P- and S-waves propagation across a rock joint with the nonlinear normal and shear deformation. Based on the principle of the momentum conservation, they derived explicit two-dimensional wave equations for the arbitrary incidence of P- and S-waves. Analytical solutions proved that those wave equations are only valid for analysing the interaction of a complex rock joint and waves with arbitrary incident angles smaller than the critical angles.

Cui et al. (2017) proposed a nonlinear DDM to investigate the normal incidence of S-wave upon a rock joint, where the continuously yielding model (CYM) was introduced to represent the complex joint deformational behaviours. In their work, the time-domain recursive method

(TDRM) was employed to derive numerical solutions of transmission and reflection coefficients. The established DDM was verified by the comparison between the TDRM-based solutions and simulated results using a build-in 3DEC mode. Compared to the DDM with the Coulomb-slip model, the DDM with the Coulomb-slip model could capture some complex interactions of waves and the joint, such as a hysteresis effect and shear stiffness degradation under higher normal stresses.

Liu et al. (2020) presented a nonlinear DDM to analyse arbitrarily incident wave propagation across single rock joints subjected to a combination of gravitational and tectonic stresses, where the B-B model and the hyperbolic nonlinear slip model were employed to describe the normal and shear joint deformational behaviours, respectively. Compared to the linear and Coulomb slip models, the hyperbolic nonlinear slip model highly depends on the stress history and shear stiffness degradation. In their study, the TDRM was utilized to derive the numerical solutions of the wave equations for oblique P- and SV-waves propagation across a rock joint under both tectonic and gravitational stresses. The parametric analyses showed that transmission and reflection coefficients were more sensitive to varying incident wave amplitude rather than the changing incident angle. Since all incident waves used in their work were limited to the half-sine shape, the applicability of the proposed DDM for analysing propagation of waves with complex waveforms is uncertain.

### 2.1.2 The layered medium models

The LMT was originally proposed by Thomson (1950), which has been widely applied to theoretically analyse the incidence of waves on an interface existing in various materials (Ewing et al., 1957, Biswas, 1967, Rokhlin and Wang, 1991). Different from the DDT, the layered medium theory (LMT) treats single joint as a perfectly bonded thin layer sandwiched between two half-spaces (Brekhovskikh, 2012). In the LMT, stresses and displacements across two interfaces between the thin layer and background half-spaces are assumed to be continuous.

Based on the LMT, Fehler (1982) studied the interaction of plane waves with single rock joints filled with a viscous fluid. In his work, single fluid-filled joint was modelled as a thin fluid layer embedded between two homogeneous rock blocks, where the fluid was viscous and characterized by a finite viscosity. To involve the effects of fluid viscosity, the wave equations were modified by replacing the Lamé parameter  $\lambda$  by  $(\kappa - \frac{2}{3}\mu)$ , where  $\kappa$  and  $\mu$  are the bulk

modulus and rigidity of the fluid, respectively. In addition,  $\mu$  was replaced by the operator  $\eta \frac{\partial}{\partial t}$  in the mathematical expression of wave equations, where  $\eta$  is the viscosity of the filling fluid. The modified wave equations were solved to obtain transmission and reflection coefficients for P, SV and SH waves incident at arbitrary angles on a fluid-filled joint. The analytical solutions showed that wave transmission and reflection highly relied on the host rock properties (i.e., bulk modulus and acoustic impedance) and filling fluid parameters (i.e., bulk and shear moduli, acoustic impedance, and layer thickness).

According to the LMT, Zhu et al. (2011) developed the displacement and stress discontinuity model (DSDM) to analyse wave propagation across single rock joints with viscoelastic behaviours. In their work, the complete analytical solutions for arbitrarily incident P, SH and SV waves on single viscoelastic joints were derived by adopting the Kelvin and Maxwell models to describe joint deformational behaviours. Particularly, for the normal wave incidence on a joint, the transmission and reflection coefficients for P, SV and SH waves across a viscoelastic rock joint sandwiched between two identical rock matrixes could be expressed as

$$T_P = \frac{2}{2 - id_P - i / \kappa'_P} \quad \text{Equation 2.34}$$

$$R_P = \frac{i / \kappa'_P - id_P}{2 - id_P - i / \kappa'_P} \quad \text{Equation 2.35}$$

$$T_{SV} = \frac{2}{2 - id_S - i / \kappa'_S} \quad \text{Equation 2.36}$$

$$R_{SV} = \frac{i / \kappa'_S - id_S}{2 - id_S - i / \kappa'_S} \quad \text{Equation 2.37}$$

$$T_{SH} = \frac{2}{2 - id_S - i / \kappa'_S} \quad \text{Equation 2.38}$$

$$R_{SH} = \frac{id_S - i / \kappa'_S}{2 - id_S - i / \kappa'_S} \quad \text{Equation 2.39}$$

where  $\kappa'_P$  and  $\kappa'_S$  are the effective joint stiffness, which are determined by

$$\frac{1}{\kappa'_P} = \frac{1}{(\kappa_P / \omega Z_P) - i(\eta_N / Z_P)}$$

(for joint characterised by the Kelvin model) *Equation 2.40*

$$\frac{1}{\kappa_p'} = \frac{1}{(\kappa_p / \omega Z_p)} - \frac{1}{i(\eta_N / Z_p)}$$

(for joint characterised by the Maxwell model) *Equation 2.41*

$$\frac{1}{\kappa_s'} = \frac{1}{(\kappa_s / \omega Z_s) - i(\eta_T / Z_s)}$$

(for joint characterised by the Kelvin model) *Equation 2.42*

$$\frac{1}{\kappa_s'} = \frac{1}{(\kappa_s / \omega Z_s)} - \frac{1}{i(\eta_T / Z_s)}$$

(for joint characterised by the Maxwell model) *Equation 2.43*

In the above formulas,  $\kappa_p$  and  $\kappa_s$  are the normal and tangential specific joint stiffnesses, respectively,  $\eta_N$  and  $\eta_T$  are the normal and tangential specific joint viscosities, respectively,  $Z_p$  and  $Z_s$  are the wave impedances of host rock for P- and S-waves, respectively. Additionally,  $d_p$  and  $d_s$  represents the impedance ratios of the joint for P- and S-waves, respectively, which are defined as

$$d_p = \frac{Z_{P-FM}}{Z_p} = \frac{\omega \rho_{FM} H}{Z_p} \quad \text{Equation 2.44}$$

$$d_s = \frac{Z_{S-FM}}{Z_s} = \frac{\omega \rho_{FM} H}{Z_s} \quad \text{Equation 2.45}$$

where H stands for the joint thickness,  $\rho_{FM}$  is the density of filled medium in the joint. The accuracy and effectiveness of the proposed DSDM have been verified by the comparison between theoretical predictions and experimental results obtained from SHPB tests on single filled rock joints. Recently, Wang et al. (2017, 2019) extended the DSDM to study the interaction of plane waves with single viscoelastic rock joints described by the standard linear solid model. Particularly, for SH wave propagation across a filled joint, the wave-induced slip behaviour of the joint was characterised by the Coulomb-slip model. In their study, the TDRM was adopted to solve wave equations and obtain the coefficients of transmission and reflection. The effectiveness of the modified DSDM was verified by the comparison of the calculated numerical results with the close-form analytical solutions in Zhu et al. (2011).

On the basis of the LMT, a thin-layer interface model (TLIM) was developed by (Li et al., 2013) to analyse P-wave propagation across single filled rock joints. In the TLIM, the filled rock joint was considered as a thin-layer interface with a nonnegligible thickness sandwiched between two rock blocks, where the filling material is equivalent as an elastic and homogeneous medium different from adjacent rock blocks. Using the MOC, they obtained the analytical solutions of one-dimensional wave equations for normal P-wave incidence upon single filled rock joints. The comparison between the analytical and SHPB test results verified the effectiveness of the TLIM in analysing P-wave propagation across single filled rock joints with linear and nonlinear elastic mechanical behaviours. However, the ability of the TLIM for analysing wave propagation across rock joints with more complex deformational behaviour were not evaluated. It should be mentioned that, different from other theoretical models, the TLIM can analyse wave propagation even if the joint normal stiffness is unknown.

## **2.2 Review on laboratory investigations into wave behaviours across individual rock joints**

Given that laboratory experiments can examine the effects of isolated factors in a controlled manner, a series of laboratory techniques have been developed and applied to study the interaction of waves with individual rock joints. In the literature, there are mainly three laboratory methods, i.e., the ultrasonic technique, resonant bar technique and split Hopkinson pressure bar (SHPB) technique, employed to investigate the role of rock joints in wave propagation over a wide frequency range. The experimental results reveal that wave attributes of individual rock joints are highly affected by a number of factors, including joint parameters (e.g., joint surface geometry, joint orientation, joint width, joint number, joint spacing and filling materials), incident wave properties (e.g., amplitude and bandwidth) and external conditions (e.g., stress states and temperature). In this section, overall progress in experimental studies on the interaction of waves with individual rock joints using the aforementioned laboratory techniques is briefly reviewed with the introduction of basic knowledge of each method.

## **2.2.1 Laboratory investigations using the ultrasonic technique**

### **2.2.1.1 Fundamental knowledge of the ultrasonic technique**

The ultrasonic technique, as a typical non-destructive testing (NDT) method, employs the low-amplitude ultrasonic waves to examine wave characteristics of the tested object, where the stresses induced by propagating waves is well below the yield stress of the materials (Basu and Aydin, 2006). The ultrasonic technique is generally categorised into the pulse-transmission mode, the pulse-reflection mode and the tomography mode. In the pulse-transmission tests, the emitting and receiving transducers are placed in corresponding points on two opposite surfaces of the tested sample, where transmitted pulses through the specimen are acquired for evaluating wave attributes. In the pulse-reflection tests, the ultrasonic waves sent into the tested specimen can penetrate it and then be reflected and refracted by both the surfaces bounding the tested sample and its inner defects, which wave properties of the specimen can be examined by monitoring reflected signals. The tomography tests can produce 2D and 3D cross sectional images of the targeted specimen via recording both refraction and reflection of propagating waves.

The ultrasonic technique was introduced by Birch (1960, 1961) to study wave characteristics of rock materials in the laboratory. To date, it has been suggested as a standard method to measure wave attributes of rock masses (e.g., wave velocity, wave attenuation and spectral contents) because it is easy to implement and has negligible effects on the tested specimen (Soil and Rock, 2008, Aydin, 2013). In general, wave velocity of the tested rock specimen can be determined through the time-domain waveforms directly obtained from the ultrasonic measurements, which is crucial to evaluating dynamic properties of rock masses. Besides, the time-domain wave amplitudes could provide insights into changes in wave energy as waves pass through the rock specimen, which could contribute to characterizing the inner structures of the tested rock masses. Furthermore, the frequency information obtained by conducting the spectral analysis or the time-frequency analysis on the time-domain signals is beneficial for determining the relations between rock properties and wave attributes in the frequency domain. In the literature, the ultrasonic technique has been utilized independently or in combination with different mechanical tests to study the interaction of waves with individual rock joints under various stress states.

### 2.2.1.2 Studies of wave propagation across rock joints without considering stress effects

In the literature, the effects of rock joints on wave propagation in rock masses under no applied external loadings have been investigated by using the ultrasonic technique independently. Specifically, the relations between different joint parameters and wave attributes were determined based on the laboratory results.

To determine the effect of contact area of joint on wave transmission, Myer et al. (1985) performed ultrasonic tests on single artificial fracture that was represented by an interface in partial contact created by separating two steel cylinders by thin strips of lead. It was found that, for both P- and S-waves, a decrease in contact area weakens joint stiffness and hence reduces amplitudes of transmitted waves.

Kahraman (2001, 2002) conducted ultrasonic tests on different rock materials with artificial joints to briefly study the correlations between P-wave velocity and joint number, Schmidt hammer rebound number as well as joint roughness. It was found that P-wave velocity decreases with the increasing number of joints. Specifically, there was an inverse linear relation between P-wave velocity and number of joints, where the slope of regression lines was defined as the sound velocity index (SVI). A linear relation between the SVI and the Schmidt hammer rebound number was observed, implying that rock with the higher strength exhibits the greater SVI value. Additionally, a polynomial relationship between P-wave velocity and fracture roughness coefficient (FRC) was found, where P-wave velocity decreases with increasing FRC value. It indicates that the rougher rock joint leads to slower P-wave velocity across the joint.

Li and Zhu (2012) conducted ultrasonic tests on marble rock specimens with single rough joints to study the effects of joint roughness on P-wave velocity. In their work, joint roughness was described by the image fractal dimension (IFD), where the high IFD value represents the rougher joint. The test results showed that P-wave velocity decreases with the increase of IFD, indicating that increasing joint roughness causes a reduction in P-wave velocity.

El Azhari and El Hassani (2013) took ultrasonic measurements on rock samples with artificial joints to examine the effects of the number and plane orientation of joint on P-wave velocity across rock masses. The test results showed that increasing number of joint reduced P-wave velocity, which was consistent with previous findings. Regarding the effects of joint orientation, it was found that the joint parallel to the direction of wave propagation could slightly enhance P-wave velocity while inclined joints caused a decrease in P-wave velocity. Specifically, joints oriented at  $45^\circ$  led to the minimum reduction in P-wave velocity than other inclined joints.



Place et al. (2016) documented ultrasonic P-wave transmission and reflection at an artificial fracture filled with various fluids (i.e., air, water and two grouts at different cement contents), where the filling fluid was almost at rest in the fracture or moving at a controlled flow rate through the fracture. They found that the types of fluids could highly affect reflected wave spectra and energy, while the internal fluid flow has negligible influences on wave reflection. Specifically, the higher cement concentration the filling liquid has, the higher energy of transmitted waves and the lower energy of reflected waves there are.

Fathollahy et al. (2021) carried out ultrasonic measurements on Andesite rock with artificial joints to evaluate the effects of joint number, opening, orientation, filling conditions and roughness on P-wave velocity. It was observed that the increases in number and roughness of joint cause a decrease in P-wave velocity, which confirmed the findings in previous studies. In addition, with the increase of joint opening, P-wave velocity decreases at an increasing rate. It was also found that velocity reduction ratio reaches a maximum for the joint perpendicular to wave propagation direction while it minimizes for joint at the dip angle of  $30^\circ$ . Besides, there was a weak correlation between P-wave velocity and the content of infilling silica in the joint.

### **2.2.1.3 Studies of wave behaviours across rock joints considering stress effects**

In nature, rock joints are usually subjected to the lithostatic stress corresponding to their depth of burial. The in-situ stress plays a critical role in local fracturing, fluid flow and tectonic processes and so on. For example, as the shear tractions on the fault surface overcome the friction and non-conformities in the two fault surfaces, the slip of fault commences. Thus, it is crucial to understand the stress dependence of wave propagation and attenuation across rock joints. To this end, considerable laboratory investigations have been performed to determine the interaction of waves and rock joints subjected to different stress states using the combination of the ultrasonic technique and different mechanical tests.

With the combination of the ultrasonic tests and uniaxial compressive tests, wave propagation and attenuation across rock joints under uniaxial compressional stresses have been extensively studied (Butt, 2001, Jung et al., 1995). For instance, Pyrak-Nolte et al. (1990) investigated wave propagation and attenuation across single rock joints on subjected to a range of axial stresses. It was observed that, for both P- and S-waves, increasing axial stress led to increases in amplitudes of both waveforms and frequency spectra, decreases in travel time and attenuation, and a shift in dominant frequency towards to higher values. Besides, the saturation of liquid in the joint increased spectral amplitudes of transmitted P- and S-waves. Based on the

laboratory results, they stated that a joint can behave as a low-pass filter that causes a frequency-dependent time delay and attenuates wave by removing high-frequency wave modes. Zhao et al. (2006) investigated P-wave propagation across single and two parallel joints at different normal stresses (no more than 20 MPa). It was observed that the increasing normal stress results in a decrease in arrival time and an increase in amplitude of transmitted waves regardless of joint number. Moreover, an increase in normal stress caused the increases in spectral amplitudes and central frequency of transmitted waves. Their test results revealed that P-wave transmission across parallel joints was highly affected by the joint spacing, and the correlation was stress-dependent. Huang et al. (2014) studied the effects of joint roughness, joint number and incident wave frequency on wave transmission across rock joints under low uniaxial stresses (1 MPa -7 MPa). it was found that, with the increase of normal stress, the transmission of waves increases at a gradually decreasing rate. the increasing normal stress also weakened the ability of joint to cut off the frequency of transmitted waves. In addition, the rougher of joint surface, the more S-wave transmission while the less P-wave transmission there is. For wave propagation across multiple joints, they observed that an increase in joint number firstly reduces wave transmission and then gradually enhances wave transmission due to the closer joint spacing.

The influences of confining pressure on the interaction of waves and rock joints have also been investigated using the combination of the ultrasonic test system and the servocontrolled triaxial equipment. Using a true-triaxial stress loading system, King (2002) measured velocities of one ultrasonic P-wave and two polarized S-waves in each of the principal directions of cubic slate specimens containing parallel joints introduced by the poly-axial loading, where those parallel joints were perpendicular to the minimum principal stress. it was observed that the presence of joints had little effect on P- and S-wave velocities propagating in a direction parallel to those joints over the tested hydrostatic stress range of 2 – 90 MPa. To determine the sensitivity of the ultrasonic wave attributes to the changes in hydraulic properties resulting from the fluid-fracture surface interactions, Kamali-Asl et al. (2019) performed the flow-through-fracture tests with concurrent measurements of the ultrasonic P- and cross-polarized S-waves propagation along the fracture. The test results showed that the decreasing fracture aperture caused a decrease in P-wave attenuation and an increase in P-wave velocity while it led to an increase in the amplitude of cross-polarized S-waves. It was also found that the frequency partitioning of the transmitted ultrasonic waves exhibited a slight shift from higher frequencies to lower frequencies and energy content slightly increased during the pressure-controlled test,

whereas the frequency partitioning seldomly changed and energy content was significantly enhanced as the displacement-controlled test processed.

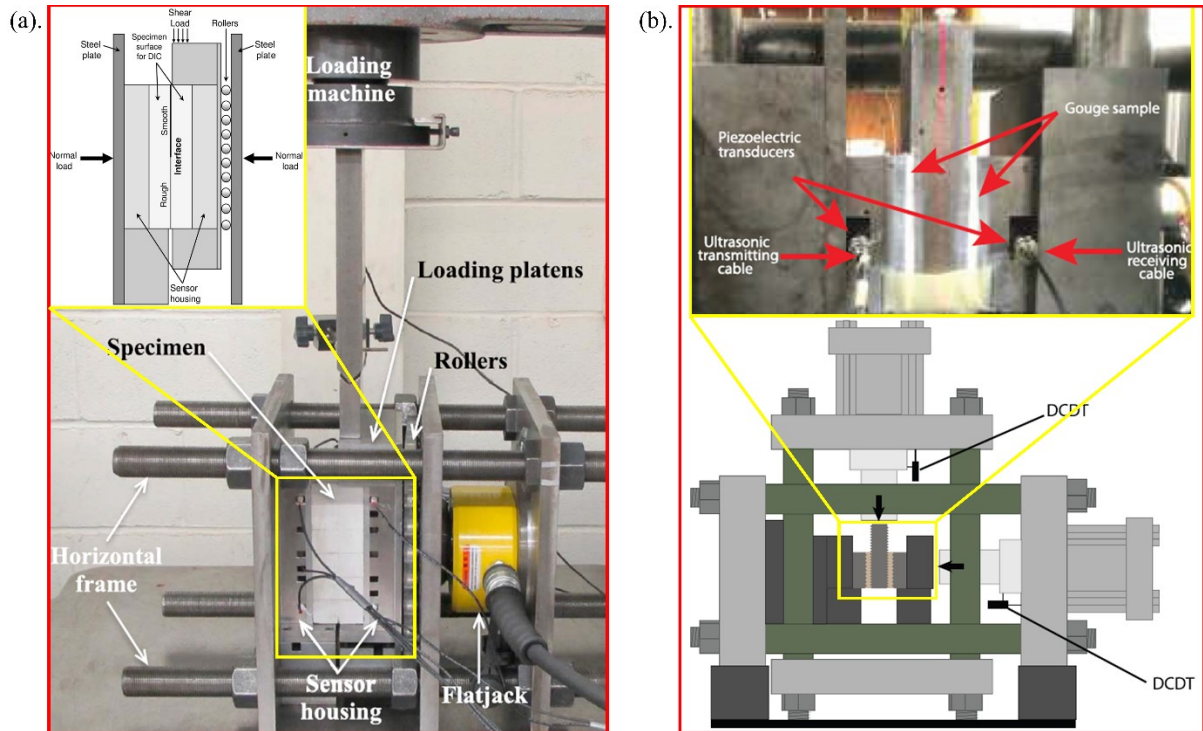


Figure 2.2 Typical experimental setup for studying wave behaviours across rock joints subjected to mix-mode loadings: (a). single-direct-shear configuration (modified from Hedayat et al., 2014), (b) double-direct-shear configuration (modified from Kenigsberg et al., 2019).

Given the great importance of understanding wave behaviours across rock joints subjected to mixed-mode loading (i.e., normal and shear stresses) to many geophysical activities, such as detecting miniscule pre-slip of earthquake faults, to mention a few, many researchers have combined the ultrasonic test system and direct shear apparatuses to investigate wave propagation across rock joints prior to and during shear failure of joints in the laboratory. There are mainly two types of loading apparatuses, i.e., the single-direct-shear configuration and the double-direct-shear configuration, developed to achieve the acoustic measurements on rock joints under different mix-mode loading conditions, as illustrated in Fig. 2.2. The direct shear apparatus is commonly composed of a horizontal loading frame to apply the normal stress on the joint and a loading machine to apply the shear stress along the joint.

Using the single-direct-shear test system, variations in wave velocities across single rock joints during the stick-slip motion was initially studied by Wang et al. (1975) in the laboratory. For a given normal stress, it was found that velocities first slightly increased while P-wave velocity

began to decrease at a shear stress of 100 bars. Appreciable decreases in both P- and S-wave velocities were observed at a later stage when more evident dilation occurred when the shear stress exceeded 250 bars. Particular, both P- and S-wave velocities sharply decreased near the rupture point even though the trend in dilation unchanged. Prior to the rupture point, the decrease in P-wave velocity was much greater than that in S-wave velocity. with the increase of applied normal stress, increases in wave velocities were observed when the shear stress is insufficient to cause the stick-slip motion. When the stick-slip commenced and maintained, no change in wave velocities was detected throughout the sliding process. Nakagawa et al. (2000) studied the conversion of seismic waves normally incident upon single rock joints subjected to shear stress. it was found that the shear stress applied to the joint led to the conversion of normally incident waves. Particularly, the increasing shear stress caused a monotonical increase in the amplitudes of converted waves, and the increase in amplitudes of converted S-waves is larger than that of converted P-waves. Hedayat and his co-workers (2014, 2018) investigated S-wave behaviours across single gypsum and limestone joints during the frictional sliding. The test results showed that the amplitude and dominant frequency of transmitted S-waves as well as wave velocity increased with the increasing shear stress and reached a maximum prior to the peak shear strength of the joint. In their work, the maximum in amplitudes of transmitted wave was identified as the ultrasonic precursor to the failure of the joint, which was well observed before slip or failure occurred along the joint.

Different from the single-direct-shear apparatus, the double-direct-shear configuration involves two synthetic fractures sandwiched between three blocks (see Fig. 2.2b). Peselnick et al. (1976) firstly used the double-direct-shear configuration equipped with ultrasonic transducers to study changes in P-wave velocity across simulated faults filled with different gouges under normal and shear stresses. For unsorted, fine-grained, well-compacted granite gouge, when the applied shear stress was above one third of critical shear stress for the occurrence of slip, the increasing shear stress caused an evident decrease in P-wave velocity, which was attributed to the reversible opening and closing of small cracks in the gouge. For sorted, coarser-grained sand gouge, with the increase of shear stress, a gradual increase in P-wave velocity was followed by a rapid and small decline in P-wave velocity from the commence of slip to continuous stable sliding, which was explained by the grain fracturing and compaction-induced readjustment of grains to a denser state of aggregation. Iwasa and Yoshioka (1998, 2006) examined P- and S-waves transmission across a simulated joint under a mix-mode loading condition in which the normal stress was kept constant at about 12 MPa

while the shear stress was gradually applied until a stick-slip occurred. They found that, for both P- and S-waves, the peak-to-peak amplitude of the first arrivals significantly increased with shear stress while its increasing rate slightly decreased prior to the stick-slip event. Besides, it was observed that the amplitude spectrum increased with shear stress, particularly for high-frequency waves, indicating that high-frequency waves were more sensitive to applied shear stress than low-frequency waves. By contrast, the phase-shift of low frequency waves increased with shear stress in a similar manner to amplitude while that of high-frequency waves were scattered with no tendency. Marone and his colleagues (2013, 2014, 2019) documented the evolution of wave propagation across synthetic faults filled with various gouges throughout the slide-hold-slide tests. The results revealed that variations in P- and S-Wave velocities and amplitudes were consistent with changing grain crack density, grain contact stiffness, grain coordination number, grain contact quality and geometry, and compacting state. They attributed the observed wave phenomena to the dilation and shear localization of the infilling gouge layer induced by loading states.

## **2.2.2 Laboratory investigations using the resonant column techniques**

### **2.2.2.1 Fundamental knowledge of the resonant column technique**

Based on the principles that ① the propagation of torsional waves in columns is nondispersive, ② the torsional wave velocity equals to the S-wave velocity in an infinite medium with the same material characteristics, and ③ S-wave propagation in a cylindrical column is not affected by geometric dispersion (Kolsky, 1963), two resonant column systems, i.e., the quasi-static resonant column (QSRC) apparatus and resonant column apparatus (RCA), have been developed and applied to investigate wave propagation and attenuation across rock joints. For those resonant column systems, where the bottom of the tested sample is fixed to the base platen while the top is free with additional masses attached to the free end, the torsion and flexure of sample in the elastic range can generate shear and compressional waves in resonant frequencies. The RCA is widely used to obtain low-strain dynamic properties of soils, while it is limited to be applied in the rock mechanics due to the restrictions on the stiffness of materials. Recently, the RCA has been improved and corrected to investigate dynamic properties of rock masses by some researchers. The main difference between those two apparatuses is the approach for signal generation. Specifically, in the QSRC apparatus, the source is implemented by applying a torque at the centre of the loading cap with a brittle pencil led to make the fracture of the lead release the column, while the source is produced by the standard magnet coil system

in the RCA (Fratta and Santamarina, 2002). Therefore, the QSRC apparatus could avoid measurement difficulties and damping bias related to the counter-electromotive force in the RCA. The detailed illustration of those two apparatuses in studying wave behaviours across rock joints are provided in the following contents.

When measuring S-wave properties using the QSRC apparatus, the column is suddenly released from a quasi-static rotation enforced at the column top and then vibrates freely, generating the torsional vibrations. It should be noted that the global strain for all tests should be below  $10^{-5}$ . The accelerometers mounted on the cap top at the diametrically opposite locations are used to monitor the signals from flexural and torsional motions, where the associated low-frequency flexural signal is filtered by subtracting the time series gathered from the two accelerometers. Then, the obtained torsional signal can be used to compute S-wave velocity as follows,

$$V_S = 4Lf_R \quad \text{Equation 2.46}$$

where  $f_R$  is the resonant frequency determined from the first-mode peak resonance of frequency spectra;  $L$  is the height of the stacked column. In addition, the damping ratio of S-wave can be determined by using least square method to best fit the acceleration function  $A(f)$  of a single degree of freedom system as below (Song and Cho, 2010)

$$A(f) = \frac{f^2 \times f_R^2}{\left| k \left( f_R^2 - f^2 + j \times 2 \times D \times f \times f_R \right) \right|} \quad \text{Equation 2.47}$$

where  $f$  is the frequency;  $j$  is an imaginary index;  $D$  is the damping ratio of S-wave;  $k$  is the stiffness.

When assessing P-wave attributes using the QSRC apparatus, P-wave signals are generated using a small steel ball dropped from a fixed height to impact the column. For each test, the global strain should be smaller than  $10^{-4}$ . Two accelerometers aligned in the vertical direction, one mounted on the lower surface of the bottom disk and the other on the top of the column, are used to monitor P-wave signals. In this system, the column cannot be regarded as a free-fixed system, and the resonance of P-wave is affected by the rod together with the weights. The P-wave velocity can be calculated as

$$V_P = \frac{L}{\Delta t} \quad \text{Equation 2.48}$$



where  $L$  is the height of the stacked column and  $\Delta t$  is the travel time of P-wave through the column. However, P-wave attenuation is impossible to be precisely determined because P-wave propagation in the column is dispersive due to the longitudinal inertial effects caused by the radial inertia (Cha et al., 2009).

When conducting a torsional test via the RCA, the electromotive force (EMF) produced by the movement between four sets of magnets and coils results in a sinusoidal excitation, which is applied to the top of the tested sample. Based on the theory of torsional elastic wave propagation in cylindrical rods (Richart et al., 1970), S-wave velocity from torsional vibrations could be calculated by

$$\frac{I}{I_0} = \beta \cdot \tan \beta \quad \text{Equation 2.49}$$

$$V_s = \frac{2\pi fl}{\beta} \quad \text{Equation 2.50}$$

where  $f$  is the resonant frequency obtained from the RCA test on the sample;  $l$  is the length of the tested sample;  $I$  and  $I_0$  are mass polar moments of inertia for the tested sample and driving plate, respectively.

When performing a flexural test through the RCA, a horizontal force is applied to the top of sample by switching off two alternate coils surrounding the magnets, which results in flexural vibrations. According to the Rayleigh's energy method, P-wave velocity  $V_p$  could be determined by (Cascante et al., 1998)

$$\omega = \frac{3EI_a}{\left[ \frac{33}{m} + \sum_{i=1}^n m_i h(htb_i, htt_i) \right] l^3} \quad \text{Equation 2.51}$$

$$V_{rod} = \sqrt{E/\rho} \quad \text{Equation 2.52}$$

$$V_p = V_{rod} \sqrt{\frac{(1-\nu)}{(1+\nu)(1-2\nu)}} \quad \text{Equation 2.53}$$

where  $\omega$  is the flexural circular frequency of the tested sample;  $E$ ,  $\rho$  and  $\nu$  are the Young's modulus, density and Poisson's ratio of the sample, respectively;  $I_a$  is the area moment of inertia of the sample;  $m$  is the mass of the sample;  $m_i$  is the mass of each additional mass

placed on top of sample such as top cap, top plate and driving plate;  $htb_i$  is the distance measured from the top of sample to the bottom of additional mass  $m_i$ ,  $htt_i$  is the distance measured from the top of sample to the top of additional mass  $m_i$ ;  $V_{rod}$  is the compression wave velocity in a bounded medium.

### 2.2.2.2 Studies of wave propagation across rock joints using the QSRC apparatus

A quasi-static resonant column (QSRC) apparatus was originally established by Fratta and Santamarina (2002) to experimentally study long-wavelength S-wave propagation through multiple parallel rock joints subjected to controlled low normal stresses. The QSRC apparatus is a free-fixed dynamic system, where the fixed boundary multiple annular discs are stacked on a large steel base. Their work suggested that the increasing normal stress resulted in higher S-wave velocity and less wave damping. In addition, the presence of clay in joints led to more wave loss. With the increase of clay thickness, S-wave velocity decreased while wave damping increased.

Following that, Cha et al. (2006, 2009) improved the QSRC apparatus to further study the effects of joint parameters (including joint surface topography, joint spacing, joint cementation and plasticity of filling materials) and loading paths on S-wave behaviors across multiple parallel rock joints under relatively high normal stresses. Moreover, they also measured P-wave velocity during the QSRC tests using two accelerometers that were mounted at the top and bottom of the column, respectively, aligned in the vertical direction next to the central orifice. The test results indicated that a larger normal stress resulted in increases in P- and S-wave velocities and a decrease in wave damping. Besides, wave velocity across filled joints were higher during unloading than loading in most cases while there was no preloading effect on wave velocity across unfilled joints. For unfilled joints, the matched grooved joints led to higher S-wave velocity and less wave attenuation compared to planar joints. As the joint surface became rougher, wave velocity was more insensitive to the normal stress. In addition, the increase of joint spacing caused increases in P- and S-wave velocities while it has negligible effects on S-wave damping. Besides, joint cementation could effectively increase S-wave velocity and lower S-wave attenuation. Compared to unfilled joints, the joints filled with gouge materials, particularly if the material is clay origin, reduced P- and S-wave velocities but enhanced S-wave attenuation. In addition, P- and S-wave velocities decreased while S-wave attenuation increased as the gauge thickness increased.



Although the effects of joint surface roughness on long-wavelength wave propagation across multiple parallel rock joints were briefly studied by Cha et al. (2006, 2009), the correlation between the 2D JRC and the wave attributes was not to be well examined in their work. In this regard, Mohd-Nordin et al. (2014) further investigated the effects of joint surface roughness on long-wavelength wave properties across multiple rock joints using the replicated QSRC apparatus, where the joint surface roughness was characterized by the 3D JRC. The test results indicated that S-wave velocity increased while P-wave velocity and S-wave damping decreased as the 3D JRC increased. The comparison between wave properties across replicated joint surfaces based on 2D and 3D joint surface profiles suggested that implication of replicated 3D joint surface was more reliable for studying wave attributes. Furthermore, Mohd-Nordin et al. (2016) comprehensively studied the evolution of joint surface morphology under the cyclic loading and its effects on wave properties through the QSRC tests. It was found that the change in the high-JRC surface exceeded that in the low-JRC surface under cyclic normal loading.

### **2.2.2.3 Studies of wave propagation across rock joints using the RCA**

With the help of the RCA, Perino and Barla (2015) experimentally examined the effects of rock joint on long-wavelength S-wave propagation. They found that the increase of joint number reduced the resonant frequency and wave velocity of the jointed sample, while it led to an increase in wave attenuation. Furthermore, Sebastian and Sitharam (2015, 2016, 2018) employed the RCA system to comprehensively investigate wave properties across frictional and filled joints under various strain levels under different confining pressures. For wave propagation through single joints, it was found that wave velocity maximized across the vertical joint (i.e., the joint is vertical to the end surface of cylindrical sample) and minimized across the horizontal joint (i.e., the joint is parallel to the end surface of cylindrical sample) regardless of the confining pressure and filling condition. However, an opposite trend of damping ratio was observed from joints with different orientation. As the joint orientation varies from  $0^\circ$  (for vertical joint) to  $90^\circ$  (for horizontal joint), the reduction of wave velocity was more evident for S-waves than P-waves. At high confining pressure, wave propagated across single joints under different orientations (except for vertical joints) at an almost identical speed. For wave propagation across multiple parallel joints, the ratio of wavelength ( $\lambda$ ) to the joint spacing ( $L$ ) is an important parameter to affect wave attributes. Specifically, the increase of  $\lambda/L$  led to decreasing wave velocity. In addition, the test results indicated that S-waves were more affected by the joint orientation and confining pressure compared to P-waves. Besides, the influence of  $\lambda/L$  on wave damping could be neglected at low strain levels, while the

influence of  $\lambda/L$  became prominent, especially for P-wave, at high strain levels. Regardless of joint numbers, the increase of confining pressure led to increasing wave velocity and decreasing wave damping, where S-wave were attenuated more than P-wave. In addition, the increasing strain level led to a decrease in wave velocity and an increase in wave damping. Moreover, their work also proved that the presence of gouge material in joints has a significant role in wave propagation and attenuation. For frictional joints, S-wave velocity was more dependent on the confining pressure than P-wave velocity. For filled joints, P-wave velocity was more dependent on the confining pressure than S-wave velocity. In addition, filled joints damped more wave energy than frictional joints.

## **2.2.3 Laboratory investigations using the split Hopkinson pressure bar technique**

### **2.2.3.1 Fundamental knowledge of the split Hopkinson pressure bar technique**

Based on the original idea of Hopkinson (1872), Kolsky (1949) initially established the split Hopkinson pressure bar (SHPB), also referred as the Kolsky bar, to measure dynamic mechanical behaviors of different materials at high strain rates ( $10^2$  -  $10^4$  s<sup>-1</sup>). With the years of development and improvement, the SHPB technique has been recommended as a standard experimental approach to measure dynamic behaviors of rock materials by the International Society of Rock Mechanics (ISRM) (Zhou et al., 2011). The SHPB tests are available and reliable to determine the dynamic properties of rock materials, including dynamic stress-strain curves, dynamic compressional and tensile strengths, dynamic fracture toughness and so on (Lindholm et al., 1974, Lundberg, 1976, Li et al., 2000, Frew et al., 2001, Li et al., 2005, Li et al., 2008, Xia et al., 2008, Chen et al., 2009, Dai et al., 2010, Zhang and Zhao, 2014, Zhou et al., 2014, Xia and Yao, 2015).

As shown in Fig. 2.3, a conventional SHPB system consists of a striker bar together with a gas gun, an incident bar, a transmitted bar, an absorption bar, and the tested specimen sandwiched between the incident and transmitted bars. Traditionally, those three bars in the SHPB system are made of the same material and have the same diameter. During each test, the striker is instantaneously released through the gas gun and impacts the incident bar, generating a compressional stress wave  $\varepsilon_{In}$  (i.e., the incident pulse). Notice that the duration of the incident wave is determined by the length and compressional wave velocity of the striker bar. The incident stress wave propagates along the incident bar towards the tested specimen. When the

incident wave reaches the interface between the specimen and the incident bar, it is partially reflected into the incident bar as a tensile stress wave  $\varepsilon_{Re}$  (i.e., the reflected pulse). Meanwhile, the remain portion of the incident stress wave travels through the specimen and then spreads into the transmitted bar as a compressional wave  $\varepsilon_{Tr}$  (i.e., the transmitted pulse). All those stress waves are measured by the strain gauges mounted on the incident and transmitted bars.

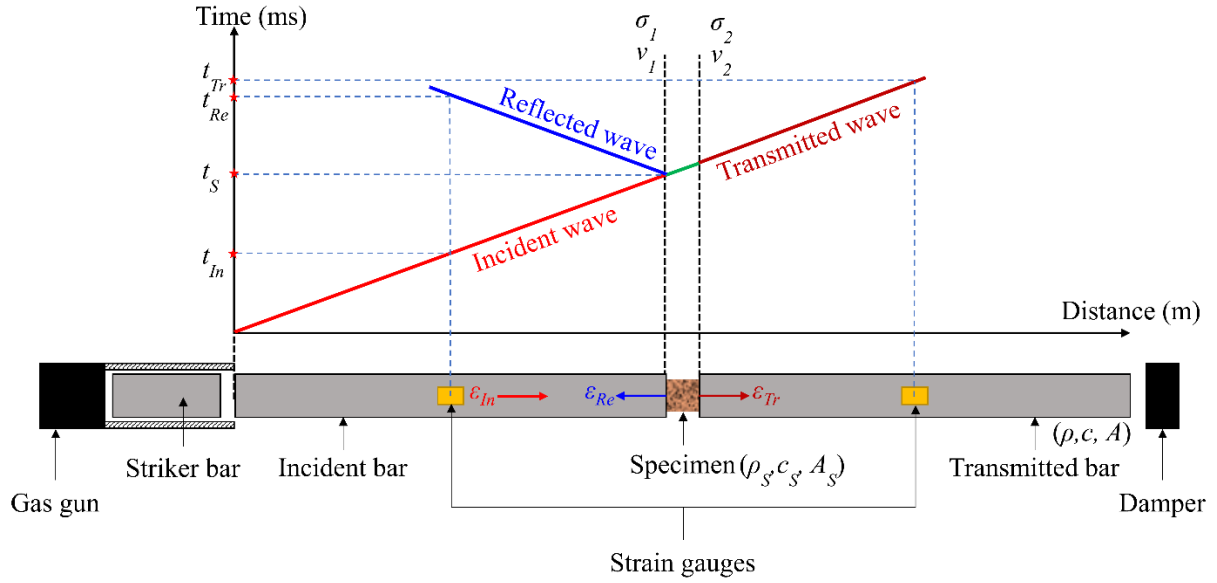


Figure 2.3 The schematic and Lagrangian wave propagation diagram of a conventional SHPB system (modified after Zhang (2014)).

The requirement for a valid SHPB test is to maintain the dynamic stress equilibrium, which guarantees that the specimen is under a uniaxial stress condition and the uniaxial stress within the specimen is uniformly distributed along its thickness. In the literature, several approaches are widely employed to achieve the dynamic stress equilibrium: ① lubricating the bar-specimen interfaces to make them in good contact, ② keeping all bars coaxial, ③ reducing the friction between the bars and the supporting framework, and ④ using the appropriate pulse shaper (Frew et al., 2002, Dai et al., 2010, Xia and Yao, 2015).

For a valid SHPB test, the signals recorded by the strain gauges mounted on the bars are considered as the pulses at the bar-specimen interfaces based on the assumption that no dispersion occurs as stress waves propagate along the incident and transmitted bars, which could be further processed to obtain the dynamic mechanical properties of the tested specimen. To be specific, the wave velocities at the bar-specimen interfaces can be acquired according to the one-dimensional (1-D) wave theory (Chen and Song, 2010)

$$v_1 = c(\varepsilon_{In} - \varepsilon_{Re}) \quad \text{Equation 2.54}$$

$$v_2 = c\varepsilon_{Tr} \quad \text{Equation 2.55}$$

where  $c$  represents the 1-D longitudinal stress wave velocity of the bar.  $\varepsilon_{In}$ ,  $\varepsilon_{Re}$  and  $\varepsilon_{Tr}$  stand for the incident, reflected and transmitted strain signals, respectively. Consequently, the strain rate of the tested specimen is obtained (Gray, 2000)

$$\dot{\varepsilon} = \frac{v_1 - v_2}{L_S} = \frac{c}{L_S} (\varepsilon_{In} - \varepsilon_{Re} - \varepsilon_{Tr}) \quad \text{Equation 2.56}$$

where  $L_S$  is the length of the specimen. Accordingly, the strain and stress in the test specimen are acquired

$$\varepsilon = \int_0^t \dot{\varepsilon} dt = \int_0^t \frac{c}{L_S} (\varepsilon_{In} - \varepsilon_{Re} - \varepsilon_{Tr}) dt \quad \text{Equation 2.57}$$

In addition, the stresses at the end surfaces of the specimen are given by

$$\sigma_1 = \frac{A}{A_S} E(\varepsilon_{In} + \varepsilon_{Re}) \quad \text{Equation 2.58}$$

$$\sigma_2 = \frac{A}{A_S} E\varepsilon_{Tr} \quad \text{Equation 2.59}$$

where  $A$  and  $A_S$  are the cross-sectional area of the bar and specimen, respectively;  $E$  is the elastic modulus of the bar. Thus, the stress in the tested specimen can be derived as (Kolsky, 1963)

$$\sigma = \frac{\sigma_1 + \sigma_2}{2} = \frac{AE}{2A_S} (\varepsilon_{In} + \varepsilon_{Re} + \varepsilon_{Tr}) \quad \text{Equation 2.60}$$

### 2.2.3.2 Studies of stress wave propagation through unfilled rock joints using the SHPB technique

In the literature, Ju et al. (2007) firstly employed the SHPB technique to investigate stress wave propagation across unfilled rock joints. In their study, a series of SHPB tests were performed on single rock joints with various irregular surface configurations to quantify the influence of joint surface roughness on stress wave propagation, where the three-dimensional joint surface roughness was characterized by the fractal dimension based on the fractal geometry method

(Xie et al., 1998). Their work suggested that the rougher the joint surface was, the more wave energy was attenuated by the joint, which was attributed to that more permanent deformation of joint was caused and led to more energy dissipation in the joint. Recently, Li et al. (2011b) utilized the SHPB technique and the fractal geometry method to investigate stress wave behaviors across single rough rock joints. They found that wave transmission decreased while wave reflection increased as the joint surface became rougher. Apart from the fractal dimension, rock joint surface roughness can also be well described by joint roughness coefficient (JRC) (Barton and Choubey, 1977). Using the modified SHPB apparatus, Li et al. (2019b) carried out extensive dynamic tests on artificial joints with different JRCs to study the effects of joint surface roughness on wave attenuation, where the jointed gypsum samples are produced via the three-dimensional printer technique. Their test results showed that the seismic quality factor of jointed sample decreases monotonously with the increase of JRC, indicating that the rougher joint causes more wave energy dissipation.

In addition to joint surface roughness, the other key joint geometrical property, i.e., joint matching condition that is characterised by the joint matching coefficient (JMC) (Zhao, 1997a, Zhao, 1997b), plays a role in stress wave propagation across rock joints. The effects of JMC on stress wave propagation across rock joints have been studied by some researchers using the SHPB technique (Chen et al., 2015, Chen et al., 2016, Li et al., 2017). In the literature, JMC equals to the contact area ratio between two coupling joint surfaces. Based on SHPB test results, it was concluded that the increase of JMC caused more wave transmission yet less wave reflection on the joint. It was also found that, for a given JMC, the joint with clustered contact area led to greater wave transmission compared with the joint with dispersed contact area.

Except for joint surface geometry, other joint properties, such as joint thickness and joint orientation, have also been focused in the literature when studying stress wave propagation across unfilled joints through the SHPB technique. Results from SHPB tests in Chen et al. (2015, 2016) indicated that less wave transmission across the joint with larger thickness. Li et al. (2019a) conducted SHPB tests on red sandstone samples with single bonded inclined joints and observed that a larger joint angle caused more wave reflection yet less wave transmission. It should be noted that the joint angle was defined as the acute angle between the dynamic loading direction and the normal line of joint direction in their study.

### 2.2.3.3 Studies of stress wave propagation through filled rock joints using the SHPB technique

Using the split Hopkinson rock bar apparatus (SHRB), i.e., a modified SHPB apparatus with granite pressure bars, Li and Ma (2009) and Li et al. (2010) conducted a series of dynamic tests on single filled joints with different joint thicknesses and water contents of filling sand to investigate stress wave propagation across the joint. In their study, the filled joint was simulated by a sand layer sandwiched between the incident and transmitted granite bars. Test results showed that larger joint thickness and higher water content of filling sand caused less wave transmission across the filled joint. It was also observed that wave transmission across the filled joint increases with the input wave energy.

Using a SHRB apparatus with norite rock bars, stress wave propagation across filled rock joints was further deeply investigated by Wu and his coworkers (2012a, 2012b, 2013a, 2013b, 2014, 2015, 2015). It was observed that the filled joint attenuated more wave energy than the unfilled joint. In addition, the increase of loading rate could lead to a larger increase in wave transmission coefficient across the filled joint compared to the unfilled joint. For the joint only filled with sand, the denser sand associated with finer particle size in the joint led to smaller wave transmission coefficient. In addition, a higher water content of filling sand caused the increase of wave attenuation factor. For the joint filled with clay-sand mixture, the wave transmission coefficient increased and maximized when the clay weight fraction was around 30%, followed by a monotonous decrease with the continuously increasing clay weight fraction. The opposite trend was observed for seismic attenuation factor. Besides, the increase of joint thickness reduced transmitted wave energy regardless of properties of filling materials. They also measured stress wave behaviors across two parallel filled rock joints. An increase in the wave transmission coefficient with the increasing joint spacing was observed when the joint spacing is much smaller than the incident wavelength, followed by a decrease in the wave transmission coefficient with the continuously increasing joint spacing due to the effects of wave superposition between those two joints. The test results also indicated that the transmitted wave across the first joint strongly affected wave behaviors across the second joint when stress wave propagates through two parallel joints with dissimilar properties.

In the above literature, the usage of SHRB apparatus restricts the amplitude of stress wave to 8 MPa for protecting rock bars from damages. Therefore, results in these studies only provided insights into low-amplitude stress wave responses to rock joints. Since stress waves in some

practical projects and natural events often have much high amplitudes (Singh, 2002, Vidale and Li, 2003, Khandelwal and Singh, 2007, Senft and Stewart, 2009), it is necessary to understand the effects of rock joints on high-amplitude stress wave propagation. To this end, Huang and his coworker (2016, 2018a, 2018b) conducted a series of impacting tests on single filled joints using an aluminum steel SHPB apparatus. Based on findings of SHPB tests on single joints filled with dry sand, they suggested that the filled joint would experience three stages, i.e., the initial compaction stage, the crushing stage and the coupled crushing-compaction stage when high-amplitude stress waves propagating the joint. In the initial compaction stage, transmission coefficient increases with increasing amplitude of stress waves because the compaction of filling material particles improves the joint stiffness. After then, in the crushing stage, the increase of stress wave amplitude results in a decrease in transmission coefficient because that particle crushing softens the joint. Following that, in the coupled crushing-compaction stage, it is difficult to further crush particles into new smaller ones as the number of small particles increases; hence the filling material would be compacted again. Consequently, the continuously increasing stress wave amplitude could harden the joint again, thereby enhancing transmission coefficient across the joint. Furthermore, the steel SHPB apparatus was also employed by Li et al. (2018) to investigate the effects of joint thickness on high-amplitude wave propagation across single joints filled with dry sand. The test results showed that the increasing joint thickness led to a decrease in wave transmission

Although the effects of water content in the sand-filled rock joint on low-amplitude stress wave propagation was studied by Wu and Zhao (2015) using a SHRB apparatus, they failed to discuss the effects of water-sand segregation when directly mixing quartz sand with water to form the wet infill. To reduce effects of water sinking caused by the gravity, Huang et al. (2018b) added the hydrophilic kaolinite clay as the water retention agent to further studied high-amplitude stress wave behaviors across single joints filled with wet materials using the steel SHPB apparatus. It was found that the transmission coefficient firstly decreased and then increased with the increasing water content. In addition, the transmission coefficient increased with the increase of stress wave amplitude for wave propagation through the joint filled with unsaturated sand-clay mixture, while it is insensitive to the joint filled with dry or fully saturated material.

More recently, Huang et al. (2020) investigated the interaction of stress waves with single rock joints full of water through the SHPB tests, where a liquid application device was introduced to simulate water-filled rock joints under undrained conditions. It was observed that an increase

in the initial joint thickness led to the decreasing transmission coefficient and increasing peak liquid pressure. By performing the curve fitting on the processed data, they established a brief relationship between the transmission coefficient and peak liquid pressure. The potential of the observed correlation for evaluating hydraulic dynamic variations of enclosed liquid-filled rock discontinuities was emphasized. However, their work focused only on the role of initial joint thickness in stress wave transmission across single joints under fully water saturating and undrained conditions.

#### **2.2.3.4 Extended studies on the interaction of rock joints and waves using the modified SHPB techniques**

It should be noted that the general SHPB test is only capable of studying primary stress wave propagation across rock joints. To study high-amplitude S-wave propagation across rock joints, a new device named as the Split Shear Plates (SSP), consisting of an incident granite rock plate, a transmitted granite rock plate, a normal loading setup, a friction bar made of stainless steel and a dynamic triggering system, was developed by Liu et al. (2017) based on the frictional slip and SHPB technique. Using the SSP apparatus, Liu et al. (2017) performed extensive tests on single rock joint filled with dry sand to determine effects of the crustal stress, joint thickness as well as particle size of filling sand on S-wave propagation across the joint. It was found that the increasing crustal stress resulted in a nonlinear increase in the transmission coefficient, while the increasing joint thickness slightly reduced the transmission coefficient. Besides, transmission coefficients for the joint filled with coarse particles were smaller than those for the joint filled with fine particles.

In addition, the traditional SHPB technique is unable to measure plane wave oblique incidence upon rock joints in laboratory. To examine seismic responses to rock joints under obliquely incident plane P-wave, Zou et al. (2019) established a new experimental system based on the SHPB technique, which consists of the impact loading system (including a striker rock plate, an incident rock plate and a transmitted rock plate), the lateral confining frame and the data acquisition scheme. Their test results indicated that transmission coefficients for transmitted P- and S-waves were insensitive to the change of incident angle, while the increase of incident angle led to an increase in reflection coefficients for reflected S-wave but a decrease in reflection coefficients for reflected P-wave. It was also observed that transmission coefficients for transmitted P-wave were much larger than those for transmitted S-waves, while reflection



coefficients for reflected S-wave was getting close to those for reflected P-wave with the increase of incident angle.

## 2.3 Existing research gap and concluding remarks

The earlier sections have briefly reviewed the progresses made in the interaction of waves and individual rock joints from the theoretical and experimental perspectives. The foregoing review indicates that the interaction of waves with individual rock joints is governed by the joint intrinsic characteristics (e.g., joint thickness, joint surface roughness, contact area and spatial orientation), infilling material properties (e.g., components and distribution) and environmental factors (e.g., stress state and temperature).

Most of the previous studies have targeted wave propagation and attenuation across individual rock joints filled with various materials. It has been shown that fluids play a role in the interaction of waves and individual rock joints. Compared to the theoretical analysis, comparatively few laboratory experiments have been reported with the aim of determining fluid effects on wave behaviours across individual rock joints. The laboratory experiments, in which physical conditions can be artificially controlled, could not only provide more insights into the extension and development of theories but also be useful for the validation of the existing theoretical models. Accordingly, laboratory observations are needed for better understanding the role of fluids in the interaction of waves and individual rock joints.

Although wave propagation across rock joints containing fluids have to some extent investigated at the laboratory scale, many gaps remain in how fluids affect the interaction of waves with individual rock joints due to the lack of laboratory observations. Specifically, for rock joints filled with fluid-solid mixture, the existing laboratory studies focused mainly on wave propagation across water-saturated sandy gouge-filled rock joints. Nevertheless, the fluid effect on the interaction of waves with individual rock joints filled with clayey gouge has not been systematically studied in the laboratory. For rock joints filled with fluids only, most of relevant studies adopted the low-intensity waves (i.e., ultrasonic waves) to determine wave responses of individual fluid-filled rock joints, where only limited cases were tested and the effects of some influencing factors are still poorly understood. Besides, the laboratory tests on the interrelations of high-intensity wave attributes and dynamic responses of fluid-filled joint have not been reported so far.

To thoroughly determine the role of fluids in the interaction of waves with individual rock joints, this research was designed and performed in the laboratory. This study is intended to examine the fluid-dependent wave behaviours across single rock joints based on the ultrasonic measurements and SHPB tests, concentrating on single clayey gouge-filled joints and fluid-filled joints. The detailed work and key findings will be described in the following chapters. The present study will be a small step towards the achievement of building up a comprehensive knowledge body of Earth science.

## CHAPTER 3 RESEARCH METHODOLOGIES

This chapter presents a detailed description of the laboratory techniques and corresponding data processing methods employed in the current research for studying the fluid effects on wave behaviours across rock joints. Specifically, section 3.1 provides a clear illustration of a self-developed ultrasonic pulse-transmission test system and the common data processing methods for analysing original acoustic waveforms. In section 3.2, a self-established SHPB test system is illustrated in detail, and the processing procedure of the collected stress waves is thoroughly demonstrated. Section 3.3 emphasizes the applications of those two experimental techniques for achieving the objectives of this research.

### 3.1 The ultrasonic pulse-transmission (UPT) test

#### 3.1.1 Experimental system and calibration

##### 3.1.1.1 The UPT test set-up and apparatuses

In this research, an ultrasonic pulse-transmission (UPT) test system was designed and established to investigate the fluid effect on low-amplitude wave attributes of individual rock joints. As illustrated in Figure 3.1, the test configuration consists of a uniaxial loading subsystem and an ultrasonic test subsystem. To be specific, the uniaxial loading subsystem is comprised of a loading cell, a hydraulic pump, a hydraulic jack, and a steel loading frame, as shown in Figure 3.1. The loading system was utilized to impose a constant external axial stress to the assembly of the tested specimen and the transducer pair, aiming to enhance the coupling of the interfaces and improve the stability of the test system.

In addition, the ultrasonic test subsystem is composed of a Tektronix digital oscilloscope (model DPO 2012B), an Olympus pulser/receiver (model 5077PR), a pair of ultrasonic transducers (i.e., a transmitter and a receiver) and a personal computer (PC), as shown in Figure 3.1. In present study, two pairs of ultrasonic P-wave transducers (i.e., Olympus model X1020, V192) and three pairs of S-wave transducers (i.e., Olympus model V150, V151 and V152) were adopted to examine both P- and S-wave responses of rock joints. For each measurement, the transmitter is excited by a 200-Voltage spike with a duration of 10  $\mu$ s at a repetition rate of 100 Hz generated by the Olympus pulser/receiver, and then the simultaneous pulses are sent into the tested specimen. After propagating through the specimen, the transmitted waves were

detected and captured by the receiver connected to the pulser/receiver. The oscilloscope connected to the pulser/receiver is used to digitize, display and record a portion of each transmitted signal with a duration of  $120\ \mu\text{s}$  at a sample interval of  $0.001\ \mu\text{s}$ . Note that 64 digitized transmitted pulses are stacked and averaged to produce a high signal-to-noise ratio and then to generate stable waveforms in each test. The received stable signals are saved on a hard disk through a PC equipped with a special data acquisition software.

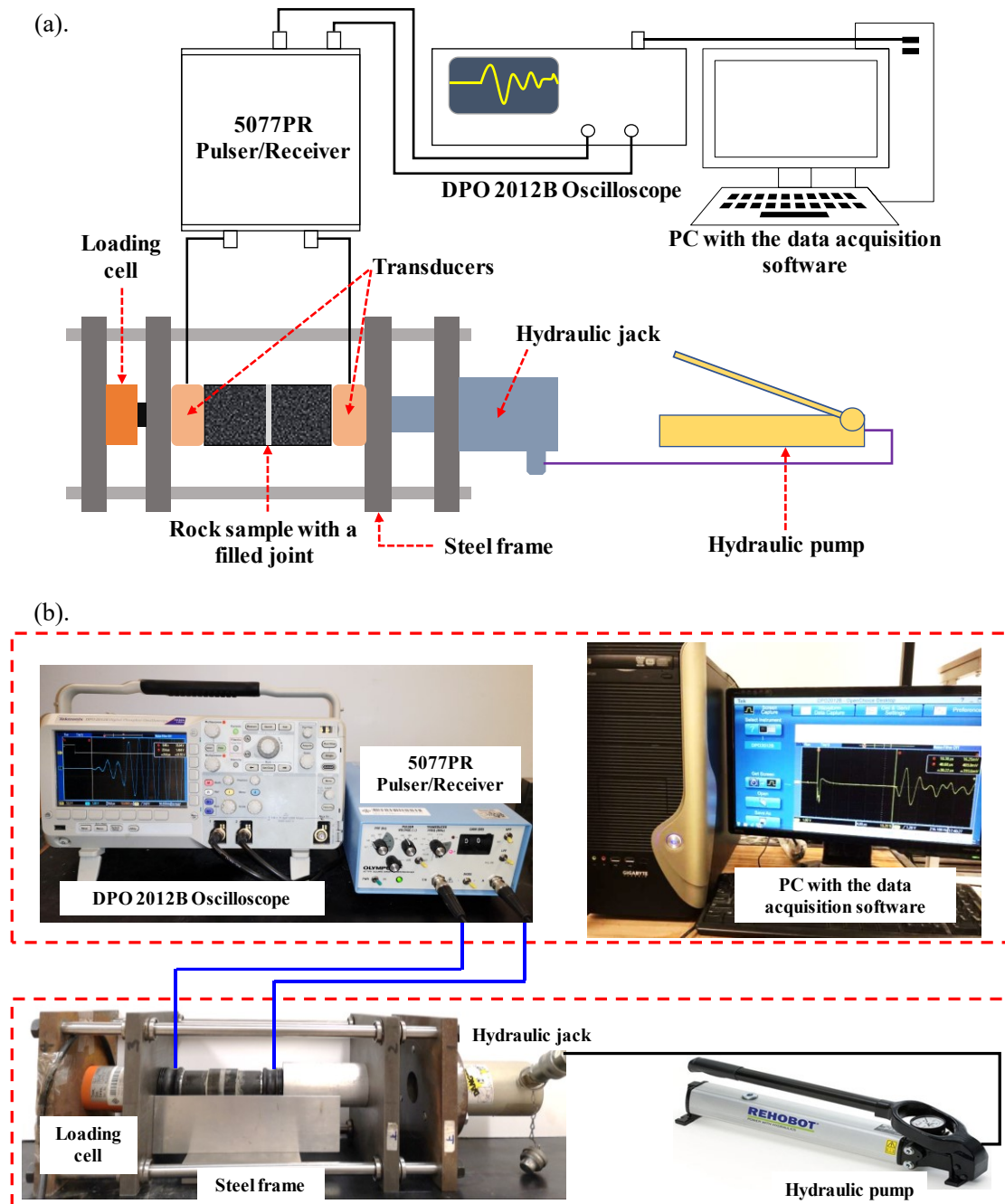


Figure 3.1 The self-established ultrasonic pulse-transmission test system used in this research: (a). the schematic of the test system, (b). the laboratory photograph of the test system.

### 3.1.1.2 Calibration of the UPT test system

The objective of calibration is to ensure that ultrasonic measurements conducted by the self-established test configuration are repeatable within an acceptable error. For this purpose, a series of calibration tests were conducted on a standard aluminium specimen under the same experimental setting. The standard aluminium specimen was fabricated with the same external dimensions as a standard rock sample, i.e., 49 mm in diameter and 100 mm in length. The density and elastic modulus of the aluminium used in this research are  $2700 \text{ kg/m}^3$  and 69 GPa, respectively.

The calibration of the UPT test system was conducted for every transducer pair used in this study. For each transducer pair, five ultrasonic measurements were repetitively performed on the aluminium specimen. Note that the experimental setup should be disassembled and then reassembled between two adjacent ultrasonic measurements to ensure the reproducibility of ultrasonic tests. Herein, the specimen assembly process was standardized to ensure the repeatability of ultrasonic measurements in this research. To be specific, a thin couplant film (the Vaseline for P-wave transducers and Olympus SWC-2 couplant for S-wave transducers) was applied at the interfaces of the target specimen and the transducers. Then, a certain small uniaxial pressure ( $\sim 0.1 \text{ kN}$ ) was imposed to the assembly of the specimen and transducer pair, which was maintained throughout the whole period of ultrasonic test to stabilize the good coupling between transducers and the tested specimen.

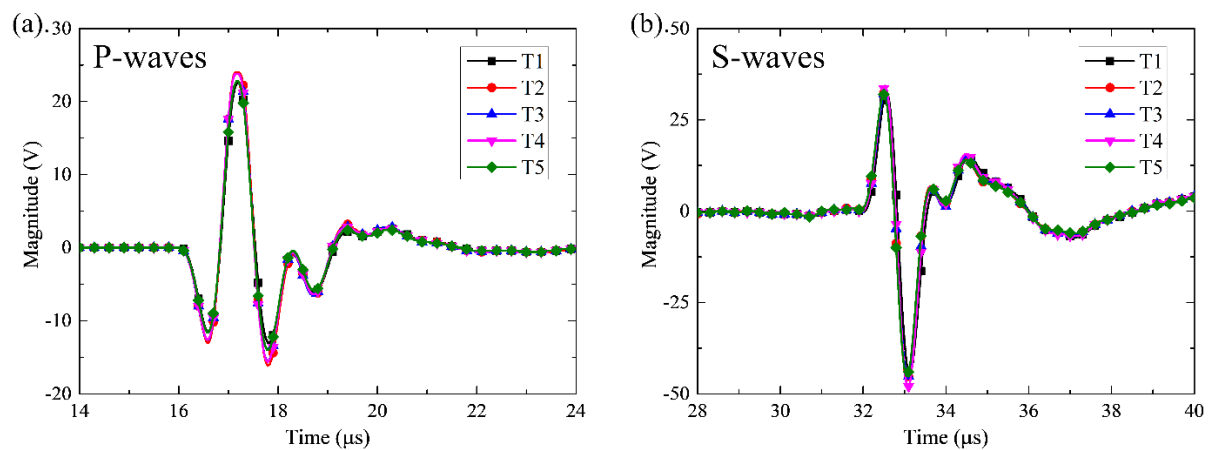


Figure 3.2 The waveforms of transmitted pulses obtained from the calibration tests on the aluminium specimen using two ultrasonic transducer pairs for generating (a). 1-MHz P-waves and (b). 1-MHz S-waves.

In Figure 3.2, the original waveforms obtained from the calibrations of a 1-MHz P-wave transducer pair (Olympus model V192) and a 1-MHz S-wave transducer pair (Olympus model V152) are presented as an example to directly identify the discrepancy between reproducible measurements. It is shown that the waveforms are almost visually identical for both P- and S-wave transducer pairs. Moreover, the error analysis was conducted on the waveforms obtained from repetitive tests for all transducer pairs, which focused mainly on the peak-to-peak amplitudes of initial pulses and wave velocity. The results of the error analysis are tabulated into Table 3.1, which show that variations in signal amplitudes and wave velocity were within 2% - 5% and 0.03% - 0.13%, respectively. It is therefore concluded that the self-established test system is reliable to conduct highly reproducible and accurate ultrasonic measurements.

**Table 3.1 The results of the error analysis on waveforms obtained from the calibration of UPT test system using different transducer pairs.**

Wave type	$f_{SET}$ (MHz)	$A$ (V)	$e_A$	$V$ (m/s)	$e_V$
P-wave	0.1	1.28±0.05	4.22%	6336.69±8.16	0.13%
	1	35.17±1.70	4.84%	6364.62±7.36	0.12%
S-wave	0.25	144.16±4.09	2.84%	2851.63±1.19	0.04%
	0.5	154.80±5.22	3.37%	3146.64±3.06	0.10%
	1	78.48±2.27	2.89%	3183.60±3.04	0.10%

### 3.1.2 Data processing methods

#### 3.1.2.1 Calculation of wave velocities

According to ASTM Standard D2845-08 (2008), wave velocity in the jointed rock sample can be calculated by

$$V = \frac{L}{t} \quad \text{Equation 3.1}$$

where  $L$  is the total length of the rock sample measured by a Vernier calliper with an accuracy of 0.01mm, and  $t$  is the travel time of wave through the rock sample determined by subtracting the delay time of transducers ( $t_d$ ) from the measured arrival time of wave through the rock specimen ( $t_a$ ). Based on ASTM Standard D2845-08 (2008), the delay time of transducers can

be determined by the face-to-face tests, where the transmitter is directly docked to the receiver during each ultrasonic measurement.

The key issue for calculating wave velocity is to accurately determine the travel time of waves in the tested specimen. In the literature, the techniques commonly employed to ascertain the travel time can be divided into two categories, i.e., the time-domain methods and frequency domain approaches, where no one method seems to stand out as being superior to the others. In this research, two popular time-domain approaches, i.e., the visual picking method and the first major peak-to-peak method, were adopted to determine the arrival time of P- and S-waves, respectively, which are illustrated in detail below.

- 1) The visual picking method is perhaps the simplest and most straightforward method for determining the arrival time of waves, which is applicable for the received signals with a clearly visual deflection at the first-arrival pulse (Viggiani and Atkinson, 1995). This method takes the first major deflection of the waveforms as the arrival time. Given that the received P-waves in this research exhibited the first significant departure from zero amplitude, the visual picking method was appropriate to access the travel time of P-waves. An example of determining the travel time of a typical transmitted P-wave from the present study is illustrated in Figure 3.3a. It should be noted that, the delay time should be eliminated to ascertain the accurate travel time of P-waves propagating through the tested specimen.
- 2) The first major peak-to-peak method is superior to the visual picking approach when the received signals do not display a distinct and sharp deflection point (Viggiani and Atkinson, 1995). In this method, the travel time of shear waves is defined as the time interval between the first major peaks on the transmitted and received signals. The laboratory data obtained in this research showed that, in most circumstances, the first arrival point of S-waves was masked by the interference which could be attributed to the background noise, distortion or near-field effect. Thus, the first major peak-to-peak method was more suitable for determining the arrival time of S-waves. Figure 3.3b presents an example of ascertaining the travel time of a typical transmitted S-wave through the tested rock specimen.

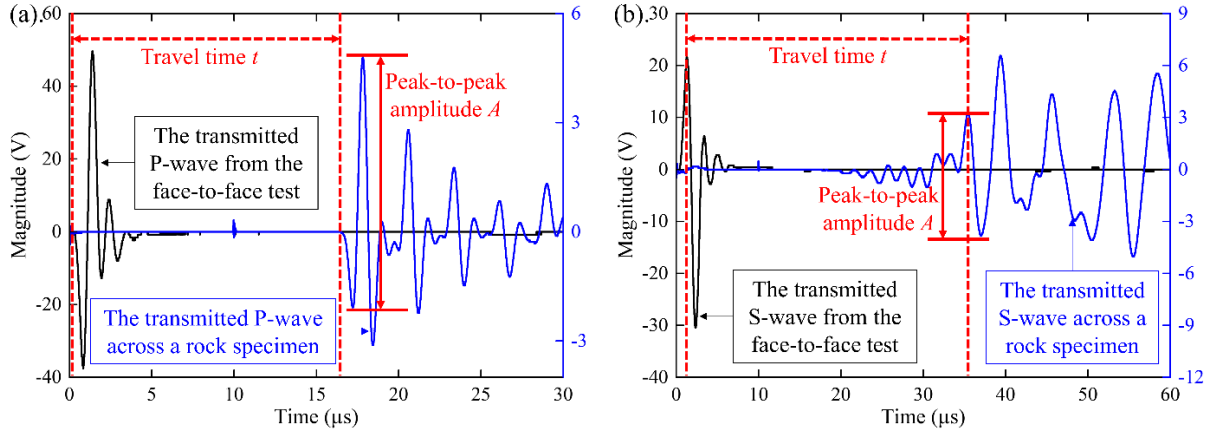


Figure 3.3 Illustration of determining the travel time and peak-to-peak amplitude of the first arrival pulses based on laboratory data for: (a). P-waves and (b). S-waves.

For propagating waves with high-frequency and short-wavelength, the travel time of wave through the jointed rock sample is equivalent to the cumulative travel time of wave through rock matrix and the joint (Fratta and Santamarina, 2002). Accordingly, the relationship among wave velocities of the whole jointed rock sample, the rock matrix and the rock joint could be described by Wyllie's time-average equation as follow (Wyllie et al., 1956)

$$V = \frac{L}{t_r + t_j} = \frac{\frac{L_r + L_j}{\frac{L_r}{V_r} + \frac{L_j}{V_j}}}{\frac{L_r}{V_r} + \frac{L_j}{V_j}} \quad \text{Equation 3.2}$$

where  $t_r$  and  $t_j$  are travel time of waves across the rock matrix and the rock joint, respectively;

$L_r$  and  $L_j$  are the length of the rock matrix and the rock joint, respectively;  $V_r$  and  $V_j$  are wave velocities in the rock matrix and the rock joint, respectively. Based on Equation 3.2, to better understand the effects of single fluid-filled rock joints on wave properties in this study, wave velocity in the rock joint can be computed by

$$V_j = \frac{L_j}{t - \frac{L_r}{V_r}} \quad \text{Equation 3.3}$$

### 3.1.2.2 Calculation of transmission ratio

Wave transmission is commonly characterized by the transmission ratio, which is physically defined as the ratio between amplitudes of the transmitted and incident waves (Achenbach,



2012). When evaluating wave transmission through rock joints, the transmitted wave through an intact rock sample is regarded as the reference incident pulse to eliminate effects of micro-pores and micro-cracks as well as interfaces between the rock sample and transducers on wave propagation (Pyrak-Nolte et al., 1990). Herein, transmission ratio could be calculated using peak-to-peak amplitudes of the first arriving pulses as suggested in the literature (Nagata et al., 2008)

$$T = \frac{A_t}{A_i} \quad \text{Equation 3.4}$$

where  $A_t$  and  $A_i$  are the peak-to-peak amplitudes of initial wave transmitted through the jointed rock sample and the intact rock sample, respectively. As shown in Figure 3.3, the peak-to-peak amplitude is the voltage difference between the crest to the trough of the first arriving pulse (Nagata et al., 2008).

### 3.1.2.3 Calculation of frequency spectra

Spectral analysis is essential to study wave propagation and attenuation since it provides information on wave energy distribution over frequency range (Stoica and Moses, 2005). The transmitted waveform is comprised of the first arrival signal and subsequent contents possibly contaminated by reflections from various interfaces in the system, where the first arrival pulse is of great importance to the determination of wave responses to rock joints (Pyrak-Nolte et al., 1990). Thus, spectral analysis is commonly performed on first arrival pulses for better understanding wave behaviours through rock joints in the frequency domain.

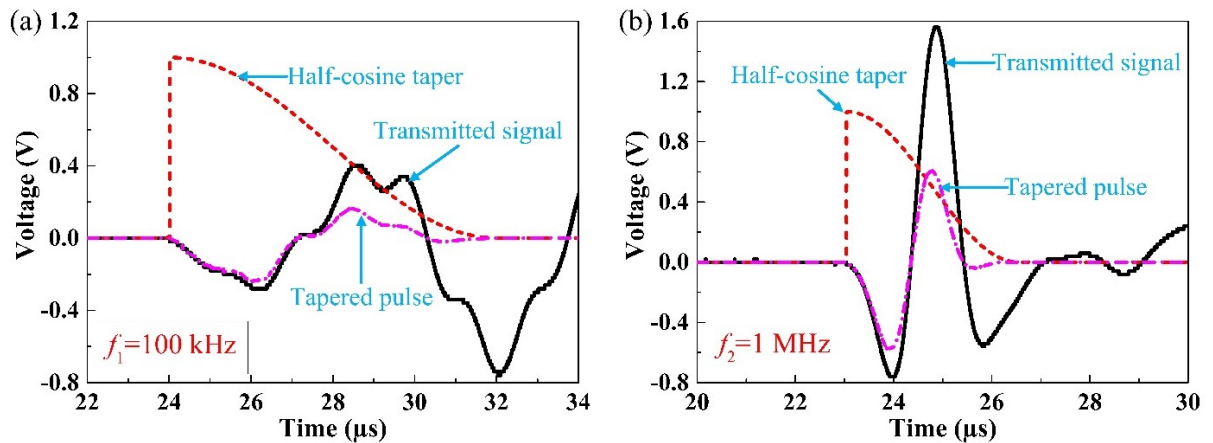


Figure 3.4 The examples for the demonstration of isolating first arrival pulses using the appropriate tapers

The initial pulses can be extracted from the original waveforms using an appropriate window function that is termed as a taper. The criteria for selecting appropriate tapers are to alter less spectra of target pulses and to preserve more low-frequency content of transmitted signals without too much distortion in the high-frequency range (Pyrak-Nolte et al., 1990). Figure 3.4 presents two examples of isolating initial signals from the transmitted P-waves obtained in this research, where half-cosine window functions with the window widths of 8.0  $\mu\text{s}$  and 3.5  $\mu\text{s}$  are applied to taper the received 100-kHz and 1-MHz P-waves, respectively. Note that all tapers have the same amplitude with the value of one. Following that, the fast Fourier transform was performed on these tapered initial pulses to calculate their corresponding frequency spectra.

#### 3.1.2.4 Calculation of attenuation quality factor

Wave attenuation in rock masses is usually quantified by the attenuation quality factor  $Q$ . In this research,  $Q$  values of rock specimens were determined using the spectral ratio method presented by Toksöz et al., where the ratio of spectral amplitudes is expressed as (Toksöz et al., 1979, Johnston et al., 1979)

$$\frac{A_1}{A_2} = \frac{G_1}{G_2} e^{-(\gamma_1 - \gamma_2)fx} \quad \text{or} \quad \ln\left(\frac{A_1}{A_2}\right) = \ln\left(\frac{G_1}{G_2}\right) + (\gamma_2 - \gamma_1)fx \quad \text{Equation 3.5}$$

where  $A(f)$  is the spectral amplitude,  $f$  is frequency,  $G(x)$  is the geometric factor related to spreading, reflections, transducer-to-sample bond effect, etc.,  $x$  is the length of wave travel path (i.e., the sample length),  $\gamma$  is a constant related to  $Q$  (i.e.,  $Q = \frac{\pi}{\gamma v}$ ), and  $v$  is the phase velocity. Subscripts 1 and 2 denote the reference and the rock sample, respectively. The  $(\gamma_2 - \gamma_1)$  can be determined by the slope of the line fitted to  $\ln(A_1/A_2)$  versus frequency when  $G_1/G_2$  is independent of frequency. To achieve the independence of  $G_1/G_2$  from frequency, the setting of sample dimensions, transducers and arrangements of test set-up for the reference sample should be the same as that for the rock sample. When  $Q$  of the reference is sufficiently high (i.e.,  $Q_1 \cong \infty$ , and thus  $\gamma_1 \cong 0$ ),  $\gamma_2$  can be obtained from the slope of the fitting curve, and hence  $Q$  of the rock sample can be determined. Conventionally, an aluminium sample with the same dimensions as the rock sample was used as the reference to estimate  $Q$  values of jointed rock samples because it has a much greater  $Q$  compared with the rock (Johnston et al., 1979).

### 3.1.2.5 Time-frequency analysis

The time-frequency analysis is a general method for examining the energy-frequency-time distributions, which has been widely in geophysics and geoengineering for data processing and interpretation (Chopra and Marfurt, 2016, Wang et al., 2018). The continuous-wavelet transform (CWT) has been proved to be a robust and efficient technique to implement the time-frequency analysis, which could provide better time-frequency resolution compared to the conventional short-time Fourier transform (Sinha et al., 2005, Pyrak-Nolte and Nolte, 1995). Mathematically, the CWT can be obtained by integrating a time-domain signal  $S(t)$  over the mother wavelet

$$W(\alpha, \tau) = \frac{1}{\sqrt{\alpha}} \int_{-\infty}^{\infty} \psi^* \left( \frac{t - \tau}{\alpha} \right) S(t) dt \quad \text{Equation 3.6}$$

where  $\alpha$  and  $\tau$  represent the scale and delay parameters, respectively, and the pre-factor is for normalization. In addition,  $\psi^*$  is the complex conjugate of the mother wavelet. Virtually, the cwt correlates the raw wave with a group of shifted mother wavelets via coefficients that characterize the similarity between the mother wavelet and the raw pulse at a certain scale and time delay.

In the present study, the CWT with a Morlet mother wavelet is utilized to perform the time-frequency analysis on the obtained transmitted waves through individual clay-filled rock joints (Morlet et al., 1982). The operation of the CWT could generate a series of time-frequency maps, providing a direct quantitative measurement of spectral contents as a function of time for waves transmitting across single rock joints. In the frequency map, the colorbar denotes the magnitude of energy resulted from the correlation between the received ultrasonic signals and the shifted mother wavelet. The frequency maps could reveal the variations in the dominant frequency, frequency partition, energy partition and maximum spectral amplitude when ultrasonic waves propagate through individual rock joints. Since the first-arrival pulse of transmitted waves plays a predominant role in examining the effects of single rock joints (Zhao et al., 2006), the time-frequency analysis focuses mainly on the initial pulses of the received waveforms in this study.

## 3.2 The Split Hopkinson pressure bar (SHPB) test

### 3.2.1 Experimental system and calibration

#### 3.2.1.1 The SHPB test set-up and apparatuses

In this research, a self-designed SHPB test system was utilized to conduct dynamic impacting tests on rock specimens with single fluid-filled joints. As shown in Figure 3.5, the SHPB test system is composed of three pressure bars with 50 mm in diameter (i.e., striker, incident and transmitted bars), a momentum trap, a launching subsystem (containing a gas gun, an air reservoir and an air cylinder), a LabVIEW data acquisition subsystem (consisting of an eight-channel Hioki 8860-50 oscilloscope and a dynamic strain meter) and a high-speed camera subsystem (including a Photron FASTCAM SA-Z high-speed camera, two high-intensity flashlights and a computer equipped with a special software). The striker, incident and transmitted bars with the length of 200mm, 2500mm and 1800 mm, respectively, are made from the hardened 60 Silico-manganese ( $\text{Si}_2\text{Mn}$ ) steel whose Young's modulus is 205 GPa and density is  $7800 \text{ kg/m}^3$ .

During each test, the striker bar is fired by the launching system and impacts the front end-surface of the incident bar. As a result, a compressive pulse (i.e., incident wave) is generated and propagates along the incident bar towards the rock specimen. When the incident wave arrives at the incident bar-rock specimen interface, a portion of the stress wave is reflected back into the incident bar as a tension pulse (i.e., reflected wave) while the remaining portion passes through the rock specimen and then transmits into the transmitted bar as a compression signal. The compression signal propagating into the transmitted bar is specified as the transmitted wave, which is eventually absorbed by the momentum trap device. In a SHPB test, the incident, reflected and transmitted waves are recorded by two sets of strain gauges mounted on the incident and transmitted bars. Note that every strain set consists of two strain gauges located in diametrically opposite positions on the bar surface. In this experiment, the strain gauges on the incident bar are 1600 mm away from the rock-incident bar interface while the strain gauges on the transmitted bar are 100 mm away from the rock-transmitted bar interface. The strain gauges are in connected to the oscilloscope through the Wheatstone bridge and dynamic strain meter to transfer the obtained strain signals into voltage signals that can be digitalized and displayed in the oscilloscope. The oscilloscope is triggered by a transistor-transistor-logic (TTL) pulse generated by the stain gauges on the incident bar. The raw data recorded by the strain

gauges are digitally filtered by a low-pass filter with a cut-off frequency of 10 kHz and then displayed on the oscilloscope, where the sampling rate of the oscilloscope is 10 MHz. Note that the filtering process aims to remove the high-frequency noise overlaying the strain signals and produce robust algorithms for determining the time-of-arrival of the stress waves. Additionally, the Wheatstone bridge is used to average out the bending strains and reduce the signal noise, and the dynamic strain meter is adopted to amplify the strain signals before storing them via the oscilloscope.

In addition, the FASTCAM SA-Z high-speed camera coupled with two ring-shaped high intensity flashlights was used to record the dynamic responses of fluid-filled rock joints under the impact loading, setting the frame rate as 160000 fps (frames per second) and the resolution as 128×400 pixels for a visual size of 40\*125 mm. The high-speed camera is in connection with the oscilloscope via a network cable, and it is triggered by the TTL pulse within a time delay of 100 ns. Thus, it is thought that the high-speed camera starts to capture images at the time triggered by the TTL pulse. Accordingly, the number of images before stress wave arriving at the specimen can be determined by

$$N = \frac{t_{spe} - t_{inc} - t_{TTL}}{t_{fra}} \quad \text{Equation 3.7}$$

where  $t_{spe}$  and  $t_{inc}$  are the arrival time when the incident wave arrives at the specimen-incident bar interface and strain gauges on the incident bar, respectively. Besides,  $t_{TTL}$  is the time when the high-speed camera is triggered TTL pulse, and  $t_{fra}$  is the inter-frame time of the high-speed camera.

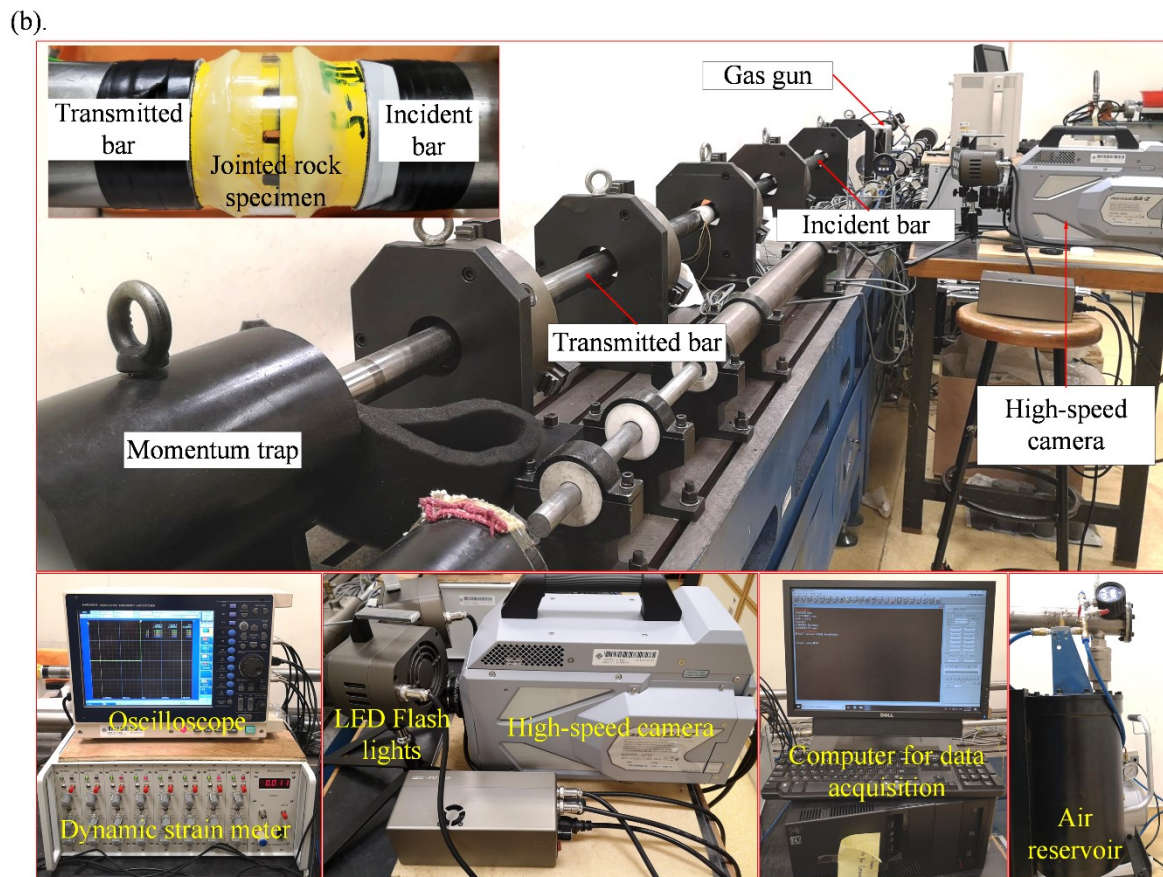
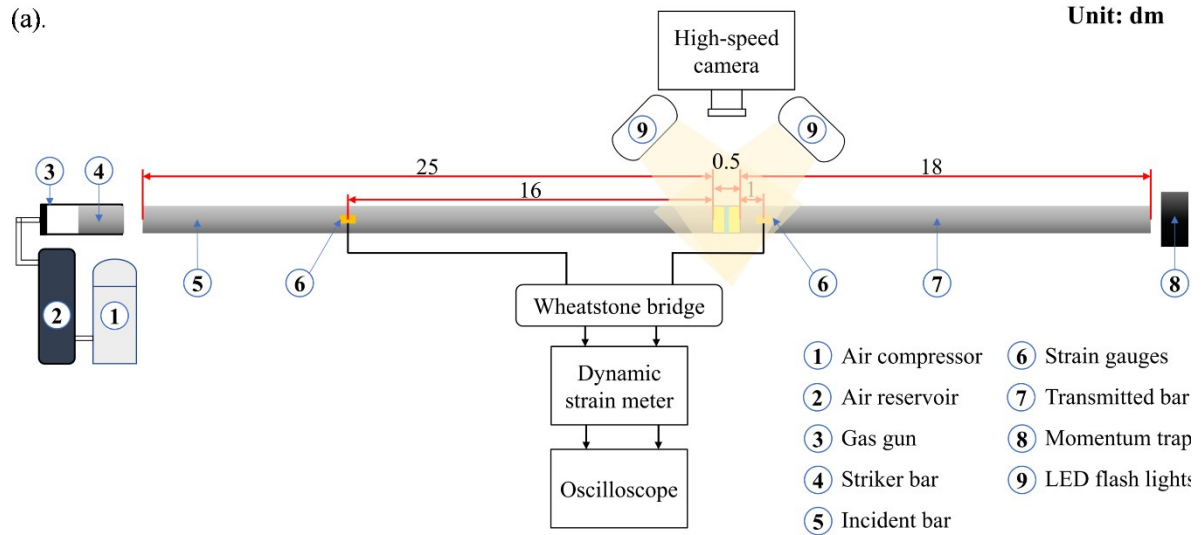


Figure 3.5 The self-established split Hopkinson pressure bar test system used in this research:  
(a). the schematic of the test system, (b). the laboratory photograph of the test system.



### 3.2.1.2 Pulse shaping

In this experiment, some actions were taken to ascertain the stress equilibrium. Firstly, the interfaces between the specimen and bars are properly lubricated with the Vaseline to minimize the end friction effect. Accordingly, the lateral inertial confinement due to the inertia can be eliminated, leading to the uniform expansion of the specimen upon loading. Secondly, all bars are adjusted to be coaxial. Finally, and perhaps most importantly, an appropriate pulse shaper was placed in the centre of the front end-surface of the incident bar to generate a non-dispersive ramped pulse.

The incident stress wave generated in a conventional SHPB test is in an approximately trapezoidal shape associated with high-level oscillations. The sharply rising signal and its resulted oscillations make it difficult to achieve the stress equilibrium in the sample. It has been found that shaping the incident wave into a slowly rising ramp pulse can well minimize the effects of dispersion and inertia and thus facilitate the dynamic stress balance (Zhang and Zhao, 2014). There are mainly two methods used to shape the incident pulse, i.e., modifying the geometrical shape of the striker bar and placing a pulse shaper (i.e., a thin disc made of ductile materials, such as copper, aluminium, and rubber) on the impacting end of the incident bar (Li et al., 2000, Frew et al., 2001, Frew et al., 2002). In this research, the appropriate incident pulses were obtained by using a pulse shaper.

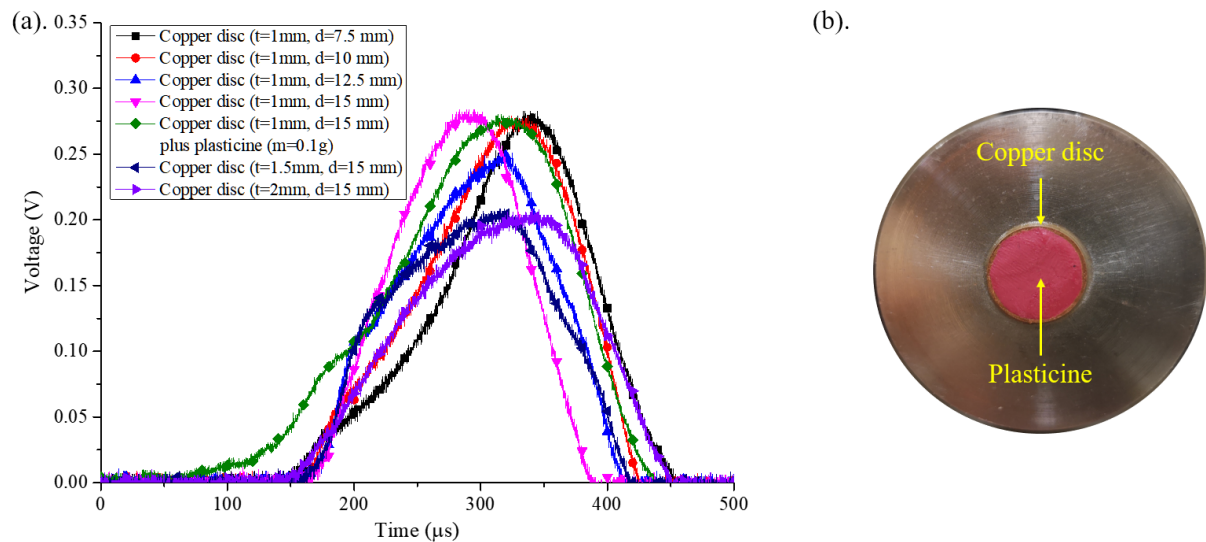


Figure 3.6 The selection of an appropriate pulse shaper: (a). the shaped incident pulses produced by different shapers, (b). the pulse shaper used in this study. Herein,  $t$  and  $d$  represent the thickness and diameter of the copper disc, respectively, and  $m$  is the weight of the plasticine.

According to the literature, the diameter and thickness of the pulse shaper diameter should be considered when choosing a proper pulse shaper. In the present study, an appropriate shaper was selected by trials and errors. The shaped incident pulses caused by different shapers were presented in Figure 3.6a. It is found that adding a lump of plasticine can effectively lengthen the rising time and smoothen the incident pulse. For a proper pulse shaper, the time duration of the produced incident pulse should be long enough to allow the stress wave to travel several times in the sample for the achievement of the stress equilibrium (Zhou et al. 2012). Accordingly, the pulse shaper that was comprised of a copper disc with 15 mm in diameter and 1 mm in thickness together with a lump of plasticine with the weight of 0.1 g (see Figure 3.6b) seems to be the most appropriate shaper for this experiment. The comparison of those shaped incident pulses indicates that placing the selected pulse shaper in the centre of the front end-surface of the incident bar can generate a non-dispersive half-cosine incident wave with a relatively long-time duration.

### 3.2.1.3 Calibrations of the SHPB test system

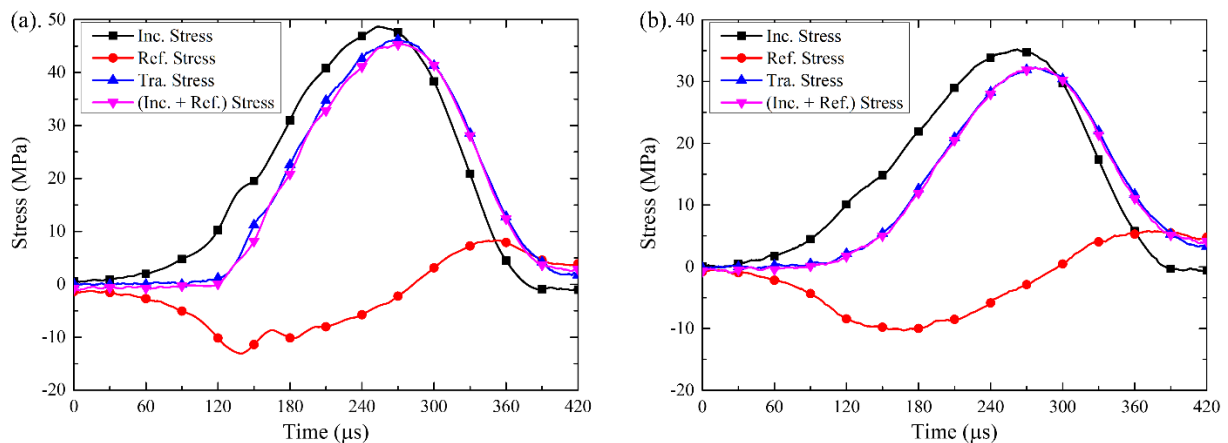


Figure 3.7 The verification of the stress equilibrium of the self-designed SHPB test system by conducting calibration tests on: (a) an intact rock specimen, (b) a typical jointed rock specimen used in this experiment. Note that the Inc. Stress, Ref. Stress and Tra. Stress denote the incident, reflected and transmitted stress waves, respectively, and (Inc. + Ref.) Stress represents the sum of incident and reflected stress waves.

The successful calibration of the SHPB test system is to verify the achievement of stress equilibrium by comparing the stresses generated at the specimen-bar interfaces. The calibration test with an intact rock specimen was firstly conducted to check the stability of the SHPB test system. Another calibration test was also carried out to ensure the achievement of stress equilibrium for the jointed rock specimen. The verification of the dynamic stress equilibrium



for the intact and jointed rock specimen is depicted in Figure 3.7. It is observed that the sum of incident and reflected stress waves agrees well with the transmitted pulse, indicating that the stresses on the incident and transmitted interfaces of the tested specimen are approximately equal during the dynamic loading period. It can be concluded that the stress equilibrium can be successfully achieved for the intact and jointed rock specimens using the self-designed SHPB test system and the selected pulse shaper.

### 3.2.2 Data processing methods

#### 3.2.2.1 Pre-processing of the original signals

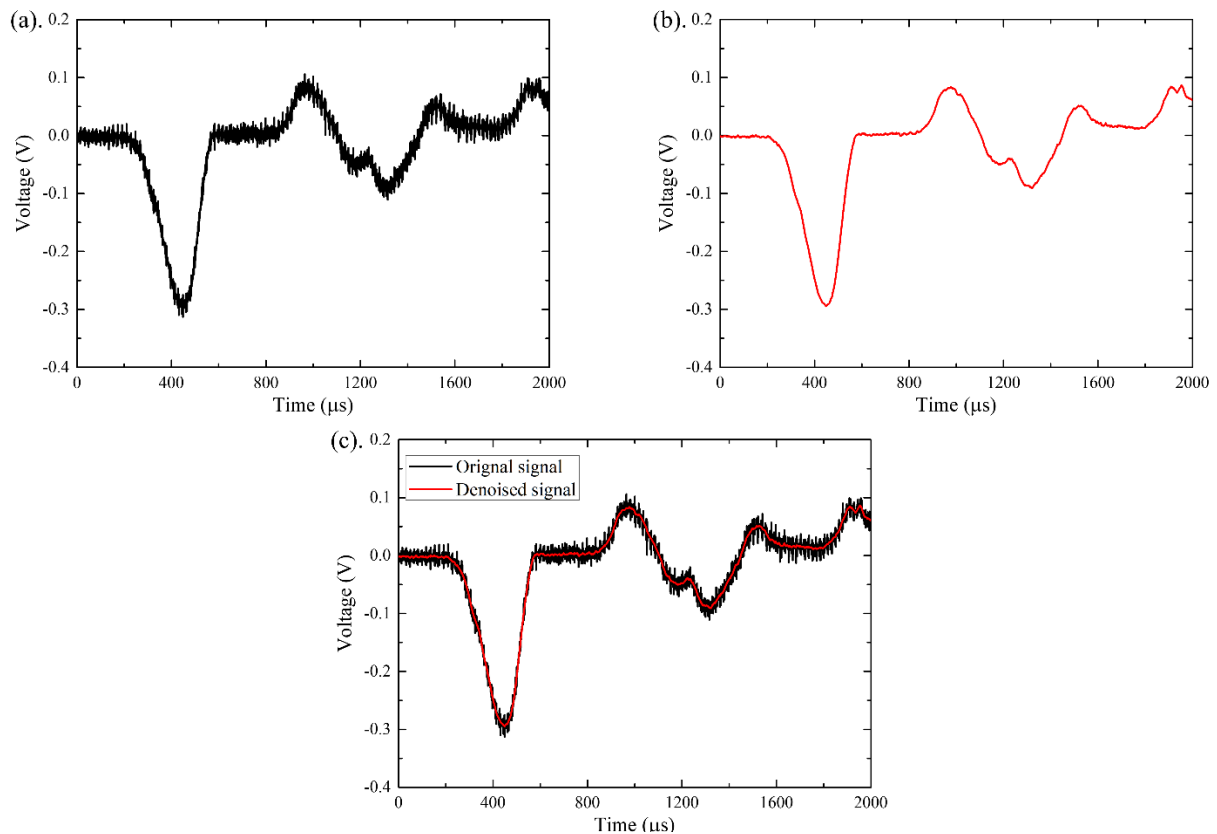


Figure 3.8 The noise elimination of a typical original signal obtained from the SHPB test using the Kalman filter: (a) a typical original signal, (b) the denoised signal, and (c) the comparison between the original and denoised pulses.

In this study, the use of high-speed camera system enhances the effect of high-frequency noises and white Gaussian noise of different amplitudes, which to some extent deteriorates the quality of the original signal obtained from the SHPB test, as illustrated in Figure 3.8a. Given that the

low-pass filter built in the dynamic strain meter and the pulse shaper could not thoroughly get rid of the noises generated in the SHPB test, the Kalman filter was adopted to pre-process the original data obtained in the current work, with the aim of eliminating the noises to a great extent. The Kalman filter is one of the most celebrated and popular data fusion algorithms in the field of signal processing due to its small computational requirement, elegant recursive properties and its status as the optimal estimator for one-dimensional linear systems with Gaussian error statistics (Kalman, 1960, Faragher, 2012). Figure 3.8b presents a smoothed signal obtained by conducting the Kalman filtering on the typical original pulse in Figure 3.8a. It is found that the Kalman filter can effectively reduce the noises associated with the SHPB test. Furthermore, the comparison between the original and denoised signals (see Figure 3.8c) reveals that the Kalman filter can successfully preserve the received signals undeformed, thus minimizing the negative effect of filtration on the test results.

### 3.2.2.2 Stress-strain relations

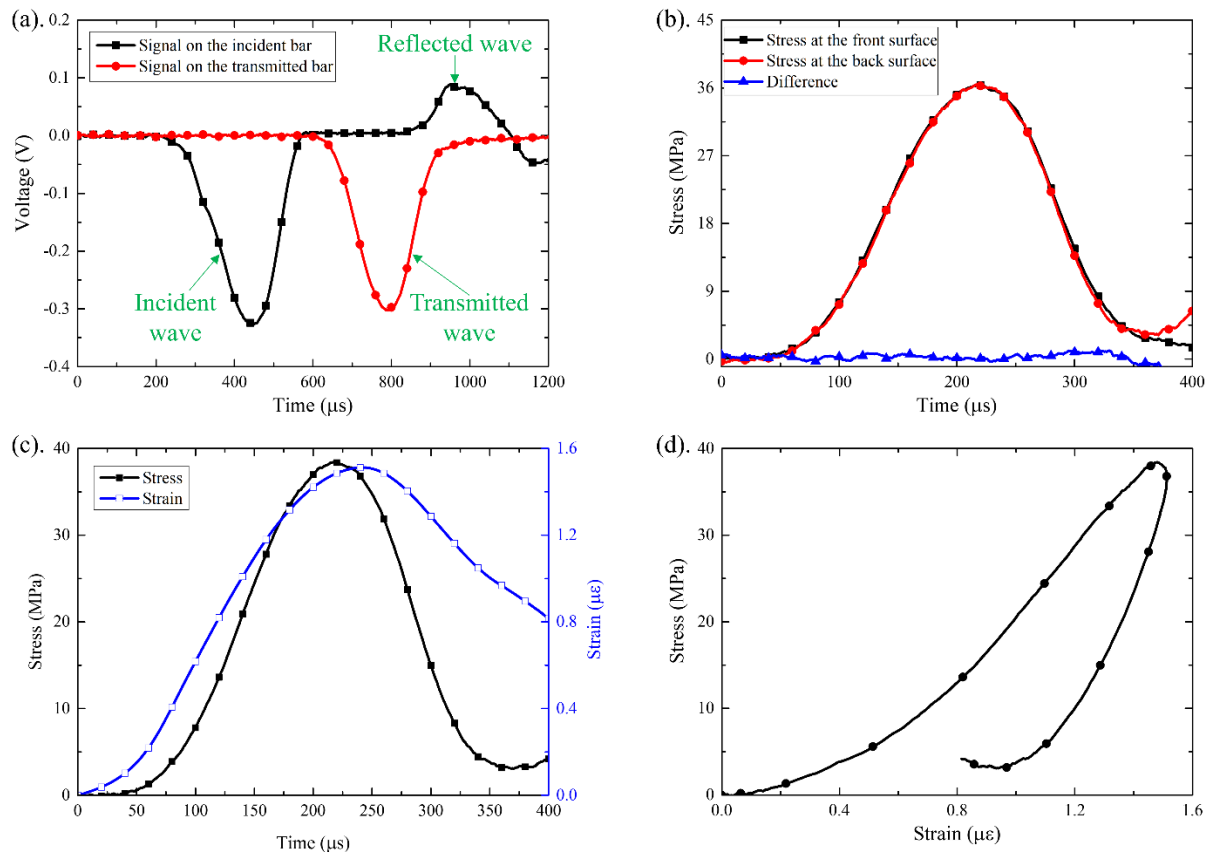


Figure 3.9 The post-processing of the denoised signals to ascertain the stress and strain in the tested rock specimen: (a). the denoised signals collected from a SHPB test; (b). the stress equilibrium check; (c). the time histories of stress and strain; (d) the stress-strain curve.

Based on the 1-D stress wave theory and the hypothesis of uniform deformation of the specimen, the postprocessing of the denoised signals (see Figure 3.9a) was performed to obtain the dynamic mechanical responses of the tested rock specimen. Prior to the post-processing, the dynamic stress equilibrium should be checked by making a comparison between stresses at the front and back sides of the tested sample. The extremely small difference between stresses on the front and back surface indicates that the stress equilibrium is maintained across the rock specimen in the SHPB test (see Figure 3.9b). When there is stress equilibrium between the tested rock specimen's front and back surfaces, the loading applied to the specimen can be termed as being one-dimensional and uniformly distributed along the specimen. Then, the dynamic compressive stress  $\sigma$ , axial strain  $\varepsilon$  and axial strain rate  $\dot{\varepsilon}$  in the rock specimen can be calculated via the following formulas (Gray, 2000)

$$\sigma = \frac{EA}{2A_s}(\varepsilon_i + \varepsilon_r + \varepsilon_t) \quad \text{Equation 3.8}$$

$$\varepsilon = \frac{c}{l_s} \int_0^t (\varepsilon_i - \varepsilon_r - \varepsilon_t) dt \quad \text{Equation 3.9}$$

$$\dot{\varepsilon} = \frac{c}{l_s} (\varepsilon_i - \varepsilon_r - \varepsilon_t) \quad \text{Equation 3.10}$$

where  $E$  is the Young's modulus of the steel bars;  $A$  and  $A_s$  denote the cross-sectional areas of the steel bars and rock specimen, respectively;  $\varepsilon_i$ ,  $\varepsilon_r$  and  $\varepsilon_t$  stand for the incident, transmitted and reflected waves recorded by strain gauges, respectively;  $c$  is P-wave velocity in the steel bars;  $l_s$  represents the length of specimen; and  $t$  is the time. The typical time histories of stress and strain in the tested jointed rock specimen are shown in Figure 3.9c, and the corresponding stress-strain relation is presented in Figure 3.9d.

### 3.2.2.3 Specific joint normal stiffness

The deformation of the jointed rock specimen  $\Delta u$  can be obtained based on the calculated strain, which is regarded as the sum of the deformation of host rock matrix  $\Delta u_R$  and the deformation of joint  $\Delta u_J$  (Jaeger et al., 2009)

$$\Delta u = \Delta u_R + \Delta u_J \quad \text{Equation 3.11}$$

Based on the Hooke's law, the Eq. (x) can be rewritten as

$$\varepsilon l_s = \frac{\sigma}{E_R} (l_s - l_j) + \Delta u_j \quad \text{Equation 3.12}$$

where  $E_R$  is the Young's modulus of rock matrix and  $l_j$  is the joint thickness. From the Eq. (x), we can obtain the joint deformation

$$\Delta u_j = \varepsilon l_s - \frac{\sigma}{E_R} (l_s - l_j) \quad \text{Equation 3.13}$$

According to (Li et al., 2017), the initial joint normal specific stiffness  $k_n$  can be calculated by

$$k_n = \frac{\sigma_{\Delta u_j/2}}{\Delta u_j} \quad \text{Equation 3.14}$$

where  $\sigma_{\Delta u_j/2}$  represents the compressive stress at the value of joint closure equalling to  $\Delta u_j / 2$ .

#### 3.2.2.4 Energy evolution characteristics

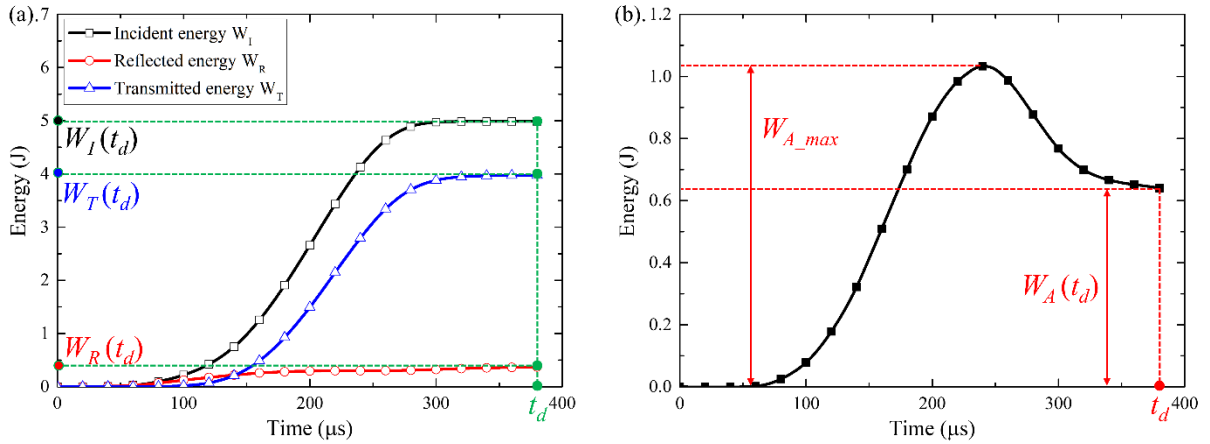


Figure 3.10 The energy evolution characteristics of a typical jointed rock sample in the SHPB test: (a) the time history curves of the incident, transmitted and reflected wave energy, and (b) the time history curve of the absorption energy.

Based on the one-dimensional elastic wave theory, the incident wave energy  $W_I$ , the reflected wave energy  $W_R$  and the transmitted wave energy  $W_T$  can be calculated by

$$W_I(t) = \frac{cA}{E} \int_0^t \sigma_i^2 dt = cAE \int_0^t \varepsilon_i^2 dt \quad \text{Equation 3.15}$$

$$W_R(t) = \frac{cA}{E} \int_0^t \sigma_r^2 dt = cAE \int_0^t \varepsilon_r^2 dt \quad \text{Equation 3.16}$$

$$W_T(t) = \frac{cA}{E} \int_0^t \sigma_t^2 dt = cAE \int_0^t \varepsilon_t^2 dt \quad \text{Equation 3.17}$$

where  $\sigma_i$ ,  $\sigma_r$  and  $\sigma_t$  represent the stresses on the bars induced by the incident, reflected and transmitted waves, respectively.

In principle, the input wave energy  $W_I(t)$  is transferred to the energy reflected into the incident bar  $W_R(t)$ , the energy transmitted into the transmitted bar  $W_T(t)$ , the energy absorbed by the specimen and the energy dissipated by the friction between the specimen and bars. The absorbed energy is mainly comprised of the kinetic energy, the deformation energy, and others (e.g., thermal energy and friction energy). For a valid SHPB test, the energy loss caused by the friction between the specimen and bars is generally neglected due to it only takes a very small portion of the input energy. As a result, the energy absorbed by the specimen is given by

$$W_A(t) = W_I(t) - W_R(t) - W_T(t) = cAE \int_0^t (\varepsilon_i^2 - \varepsilon_r^2 - \varepsilon_t^2) dt \quad \text{Equation 3.18}$$

With the help of the Equations 3.15-3.18, the energy evolutions curves for a typical jointed rock specimen in this research were obtained from the strain signals collected in the SHPB test, as shown in Figure 3.10.

### 3.2.2.5 Transmission and reflection coefficients

Based on the calculated stress wave energies, the transmission and reflection coefficients for the jointed rock sample can be obtained via the following formula (Lundberg, 1976, Li et al., 2019a)

$$T_e = \frac{W_T(t_d)}{W_I(t_d)} \quad \text{Equation 3.19}$$

$$R_e = \frac{W_R(t_d)}{W_I(t_d)} \quad \text{Equation 3.20}$$

where  $W_I(t_d)$ ,  $W_T(t_d)$ , and  $W_R(t_d)$  are the total incident energy, transmitted energy and reflected energy within the loading duration  $(0, t_d)$  of the stress waves, respectively, as marked in Figure 3.10a.

### 3.2.2.6 Seismic attenuation quality factor

The seismic attenuation quality factor  $Q_{sei}$  is commonly used to characterize the wave energy attenuation caused by the tested rock specimen, which is defined as the ratio of the stored energy to the dissipated energy in one cycle harmonic wave across the tested rock specimen (Knopoff, 1964). According to Li et al. (2019b), the seismic quality factor  $Q_{sei}$  can be directly calculated using the stress wave energies obtained from the SHPB tests with the help of the wave energy approach. In this method, the seismic quality factor  $Q_{sei}$  of rock specimens with single fluid-filled rock joints is computed by (Li et al., 2019b)

$$Q_{sei} = 2\pi \frac{W_{A\_max}}{\Delta W} \quad \text{Equation 3.21}$$

where  $W_{A\_max}$  denotes the maximum stored energy in the specimen, i.e.,  $W_{A\_max} = \max(W_A(t))$ , and  $\Delta W$  represents the dissipated energy, as illustrated in Figure 3.10b. Physically,  $\Delta W$  is the difference between the total energy of incident wave and the sum of total energy of reflected and transmitted waves. Therefore, the value of  $\Delta W$  equals to the magnitude of the absorbed energy at the ending time of loading duration  $(0, t_d)$ , that is,  $\Delta W = W_A(t_d)$ .

### 3.2.2.7 Frequency spectra

To determine the effects of fluid-filled rock joints on stress wave characteristics in the frequency domain, the frequency spectra of the measured stress waves were evaluated in this research. In detail, a rectangular window function with the amplitude of one was firstly adopted to extract specific pulses from the original waves, where the length of function equalled to the maximum loading duration in all SHPB tests. It should be noted that the same window function was used for the incident, transmitted and reflected waves obtained from all tests in this study. After then, the fast Fourier transform (FFT) was performed on the extracted waves to calculate the spectral contents of the incident, transmitted and reflected waves for the tested rock specimen.

### 3.3 Concluding remarks

In this chapter, the experimental methods used in the research, i.e., the UPT and the SHPB techniques, were thoroughly illustrated regarding the test configuration, apparatuses and data processing approaches. The self-developed UPT test system described in this chapter was used to study the effects of fluids on wave propagation and attenuation across individual rock joints, including clayey soil-filled rock joints and fluid-filled rock joints. The detailed experimental procedure, test results and discussion are presented in full detail in chapters 4 and 5. It is known that ultrasonic waves produced in the UPT tests carry out low energy and thus have negligible effects on deformation of rock joints. Therefore, the experiments in chapters 4 and 5 could only add insights into the interaction of seismic waves with rock joints subjected to insignificant dynamic response. Different from the ultrasonic tests, the SHPB technique can generate high-amplitude stress waves and thus causing evident deformation and dynamic responses of rock joints. In this regard, a self-established SHPB test system, as demonstrated in this chapter, was utilized to investigate the fluid effects on the interaction of single rock joints with high-intensity stress waves. The details regarding the experimental programme, data analysis, findings and discussion of the SHPB tests on single fluid-filled rock joints are provided in chapter 6.

# **CHAPTER 4      FLUID EFFECTS ON LOW-INTENSITY WAVE BEHAVIOURS ACROSS INDIVIDUAL CLAY-RICH ROCK JOINTS**

## **4.1 Introduction**

The literature review in chapter 2 reveals that wave characteristics of soil-filled rock joints are strongly affected by infill soil material properties, such as mineralogical compositions, particle sizes, water content and so on. Laboratory observations and theoretical analysis suggested that the presence of fluids highly affects wave propagation and attenuation across rock joints. However, little attention has been paid to fluid effects on wave propagation and attenuation across rock joints filled with clay-rich soils. It should be mentioned that the rock joint surfaces are often coated with thin clay layers, whose properties are prone to significantly vary with fluid saturation conditions in the joint. Specifically, the interaction of liquid-clay could lead to various degrees of swelling, dispersion and migration and then alter characteristics of rock joints (e.g., the permeability, conductivity and rheological responses), exerting complicated influences on seismic behaviours across rock joints (Fang et al., 2017). To our knowledge, there are few laboratory documents on wave attributes of rock joints filled with wet clays. Suárez-Rivera et al. (1992) briefly measured the transmission and reflection of S-wave across thin montmorillonite clay layers variably saturated with water, ethyl alcohol and decane at different applied stress levels. They found that the absorption of polar liquids (i.e., water and ethyl alcohol) could hydrate the clay and thus enhance S-wave reflection yet weaken S-wave transmission, whereas the nonpolar liquid (decane) only has a minimal effect on S-wave reflection. However, in their work, only two or three saturation cases were tested for the montmorillonite clay saturated with the same liquid, which is insufficient to draw reliable conclusions on the fluid-dependent S-wave characteristics of different clay layers. Besides, their study did not evaluate P-wave behaviours across thin wet clay layers. In this regard, it is necessary to conduct out more laboratory experiments for better understanding the effects of fluids on the interaction of seismic waves and clay-rich soil-filled rock joints.

The main objective of this chapter is to comprehensively and systematically investigate the role of water in wave behaviors across single rock joints filled with clay-rich soils via the ultrasonic



pulse-transmission tests. Specifically, two representative clays, i.e., kaolinite and bentonite, were used to prepare a series of infill clay-rich soil specimens at different water saturation degrees. The shear modulus and viscosity of those filling soil specimens are measured at low shear strains through the amplitude sweep tests, which could provide some insights for interpretation of wave responses to single clay-filled rock joints from a microstructural perspective. The prepared soil specimens are filled into an artificial planner rock joint to produce a series of clay-rich soil-filled joints. Following that, ultrasonic measurements on single clay-filled rock joints are carried out using different P- and S-wave transducers. Based on the obtained laboratory data, some key wave signatures, including wave velocity, transmission ratio and energy-frequency-time distribution, are elaborated and analysed. The mechanisms lying behind the experimental results are discussed.

## **4.2 Experimental procedure**

### **4.2.1 Specimen description**

#### **4.2.1.1 Filling clay-rich gouge specimens**

In this experiment, two representative clays, i.e., kaolinite and bentonite, were utilized to prepare a series of filling clay-rich gouge specimens at different water saturation degrees. The kaolinite and bentonite were mined from England and Germany, respectively (see Figure 4.1), and the particle size distribution of those two clays was measured and presented in Figure 4.1. It is found that both of those two clays are fine-grained and have the similar particle size distribution. According to the British Standard 1377 (British Standards Institution 1990), some basic properties of those two clays were measured in the laboratory and tabulated in Table 4.1.

Prior to producing wet clay-rich gouge specimens, the clay powders were oven-dried at a constant temperature of 60 °C in an oven for about 72 hours. Due to the significant difference in water absorption ability between dry kaolinite and bentonite, wet kaolinite and bentonite specimens were generated in different ways. Specifically, to obtain bentonite specimens at different saturation degrees, the fully water-saturated bentonite sample was firstly produced and then was equally put into seven identical containers. Those bentonite specimens at fully saturating condition were air-dried for 36 hrs, 54 hrs, 72hrs, 90 hrs, 108 hrs, 126 hr, 144hrs, respectively, to get different partially-saturated bentonite specimens. On the other hand, various wet kaolinite specimens were generated by thoroughly mixing the dry kaolinite at the certain mass (80 g) with water at different masses (i.e., 48g, 56g, 64g, 72g, 80g, 88g, 96g and

100g). Those wet kaolinite specimens were rested for 48 hrs in a sealed condition before filling them into the open rock joint for acoustic measurements. The detailed information about all filling clay specimens is summarized in Table 4.2.

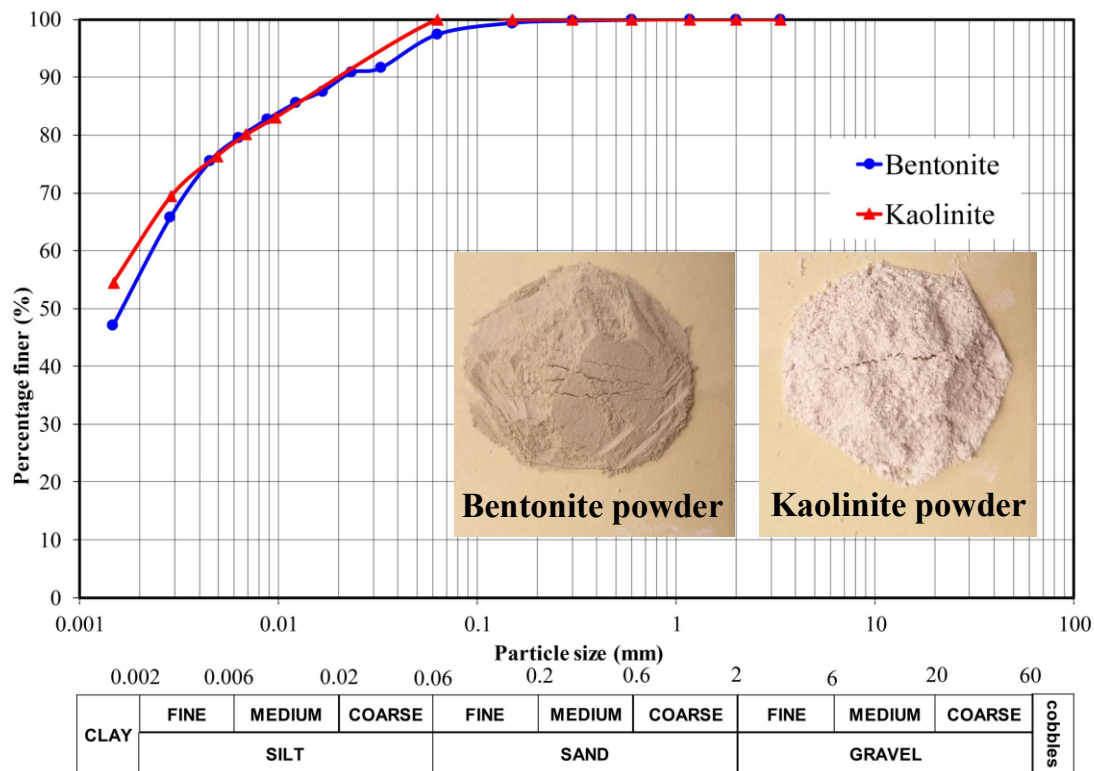


Figure 4.1 The grain-size distribution curves for clayey soils used in this study.

Table 4.1 Some basic properties of clayey soils used in the study

Soil type	Specific gravity (Mg/m <sup>3</sup> )	Liquid limit $w_L$ (%)	Plastic limit $w_P$ (%)	Plasticity index $I_P$ (%)	Mineralogical compositions
Kaolinite	2.58	58.84	32.27	26.57	Kaolinite: 94% Mica: 4% Montmorillonite: 1% Feldspar and quartz: 1%
Bentonite	2.5	387.72	89.53	298.19	Montmorillonite: 80% Quartz: 12% Mica: 7% Clinopitile: 1%

Table 4.2 The information about the prepared clay-rich soil specimens used in the study

Groups	No. of soil samples	Water content $w$ (%)	Degree of saturation $S_r$ (%)	Bulk density $\rho_b$ (Mg/m <sup>3</sup> )
kaolinite specimens	KS1	60	48	1.892
	KS2	70	56	1.811
	KS3	80	64	1.774
	KS4	90	72	1.726
	KS5	100	80	1.690
	KS6	110	88	1.662
	KS7	120	96	1.633
bentonite specimens	BS1	497	48.7	1.326
	BS2	549	53.8	1.315
	BS3	604	59.2	1.304
	BS4	663	65	1.295
	BS5	728	71.4	1.287
	BS6	807	79.1	1.279
	BS7	888	87.1	1.273

#### 4.2.1.2 Rock specimens

The rock samples for this study were manufactured using the high-quality black gabbro produced in Shanxi, China, as shown in Figure 4.2a. The black gabbro rock was chosen for this investigation because of its good integrity and homogeneity. Hence wave attenuation and slowness caused by gabbro rock matrix is negligible compared with those caused by rock joints, thereby highlighting the influence of rock joints on wave propagation in this study. The mineralogical components of the gabbro (see Figure 4.2b) are plagioclase (75%), clinopyroxene (20%), quartz (3%), amphibole (1%) and biotite (1%). The grain sizes of this rock are in the range of 0.05–2 mm, which are determined by making a modal analysis on a rock slab using a petrographic microscope. The other physical and mechanical properties of the gabbro were measured and listed in Table 4.3.

In this experiment, the rock specimen with a synthetic planar open joint was firstly manufactured by combining two identical rock cylinders using a PMMA tube, where 3M DP460NS epoxy adhesive was utilized to stick the tube and two rock cylinders together, as

shown in Figure 4.2a. Those two rock cylinders were 50 mm in diameter and 49 mm in height. The PMMA tube was used to not only connect these two intact rock cylinders but also prevent the outflow of filling materials with the help of sealing layer produced by the epoxy adhesive. Moreover, a pre-set hole with a diameter of 2 mm on the PMMA tube was made for filling wet clay-rich soils into the open rock joint. The length of the jointed rock specimen is about 100 mm while the joint thickness is around 2mm. Herein, a series of clay-rich soil-filled rock joints were generated by filling different clay-rich soil specimens into the artificially open rock joint. In addition, an intact rock specimen with the same dimensions as the jointed rock specimen was manufactured using the same rock block (see Figure 4.2a). The intact rock specimen was used to obtain the reference signals for the analysis on wave responses to single clay-filled joints. Note that the end surfaces of all rock specimens were carefully polished to meet the requirements for parallelism and perpendicularity in ISRM suggested standards.

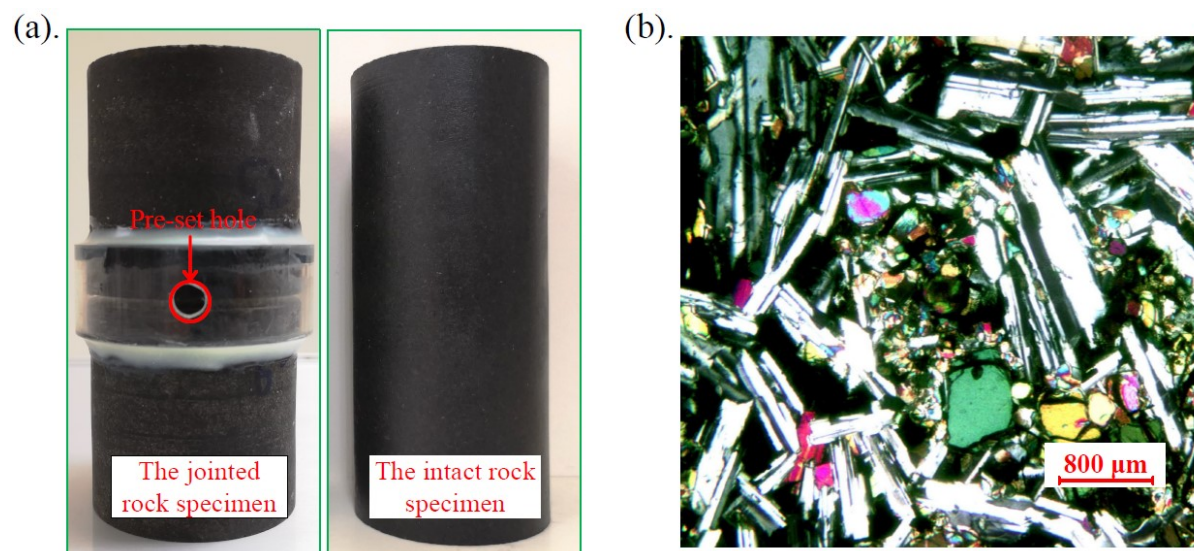


Figure 4.2 The gabbro rock used in the study: (a). The jointed and intact rock specimens; (b) the representative microphotograph of gabbro.

Table 4.3 Physical and mechanical properties of rock specimens used in the study

Rock type	Density (kg/m <sup>3</sup> )	Young's modulus (GPa)	Poisson's ratio	Porosity (%)	Uniaxial compressive strength (MPa)
Gabbro	2818.82	100.36	0.29	1.31	312.44

## 4.2.2 Test programme

### 4.2.2.1 The amplitude sweep tests for measuring rheological properties of clay-rich soil specimens

In this study, to better understand the effects of clay-rich soil-filled rock joints on wave propagation from the microscale level, shear modulus and viscosity of infill clay-rich soil specimens in the low strain range were measured through the amplitude sweep method. In the literature, the amplitude sweep test is one kind of oscillatory shear tests characterized by a variable amplitude (shear stress or deformation) and a constant frequency, including the controlled shear stress (CSS) and the controlled shear deformation (CSD) modes, which has been successfully applied to investigate rheological properties of soil materials in the laboratory (Ghezzehei and Or, 2001, Markgraf and Horn, 2006, Holthusen et al., 2010, Baumgarten et al., 2013, Pértile et al., 2018). In the current work, the Modular Compact Rheometer (Anton Paar MCR702 Twin Drive, Graz, Austria) with a parallel-plate system, as shown in Figure 4.3 was employed to perform a series of amplitude sweep tests under the CSD on infill clay-rich soil specimens to determine their rheological properties.

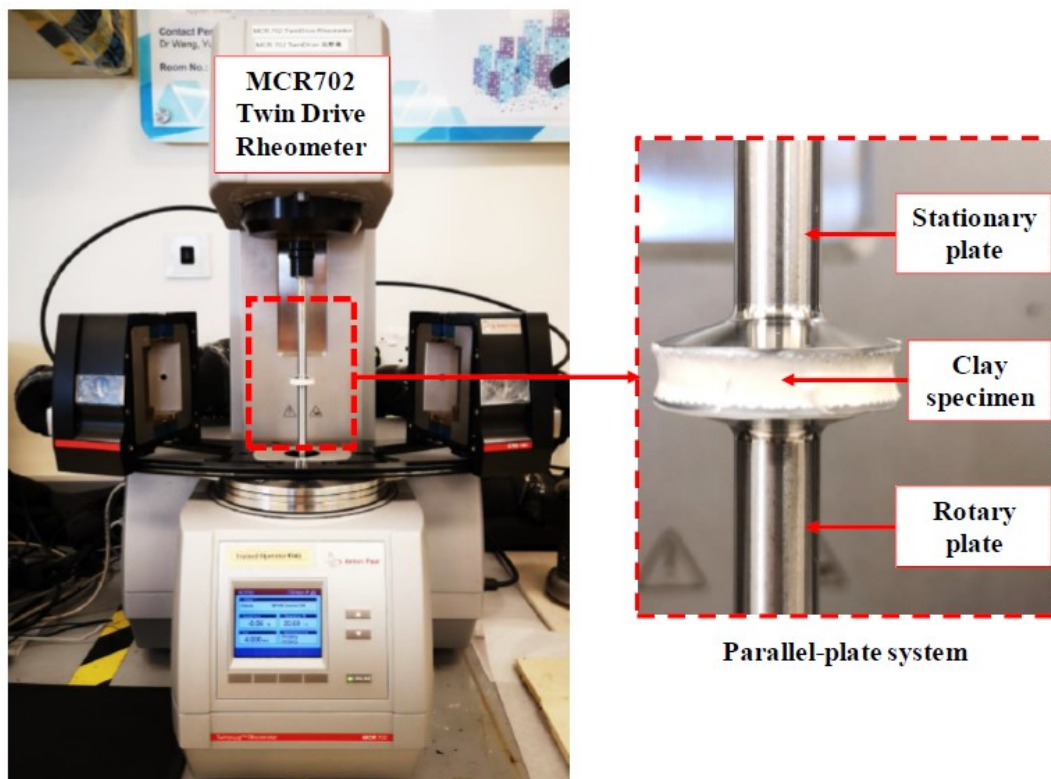


Figure 4.3 The Modular Compact Rheometer with a parallel-plate system for conducting amplitude sweep tests

Prior to each measurement, the clay specimen was placed between the stationary plate (Anton PP25 44151) and the rotary plate (Anton PP25 44151) at a constant distance between the plates. Table 4.4 lists the pre-setting parameters for all tests, which are chosen according to previous studies on soil rheological properties using the same method (Markgraf et al., 2006). The measured shear moduli and viscosities of various infill clay specimens are presented and analysed in Section 4.3.1.

**Table 4.4 The pre-setting parameters for the amplitude sweep tests conducted in this study**

Parameters	Specification
Diameter of measuring plates	$R = 25 \text{ mm}$
Distance between two plates	$d = 4 \text{ mm}$
Shear deformation	$\gamma = 0.0001\% \dots 100\%$
Frequency	$f = 0.5 \text{ Hz}$
The number of measuring points	$N = 30 \text{ pts}$
Duration for each measurement	$DT \approx 20 \text{ mins}$
Test temperature	$T = 20 \text{ }^{\circ}\text{C}$

#### **4.2.2.2 The UPT tests for determining wave attributes of individual clay-rich soil-filled rock joints**

To investigate the effects of single clay-filled rock joints on both P- and S-waves behaviours, two pairs of ultrasonic P-wave transducers (i.e., Olympus model X1020, V192) and three pairs of S-wave transducers (i.e., Olympus model V150, V151 and V152) were employed to generate five types of input signals, including 0.1-MHz and 1MHz P-waves as well as 0.25-MHz, 0.5-MHz and 1-MHz S-waves. Prior to conducting ultrasonic measurements on rock specimens, the testing system was calibrated using the face-to-face test under constant pressures and temperature (Soil and Rock, 2008). Precisely, the face-to-face test is to perform ultrasonic measurements by placing the transmitter and receiver in direct contact. The calibration of each pair of transducers could provide the time delay between the input and output pulses of the transducers as well as the polarity of the output pulse for a given incident wave. The detailed information about signals generated by those transducers is given in Table 4.5. Using each pair of ultrasonic transducers, wave attributes of different rock joints filled with bentonite and kaolinite at different water saturation degrees were measured respectively. In addition,



ultrasonic measurements on the intact rock specimen were performed to obtain the reference data for further analysis on effects of individual clay-rich soil-filled rock joints. The measured wave velocity and dominant frequency of transmitted wave across the intact rock specimen are provided in Table 4.5. Notably, five tests are conducted for each case to ensure the repeatability and to minimize the interference caused by operation errors and noises. As a result, there were totally 400 tests performed in this study, where all tests were carried out at the room temperature (about 20 °C).

**Table 4.5 The information about waves generated by ultrasonic transducers and transmitted waves across the intact rock specimen in this study**

Wave type	$f_{SET}$ (MHz)	$f_{IR}$ (MHz)	$V_{IR}$ (m/s)	$\lambda$ (mm)
P-wave	0.1	0.137	6541.38	65.41
	1	0.641	6646.16	6.65
S-wave	0.25	0.229	3420.56	13.68
	0.5	0.473	3472.97	6.94
	1	0.672	3718.58	3.72

## 4.3 Experimental results and analysis

### 4.3.1 Rheological properties of infill clay-rich soil specimens

Figure 4.4 presents the measured shear moduli and viscosities of all infill clay-rich soil specimens used in this study, where the values within the linear viscoelastic (LVE) range are highlighted using yellow boxes. Note that the LVE range represents the shear strain range where the complex modulus and viscosity approximately display constant plateau values due to no significant changes in clay structure at these low strains (Mezger, 2006). The curves within the LVE range suggests that the shear modulus and viscosity of clay specimens are highly affected by their mineralogical compositions and water saturation degrees. It has been found that the piezoceramic transducers generate a low shear strain less than 0.0001%, creating elastic deformation of the tested sample (Leong et al., 2004, Sukolrat, 2007, Nourifard et al., 2019). Accordingly, the results within the LVE range are more important to interpreting the effect of rheological properties of infill clays on ultrasonic wave behaviours across the filled joint.

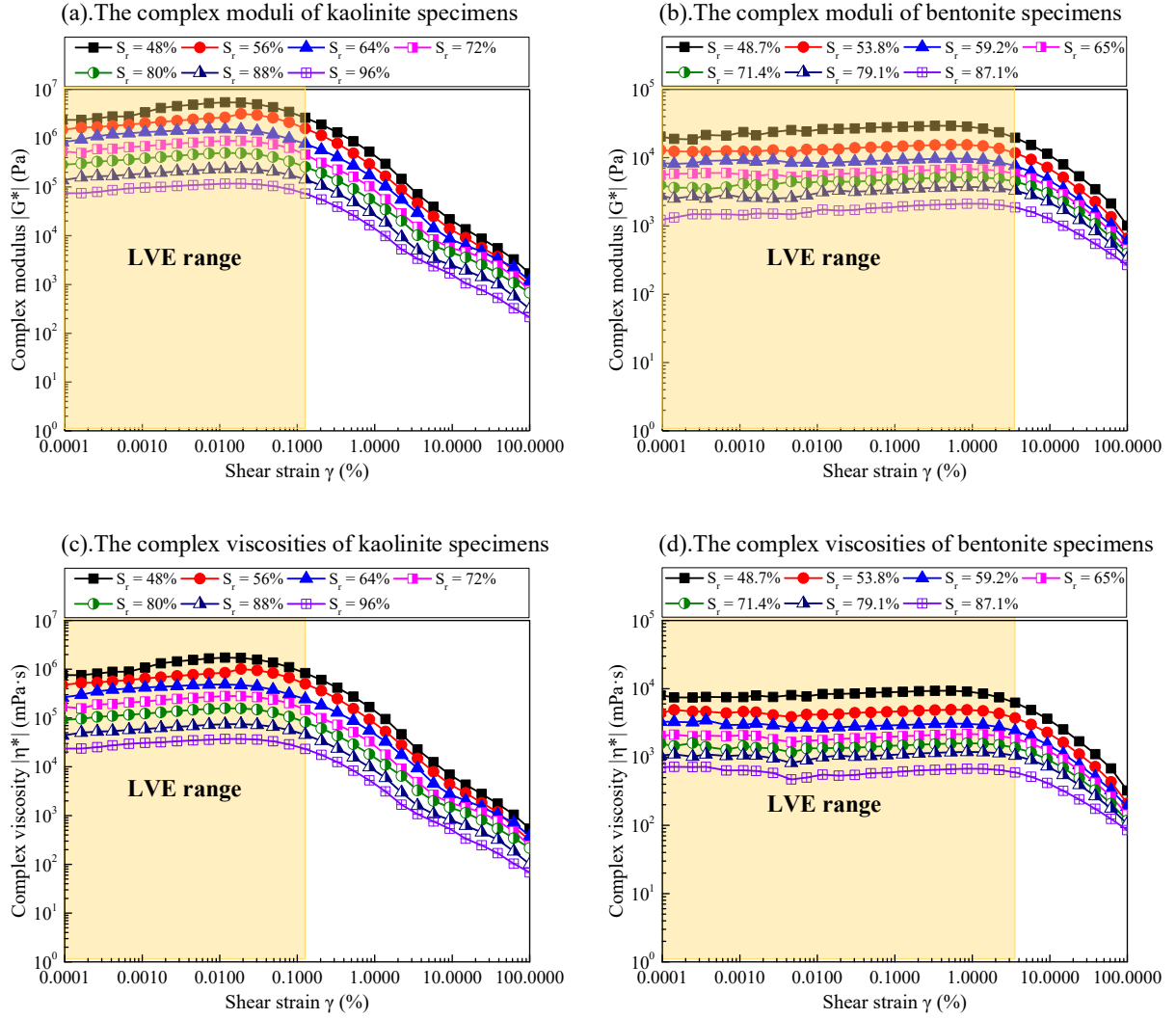


Figure 4.4 The shear moduli and viscosities of kaolinite specimens (a), (c) and bentonite specimens (b), (d) measured by the amplitude sweep tests. Herein,  $S_r$  denotes the degree of water saturation of clay-rich specimens.

It is found from Figure 4.4 that an increase in water saturation reduces the complex shear modulus and viscosity of both kaolinite and bentonite clay specimens in the LVE range. For instance, when saturation degree of kaolinite increases from 64% to 80%, both of the shear modulus and viscosity of kaolinite decrease by around 65%. Additionally, for saturation degree of bentonite increasing from 65% to 79.1%, both of the shear modulus and viscosity decline by about 55%. The principal explanation is that the increasing water saturation results in more water molecule layers coating the clay particles and aggregates, enhancing their mobility (Ghezzehei and Or, 2001). Consequently, the particle linkages and solid-solid friction declines with increasing water saturation, causing a decrease in the shear resistance of clay. On the other hand, the increase in the amount of water menisci weakens the contraction force between



particles induced by the water menisci and thus lessens the shear resistance (Horn and Peth, 2011). The result could also be attributed to that the increase of water saturation could enlarge the intergranular spacing (Ghezzehei and Or, 2001). Accordingly, the additional resistance to deformation caused by the solid-solid interactions decreases, resulting in smaller values of the shear modulus and viscosity (Markgraf and Horn, 2006).

Furthermore, it is observed that the values of the complex shear modulus and viscosity of kaolinite specimens (see Figures 4.4a and 4.4c) are about two orders of magnitude higher than those of bentonite specimens (see Figures 4.4b and 4.4d) over the tested water saturation range. The principal explanation is that the friction and shear strength of interparticle bonds in kaolinite specimens are much higher than those in bentonite specimens. Specifically, the interlayer spaces of montmorillonite (the key mineralogical component in bentonite specimens) can be hydrated while those of kaolinite (the principal mineralogical component in kaolinite specimens) are practically anhydrous (Chenu, 1995). As a result, the larger portion of water is held in inter-cluster spaces of kaolinite specimens, causing the localization of the effective stress in few inter-cluster contacts, which induces the ordered molecular layering and significant resistance to shearing (Schoen et al., 1989). Moreover, for kaolinite, the internal friction angle remains high ( $20 - 25^\circ$ ) even at high deformation and the residual friction angle equals to the critical-state friction angle (Smith and Reitsma, 2002). By contrast, the residual friction angle in montmorillonite decreases with the increasing deformation, which leads to a sliding shear behaviour at the low friction angle ( $5 - 15^\circ$ ) (Markgraf and Horn, 2006). Consequently, bentonite has a lower shear strength than kaolinite. Meanwhile, Figure 4.4 shows that the LVE range for bentonite is broader than that for kaolinite, which is consistent with findings in the literature (Pétille et al., 2016). It indicates that bentonite has a larger elastic strength to resist greater deformations compared to kaolinite. This is because that the adsorbed water and the cations in the solution, and on surfaces and in the interlayer of montmorillonite increases the capillary forces and electrostatic and molecular forces, enhancing the elasticity of bentonite specimens (Mitchell and Soga, 2005).

### **4.3.2 P-wave attributes of single rock joints filled with wet clay-rich soils**

#### **4.3.2.1 P-wave velocity**

Figure 4.5 displays P-wave velocities of clay-rich soil-filled joints and the corresponding jointed rock specimens with respect to water saturation degree. It can be observed that the

variations in P-wave velocity of the entire jointed rock sample resemble the changes in P-wave velocity across the corresponding clay-rich soil-filled joint, implying that individual clay-rich soil-filled joints highly dominate the P-wave velocity of rock masses. Furthermore, Figure 4.5 indicates that the water saturation and clay minerals have profound influences on the P-wave velocity across single clay-rich soil-filled rock joints regardless of the dominant frequency of incident wave, which are carefully elaborated and analysed as follows.

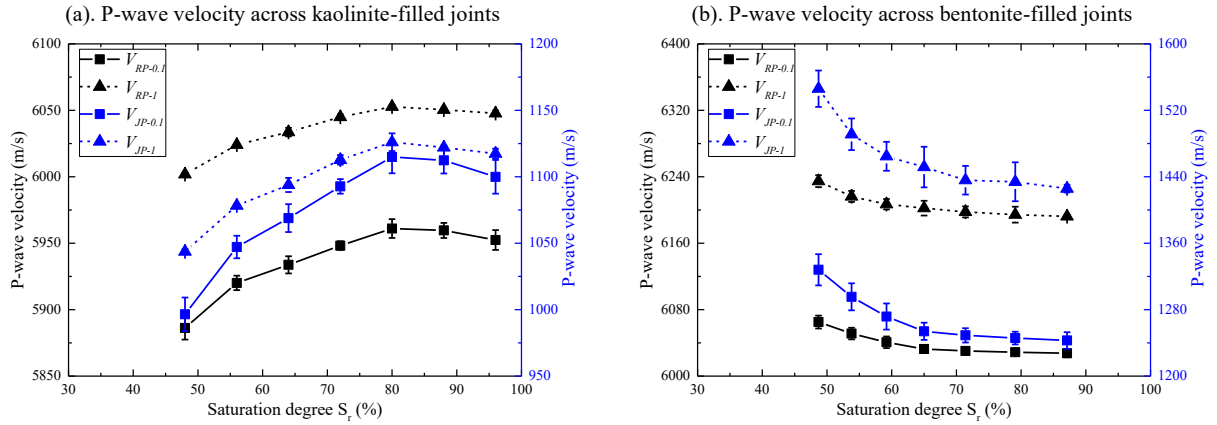


Figure 4.5 P-wave velocity across rock samples with single: (a). kaolinite-filled joints, (b) Bentonite-filled joints. Herein,  $V_{RP-0.1}$  and  $V_{RP-1}$  represent P-wave velocities across the entire rock specimen for 0.1-MHz and 1-MHz incident waves, respectively;  $V_{JP-0.1}$  and  $V_{JP-1}$  denote P-wave velocities across the clay-rich joint for 0.1-MHz and 1-MHz incident waves, respectively.

Figure 4.5a shows that, within the water saturation range of 48% - 80%, P-wave velocity across the kaolinite-filled joint gradually increases with increasing water saturation. According to the local flow mechanism, the increasing water saturation results in a gradual increase in water content accumulated in the soft pores, promoting the wave-induced fluid flow and thus stiffening the compliant parts of the infill kaolinite clay (Knight et al., 1998). Alternatively, an increase in water saturation could reduce the volume fraction of air in the pore space of kaolinite clays, decreasing the compressibility and then enhancing the bulk modulus of the infill kaolinite clay (Mavko et al., 2020). Besides, the decreasing bulk density of infill kaolinite clay induced by increasing water saturation (see Table 4.2) could be partly responsible for the increase in P-wave velocity. By contrast, within the saturation range of 80% - 96%, the increasing water saturation results in a gradual decrease in P-wave velocity across the kaolinite-filled joint, as shown in Figure 4.5a. It is mainly due to that the higher water saturation apparently weakens the grain contact stiffness of the kaolinite clay, which surpasses the effects

of the local flow and decreasing density (Atkinson, 1984, Xu et al., 2020). Accordingly, the infill kaolinite clay becomes softening and exhibits a decreasing trend of bulk modulus with increasing water saturation, causing a slower P-wave velocity across the kaolinite-filled joint.

Figure 4.5b illustrates that P-wave velocity across the bentonite-filled rock joint monotonously decreases as water saturation increases from 48.7% - 87.1%, which gradually tends to a plateau of a minimum value. It could be attributed to the fact that the bulk modulus of infill bentonite decreases progressively with the increasing water saturation (Zheng and Zaoui, 2018). Precisely, an increase in water saturation promotes the absorption of water at the particle surfaces, thereby increasing the particle size and void ratio as well as the consumption of surface energy (Khazanehdari and Sothcott, 2003, Tutuncu et al., 1998). Consequently, the contact stiffness between bentonite particles is evidently weakened, causing a decrease in the bulk modulus of bentonite clays. From the molecular perspective, more absorption of water could enlarge the basal layer spacing in basic units of bentonite, causing a decrease in the macroscale elastic bulk modulus associated with a relatively slight decrease in bulk density of bentonite clays (Chen and Evans, 2006, Carrier et al., 2014). Note that the slight decrease in bulk density has a negligible effect on P-wave velocity of bentonite clays compared to the decrement of bulk modulus (Ebrahimi et al., 2012). Besides, the clay flocculation enhanced by the increasing water saturation increases the quantity of air trapped in the bentonite clay flakes, probably reducing the bulk modulus of filling bentonite clay (Vanorio et al., 2003). On the other hand, since most of water absorbed by the bentonite exists in the form of the bound water with a much lower mobility, the local flow effect is negligible for P-wave propagation across the bentonite-filled rock joint. Figure 4.5b also shows that the higher the water saturation degree, the smaller the decreasing rate of P-wave velocity. It is likely due to that the rate of water absorption becomes slower with the increasing saturation (Ebrahimi et al., 2012). Accordingly, the water softening effect on infill bentonite clays gradually levels off, hence the decreasing rate of the bulk modulus gradually becomes slower.

The comparison of Figures 4.5a and 4.5b reveals that P-wave velocity across the bentonite-filled joint is higher than that through the kaolinite-filled joint at an approximately identical water saturation degree. For example, at the saturation degree of approximately 80%, wave velocities for 1-MHz P-wave across the bentonite- and kaolinite-filled joint are 1433.95 m/s and 1126.01 m/s, respectively. The principal explanation is that the bentonite clay has a larger bulk modulus (see Figure 4.4) and a smaller bulk density (see Table 4.2) compared to the kaolinite clay. Specifically, the bentonite clay could produce a greater amount of bound water

because of its larger specific surface area compared to the kaolinite clay (Cosenza and Tabbagh, 2004). The bound water is less compressible and has a lower density than bulk water (Sun et al., 1986). Consequently, the wet bentonite clay owns a lower compressibility and a smaller density than the wet kaolinite clay, resulting in a faster P-wave velocity across the bentonite-filled joint. Furthermore, it is found that P-wave velocity across the bentonite-filled joint is more sensitive to the change of water saturation at lower saturation degrees. For example, 1-MHz P-wave velocity of the bentonite-filled joint decreases by about 6.1% for water saturation increasing from 48.7% to 65%, whereas that of the kaolinite-filled joint increases by around 4.8% for water saturation increasing from 48% to 64%. This is mainly owing to that, within the low water saturation range, the hydration of bentonite caused by the water absorption is apparently stronger than that of kaolinite (Li et al., 2020).

#### 4.3.2.2 P-wave transmission ratio

Transmission ratios for P-waves propagation across single clay-filled rock joints are plotted as a function of water saturation degree in Figure 4.6. It is shown that P-wave transmission across the clay-filled rock joint is strongly dependent on water saturation and clay minerals of infill clay no matter what the dominant frequency of input waves. Specifically, the saturation-dependent P-wave transmission for single kaolinite-filled joints exhibits an opposite trend to that for single bentonite-filled rock joints. The detailed demonstration and analysis are provided below.

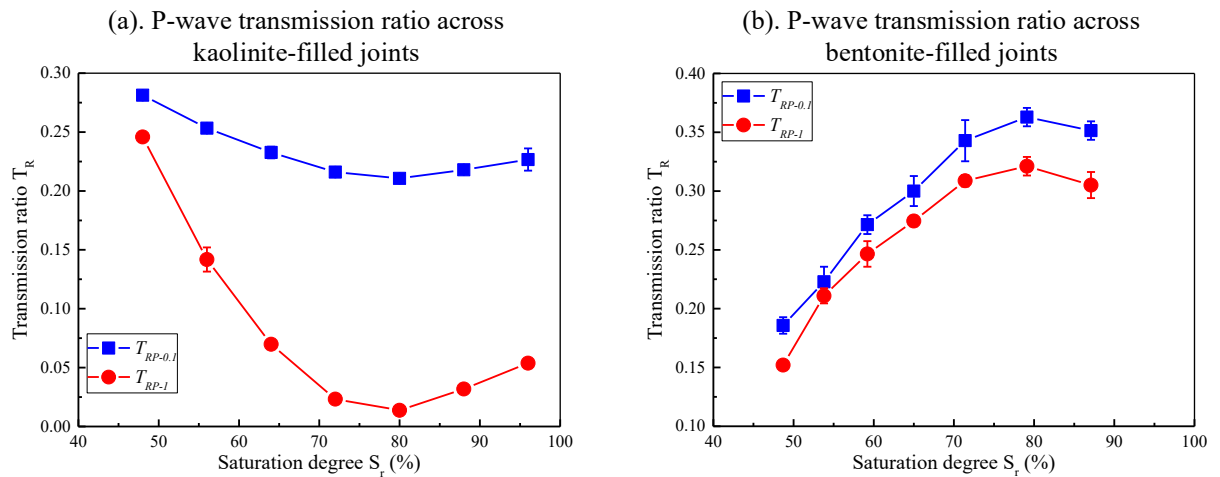


Figure 4.6 P-wave transmission ratio across rock samples with single: (a). kaolinite-filled joints, (b) Bentonite-filled joints. Herein,  $T_{RP-0.1}$  and  $T_{RP-1}$  represent transmission ratios across the rock specimen for 0.1-MHz and 1-MHz incident P-waves, respectively.

Figure 4.6a shows that, as P-wave passes through the kaolinite-filled joint, the transmission ratio significantly decreases when the degree of saturation increases from 48% to 80%. It indicates that more wave energy is attenuated by the kaolinite-filled joint with increasing water saturation. This could be mainly explained by that the increasing water saturation enhances the local flow effect. Specifically, the passing P-waves compress the infill kaolinite clay, leading to local fluid flow between soft and compliant regions in the kaolinite clay. The local flow relative to the clay matrix could be promoted by the increasing water saturation, thereby causing more wave energy loss (Amalokwu et al., 2014). By contrast, within the saturation range of 80% - 96%, the transmission ratio of P-wave increases with the increasing water saturation, as illustrated in Figure 4.6a. It implies that, at higher water saturation degrees, the increase in water saturation could lessen P-wave attenuation across the kaolinite-filled joint. This is likely due to that the increasing water saturation apparently weakens the viscosity of infill kaolinite over the saturation range (see Figure 4.4). Alternatively, the increasing water saturation leads to an increase in pore space filled with water, reducing wave scattering in infill kaolinite clay.

Figure 4.6b illustrates that, for P-wave propagation across single bentonite-filled rock joints, the transmission ratio increases as water saturation increases from 48.7% to 79.1%, followed by a slight decrease with further increasing water saturation. This implies that, within the saturation range of 48.7% - 79.1%, the increasing water saturation could evidently reduce wave attenuation across the bentonite-filled rock joint. It could be principally attributed to that the viscosity of bentonite clay apparently decreases with increasing water saturation (see Figure 4.4). The increase in water saturation promotes the softening of bentonite, causing smaller viscosity of bentonite. Accordingly, wave dissipation induced by frictions between grain-to-grain and water-particle contacts is significantly reduced. Meanwhile, most of water molecules are absorbed around bentonite particles in the form of bound water with very small mobility between bentonite layers, leading to the swelling of bentonite and then reducing its permeability (Fang et al., 2017). As a result, the viscous loss caused by the squirt flow are negligible compared to the enhanced joint stiffness induced by smaller viscosity of the entire bentonite layer. In addition, the absorbed water has larger stiffness than bulk water, thus more absorbed water could transmit more P-wave energy. By comparison, when saturation degree increases from 79.1% to 87.1%, a slight decrease in transmission of P-wave across the bentonite-filled rock joint is observed from Figure 4.6b. It means that, within the saturation range of 79.1% - 87.1%, the higher water saturation for infill bentonite, the greater P-wave

attenuation across the bentonite-filled joint. This is likely due to that the wave-induced local flow in wet bentonite clay becomes more evident and takes advantages over other factors responsible for promoting wave transmission across the bentonite-filled joint when water saturation degree is larger than 79.1%.

#### 4.3.2.3 Time-frequency-energy distribution of P-waves

The typical time-frequency maps for P-waves propagating across different kaolinite- and bentonite-filled rock joints are shown in Figures 4.7 - 4.10, respectively. It should be mentioned that the time-frequency maps for transmitted P-waves across the intact rock specimen are referred to as the baseline to evaluate the effects of single clay-filled joints (see Figures 4.7a, 4.8a, 4.9a and 4.10a). Particularly, for 0.1-MHz P-wave propagation across the intact rock reference, Figures 4.7a and 4.9a indicate that the frequency contents of transmitted waves mainly concentrate in the range of 0.07 - 0.20 MHz. On the other hand, for 1-MHz P-wave propagation through the intact rock reference, the frequency contents of transmitted waves primarily centre in the band from 0.5 MHz to 1.2 MHz, as shown in Figures 4.8a and 4.10a. Furthermore, Figures 4.7 - 4.10 indicate that single clay-filled rock joints highly attenuate the energy of P-waves while it has relatively smaller effects on frequency partition of transmitted pulses. It is also found that the clay-filled joint leads to apparent changes in magnitudes of transmitted wave energy for both of 0.1-MHz and 1-MHz input P-waves while its effect on frequency contents prefers to manifest for high-frequency incident P-wave. In addition, it is shown that the saturation dependence of frequency contents and energy partition of transmitted P-waves are predominantly dependent on mineralogical compositions of infill clays, which is consistent with the findings of P-wave velocity and transmission ratio.

Figures 4.7 and 4.8 illustrate the effects of single kaolinite-filled rock joints on frequency contents and energy partition of the first-arriving pulses for transmitted 0.1-MHz and 1-MHz P-waves, respectively. Regarding energy of transmitted P-waves, Figures 4.7 and 4.8 show that magnitudes of energy decrease and then increase with progressively increasing water saturation, minimizing at the water saturation degree of 80%, which is agreement with the saturation-dependent transmission ratio for 1-MHz P-wave passing across single kaolinite-filled joint (see Figure 4.6a).

Specifically, for 0.1-MHz P-waves passing through the kaolinite-filled joint, Figures 4.7b - 4.7f reveal that most of transmitted wave energy primarily centres in the frequency range of 0.09 - 0.12 MHz, where the frequency band for energy concentration scarcely changes with varying

water saturation. Additionally, Figures 4.7b - 4.7f illustrate that, as the water saturation progressively increases, energy magnitudes in the dominant frequency band decreases within the saturation range of 48% - 80% before slightly increasing for water saturation higher than 80%, which is consistent with findings of P-wave transmission ratio (see Figure 4.6a). Furthermore, an interference frequency band with lower energy is observed in Figures 4.7b - 4.7h, which could be resulted from the interference signal generated by the transducer itself. Thus, changes in the interference signal induced by the varying water saturation would not be analysed in the current work. On the other hand, for 1-MHz incident P-waves, Figures 4.8b - 4.8f show that the frequency band where most of transmitted wave energy concentrates gradually shift towards higher values as the water saturation increases to the critical value of 80%, after which it moves back forward a little bit with continuously increasing water saturation. It could be attributed to that, within the saturation range of 48% - 80%, the increasing water content promotes the local flow, locally enhancing the joint stiffness of some regions in the kaolinite clay. As a result, the dominant spectral energy shifts towards higher frequencies (Pyrak-Nolte et al., 1990). However, following with a slight increase as water saturation increases from 80% to 96%.

Figures 4.9 and 4.10 unravel the influences of single bentonite-filled rock joints on frequency spectra and energy distribution of P-waves propagating across rock samples. Particularly, for 0.1-MHz P-waves propagating across the bentonite-filled joint (see Figures 4.9b - 4.9f), an evident shift in the frequency band where most of transmitted wave energy centres is observed with water saturation increasing from 48.7% to 59.2%. Following that, energy of transmitted waves mainly centres in the frequency range from 0.1 MHz to 0.14 MHz, with few changes caused by the increasing water saturation. The similar trends of frequency contents can be observed for 1-MHz input waves passing through the bentonite-filled joint, as shown in Figure 4.10b - 4.10f. It could be attributed to the fact that joint stiffness is significantly reduced by the increasing water saturation within the range of 48.7% to 59.2%. By comparison, for water saturation degree higher than 59.2%, changes in the joint stiffness due to the increasing water saturation are too small to play a predominant role in frequency partition of transmitted P-waves. Thus, the frequency contents corresponding to the dominant spectral energy seldomly change with water saturation.



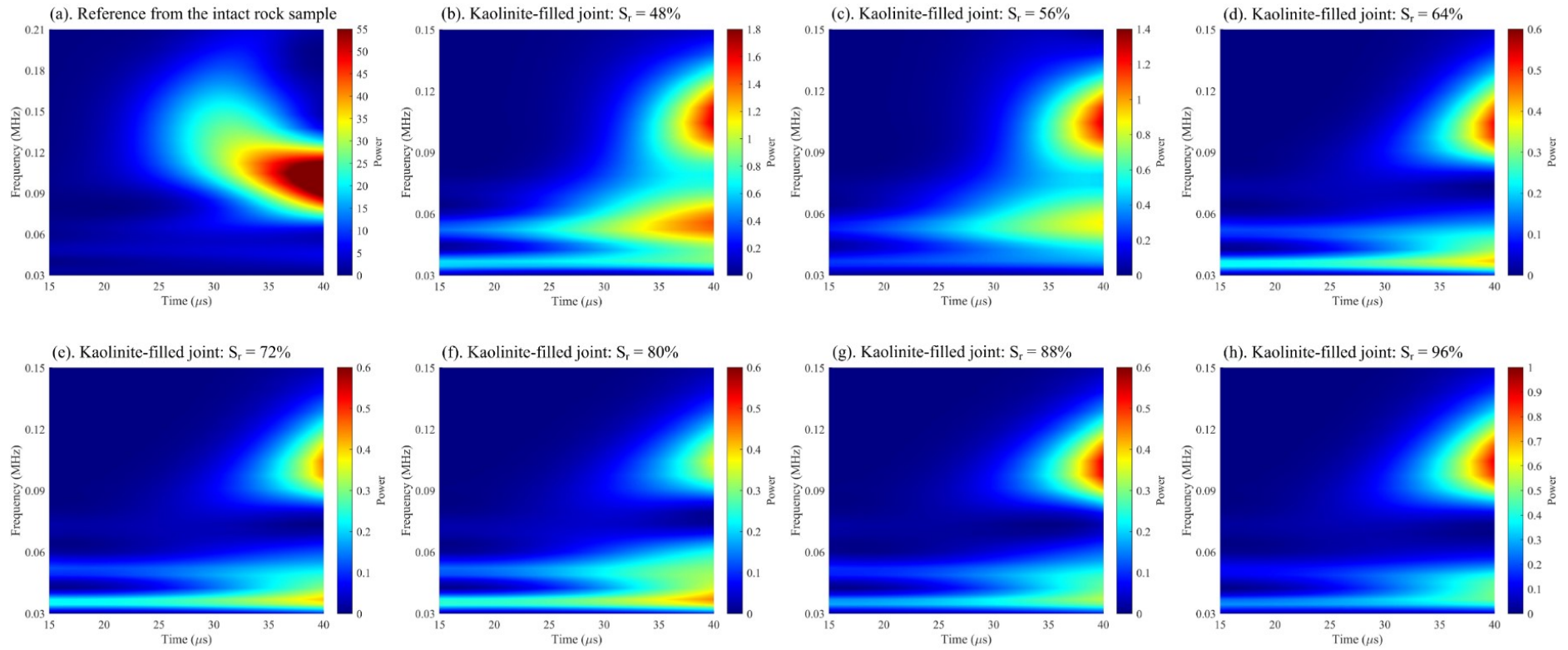


Figure 4.7 Time-frequency maps for transmitted 0.1-MHz P-waves across individual rock joints filled with kaolinite at different saturation degrees. Herein,  $S_r$  denotes the degree of water saturation of clay-rich specimens.



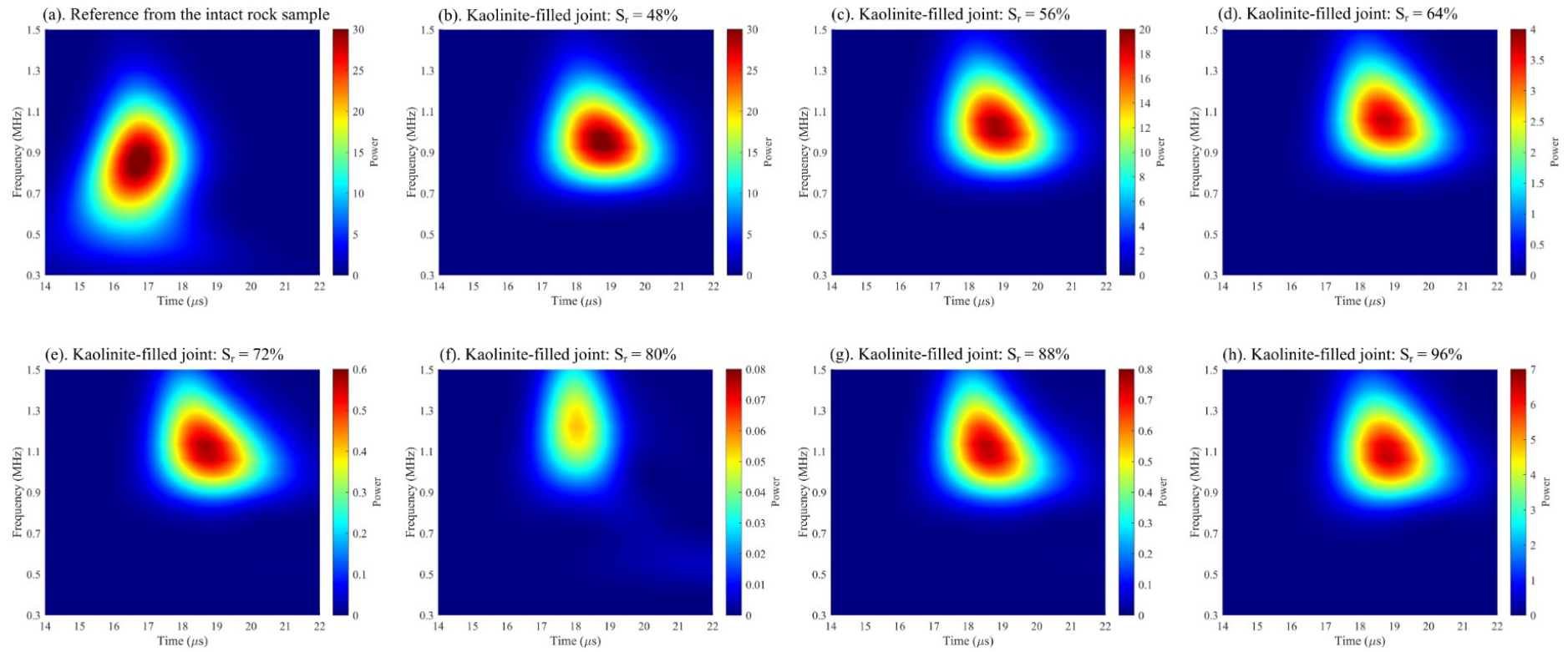


Figure 4.8 Time-frequency maps for transmitted 1-MHz P-waves across individual rock joints filled with kaolinite at different saturation degrees. Herein,  $S_r$  denotes the degree of water saturation of clay-rich specimens.

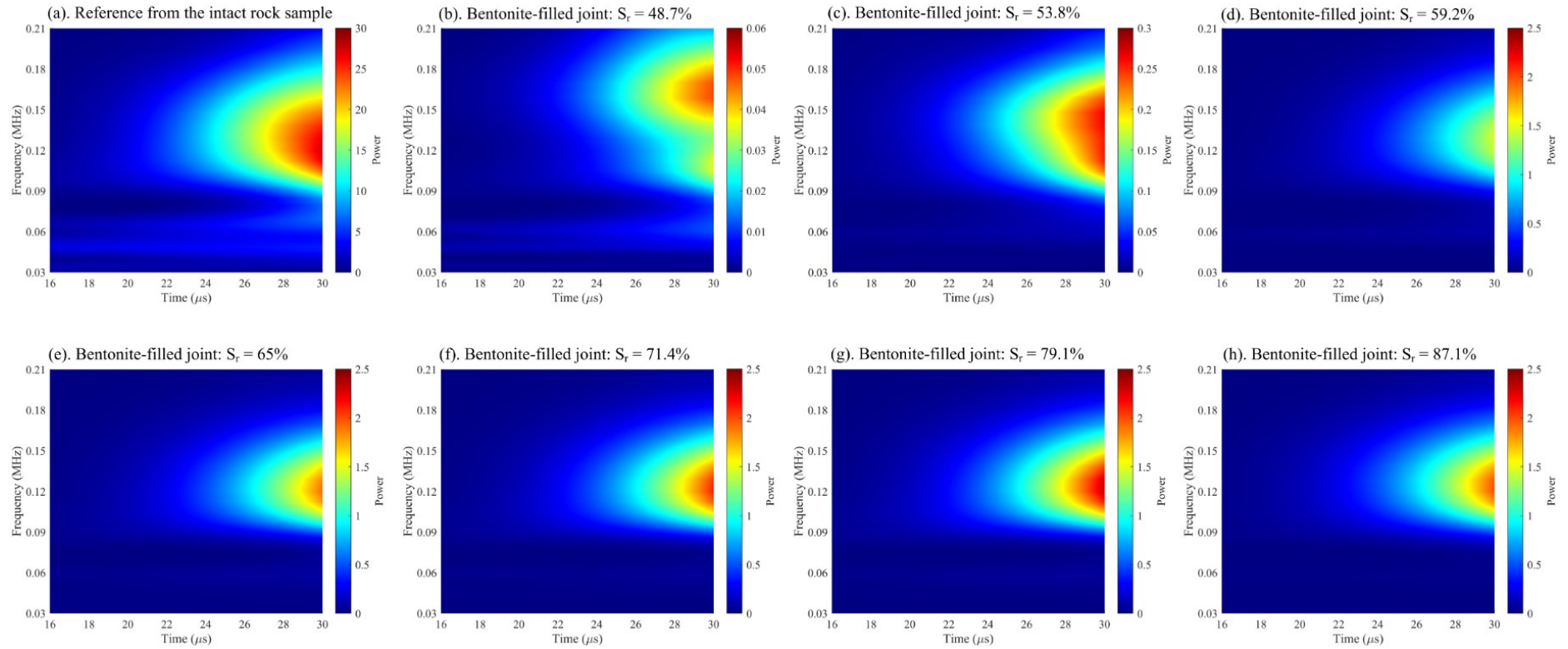


Figure 4.9 Time-frequency maps for transmitted 0.1-MHz P-waves across individual rock joints filled with bentonite at different saturation degrees. Herein,  $S_r$  denotes the degree of water saturation of clay-rich specimens.

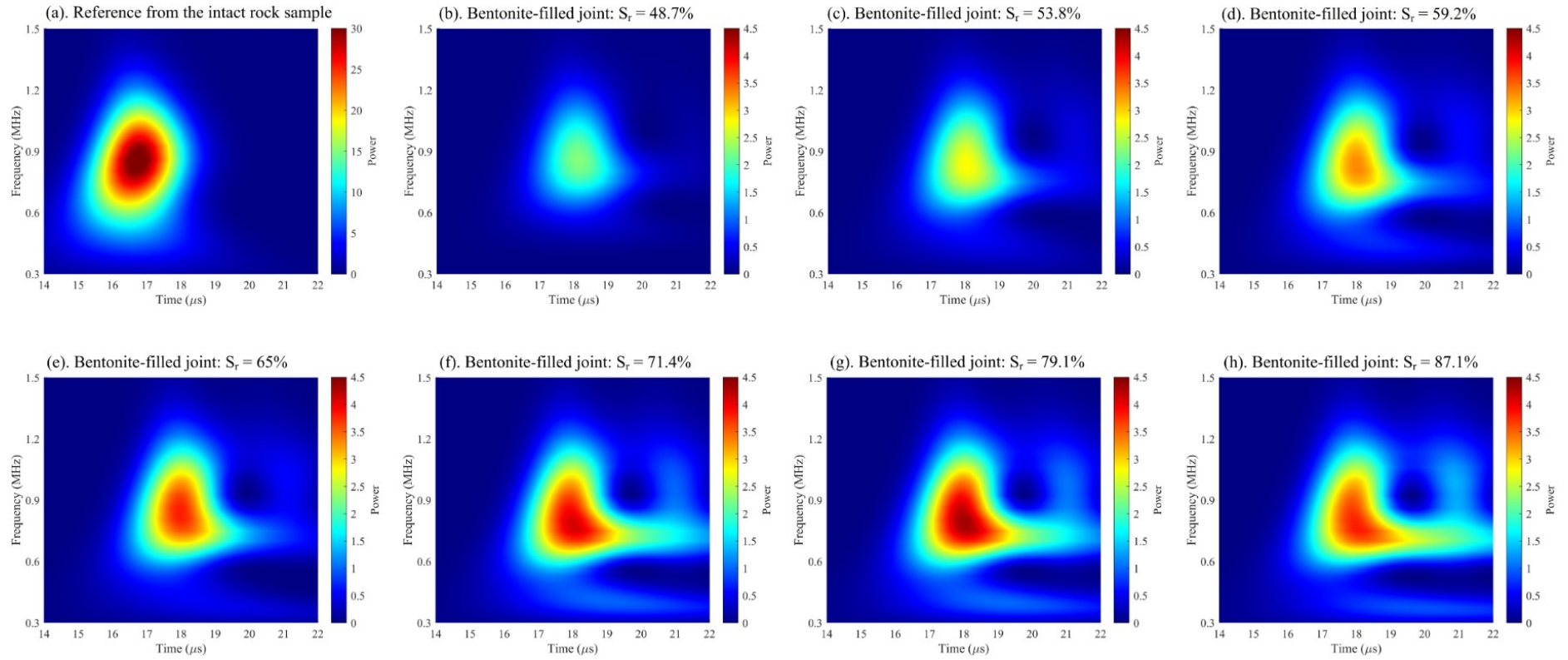


Figure 4.10 Time-frequency maps for transmitted 1-MHz P-waves across individual rock joints filled with bentonite with different saturation degrees. Herein,  $S_r$  denotes the degree of water saturation of clay-rich specimens.

On the other hand, Figures 4.9 and 4.10 indicate that magnitudes of transmitted P-waves across the bentonite-filled joint increases with increasing water saturation and maximizes at the critical saturation degree of 79.1%, followed by a minor decrease with continuously increasing water saturation. The principal explanation is that the increasing water content significantly declines the viscosity of the filling bentonite clay layer. Consequently, energy loss of wave induced by friction is highly reduced, resulting more wave energy transmitting across the bentonite-filled joint. However, at higher water saturations (i.e., within the range of 79.1% - 87.1%), the effects of wave impedance contrast between rock matrix and filling bentonite layer may be superior to that of viscosity. Accordingly, more wave reflection occurs at the rock joint surface, causing less wave energy passing through the bentonite-filled joint.

### 4.3.3 S-wave attributes of single rock joints filled with wet clay-rich soils

#### 4.3.2.1 S-wave velocity

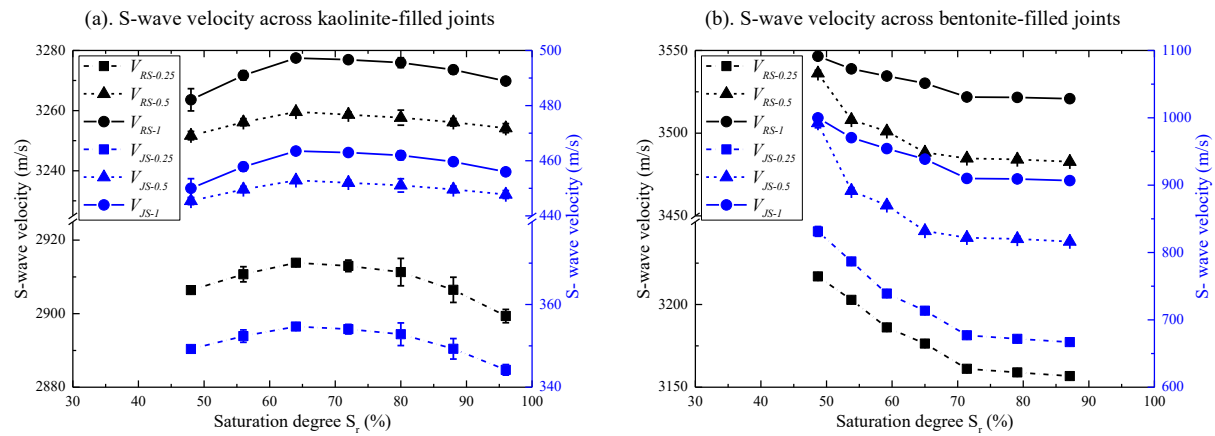


Figure 4.11 S-wave velocity across rock samples with single: (a). kaolinite-filled joints, (b) Bentonite-filled joints. Herein,  $V_{RS-0.25}$ ,  $V_{RS-0.5}$  and  $V_{RS-1}$  represent S-wave velocities across the entire rock specimen for 0.25-MHz, 0.5-MHz and 1-MHz incident waves, respectively;  $V_{JS-0.25}$ ,  $V_{JS-0.5}$  and  $V_{JS-1}$  represent S-wave velocities across the clay-rich joint for 0.25-MHz, 0.5-MHz and 1-MHz incident waves, respectively.

S-wave velocities of single clay-filled joints and the corresponding jointed rock samples are plotted as a function of water saturation degree in Figure 4.11. It is shown that variations of S-wave velocity across jointed rock samples resembles changes in S-wave velocity of their containing clay-filled joints, implying that individual clay-filled rock joints primarily dominate S-wave velocity of rock masses. Additionally, Figure 4.11 reveals that S-wave velocity across the clay-filled joint highly depends on the water saturation and mineralogical compositions of

filling clay regardless of the dominant frequency of input waves, which is demonstrated in detail as follows.

Figure 4.11a shows that, within the saturation range of 64% - 96%, S-wave velocity of the kaolinite-filled joint slowly decreases from 452.90 m/s to 447.75 m/s with increasing water saturation. Likewise, S-wave velocity across the bentonite-filled joint gradually declines from 831.34 m/s to 666.91 m/s as water saturation progressively increases from 48.7% to 87.1%, as shown in Figure 4.11b. These observations could be attributed to the fact that the increase in water saturation evidently reduces the shear modulus of clays. On one hand, the increasing water saturation enhances the hydration of clay, consuming more surface energy and then weakening the stiffness of grain contacts in clays (Atkinson, 1984, Li et al., 2020). On the other hand, the increasing water saturation leads to a decrease in matric suction, reducing the interparticle contact forces in bentonite (Clariá and Rinaldi, 2007), where the matric suction represents the capillary forces (tensile stresses) generated by the development of water menisci at the particle contacts (Cho and Santamarina, 2001). As a result, the shear modulus of clays decreases upon water saturation, which is in agreement with observations from the amplitude sweep tests (see Fig. 4). It should be mentioned that the increasing water saturation could to some extent cause a decrease in bulk density (see Table 4.2), but the decrement of clay density is negligible compared to that of shear modulus. Accordingly, S-wave velocity of the clay-filled joint exhibits a declining trend as the water saturation increases.

In contrast, within the saturation range from 48% to 64%, the increasing water saturation leads to a slight increase in S-wave velocity across the kaolinite-filled joint (see Figure 4.11a). It is similar to the observations reported by other researchers (Pyrak-Nolte et al., 1990), which could be interpreted via the viscous coupling and frequency dispersion mechanisms. The increasing water saturation means that air in the kaolinite clay is gradually substituted by water, where water owns a higher viscosity than air. According to the viscous coupling mechanism, the increasing water saturation could increase the shear modulus of the kaolinite clay at ultrasonic frequencies (Khazanehdari and Sothcott, 2003). Based on the frequency dispersion mechanism, the local flow could give a rise to a larger shear modulus of infill kaolinite as water saturation increases (Mavko and Jizba, 1994). In addition, the decrease in bulk density caused by increasing water saturation could partly contribute to the increase in S-wave velocity. It is worth to mention that the increase in shear modulus induced by the increasing water saturation is inconsistent with the variation of shear modulus measured by the amplitude sweep tests. This is likely due to that the shear strain generated by amplitude sweep tests could be destructive for



the kaolinite clay, causing the damage of grain contacts between clay particles and then manifesting as the reduction of shear modulus (Khazanehdari and Sothcott, 2003).

#### 4.3.2.2 S-wave transmission ratio

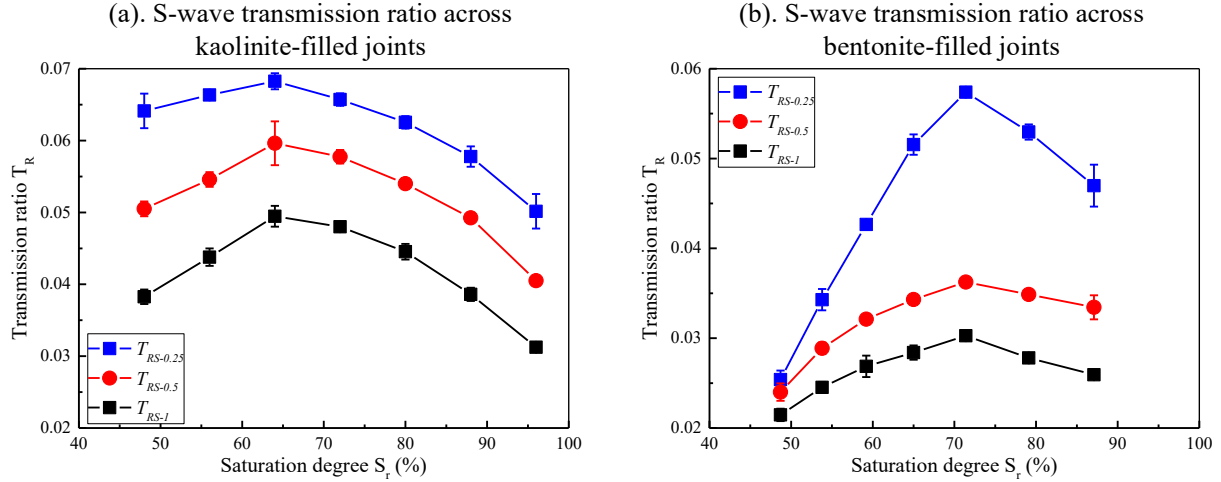


Figure 4.12 S-wave transmission ratio across rock samples with single: (a). kaolinite-filled joints, (b) Bentonite-filled joints. Herein,  $T_{RS-0.25}$ ,  $T_{RS-0.5}$  and  $T_{RS-1}$  represent transmission ratios across the rock specimen for 0.25-MHz, 0.5-MHz and 1-MHz incident S-waves, respectively.

Transmission ratios for S-waves propagating across single clay-filled rock joints are plotted with respect to the water saturation of filling clay in Figure 4.12. It is found that the transmission ratio of S-wave increases with increasing water saturation until reaching a maximum, after which it begins to decrease with continuously increasing water saturation regardless of clay minerals in the joint. Particularly, the transmission ratio maximizes at saturation degree about 64% for the kaolinite-filled joint (see Figure 4.12a) while it reaches the maximum at saturation degree near 71.4% for the bentonite-filled joint (see Figure 4.12b). This implies that wave attenuation caused by single clay-filled rock joints decreases and then increases with the progressively increasing water saturation no matter what the infill clay it is. Particularly, at lower saturation degrees, the increasing water saturation reduce the viscosity of infill clay layer (see Figure 4.4). Accordingly, the friction loss caused by the relative fluid-solid motion and solid-solid motion gradually decreases, causing less wave attenuation across the clay-filled joint. By comparison, when the water saturation exceeds a critical value, wave attenuation begins to increase with increasing water saturation, which could be attributed to the local flow in filling clay and wave reflection at the rock-clay interface. On one hand, the increasing water saturation enhances the local flow effect, resulting more wave dissipation (Winkler and Nur, 1979). On the other hand, the increasing water content reduces the shear

modulus of infill clay layer (see Figure 4.4). According to the displacement discontinuity theory, more wave reflection occurs at the rock-clay interface as the shear modulus of clay decreases, causing less wave energy transmitting into the clay-filled joint. The increase in wave attenuation induced by those two factors could conceal the decrement of wave attenuation caused by the reducing viscous loss, resulting in more wave attenuation across the clay-filled joint. Our findings are in accordance with predictions from theoretical models presented by (Lo et al., 2007).

#### **4.3.2.3 Time-frequency-energy distribution of S-waves**

Some typical time-frequency maps for transmitted 0.25-MHz, 0.5-MHz and 1-MHz input S-waves propagating across individual kaolinite- and bentonite-filled rock joints are presented in Figs. 13-18, respectively. Note that the time-frequency maps for different S-waves propagating through the intact rock sample are included in Figures 4.13 - 4.18 for better demonstrating the effects of individual clay-filled rock joints on S-wave behaviours across rock masses (see Figures 4.13a - 4.18a). Figures 4.13a - 4.18a show that energy of transmitted 0.25-MHz, 0.5-MHz and 1-MHz S-waves through the intact rock reference is mostly stored in the frequency ranges of 0.13 - 0.36 MHz, 0.2 - 0.8 MHz and 0.3 - 1.3 MHz, respectively, implying that the frequency partition of transmitted S-waves across the intact rock is dependent on the dominant frequency of input waves. It is found that the wavelet transform for the intact rock is a single wave-packet without additional structure regardless of the dominant frequency of input S-waves. By comparison, the wavelet transforms of S-waves transmitting across the clay-filled joint have complicated structure, with energy arriving significantly later than that for the intact rock and with lower frequency contents. It means that the clay-filled joint could act as a low-pass filter for propagation of S-waves (Pyrak-Nolte and Nolte, 1995). Notably, the first-arriving frequency band in the frequency maps for the jointed rock samples corresponds to the initial signals while the following others corresponds to the later signals interfered by multiple reflections and refractions; hence, the analysis on spectral contents of transmitted S-waves focuses mainly on the first arriving frequency band.

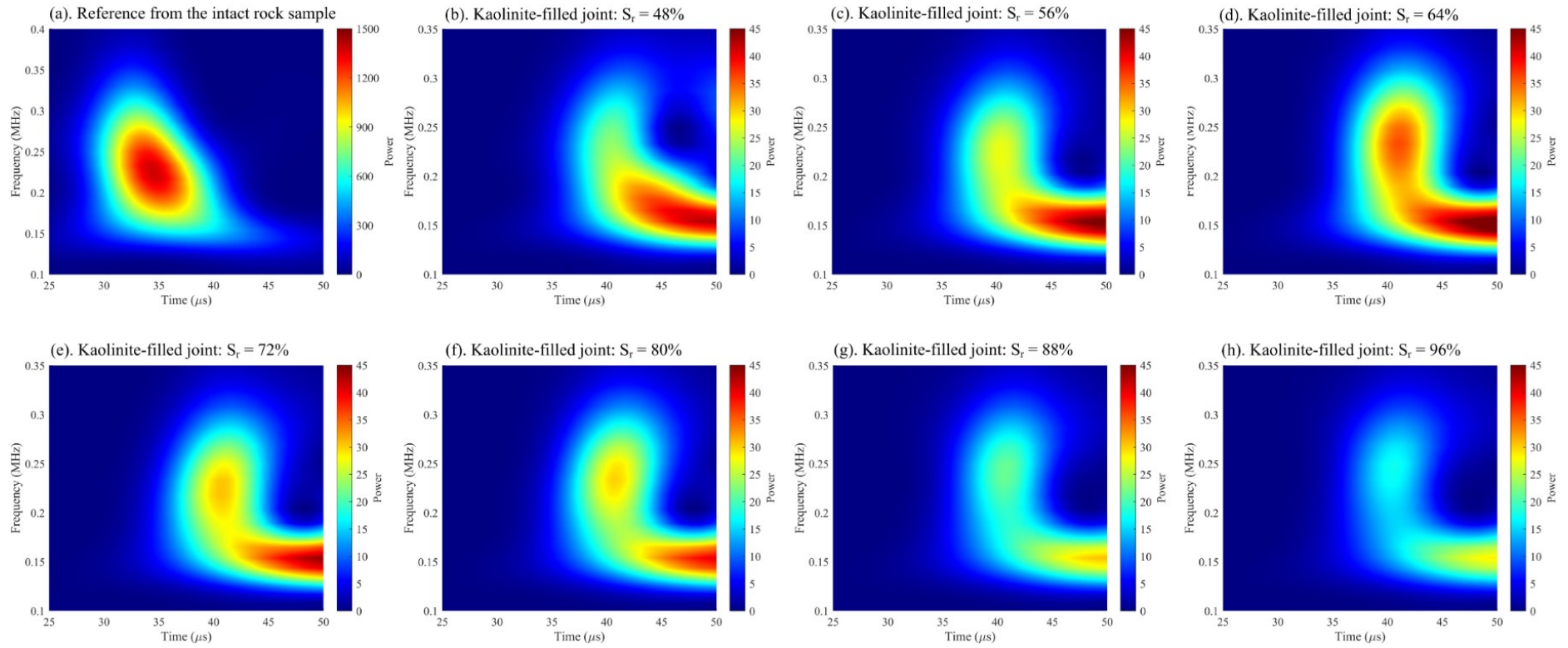


Figure 4.13 Time-frequency maps for transmitted 0.25-MHz S-waves across individual rock joints filled with kaolinite at different saturation degrees. Herein,  $S_r$  denotes the degree of water saturation of clay-rich specimens.



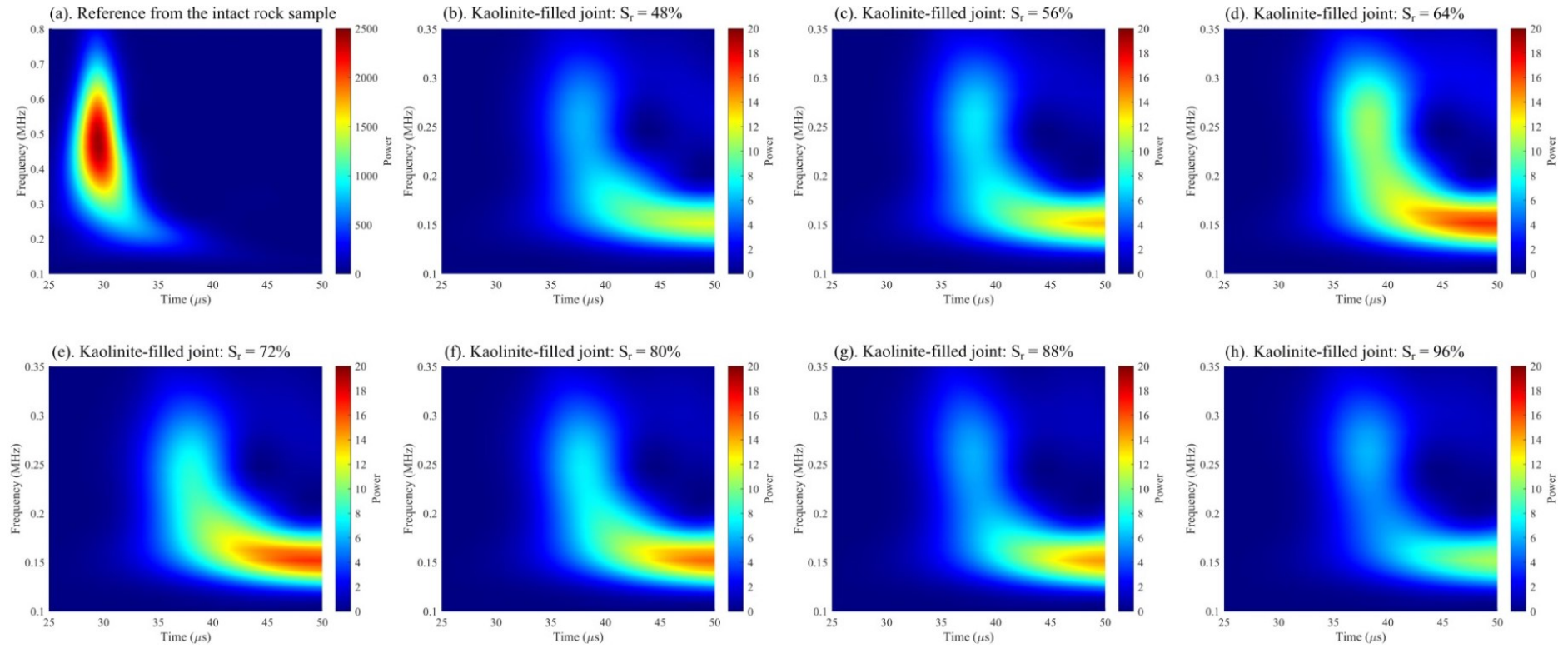


Figure 4.14 Time-frequency maps for transmitted 0.5-MHz S-waves across individual rock joints filled with kaolinite at different saturation degrees. Herein,  $S_r$  denotes the degree of water saturation of clay-rich specimens.

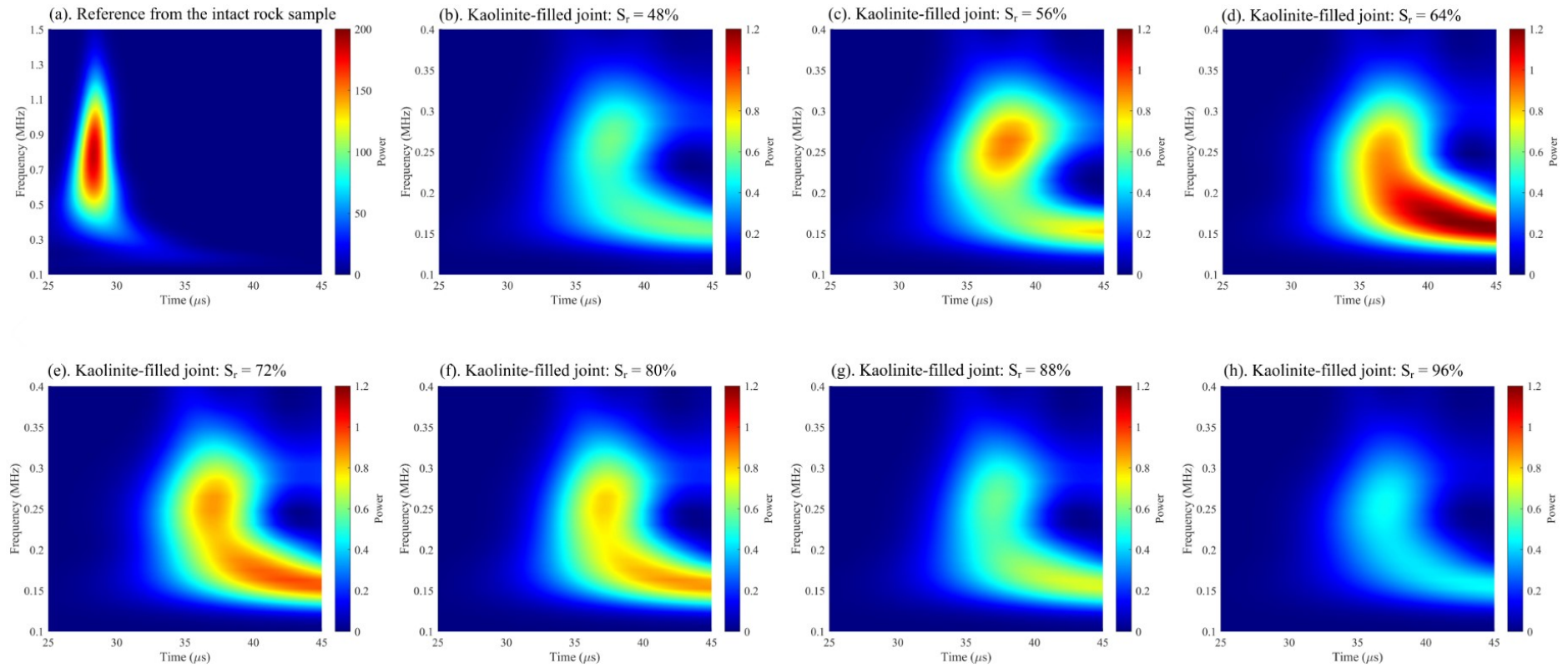


Figure 4.15 Time-frequency maps for transmitted 1-MHz S-waves across individual rock joints filled with kaolinite at different saturation degrees. Herein,  $S_r$  denotes the degree of water saturation of clay-rich specimens.

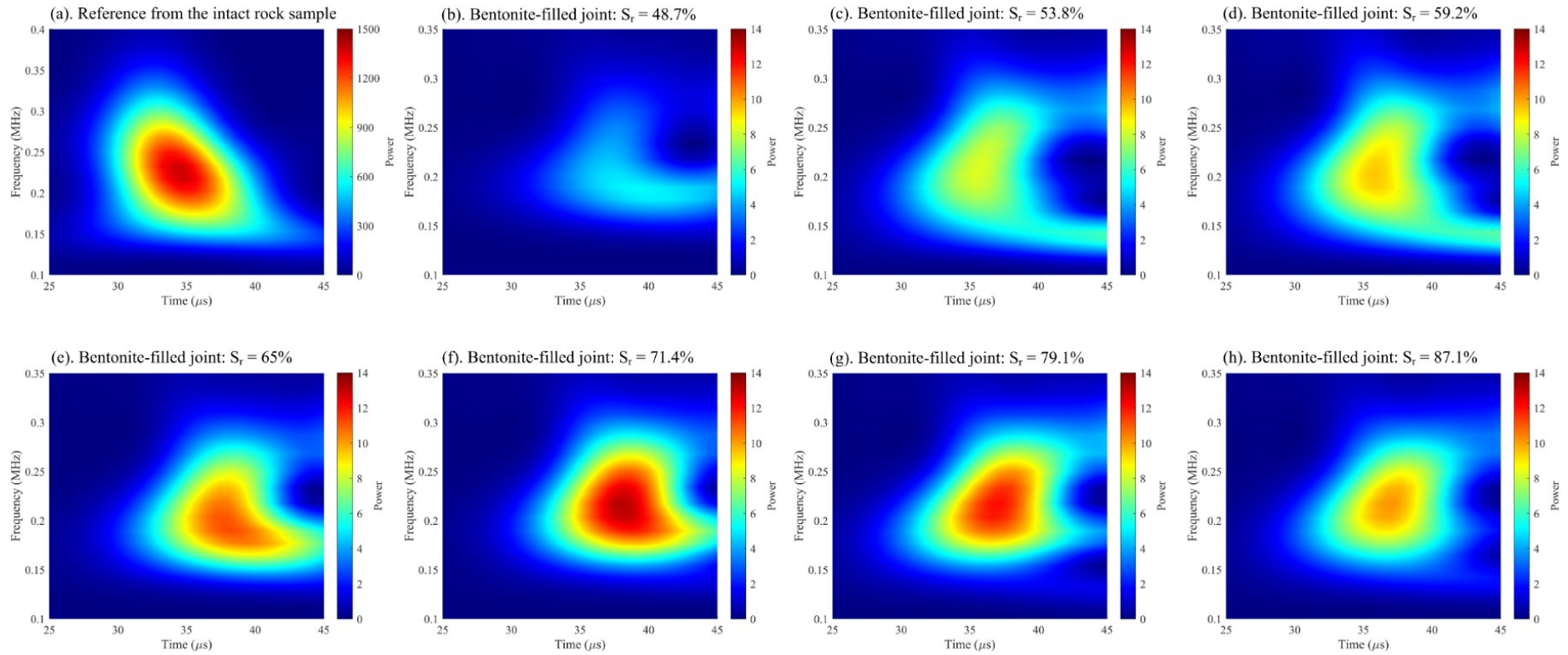


Figure 4.16 Time-frequency maps for transmitted 0.25-MHz S-waves across individual rock joints filled with bentonite at different saturation degrees. Herein,  $S_r$  denotes the degree of water saturation of clay-rich specimens.

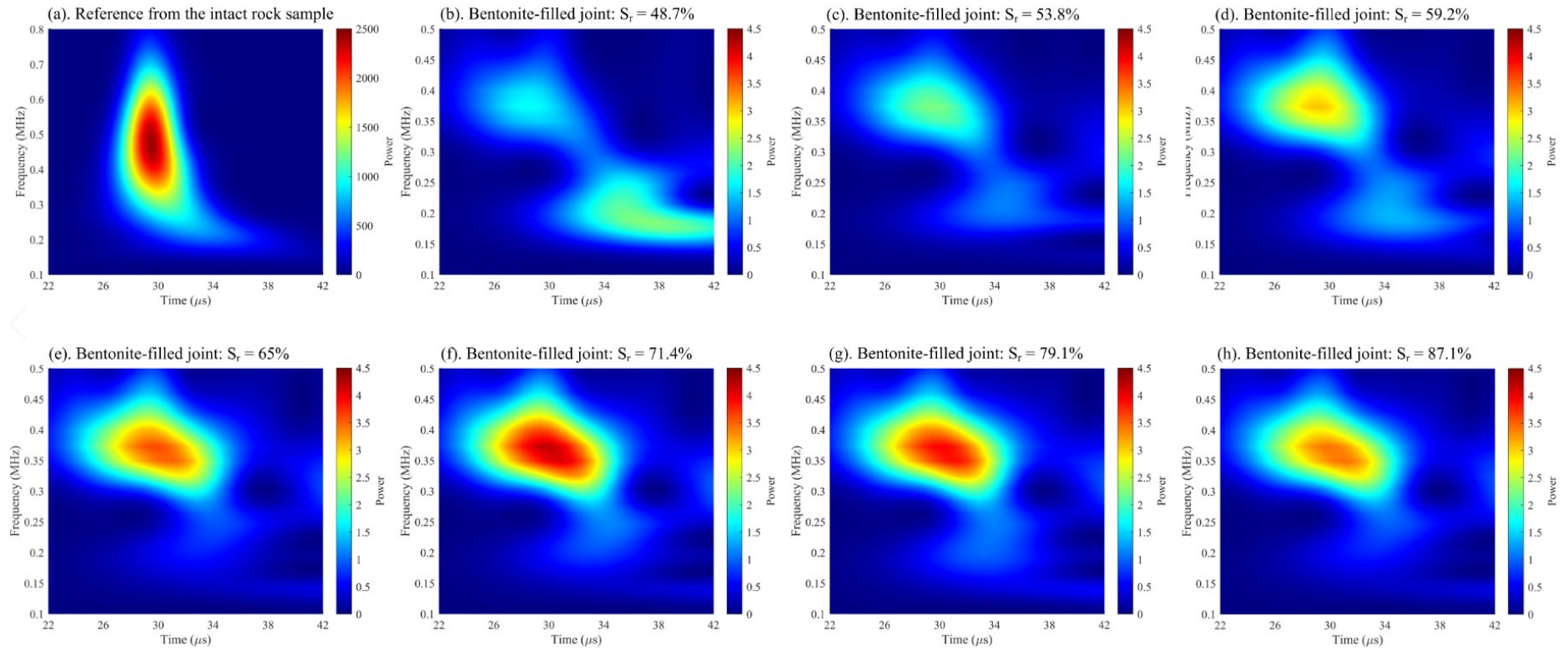


Figure 4.17 Time-frequency maps for transmitted 0.5-MHz S-waves across individual rock joints filled with bentonite at different saturation degrees. Herein,  $S_r$  denotes the degree of water saturation of clay-rich specimens.



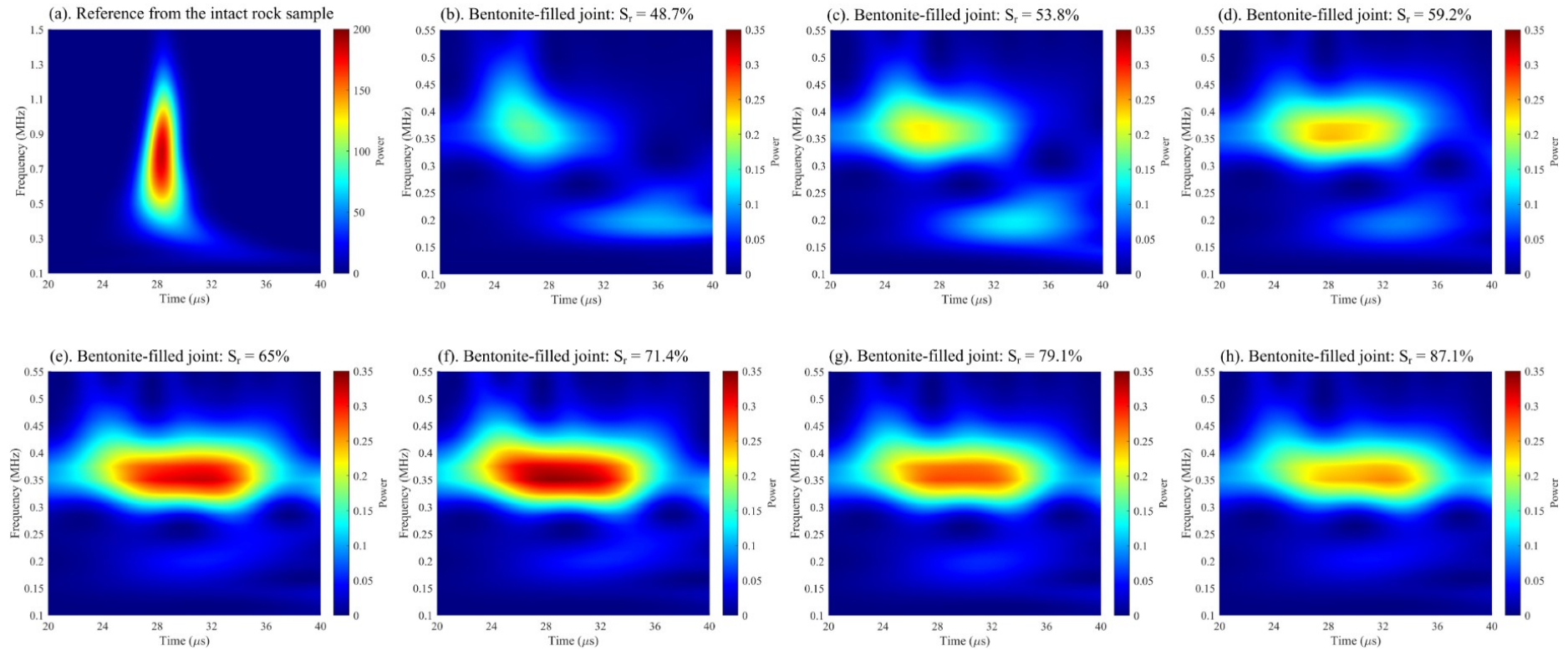


Figure 4.18 Time-frequency maps for transmitted 1-MHz S-waves across individual rock joints filled with bentonite at different saturation degrees.

Herein,  $S_r$  denotes the degree of water saturation of clay-rich specimens.

As illustrates in Figures 4.13 - 4.18, the clay-filled joint strongly affects the frequency partition of transmitted S-waves through rock samples. Specifically, compared to the intact rock sample, the rock sample with single clay-filled joint severely shifts the frequency range where wave energy is largely stored towards lower values. For rock samples with single kaolinite-filled joints, it is observed that transmitted S-wave energy mainly concentrates on the frequency band from 0.15 MHz to 0.3 MHz regardless of the dominant frequency of input waves (see Figures 4.13b - 4.13h, 4.14b - 4.14h and 4.15b - 4.15h). This indicates that S-waves at frequencies higher than 0.3 MHz could be significantly attenuated by the kaolinite-filled joint. On the other hand, for rock samples with individual bentonite-filled joints, it is found that transmitted wave energy for 0.25-MHz input S-waves is mostly stored in the frequency range of 0.15 - 0.3 MHz (see Figures 4.16b - 4.16h) while that for 0.5-MHz and 1-MHz input S-waves is largely stocked over the frequency band of 0.28 - 0.48 MHz (see Figures 4.17b - 4.17h and 4.18b - 4.18h). This implies that the bentonite-filled joint prefers to transmit S-waves at frequencies lower than 0.5 MHz. The above observations suggest that the clay-filled joint could act as a high-frequency S-wave filter, where the filtering range predominantly depends on filling clay minerals. It could also be concluded that the alternation of the frequency range storing energy of transmitted wave across the clay-filled joint is more significant for incident waves with higher dominant frequency.

Furthermore, Figures 4.13 - 4.18 indicate that the transmitted S-wave energy of rock samples is significantly attenuated by the clay-filled rock joint. To be specific, magnitudes of energy for transmitted 0.25-MHz, 0.5-MHz and 1-MHz S-waves across the intact sample are about 30, 125 and 200 times larger than those for corresponding transmitted S-waves across rock samples with individual kaolinite-filled joints, respectively, as shown in Figures 4.13 - 4.15. On the other hand, magnitudes of energy for transmitted 0.25-MHz, 0.5-MHz and 1-MHz S-wave through the intact sample are approximately 100, 555 and 570 times greater than those for corresponding transmitted signals across rock samples with individual bentonite-filled joints, as can be seen from Figures 4.16 - 4.18. The above findings also reveal that the larger the dominant frequency of input S-waves, the greater wave attenuation induced by the clay-filled joint. Besides, compared with the frequency partition, magnitudes of transmitted S-wave energy are more sensitive to the presence of clay-filled joints in rock masses.

In addition, Figures 4.13 - 4.18 show that water saturation degree of infill clay has significant influences on the energy and frequency partition of transmitted waves across individual clay-filled joints regardless of input wave frequency. To be specific, water saturation evidently

affects transmitted S-wave energy while it has little influences on the frequency partition of transmitted S-waves. For the same input S-waves, the magnitudes of transmitted S-wave energy across the clay-filled rock joint are firstly promoted and then reduced by the progressively increasing water saturation. Furthermore, the transmitted S-wave energy maximizes at saturation degree of 64% for rock samples with kaolinite-filled joints (see Figures 4.13 - 4.15) while it reaches the maximum at saturation degree of around 71.4% for rock samples with bentonite-filled joints (see Figures 4.16 - 4.18). By comparison, for the identical incident S-waves, the frequency partition of transmitted S-waves seldomly changes with the varying water saturation no matter which type of clay filling in the joint.

## 4.4 Discussion

### 4.4.1 The discrepancies in P-wave behaviours across single kaolinite- and bentonite-filled rock joints

Figure 4.5 reveals that the saturation dependence of P-wave velocity across single kaolinite-filled joint is approximately opposite to that across single bentonite-filled rock joints, which could be attributed to the difference in heterogeneity saturation between wet kaolinite and bentonite clays over the tested saturation range (Knight et al., 1998). Particularly, the saturation-velocity behaviour across single kaolinite-filled joints is approximately analogous to the upper bound for P-wave velocity across partially saturated porous media predicted by the Gassmann-Biot model (King et al., 2000). It implies that, for the kaolinite clay, any small heterogeneities in pore-size distribution could cause patchy saturation at the small wavelengths associated with ultrasonic measurements (Knight et al., 1998). Notably, the patchy saturation distribution refers to as that some patches in porous media are partially saturated while others are entirely saturated, where the patchy is on a scale containing many pores (Mavko and Nolen-Hoeksema, 1994). Accordingly, the increasing water saturation results in more pore space fully saturated with water and thus stiffens the compliant regions in the kaolinite clay, increasing the P-wave velocity. In contrast, the saturation dependence of P-wave velocity across individual bentonite-filled rock joints approximately resembles the trend of the lower bound for P-wave velocity in porous media predicted by the Gassmann-Biot model (King et al., 2000). It means that the fluid saturation is homogeneously distributed in the bentonite clay. Specifically, for

the wet bentonite clay, all pores or regions of the pore space prefer to contain both water and air, resulting in an nearly constant saturation at all locations (Knight et al., 1998).

Likewise, the saturation dependence of P-wave attenuation exhibits an approximately opposite relationship between the kaolinite- and bentonite-filled rock joints, as illustrated in Figure 4.6. The discrepancy could also be explained by the difference in heterogeneity saturation between those two clays. Particularly, for the kaolinite with fully saturated pores adjacent to partially saturated elements (i.e., a heterogenous distribution), the increasing water saturation promotes the local flow effect. As a result, more frictional loss due to the water flow relative to clay matrix occurs, increasing wave dissipation in the kaolinite clay and then the total wave attenuation through the kaolinite-filled clay. Nevertheless, when the water saturation degree exceeds 80%, the soft and stiff regions reach an equilibrium, and hence wave transmission becomes dependent on the elastic modulus of the entire kaolinite layer rather than its stiffer regions, the progressively increasing water saturation could also average the soft and hard area to make the kaolinite be more homogenous. Consequently, wave loss due to solid-solid and solid-fluid friction declines with the decreasing viscosity of the kaolinite, resulting in less wave attenuation of P-wave. By contrast, for the bentonite clay with a more homogeneous distribution (i.e., an approximately constant saturation at all locations), the local effect could be neglected. The viscosity of bentonite decreases, which leads to smaller wave energy loss and then more transmitted wave energy across the bentonite-filled joint. However, if the water saturation degree goes over 87.1%, the absorption water could cause the breakage of grain contacts and thus increase the heterogeneities in bentonite, promoting the local flow effect.

Furthermore, Figures 4.7 - 4.10 shows that more significant wave dispersion occurs as P-waves propagates through the kaolinite-filled joint rather than the bentonite-filled joint, especially for 1-MHz input P-waves. Particularly, compared to the intact rock reference, the presence of kaolinite-filled rock joint shifts the frequency range where the transmitted P-wave energy is mainly stored to the higher values (0.9 - 1.5 MHz), whereas the existence of bentonite-filled joint seldom changes the central frequency band. This is mainly due to that the significant inhomogeneity of kaolinite clays induced by water addition leads to the coexistence of slow and fast paths, causing evident wave dispersion of P-waves. As a result, P-waves arrive at slightly different times, blurring the transmitted signals. Furthermore, magnitudes of transmitted wave energy are more sensitive to the changing water saturation when P-wave passes across the kaolinite-filled joint instead of bentonite-filled joint. It could be mainly attributed to the difference in the local flow effect between wet kaolinite and bentonite clays.



The absorption of water results in the permeability reduction of bentonite and then constrains the flow of liquid in bentonite, whereas it enhances heterogeneities of kaolinite clay and thus provides more regions for the occurrence of squirt flow induced by the compression of propagating P-wave. As a result, the addition of water causes significant energy consumption due to the wave-induced squirt flow in the kaolinite while it slightly changes energy of transmitted wave across the infill bentonite layer.

#### 4.4.2 The discrepancies in S-wave behaviours across single kaolinite- and bentonite-filled rock joints

It is found that S-wave velocity across the bentonite-filled joint is faster than that through the kaolinite-filled joint (see Figure 4.11). This could be attributed to the fact that the hydration process makes the wet bentonite clay much more homogenous than the wet kaolinite clay. Accordingly, S-wave velocity across the kaolinite-filled joint is governed by the porosity and shear modulus while that across the bentonite-filled joint is mainly dependent on shear modulus.

According to  $V_s = \sqrt{G/\rho}$ , the decrease in shear modulus results in slower S-wave velocity across the bentonite clay layer, thereby declining the whole wave velocity across the jointed rock sample (Sheriff and Geldart, 1995). Furthermore, S-wave velocity of the bentonite-filled joint is more sensitive to the varying water saturation compared to that of the kaolinite-filled joint regardless of the dominant frequency of input S-wave. For instance, the measured wave velocity of 0.25-MHz S-wave across the bentonite-filled joint decreases by near 5.15 m/s while that across the kaolinite-filled joint reduces by approximately 3.51 m/s as water saturation increases by about 8% (i.e., increasing from 72% to 80% for kaolinite and from 71.4% to 79.1% for bentonite). It is mainly attributed to the fact that the bentonite has a larger surface area than the kaolinite (Li et al., 2017). The larger the accessible surface area of clay particles to the pore fluid, the greater the reduction in shear modulus of clay (Khazanehdari and Sothcott, 2003). Consequently, the shear weakening induced by water absorption has stronger effects on elastic properties of bentonite compared to kaolinite.

Moreover, Figure 4.12 suggests that the critical saturation degree at which the attenuation minimizes depends on the type of infill clay, which is partly consistent with analytical results presented in Albers (2011). It is mainly attributed to that the difference in water-clay interaction between different clay minerals. Figure 4.12 also shows that the transmission ratio of S-wave across the bentonite-filled joint is smaller than that across the kaolinite-filled joint at an

approximately identical water saturation, which is more pronounced for input S-waves at higher frequencies (i.e., 0.5-MHz and 1-MHz S-waves). For example, as 0.5-MHz S-wave passes across the clay-filled joint, the transmission ratio is about 0.036 for the infill bentonite with the saturation degree of 71.4% while it is approximately 0.058 for the infill kaolinite at the saturation degree of 72%. It implies that the bentonite-filled rock joint attenuates more S-wave energy compared to the kaolinite-filled joint. The main explanation is that more wave scattering occurs in the bentonite clay rather than the kaolinite. According to Li et al. (2017), the higher specific surface area of clay it is, the larger volume of associated low-aspect-ratio pores there are. Thus, bentonite owns more pores than kaolinite due to its larger surface area, resulting more scattering of S-wave energy.

Based on the energy-frequency-time distribution of transmitted S-waves (see Figures 4.13 - 4.18), we found that the bentonite-filled joint allows higher-frequency S-wave modes to transmit compared to the kaolinite-filled joint under an approximately identical water saturation degree. By contrast, less S-wave energy could transmit across the bentonite-filled joint rather than the kaolinite-filled joint. Those observations are consistent with findings of transmission ratio for S-waves (see Figure 4.12), which could also be explained by the combined effects of wave attenuation in filling clays and wave refraction at joint surfaces. Changes in wave attenuation due to varying water saturation degree could be explained by three mechanisms. The reduced water content causes that water menisci exhibits stronger contracting forces, but the number of menisci strongly decreases. Consequently, the reduction in the contact area of water menisci weakens the particle linkages while the loss of water molecular film enhances friction and shear resistance between particles. Based on our experimental findings, we suggest that the effects of water saturation on transmitted S-wave energy across single clay-filled rock joints is controlled by a competition between wave transmission at the joint surface and wave attenuation (including dissipation and scattering) in the filling clay layer. We posit that (1) the increase in transmitted S-wave energy is mainly due to the lower viscosity of infill clay that leads to less viscous loss in the infill clay, whereas the following decrease in transmitted S-wave energy results from the enlarged wave impedance contrast between the infill clay and host rock that causes less wave transmission into the joint.

#### 4.4.3 The comparison between P- and S-wave behaviours across single clay-rich soil-filled rock joints

In present study, we found that the effects of single clay-filled rock joints on P-wave attributes are significantly different from those on S-wave characteristics. The discrepancies between P- and S-wave behaviours across individual clay-filled rock joints could be attributed to that propagation of S-waves mainly depends on the properties of skeletal frame while propagation of P-wave is generally governed by the properties of solid material, the skeletal frame and the pore fluid (Leurer, 1997). On one hand, it is found that the saturation dependency of P-wave velocity across the kaolinite-filled joint exhibits an approximately opposite trend to that of the bentonite-filled joint, while the saturation dependency of S-wave velocity is slightly affected by the clay minerals in the rock joint. It could be attributed to that clay softening causes a stronger shear weakening than bulk elastic properties, which plays a more significant role in S-wave velocity. On the other hand, it is observed that the clay-filled rock joint attenuates much more energy of S-waves rather than P-waves (see Figures 4.6 - 4.10 and 4.12 - 4.18), which is consistent with observations of some porous rocks (Lucet and Zinszner, 1992). The effects of water saturation on attenuation of wave at ultrasonic frequencies in filling clay samples are pronounced for S-waves than P-waves, in agreement with theoretical predictions by (Pham et al., 2008). A possible explanation is that, when S-wave propagates through the clay-filled joint, heterogeneities of infill clays at the scale of wavelength cause scattering of S-waves, resulting in high attenuation of S-waves (Johnston et al., 1979). Alternatively, it is likely due to that shear wave splitting could occur as S-waves pass through the clay-filled joint, causing an extrinsic attenuation. To be specific, an arbitrary polarized S-wave at ultrasonic frequencies that enters the anisotropic clay could be split into two polarizations, and then the two split phases could propagate at different velocities and be combined at the other side of the joint into another shear wave with a different shape (frequency content and amplitude) from the incident wave, which could lead to an evidently strong external attenuation of S-waves (Auld, 1973).

In addition, it is found that both of P- and S-wave attributes of single clay-filled rock joints are dependent on the dominant frequency of incident waves. Specifically, for both of P- and S-waves, wave velocity and wave attenuation consistently increase with the dominant frequency. It could be attributed to the fact that the propagation of waves at ultrasonic frequencies is path-dependent. According to the Fermat's principle, for ultrasonic waves passing through a heterogeneous material with high and low compressible regions, a portion of the ultrasonic

pulse prefers to propagate along the incompressible, high-speed regions (Adam et al., 2009). On the other hand, the observed frequency-dependent wave behaviours could be partially explained by the local flow mechanism, especially for wave propagation across the kaolinite-filled joints. Precisely, the fluid flow relative to the clay matrix induced by the propagation of waves at high frequencies has insufficient time to relax (Pham et al., 2008). As a result, the bulk and shear moduli of the infill clay layer are stiffer, leading to faster P- and S-wave velocities. In addition, the enhanced fluid flow relative to solid particles could cause more frictional loss of wave energy.

#### **4.4.4 The physical mechanisms lying behind wave behaviours across single clay-rich soil-filled joints**

The current work reveals that the clay minerals and water saturation play a predominant role in acoustic wave behaviours across single clay-filled rock joints, which could be interpreted via an integration of three physical mechanisms: (1) clay softening, (2) local flow effect and (3) wave reflection and refraction at the rock-clay interface. It is found that the saturation dependence of wave responses to single clay-filled rock joints are predominantly controlled by the infill clay minerals. Specifically, wave attributes of single kaolinite-filled joints are mainly governed by the competition between the squirt flow and softening of kaolinite, while the softening of bentonite plays a predominant role in wave attributes of single bentonite-filled joints, which is more pronounced for propagation of P-wave. The discrepancies in wave properties between kaolinite- and bentonite-filled rock joints is mainly attributed to the difference in the heterogeneity saturation between wet kaolinite and bentonite, which is highly dependent on the clay softening.

From the perspective of soil mechanics, the softening of clay is mainly attributed to the hydration effect (Li et al., 2020). To be specific, the hydration of clays refers to the process that clays absorb water via their characteristic layered structures and then produce strong repulsive forces, which is a complicated physico-chemical procedure consuming surface energy of clays (Karaborni et al., 1996). The hydration is generally classified into two types, including particle-surface hydration and cation hydration. Specifically, the particle-surface hydration reduces surface energy by chemical action while the cation hydration consumes surface energy via contact deformation. Previous studies have found that the hydration of kaolinite clay only occurs at the particle surfaces while the hydration of bentonite simultaneously appears at the particle surface and around the cations, which is mainly

attributed to the difference in their crystal-chemical structures (Bathija et al., 2009). More specifically, the basic structure of kaolinite is a tetrahedral sheet alternating with an octahedral sheet (i.e., 1:1 crystalline structure); thus, the inter-molecular forces are strong enough to prevent the exchange of aluminium cations inside the crystal lattice with other external cations (Aksu et al., 2015). By contrast, the basic unit of montmorillonite (the major component of bentonite) is a 2:1 weakly constrained crystalline structure (i.e., an octahedron sandwiched between two tetrahedrons), resulting in weak bonds between platelets that allow water molecules to be intercalated into the crystalline structure (Lu and Khorshidi, 2015). Consequently, the cation hydration only occurs in the bentonite clay while the particle-surface hydration happens to both kaolinite and bentonite clays. Notably, the particle-surface hydration in bentonite is much stronger than that in kaolinite because of that the specific surface area of montmorillonite is much larger than that of kaolinite (Li et al., 2020). Accordingly, the hydration of bentonite produces a large amount of bound water and thus leads to an approximate homogeneously saturation state of the bentonite clay. By comparison, the hydration of kaolinite is evidently weaker and then most of the adding water exists in the form of free water, causing the patchy saturation of kaolinite clays. In this regard, the local flow effect is more pronounced for kaolinite-filled joint.

## 4.5 Concluding remarks

In this chapter, fluid effects on the low-intensity wave behaviours across individual clay-rich rock joints were quantitatively investigated by conducting a great deal of ultrasonic pulse-transmission tests on a series of synthetic clay-rich rock joints with various degrees of water saturation. The wave velocity, wave transmission and time-frequency-energy distribution of transmitted waves were estimated and elaborated to systematically quantify the role of water saturation in wave responses to single clay-rich rock joints.

The experimental results show that the clay mineral plays a controlling on the saturation dependence of P-wave attributes of single clay-rich rock joints. Specifically, P-wave velocity across single kaolinite-filled rock joints increases and then decreases as water saturation progressively increases. It could be explained by that the heterogeneities within the kaolinite-rich layer are distributed in the form of patchy saturation due to the weak hydration of kaolinite. As a result, the addition of water enlarges the patchy saturation region and thus enhance the squirt flow effect, resulting in a locally increasing bulk modulus and wave velocity. However,

as water saturation exceeds a critical value, the damage of grain contacts occurs and the stiffness of solid skeleton decreases, which conceals the local stiffening caused by the local flow and causes a decrease in wave velocity. In contrast, P-wave velocity across single bentonite-filled rock joints decreases nonlinearly with increasing water saturation. This is mainly attributed to the homogenous saturation distribution within the bentonite-rich layer induced by the strong hydration of montmorillonite. More specifically, water molecules are prone to be intercalated into the basic unit of bentonite and exist in the form of bound water between platelets. Consequently, the addition of water causes thicker water molecule layer and weakens the bonds between bentonite platelets, thereby reducing the bulk modulus and slowing P-wave velocity. On the other hand, P-wave energy transmission across single kaolinite-rich rock joints significantly decreases before increasing with water saturation. The evident decrease in P-wave energy transmission across kaolinite-rich joints could be mainly explained by that the addition of water broadens patchy saturation regions and thus increases the apparent number of contact planes. Accordingly, more wave scattering occurs during the propagation of P-waves, causing an evident decrease in transmitted wave energy. After reaching a minimum, P-wave energy transmission slightly increases with water saturation, which is principally because that the viscous frictions between solids are strongly weakened at high water saturation degrees and causes much less wave energy dissipation. Conversely, P-wave energy transmission across single bentonite-rich rock joints increases and then declines with water saturation. This could be explained by two competing factors: a decrease in frictional loss caused by reducing viscosity and an increase in reflected wave energy due to the weakening joint stiffness. More specifically, the decrease in viscosity induced by water addition firstly dominates and thus improves the total wave energy transmission, whereas the reduction in joint stiffness plays a controlling at high water saturation degrees and declines the overall wave energy transmission across single bentonite-rich rock joints.

The current work also reveals that the clay mineral has a modest effect on the saturation dependence of S-wave attributes of single clay-rich rock joints. Particularly, for both kaolinite- and bentonite-rich rock joints, S-wave velocity across the joint generally decreases with increasing water saturation. It could be explained by that increasing water saturation weakens the bonding between clay platelets and thus reduce the bulk modulus of the skeleton of clay-rich layer. Consequently, S-wave velocity across the clay-rich rock joint slightly decreases with water saturation no matter which clay mineral there is in the joint. On the other hand, for both kaolinite- and bentonite-rich rock joints, S-wave energy transmission increases and then

decreases as the degree of water saturation progressively increases. It could be a result from the trade-off between the decreasing viscosity and stiffness of the clay-rich gouge layer. To be specific, the increase in S-wave energy transmission is due to that the reduction in viscosity of clay-rich layer induced by water addition dominates the overall wave energy dissipation across the clay-rich rock joint within the specific water saturation range. By contrast, at higher water saturation degrees beyond the specific range, the decreasing skeleton stiffness of clay-rich layer caused by the adding water results in much more wave reflection and therefore leads to a decrease in the total S-wave energy transmission across the clay-rich rock joint.

Also, the time-frequency analysis on the received time-domain waveforms unravels the saturation-dependence of wave responses to single clay-rich rock joints in the frequency domain. On one hand, the dominant frequency range gradually shifts towards higher values and then slightly declines with increasing water saturation as P-wave passes through single kaolinite-rich rock joints, whereas the approximately opposite trend of the dominant frequency band is observed from P-wave propagation across individual bentonite-rich rock joints. Additionally, regardless of the clay mineral, the central frequency band generally goes down as water saturation increases for the passing of S-waves. These observations are in accordance with the findings of the saturation-dependent wave velocities across single clay-rich rock joints. On the other hand, as water saturation progressively increases, the magnitudes of power within the dominant frequency range evidently decline and then increase for P-wave transmitted across individual kaolinite-rich rock joints while those for P-wave transmitted across single bentonite-rich rock joints exhibit nearly opposite variations. Besides, independent of the filling clay mineral, the magnitudes of power within the central frequency band increase and then decrease with water saturation when S-wave propagates through single clay-rich rock joint. The observed variations in the magnitudes of power within the central frequency band resemble the saturation dependent transmission ratio across single clay-rich rock joints. These saturation-dependences of the frequency contents and energy partitions for different clay-rich rock joints further suggest that wave behaviours across single clay-rich rock joints could be concurrently affected by the local flow effect, the viscous friction and the clay hydration of the filling clay-rich gouges.

The results in this study focus mainly on acoustic wave behaviours across single clay-rich soil-filled rock joints at ultrasonic frequencies, which may not be directly applicable for seismic exploration and sonic logging but are instructive for the interpretation of field-observed acoustic data on characterizing and monitoring the subsurface rock discontinuities. On the other

hand, the findings of the water-dependent wave attributes through single clay-rich soil-filled rock joints not only compensate for the lack of laboratory documents on the fluid effects on the interaction of seismic waves and clay-rich soil-filled rock joints but also could provide additional insights into the development of theoretical models for describing acoustic wave propagation and attenuation across filled rock joints.



# CHAPTER 5      FLUID EFFECT ON LOW-INTENSITY WAVE BEHAVIOURS ACROSS INDIVIDUAL FLUID-FILLED ROCK JOINTS

## 5.1 Introduction

In chapter 4, the significant influences of fluids on wave attributes of individual clay-rich soil-filled rock joints have been well determined by conducting massive ultrasonic measurements, enhancing the understanding of fluid effects on wave behaviours across rock joints filled with the mixture of fluids and solid geomaterials. However, compared to the rock joints filled with the dry or wet geomaterials, the understanding of wave behaviours across the rock joints filled with fluids is still at its infancy. To date, the interaction of seismic waves and fluid-filled rock joints has been a hotspot of geophysics and rock mechanics because it is of great importance to many kinds of practical engineering applications, such as reservoir detection and characterization, geothermal exploration and extraction, underground engineering appraisal, exploration seismology and earthquake engineering (Soma et al., 2000, Chavarria et al., 2003, De Matteis et al., 2008, Reshetnikov et al., 2010), Reiser et al., 2020).

The state-of-the-art review in chapter 2 indicates that a few studies have been conducted on wave properties of fluid-filled rock joints. Nevertheless, the effects of some important factors, including filling fluid parameters (e.g., type, composition and distribution), joint features (such as joint orientation and joint roughness), and external conditions (e.g., temperature and stress state), on the interaction of seismic waves and fluid-filled rock joints are still not well understood. Therefore, it is necessary to further investigate wave behaviours through fluid-filled rock joints.

In this chapter, a great deal of UPT tests is carried out to examine compressional wave propagation and attenuation across individual fluid-filled rock joints. Particularly, the influences of infill fluid type and composition, joint orientation and thermal conditions on P-wave attributes of single fluid-filled rock joints, including wave velocity, frequency spectra, transmission coefficient and attenuation quality factor  $Q$ , are quantified based on the laboratory

data. The physical mechanisms lying behind the experimental results are further analysed and discussed in terms of acoustic properties of rock discontinuities and filling fluids.

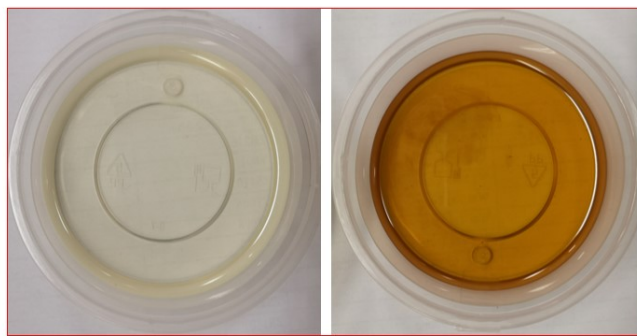
## 5.2 Experimental procedure

### 5.2.1 Specimen description

#### 5.2.1.1 Infill fluid specimens

In this experiment, filling fluids include air, distilled water and two types of light oils, i.e., Shell Morlina S2 BL10 and Shell Tellus S2 M68 (see Figure 5.1a). For convenience, Shell Morlina S2 BL10 and Shell Tellus S2 M68 are abbreviated to BL10 and M68 respectively in this study. The properties of different fluids at room temperature are shown in Table 5.1, among which attributes of two light oils were measured carefully in the laboratory (Cengel and Boles, 2007, Street et al., 1996). Furthermore, according to the method suggested in ASTM Standard D445 (2006), the kinematic viscosities of the water and M68 at different temperatures were measured using a rheometer (model MCR 702) in the laboratory, which are tabulated in Table 5.2.

(a).



Shell Morlina S2 BL10      Shell Tellus S2 M68

(b).

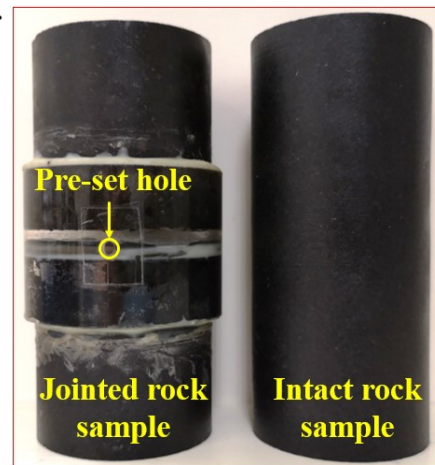


Figure 5.1 Materials used in this study: (a) Light oils, (b) Gabbro rock specimens.

#### 5.2.1.2 Rock specimens

According to the method described in chapter 4 (see section 4.2), a rock specimen with a single planar joint at its midplane was manufactured using the black gabbro rock from Shanxi, China (see Figure 5.1b). The lithological, mechanical and physical properties of black gabbro have been given in chapter 4 (see section 4.2). Herein, the length of the artificially jointed rock

specimen was measured to be around 106 mm, and hence the thickness (aperture) of the artificial joint sandwiched between two rock cylinders was about 6 mm. Using the artificial open joint, a series of fluid-filled rock joints could be generated by injecting fluids into the joint aperture through the pre-set hole on the tube. To quantitatively analyse wave responses to fluid-filled rock joints, an intact rock sample with the same size as the jointed rock sample was prepared to obtain reference data (see Figure 5.1b). Note that end surfaces of all cylindrical rock specimen used in this study were ground flat, smooth and parallel within 0.01mm.

Table 5.1 Properties of filling fluids at room temperature (about 20 °C)

Fluids	Density (kg/m <sup>3</sup> )	Viscosity (kg/m·s)
Air *	1.204	$1.825 \times 10^{-5}$
Water ++	998.2	$1.002 \times 10^{-3}$
Shell Morlina S2 BL10	872.5	$31.86 \times 10^{-3}$
Shell Tellus S2 M68	875.1	$178.3 \times 10^{-3}$

\* Adopted from Cengel, A. (1998). ++ Adopted from Vennard, J.K. (2013).

Table 5.2 Kinematic viscosities of water and M68 (light oil) at different temperatures

Temperature (°C)	Kinematic viscosity (mm <sup>2</sup> /s)	
	Water	M68
10	1.31	364.53
20	1.00	203.78
30	0.80	124.11
40	0.66	83.89
50	0.55	60.16
60	0.47	47.65
70	0.41	--
80	0.36	--

### 5.2.2 Test programme

The present experiment was composed of two parts. One part aimed to examine the influences of fluid types and compositions as well as joint orientation, while the other intended to determine the thermal effect on ultrasonic P-wave behaviours across fluid-filled joints.

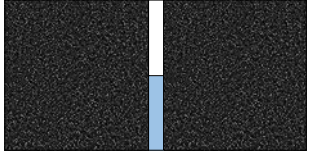
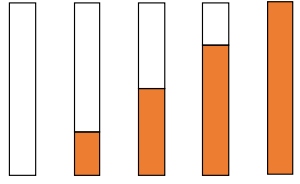
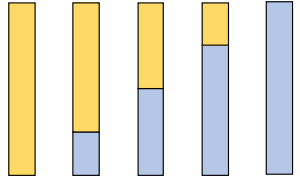
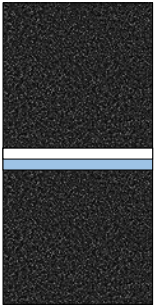
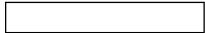









#### 5.2.2.1 The UPT tests for determining the influences of joint parameters

In this part, various filling conditions of single fluid-filled rock joints were tested to determine the effects of fluid types and compositions as well as joint orientation, as listed in Table 5.3. Specifically, three types of liquids, i.e., water, BL10 and M68, were injected into the joint in different combination modes to prepare multiple fluid-filled joints (with clear fluid stratification rather than mixed fluid). For clarity, all testing cases can be divided into two groups, i.e., group A for the single-liquid filled joint that is filled with air and one kind of liquid (water, BL10 or M68), and group B for the dual-liquid filled joint that is fully filled with two kinds of liquids among water, BL10 and M68.

Since the joint spatial orientation might affect the distribution and stratification of fluids in the joint, fluid-filled joints at both vertical and horizontal orientations (corresponding to joint dip angles of  $90^\circ$  and  $0^\circ$ , respectively, for in-situ condition) were tested in each group. Herein, the loading system and the rock sample were horizontally placed when studying wave propagation across vertical fluid-filled rock joints. In comparison, to measure wave attributes of horizontal fluid-filled rock joints, both the loading system and the rock sample were vertically arranged.

Furthermore, two types of incident waves with central frequencies of 100 kHz and 1 MHz were applied to study the effects of incident wave bandwidth on wave propagation and response through individual fluid-filled rock joints. To guarantee the repeatability and effectivity of all the above testing cases in this study, five tests were conducted for each case to minimize the system noises and operation errors. Besides, a cylindrical aluminium sample of the same dimensions was also prepared, which would be used to provide the reference frequency spectra for effective evaluation and analysis of wave attenuation in jointed rock samples.

Table 5.3 Horizontal and vertical fluid-filled joints under different filling conditions tested in this study

Types of jointed rock sample	Single-liquid filled joints	Dual-liquid filled rock joints	Fluid filling conditions
 <p>Rock sample with single vertical fluid-filled joint</p>	 <p>V1 V2 V3 V4 V5</p>	 <p>V6 V7 V8 V9 V10</p>	<p>V1 &amp; H1: <math>P_W</math> (or <math>P_O</math>) = 0%</p> <p>V2 &amp; H2: <math>P_W</math> (or <math>P_O</math>) = 25%</p> <p>V3 &amp; H3: <math>P_W</math> (or <math>P_O</math>) = 50%</p> <p>V4 &amp; H4: <math>P_W</math> (or <math>P_O</math>) = 75%</p> <p>V5 &amp; H5: <math>P_W</math> (or <math>P_O</math>) = 100%</p>
 <p>Rock sample with single horizontal fluid-filled joint</p>	<p>H1 </p> <p>H2 </p> <p>H3 </p> <p>H4 </p> <p>H5 </p>	<p>H6 </p> <p>H7 </p> <p>H8 </p> <p>H9 </p> <p>H10 </p>	<p>V6 &amp; H6: <math>P_W = 0\%</math>, <math>P_O = 100\%</math></p> <p>V7 &amp; H7: <math>P_W = 25\%</math>, <math>P_O = 75\%</math></p> <p>V8 &amp; H8: <math>P_W = 50\%</math>, <math>P_O = 50\%</math></p> <p>V9 &amp; H9: <math>P_W = 75\%</math>, <math>P_O = 25\%</math></p> <p>V10 &amp; H10: <math>P_W = 100\%</math>, <math>P_O = 0\%</math></p>

**Note:**  $P_W$  and  $P_O$  represent the volume contents of water and oil relative to the whole volume the open rock joint, respectively.

### 5.2.2.2 The UPT tests for determining the influences of temperature

The main objective of this part was to study the thermal effects on low-intensity P-wave behaviours across single fluid-filled rock joints. Herein, water increasing from 10 °C to 80 °C at an interval of 10 °C was injected into the open joint to simulate a series of water-filled joints. Similarly, the light oil, Shell Tellus S2 M68 (abbr. M68 in this paper, which is produced by the Royal Dutch Shell PLC), increasing from 10 °C to 60 °C at an interval of 10 °C, was injected into the empty joint to simulate different oil-filled joints. Table 5.4 summarizes test conditions of the fluid-filled rock joints under a typical range of laboratory temperatures. It should be mentioned that the fluid-filled joint under a certain condition was tested for five times to guarantee the repeatability of the ultrasonic measurements.

**Table 5.4 Rock joints filled with fluid (water or M68) at different temperatures**

Types of fluid-filled joints	Temperatures of filling fluids (°C)							
Water-filled joints	10	20	30	40	50	60	70	80
M68-filled joints	10	20	30	40	50	60	--	--

## 5.3 Results and analysis

### 5.3.1 Typical transmitted waveforms

#### 5.3.1.1 Transmitted waveforms for fluid-filled rock joints with different fluid compositions and spatial orientation

Figure 5.2 presents the selected transmitted pulses for 100-kHz and 1-MHz incident P-waves propagation across rock samples with single-liquid filled joints. Herein, single-liquid filled joint refers to the joint filled with air and one kind of liquid (i.e., water, BL10 or M68 in this study), which can be classified into water-, BL10- and M68-filled joints. For rock samples containing vertical single-liquid filled rock joints (Figures 5.2a and 5.2c), it is found that increasing liquid content results in a decrease in the arrival time and an increase in the magnitudes of transmitted waves. Compared to the arrival time, amplitudes are much more sensitive to the change in liquid content. For rock samples having horizontal single-liquid filled joints (Figures 5.2b and 5.2d), similar variations of the arrival time and magnitudes of transmitted pulses caused by an increase in liquid content are observed when liquid content in

the joint is larger than 50%. In contrast, transmitted signals remain almost constant with increasing liquid content if liquid content is lower than 50%. Moreover, Figure 5.2 shows that water results in slightly greater amplitudes of transmitted waves through jointed rock sample compared to light oils.

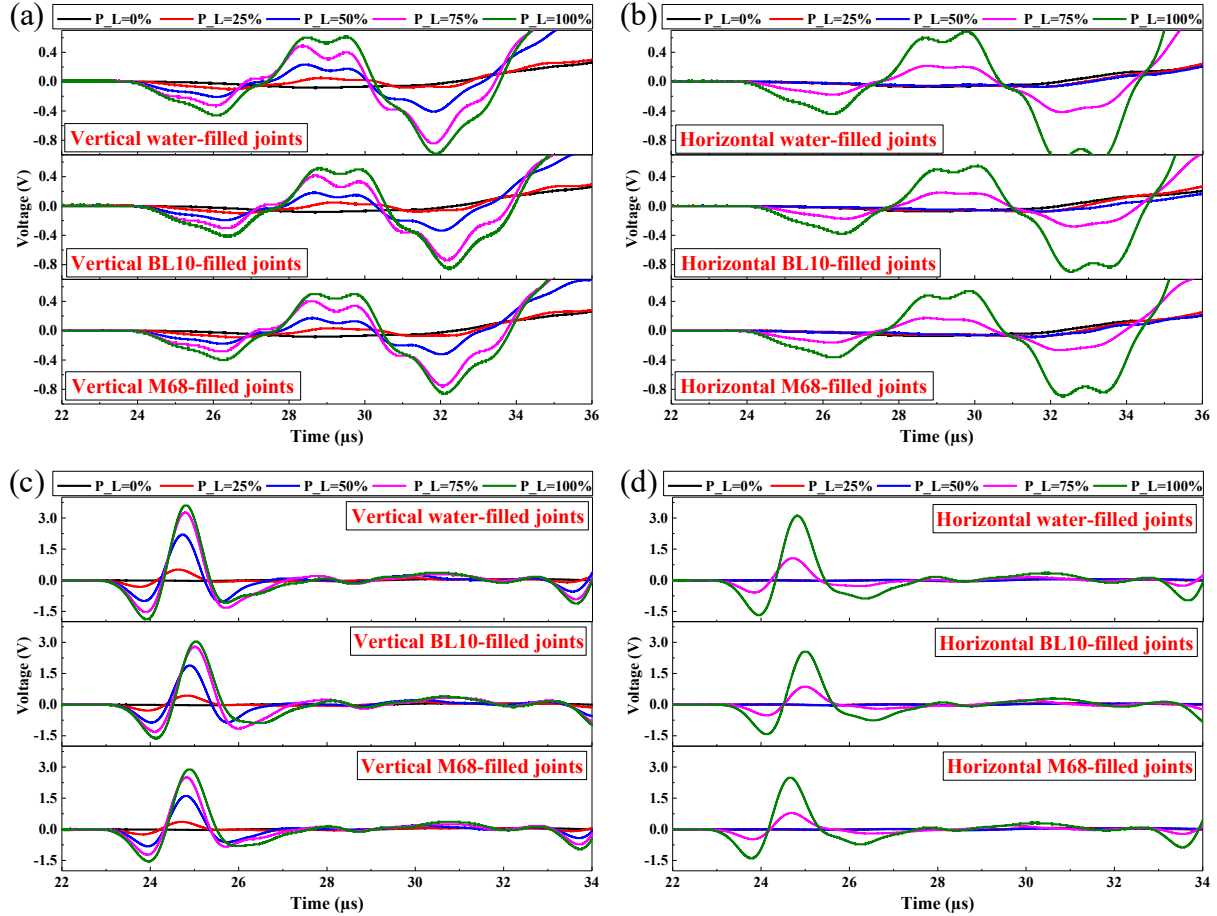


Figure 5.2 Selected transmitted waveforms for P-waves propagation through rock samples with single-liquid filled joints: 100-kHz input waves across (a) vertical and (b) horizontal joints; 1-MHz input waves across (c) vertical and (d) horizontal joints.

Figure 5.3 illustrates a series of typical transmitted signals for 100-kHz and 1-MHz input P-waves propagation across rock samples with dual-liquid filled joints. Herein, dual-liquid filled rock joints could be divided into two categories, including water-BL10 filled joint that is fully filled with water and BL10, and water-M68 filled joint that is entirely filled with water and M68. It is shown that increasing water content in both water-BL10 and water-M68 filled joints leads to shorter travel time and greater amplitudes. Besides, water-M68 filled joints results in smaller amplitudes of transmitted waves compared to water-BL10 filled joints when water content is fixed. In addition, no clear differences in transmitted waveforms across vertical and

horizontal dual-liquid filled joints are observed, which is significantly different from the effects of joint orientation on transmitted pulses across single-liquid filled rock joints.

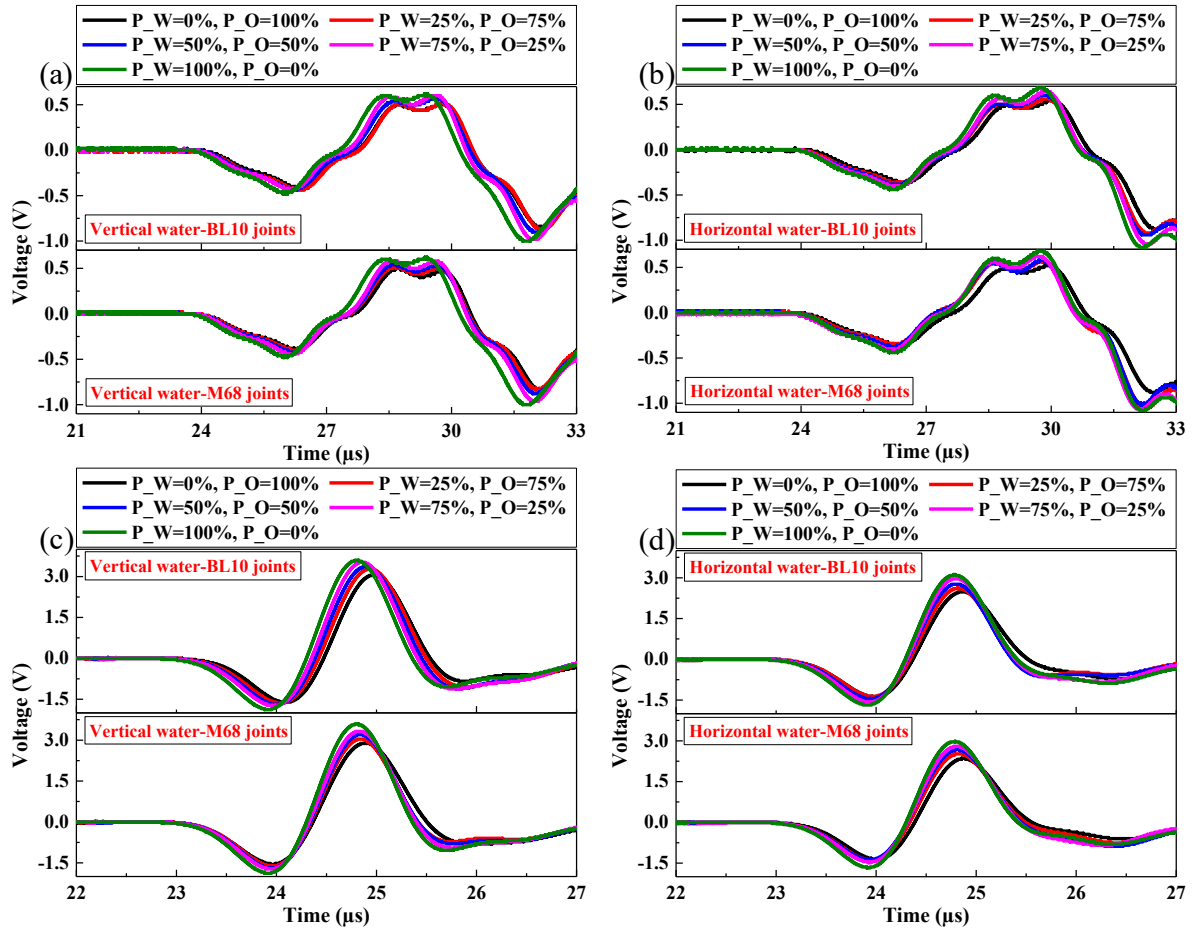


Figure 5.3 Selected transmitted waveforms for P-waves propagation through rock samples with dual-liquid filled joints: 100-kHz input waves through (a) vertical and (b) horizontal joints; 1-MHz input waves through (c) vertical and (d) horizontal joints.

### 5.3.1.2 Transmitted waveforms for fluid-filled rock joints under different thermal conditions

Figure 5.4 presents some typical waveforms of transmitted pulses across individual fluid-filled rock joints under different thermal conditions. It shows that the arrival time and magnitudes of waveforms vary with changing temperature regardless of infill fluid type, whereas the thermal-dependent wave behaviours across rock joints rely on the type of infill fluid. The detailed analyses of those laboratory data are provided in the following contents.



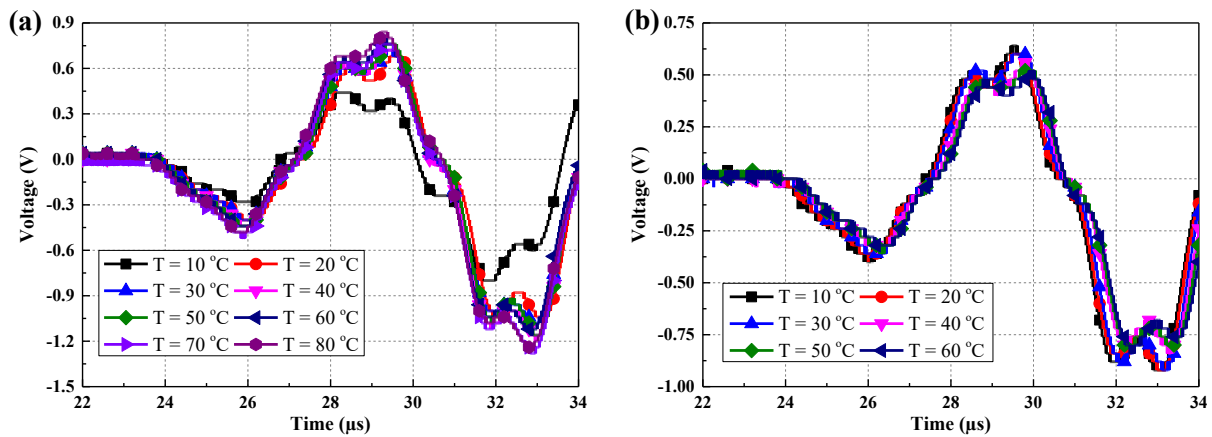


Figure 5.4 The typical waveforms of transmitted pulses through jointed rock samples with: (a) single water-filled joints; and (b) single M68-filled joints under different thermal conditions.

### 5.3.2 Effects of fluid type and composition on wave behaviours across single fluid-filled rock joints

#### 5.3.2.1 Wave velocity

Figure 5.5 shows the average wave velocities of single-liquid filled rock joints and corresponding jointed rock samples for incident P-waves with different central frequencies (i.e., 100 kHz and 1 MHz). Herein, single-liquid filled joints refers to the joints filled with air and one kind of liquid (i.e., water, BL10 or M68 in this study), including water-, BL10- and M68-filled joints.

Figures 5.5a and 5.5b illustrate that wave velocity of vertical water-filled joint increases with increasing volume content of filling water. Similar variations of wave velocities for light oil-filled rock joints and their corresponding jointed samples with increasing filling light oil content are also observed in Figures 5.5a and 5.5b. In addition, for horizontal single-liquid filled joints, increasing volume content of filling liquid evidently leads to an increase in wave velocity when the liquid content is larger than 50%, as shown in Figures 5.5c and 5.5d. The above observations indicate that, in most circumstances, higher filling liquid content in the joint results in higher wave velocity across the joint. On the one hand, the Wood's law demonstrates that the effective bulk modulus of air-liquid layer is inversely proportional to the air volume content (Wood and Lindsay, 1956). Consequently, a higher liquid volume content, i.e., a decreasing air volume content, highly increases the bulk modulus of the joint, causing

faster compressional wave velocity across the air-liquid filled joint. On the other hand, filling liquid introduces viscous coupling between two joint surfaces due to the inertia of liquid, thereby increasing bulk modulus of the joint (Pyrak-Nolte et al., 1990). The more filling liquid there is, the more significant viscous effect between rock matrix and the joint it is. Accordingly, a higher liquid content leads to an increase in bulk modulus of the joint, causing a fast wave velocity.

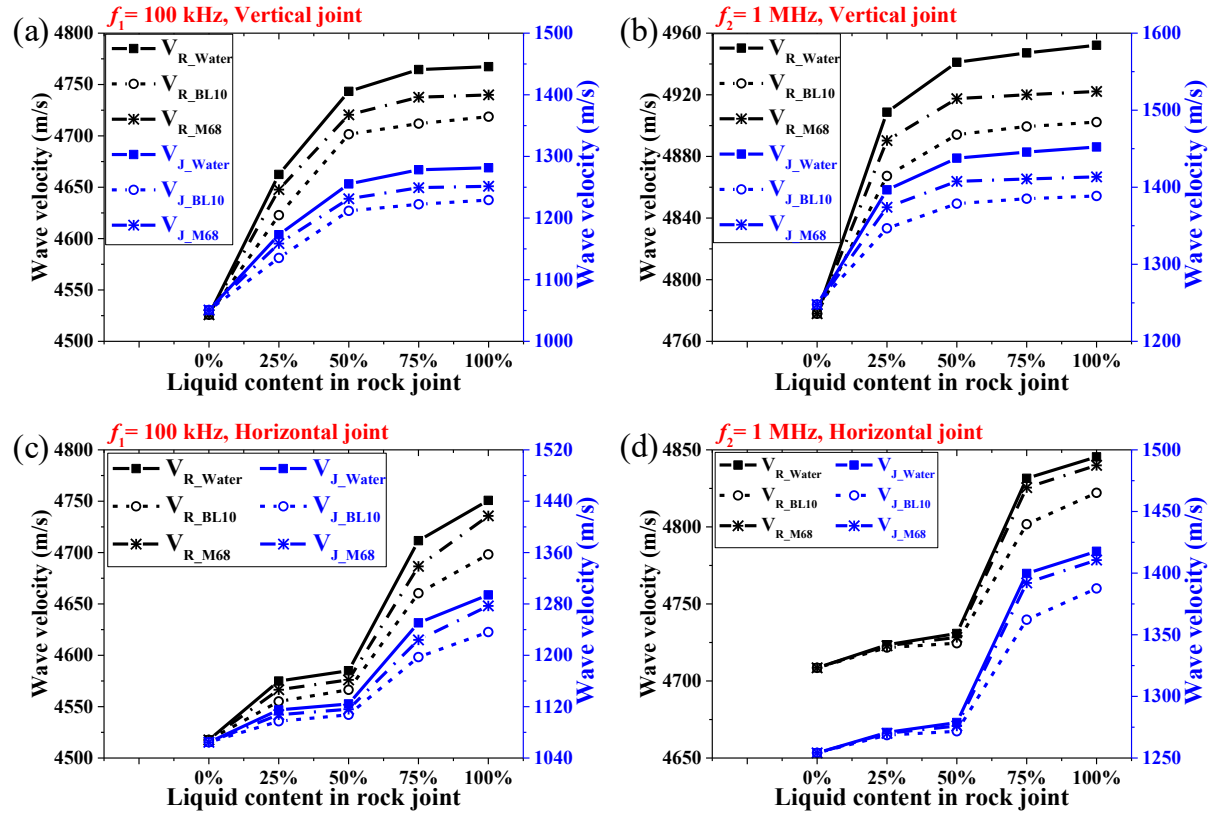


Figure 5.5 The average wave velocities in single-liquid filled rock joints and corresponding jointed rock samples: (a) and (b) For 100-kHz and 1-MHz incident P-waves across vertical joints, respectively; (c) and (d) for 100-kHz and 1-MHz incident P-waves across horizontal joints, respectively. Herein, R and J represent the rock sample and joint, respectively.

Moreover, Figure 5.5 reveals that wave velocity of water-filled rock joint is higher than that of light oil-filled rock joint. This is mainly because that acoustic wave propagates faster in water due to its relatively larger bulk modulus of elasticity compared with light oils used in this study (see Table 5.1) (Wang and Nur, 1990). It is also found that filling M68 in the joint results in a slightly higher wave velocity across the joint compared to BL10. This is because that viscosity of M68 is about six times larger than that of BL10 while the difference between their densities is negligible (as shown in Table 5.1). Consequently, filling M68 results in more significant

coupling between rock matrix and the joint, thereby causing greater bulk modulus of the filled rock joint (Wang and Nur, 1991). Besides, Figure 5.5 demonstrates that liquid content in the single-liquid filled joint has more significant effects on wave velocity compared with the type of filling liquid, which could be explained by the fact that bulk modulus of the joint varies drastically with volume content of filling liquid.

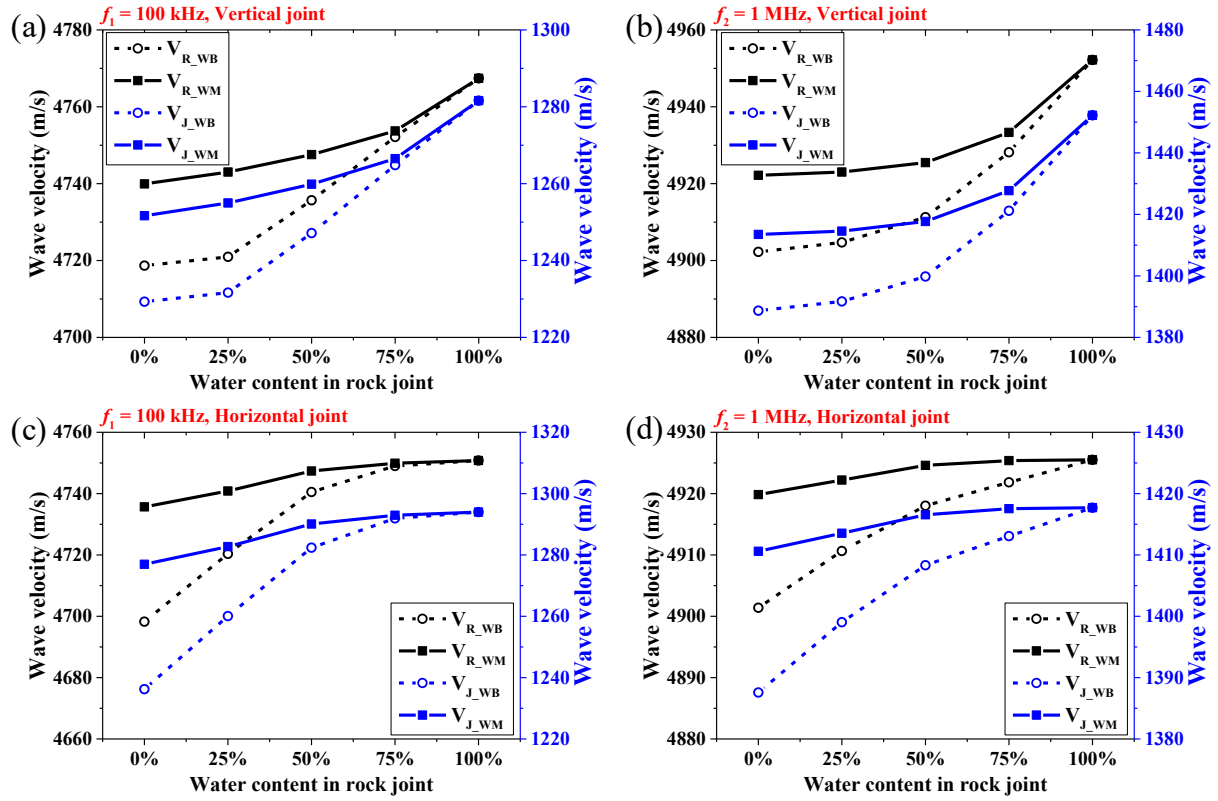


Figure 5.6 The average wave velocities in dual-liquid filled rock joints and corresponding jointed rock samples: (a) and (b) For 100-kHz and 1-MHz incident P-waves across vertical joints, respectively; (c) and (d) for 100-kHz and 1-MHz incident P-waves across horizontal joints, respectively. Herein, R and J represent the rock sample and joint, respectively.

Figure 5.6 shows wave velocities across dual-liquid filled joints and the corresponding jointed rock samples at different wave frequencies (i.e., 100 kHz and 1 MHz). In this study, dual-liquid filled rock joints are divided into two categories, i.e., water-BL10 filled joint that is fully filled with water and BL10, and water-M68 filled joint which is fully filled with water and M68. As water content in the dual-liquid joint increases, a nonlinear increase in wave velocity could be observed. Additionally, wave velocity of water-M68 filled joint is higher than that of water-BL10 filled joint. It is mainly due to that the bulk modulus of M68 is larger than that of BL10, causing higher bulk modulus of the water-M68 layer compared to the water-BL10 layer. These findings further indicate that filling water results in higher wave velocity of rock joint

compared to light oils, while filling M68 instead of BL10 could lead to faster wave propagation across the joint.

Results in Figures 5.5 and 5.6 indicate that different from single-liquid filled rock joints, the increase in wave velocity across dual-liquid filled joints with changing liquid composition in the joint is small. It is probably because that, compared with single-liquid filled joints, dual-liquid filled joints are always fully filled with liquids. Thus, variation of filling liquid composition has small effects on the bulk modulus and density of the filled joint. Moreover, tendencies of wave velocity in jointed rock samples resemble those of wave velocity across their corresponding fluid-filled rock joints, implying that wave velocity of jointed rock masses is dominated by individual fluid-filled rock joints.

### 5.3.2.2 Transmission ratio

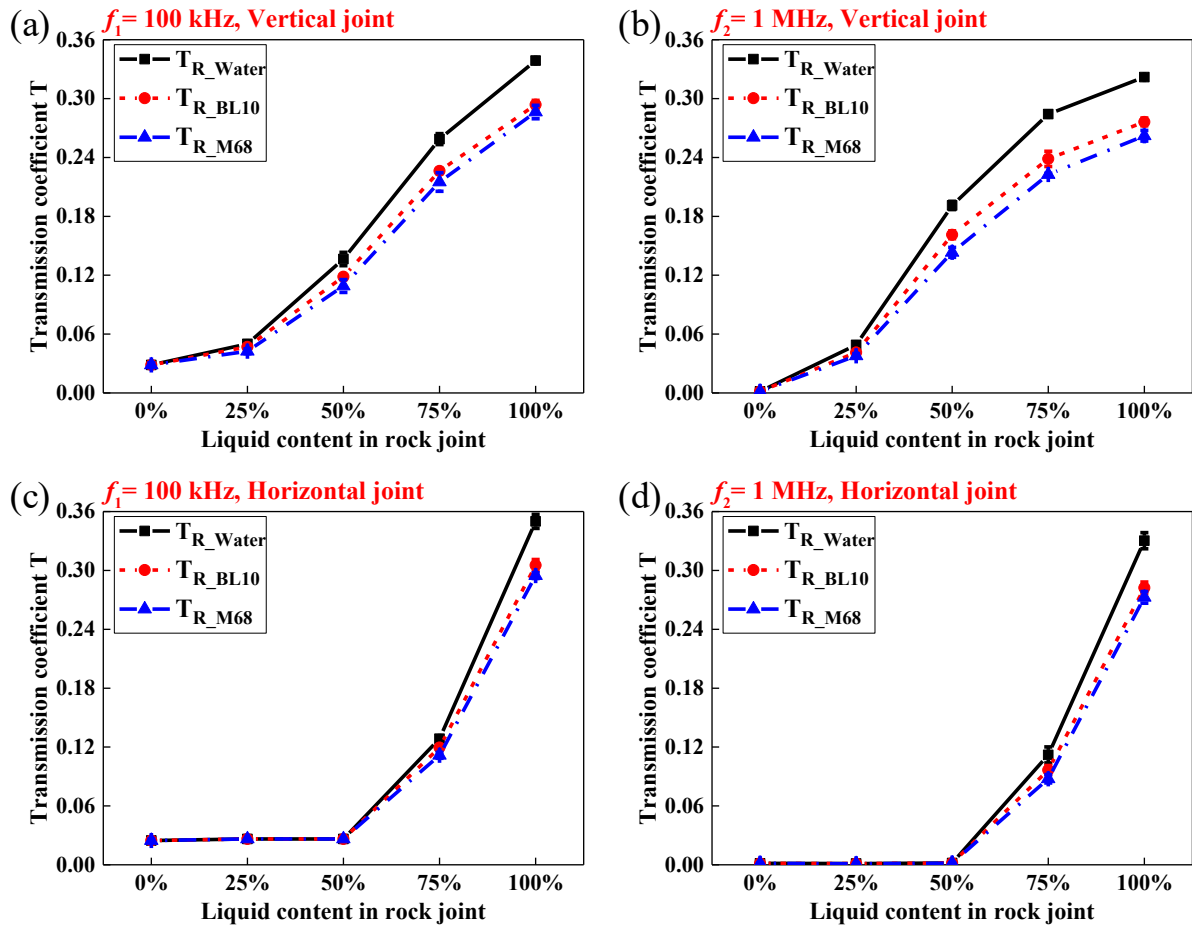


Figure 5.7 Transmission ratios for rock samples with single-liquid filled rock joints: (a) and (b) For 100-kHz and 1-MHz incident P-waves across vertical joints, respectively; (c) and (d) for 100-kHz and 1-MHz incident P-waves across horizontal joints, respectively.

The calculated transmission ratios for P-wave propagation through the single-liquid filled joints as a function of liquid content in the joint are plotted in Figure 5.7. Figures 5.7a and 5.7b illustrate that increasing water content in vertical rock joints significantly improves wave transmission across the joint. The similar trends of transmission coefficients across M68- and BL10-filled joints caused by the growth of liquid content were also observed. In addition, under certain conditions, the larger filling liquid content in horizontal rock joints could also results in more wave transmission, as shown in Figures 5.7c and 5.7d. The main reason for these findings is that wave impedance of air is much lower than those of rock matrix and filling liquid (Winkler and Murphy III, 1995). Thus, wave reflection at the air-rock interface decreases by the reducing interface area due to the increase of filling liquid content. Besides, the specific stiffness of the joint increases with the growth of fractional contact area between liquid and rock matrix caused by the rising liquid content, which could enhance wave transmission across the joint (Petrovitch et al., 2014).

Figure 5.7 also reveals that transmission coefficients across water-filled rock joints are larger than those across light oil-filled joints under the same liquid content. It is because more wave transmission occurs at the water-rock interface due to the larger wave impedance of water compared to light oils (Zhu et al., 2011). Note that the wave impedance of a fluid is the product of wave velocity and density. Besides, energy loss of wave is less in water rather than oils because of smaller viscosity of water. Consequently, filling water results in larger transmission coefficients of wave across the whole joint. Additionally, at a given liquid content, transmission coefficient is slightly larger when the joint is filled with BL10 rather than M68. It is mainly because that the viscosity of BL10 is evidently lower than that of M68 (see Table 5.1). Although a little more wave energy could transmit through the M68-rock interface compared to the BL10-rock interface, the increment is very small due to the tiny difference in wave impedance between those two oils. Since BL10 has a much smaller viscosity than M68, more wave energy can travel through BL10 rather than M68, which might compensate for the increment induced by the difference in wave impedance. Thus, filling BL10 leads to the larger total wave transmission across the joint.

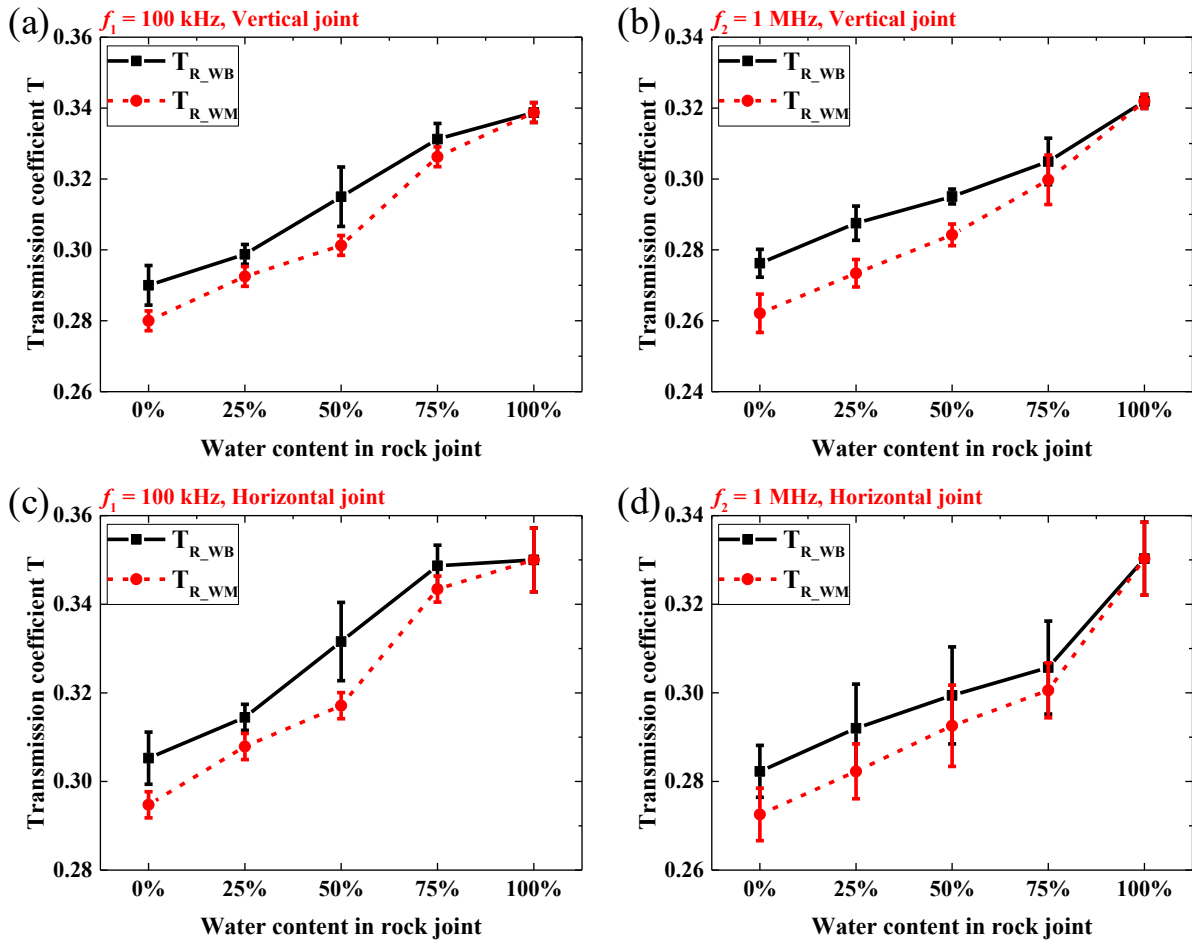


Figure 5.8 Transmission ratios for rock samples with dual-liquid filled rock joints: (a) and (b) For 100-kHz and 1-MHz incident P-waves across vertical joints, respectively; (c) and (d) for 100-kHz and 1-MHz incident P-waves across horizontal joints, respectively.

Figure 5.8 illustrates transmission coefficients for P-wave propagation through the dual-liquid filled joints as a function of water content. It is found that increasing water content in dual-liquid filled joints results in higher transmission coefficients, indicating that water allows more wave to transmit through the joint compared to light oils. In addition, at a given water content, transmission coefficients are slightly larger when BL10 rather than M68 exists in the joint, implying that BL10 allows more wave transmission compared to M68. These findings are consistent with the discrepancies in wave transmission between different single-liquid filled joints observed from Figure 5.7. One possible explanation is that the wave impedance of water is greater than that of light oils used in this study. Specifically, the difference between wave impedances of rock matrix and water is the smallest, thus more wave energy transmits across the rock-water interface of the joint (Zhu et al., 2011). Apart from that, it could also be attributed to the contrast in liquid viscosity (Wood and Lindsay, 1956, Fehler, 1982, Place et

al., 2016). Viscosity of water is smallest among these three liquids, and viscosity of M68 is much greater than that of BL10, as shown in Table 5.1. Consequently, filling water results in the lowest wave absorption in the joint. Besides, BL10 leads to less wave energy loss across the joint compared to M68.

### 5.3.2.3 Frequency spectra

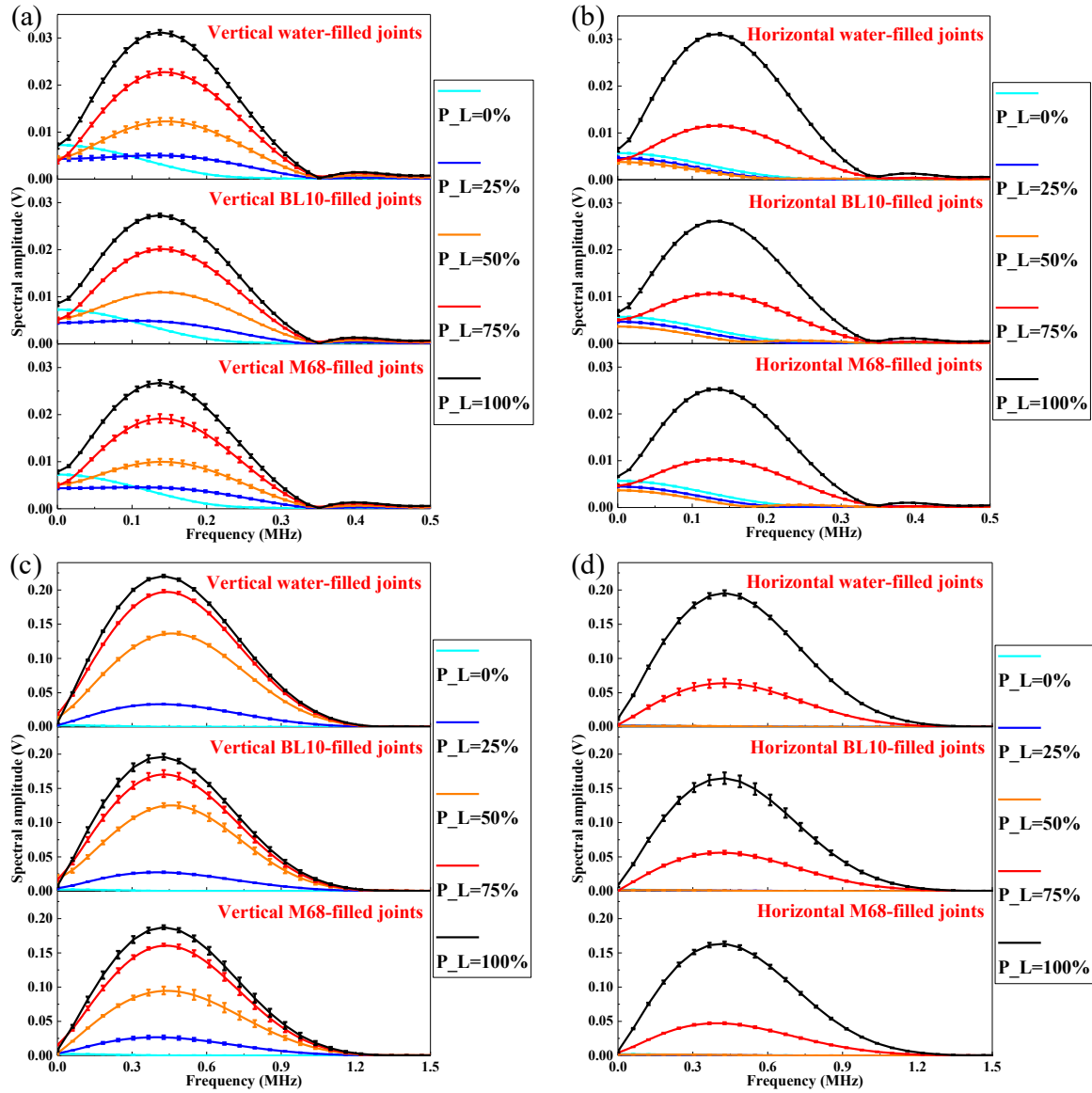


Figure 5.9 Frequency spectra of transmitted waves through rock samples with different liquid volume content in single-liquid filled joints: 100-kHz P-waves across (a) vertical and (b) horizontal joints; 1-MHz P-waves across (c) vertical and (d) horizontal joints. Note that the single-liquid filled joint is filled with one kind of liquids among water, BL10 and M68. For water-filled joints,  $P_L$  represents volume content of water; for BL10-filled joints,  $P_L$  stands for volume content of BL10; for M68-filled joints,  $P_L$  refers to volume content of M68.



In addition, Figures 5.9a and 5.9c show that the dominant frequency slightly shifts to a greater value with the increase of liquid content when waves propagate through the vertical air-liquid filled joints. It is likely due to that the increasing liquid content results in an increase in the area of liquid-rock interface, causing more wave modes at high frequencies transmitting across the joint. The similar shape of frequency spectra and changes in the dominant frequency are observed for horizontal air-liquid filled joints with liquid contents of 75% and 100%, as illustrated in Figures 5.9b and 5.9d. It is because that, like vertical joints containing liquids, horizontal joints with liquid content of 75% and 100% result in the connection between two joint surfaces through the filling liquid, generating the liquid-rock interface at all joint boundaries. As a result, waves mainly transmit into the joint through the liquid-rock interface at the joint surfaces. Consequently, the received transmitted pulses are mainly dependent on properties and volume contents of filling liquid. By comparison, Figures 5.9b and 5.9d show that the frequency spectra for horizontal joints with liquid contents of 25% and 50% are noticeably different from the above cases, which resemble the frequency spectrum for the horizontal joint without liquids (i.e., air-filled joints). It is because that, similar with the air-filled joint (i.e., liquid content is 0%), the free surface (i.e., air-rock interface) exists in horizontal joints with liquid contents of 25% and 50%. To be specific, filling liquid only adheres to one joint surface while it cannot reach another one for the liquid volume content of 25% or 50%. Thus, when waves impinge on those joints, the joint surface without liquid would function as a free surface to reflect almost all incident wave energy. It is worthy to notice that a very small portion of wave may propagate along the surface of PMMA tube enclosed the joint. Accordingly, for horizontal joints with liquid contents of 0%, 25% and 50%, the frequency spectra of transmitted signals presumably result from surface waves transmitted by the PMMA tube. Additionally, Figure 5.9 demonstrates that the type of filling liquid seldomly affects the dominant frequencies of spectra. It is likely due to that the difference in wave impedances among three liquids used in this study is small.

Figure 5.10 shows spectral contents of transmitted P-waves through dual-liquid filled joints with different liquid compositions. It is observed that an increase in water content leads to larger spectral amplitudes of transmitted waves across water-oil filled rock joints. The explanation is that which is mainly attributed to the larger wave impedance and lower viscosity of water compared to oils. Besides, Figure 5.10 reveals that the type and fraction of filling liquid exert few influences on the dominant frequencies and shapes of frequency spectra when waves propagate across the joint filled with water and one kind of oil. It is because that all dual-



liquid filled joints are always fully saturated with liquids, causing entirely coupling between two joint surfaces through the filling liquids. Changes in liquid types and volume contents have fewer effects on wave impedance of the effective water-oil layer. Consequently, wave transmission across joints filled with the water-oil layer slightly changes, thereby scarcely altering the shape of frequency spectra. That is likely due to that more high-frequency wave modes can transmit through liquid rather than air.

To further understand effects of fluid type and composition in rock joints on spectral contents, the maximum amplitudes of frequency spectra in Figures 5.9 and 5.10 were summarized in Table 5.5. It shows that, for single-liquid filled joints at a given liquid content, the maximum amplitudes of transmitted waves across water-filled joints are the largest, followed by BL10-filled joints. Additionally, for dual-liquid filled joints with the same water content, joints containing BL10 result in larger maximum amplitudes compared to those filled with M68. These findings indicate that filling water allows more wave energy transmission across the rock joint compared to BL10 and M68, while BL10 transmits more wave energy than M68, which are consistent with results in Figures 5.9 and 5.10. The explanation is that water has a larger impedance and smaller viscosity than light oils, resulting in more wave energy transmission across the joint. Besides, since the difference in impedance between M68 and BL10 is very small, their viscosities highly determine the discrepancy in total wave energy transmitted through joints. Moreover, compared with the dominant frequency, spectral amplitudes of transmitted waves become more sensitive to type and composition of filling liquid in the joint.

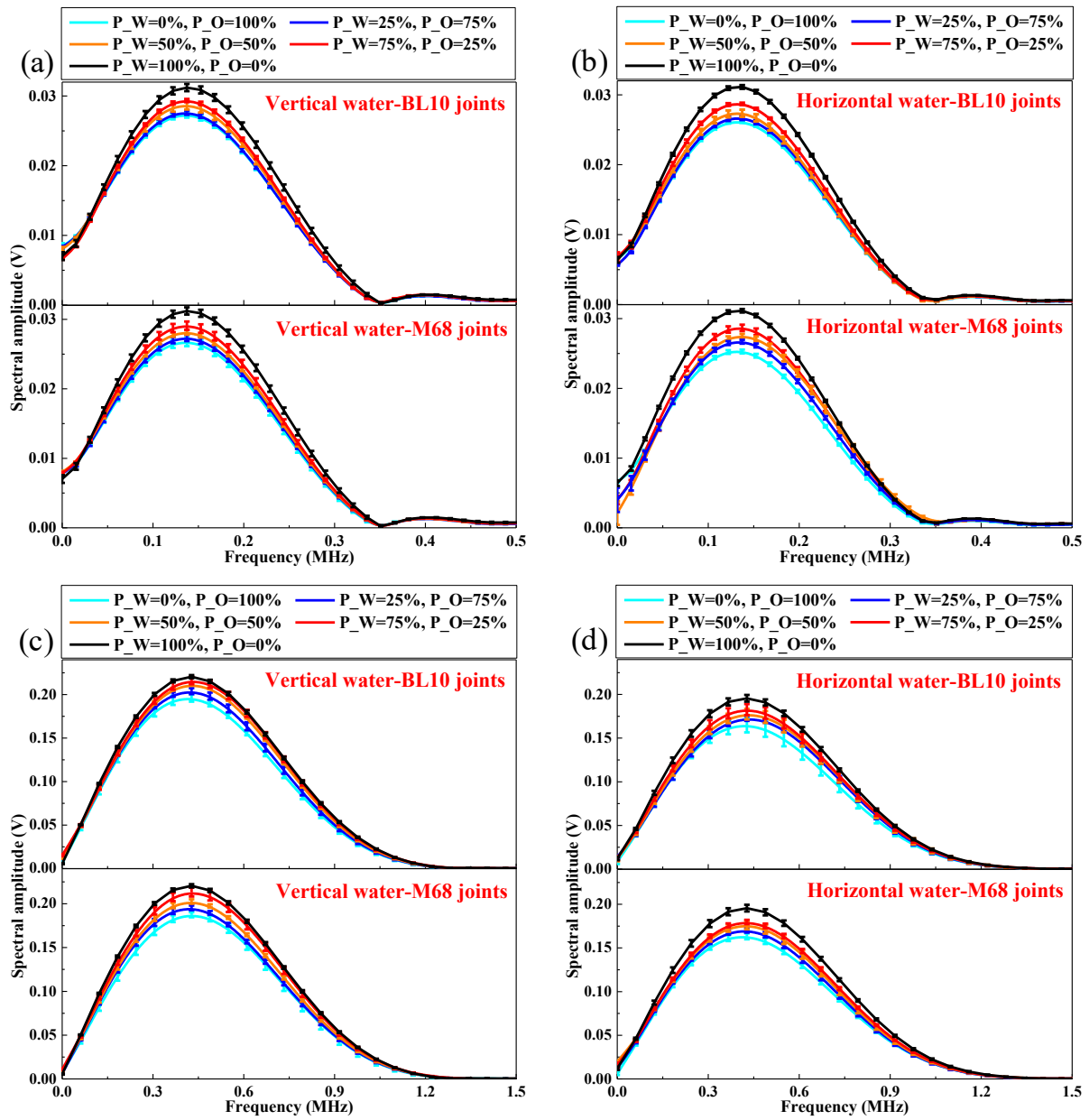


Figure 5.10 Frequency spectra of transmitted waves through rock samples with dual-liquid filled joints: 100-kHz input waves through (a) vertical and (b) horizontal joints; 1-MHz input waves through (c) vertical and (d) horizontal joints. Note that the dual-liquid filled joint is fully filled with two kinds of liquids among water, BL10 and M68. P\_L represents volume contents of water while P\_O refers to volume contents of light oil (BL10 or M68).

Table 5.5 Maximum amplitudes of frequency spectra for transmitted waves through rock samples with different fluid-filled joints

P_L	Input waves	Joint orientation	Maximum amplitudes (V)				
			Single-liquid filled joints			Dual-liquid filled joints	
			water	BL10	M68	water-BL10	water-M68
25%	$f_1 = 100\text{kHz}$	V	0.0051	0.0049	0.0046	0.0276	0.0273
		H	0.0047	0.0046	0.0045	0.0267	0.0266
	$f_2 = 1\text{MHz}$	V	0.0333	0.0274	0.0267	0.2040	0.1953
		H	0.0017	0.0014	0.0012	0.1725	0.1702
50%	$f_1 = 100\text{kHz}$	V	0.0123	0.0110	0.0010	0.0287	0.0281
		H	0.0039	0.0036	0.0036	0.0274	0.0273
	$f_2 = 1\text{MHz}$	V	0.1368	0.1254	0.0951	0.2117	0.2025
		H	0.0014	0.0014	0.0013	0.1774	0.1762
75%	$f_1 = 100\text{kHz}$	V	0.0228	0.0202	0.0192	0.0293	0.0288
		H	0.0116	0.0107	0.0103	0.0287	0.0285
	$f_2 = 1\text{MHz}$	V	0.1984	0.1716	0.1617	0.2162	0.2133
		H	0.0642	0.0563	0.0472	0.1828	0.1798
100%	$f_1 = 100\text{kHz}$	V	0.0312	0.0273	0.0267	0.0312	0.0312
		H	0.0311	0.0261	0.0253	0.0311	0.0311
	$f_2 = 1\text{MHz}$	V	0.2205	0.1962	0.1874	0.2205	0.2205
		H	0.1956	0.1649	0.1633	0.1956	0.1956

**Note:** H and V stand for horizontal and vertical directions, respectively. For single-liquid filled joints, P\_L represents volume contents of water, BL10 or M68. For dual-liquid filled joints, P\_L refers to volume contents of water in the joint.

#### 5.3.2.4 $Q$ value

Figure 5.11 shows  $Q$  values of rock samples with single-liquid filled rock joint versus liquid content in joint. As liquid content in rock joint increases,  $Q$  values get greater regardless of the type of filling liquid. It indicates that the existence of liquid could reduce wave attenuation through single-liquid filled joints, which is consistent with laboratory results in Pyrak-Nolte et al. (1990). The reason is that the presence of liquid makes rock joints stiffer, allowing more wave energy transmission. It is also illustrated that the water-filled joint results in the greatest

$Q$  values, followed by the BL10-filled joint. It means that water-filled rock joints attenuate less wave energy than BL10- and M68-filled joints, and more wave attenuation occurs in M68-filled joints rather than BL10-filled joints. The observed small discrepancy in wave attenuation caused by different filling liquids could be attributed to the significant difference in viscosities of these liquids (Fehler, 1982, Place et al., 2016).

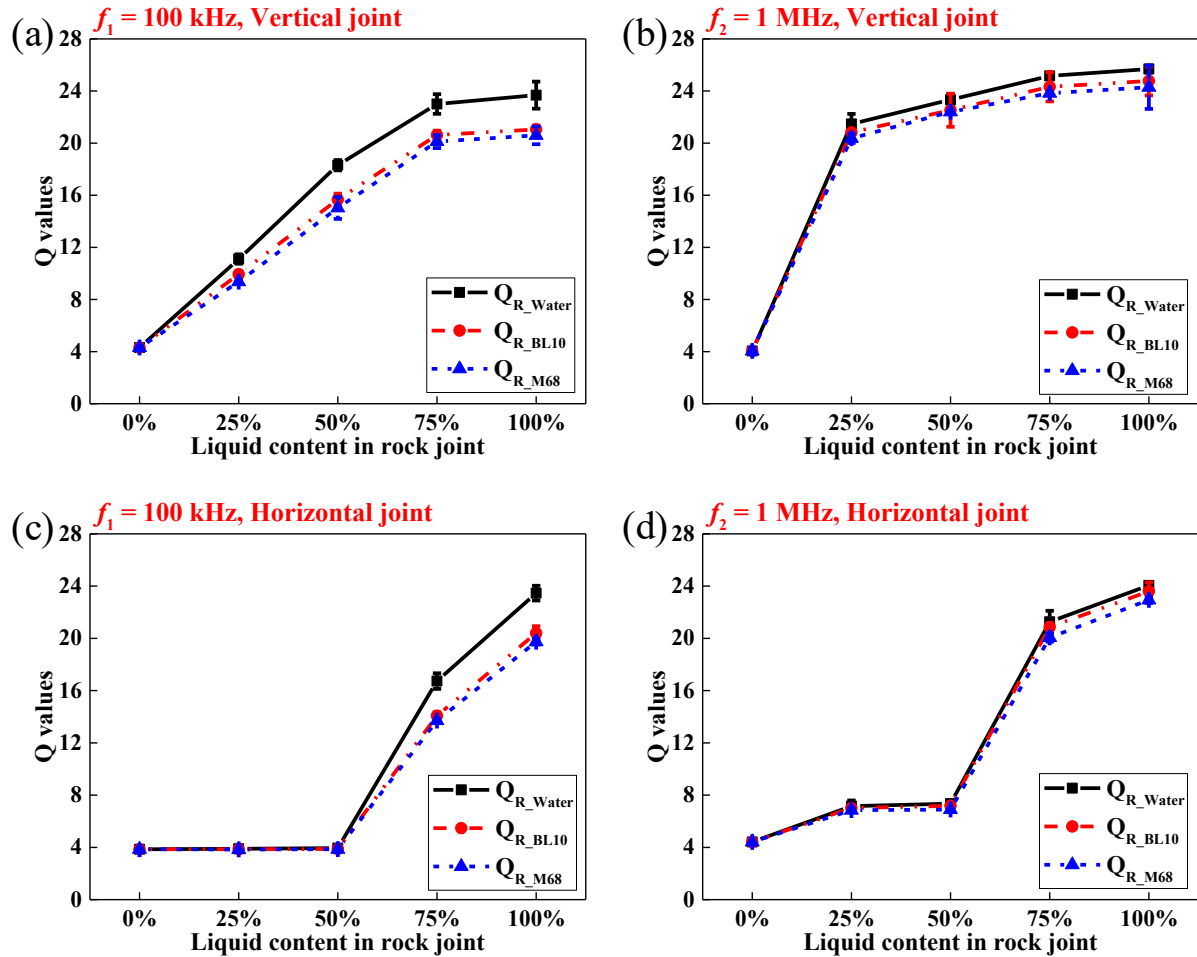


Figure 5.11 Attenuation quality factor  $Q$  of rock samples with single-liquid filled rock joints versus liquid content in rock joint: (a) and (b) for 100-kHz and 1-MHz incident P-waves across vertical joints, respectively; (c) and (d) for 100-kHz and 1-MHz incident P-waves across horizontal joints, respectively.

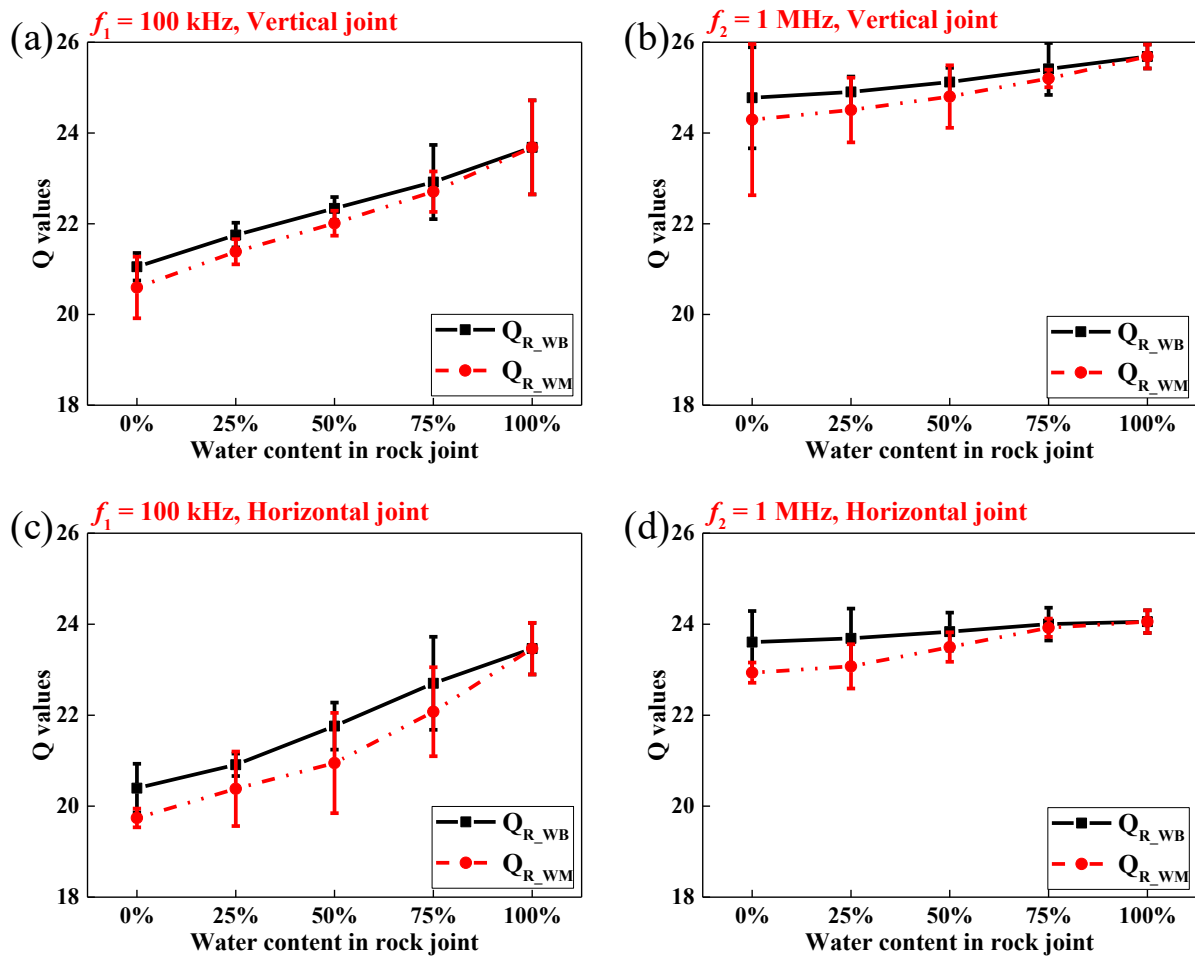


Figure 5.12 Attenuation quality factor  $Q$  of rock samples with dual-liquid filled rock joints vs water content in rock joint: (a) and (b) for 100-kHz and 1-MHz incident P-waves across vertical joints, respectively; (c) and (d) for 100-kHz and 1-MHz incident P-waves across horizontal joints, respectively.

Figure 5.12 presents  $Q$  values for rock samples with dual-liquid filled joints versus water content in the joint. It shows that increasing water content leads to greater  $Q$  values of rock samples with dual-liquid filled joints, implying that filling water reduce wave attenuation across the dual-liquid filled rock joints. It is also found that dual-liquid filled joints containing BL10 result in greater  $Q$  values than those filled with M68, suggesting that filling M68 attenuate more wave energy compared to BL10. These findings are in accordance with observations from different single-liquid filled rock joints shown in Fig. 10, which could also be explained by the differences in viscosities of liquids (i.e., water, BL10 and M68 in this study). More specifically, less wave energy is absorbed by filling water because of its lower viscosity compared to light oils.

### 5.3.3 Effects of joint orientation on wave behaviours across single fluid-filled rock joints

#### 5.3.3.1 Wave velocity

Figure 5.5 illustrates that wave velocity of single-liquid filled rock joints is highly dependent on the joint orientation. More specifically, for vertical single-liquid filled rock joint (see Figures 5.5a and 5.5b), the wave velocity drastically increases when filling liquid content increases from 0% to 25%, followed by a continuous increase at a decreasing rate as liquid content gradually rises to 100%. By comparison, for horizontal single-liquid filled joint (see Figures 5.5c and 5.5d), the wave velocity seldom changes for liquid content below 50%, while it increases remarkably as liquid content further rises from 50% to 100%. The discrepancy could be attributed to different effects of fluid surface tension at various joint orientations (Li et al., 2001, Gurevich, 2002, Liu, 2005, Dimri et al., 2012). Precisely, for vertical rock joints, air and liquid are almost perfectly stratified along the joint surface, where the fluid tension at the air-liquid interface has negligible influences on joint surface conditions. As a result, two joint surfaces have the identical boundary which is comprised of the liquid-rock interface and air-rock interface. Wave velocity mainly depends on the effective properties of the joint, which is highly affected by the volume content of liquid. On the contrary, for horizontal rock joints, there is a critical value of liquid content, which depends on the air-liquid meniscus interface caused by the surface tension, highly affects the boundary conditions of the joint surfaces (Munson et al., 2013). To be specific, when filling liquid content exceeds the critical value, i.e., 75% and 100% in this study, one joint surface is full covered by liquid while the other is partially wetted. Similar with vertical joints containing liquids, wave velocity under those cases are strongly affected by volume content of liquid. However, when filling liquid content is lower than the critical value, i.e., 25% and 50%, filling liquid only adheres to one joint surface and the other is directly exposed to the air. Thus, almost all of wave is reflected at the air-rock surface while a very small portion of wave may propagate along the PMMA tube. Consequently, wave velocity relies on material properties of the PMMA and hardly changes with increasing liquid content. The critical value of filling liquid in a horizontal joint mainly depends on surface tensions at the liquid-air-PMMA interface, which needs more tests to determine in future work.

For dual-liquid filled rock joints, the joint orientation has some minor effects on wave velocity, as shown in Figure 5.6. With increasing water content in dual-liquid rock joints, a downward concave increase in wave velocity across vertical joints is observed in Figures 5.6a and 5.6b,

while an upward convex increase in wave velocity of horizontal joints is shown in Figures 5.6c and 5.6d. The minor discrepancy could be attributed to different effects of surface tension on fluid distribution in vertical and horizontal dual-liquid filled joints. Specifically, two liquids are purely stratified along the joint surface in vertical joints, while one liquid with smaller content would form a pocket surrounded by the other liquid in horizontal joints. Consequently, the effective elastic moduli of vertical joints mainly depend on elastic moduli of those two liquids, while those of horizontal joints could also be affected by capillary pressure caused by the inner liquid pocket in the joint.

Figures 5.5 and 5.6 show that, compared with single-liquid filled rock joints, changes in wave velocities across dual-liquid filled joints caused by varying fluid composition are much smaller regardless of the joint orientation. It is because that dual-liquid filled rock joints are always full of liquids with small differences in the density and bulk modulus. Therefore, the evident coupling and stiffening effects caused by filling liquids slightly change with fluid composition in dual-liquid filled rock joints.

### 5.3.3.2 Transmission ratio

As demonstrated in Figures 5.7a and 5.7b, a relatively uniform increase in transmission coefficient can be observed for the vertical single-liquid filled joint as liquid content gradually increases. By contrast, for the horizontal single-liquid filled joint, transmission coefficient rarely changes when the liquid content in joint is below 50%, while it sharply increases for the liquid content in joint beyond 50%, as illustrated in Figures 5.7c and 5.7d. These findings could be attributed to the differences in joint surface conditions between vertical and horizontal joints. To be specific, for a vertical joint, two joint surfaces are composed of air-rock and liquid-rock interfaces due to the purely stratified distribution of air and liquid. Consequently, the increase of filling liquid content directly results in larger area of liquid-rock interface, thereby enhancing wave transmission across the joint. On the contrary, for a horizontal joint with the lower liquid content (i.e.,  $\leq 50\%$  in this study), one of its joint surfaces is the air-rock interface on which almost all wave energy is reflected; and hence increasing liquid content has few effects on wave transmission across the joint. When the liquid content exceeds a critical value (which is between 50% and 75% in this study), two joint surfaces are connected through filling liquids, generating the liquid-rock interface on all joint surfaces, which could highly enhance wave transmission through the joint. As the liquid content further increases, the area of liquid-rock interface becomes larger, causing an increase in wave transmission across the joint.

Regarding the dual-liquid filled joints (see Figure 5.8), the consistent increasing trends of transmission coefficients with increasing water content for both vertical and horizontal joint orientations were observed. It indicates that the joint orientation has few effects on the dependence of transmission coefficient of dual-liquid filled rock joints on the water content in joint. This is mainly due to the fully saturated state of all dual-liquid filled joints at different joint orientations, though the respective content of each of the two liquids in the joint is different. It means that both surfaces of a joint are liquid-rock interfaces regardless of the joint orientation. Apart from that, elastic moduli and wave impedance of the joint slightly vary with fluid distribution modes because of small contrast in these parameters among water and two kinds of light oils in this study. As a result, changes in joint surface conditions caused by varying joint orientation have few effects on wave transmission across the joint.

### 5.3.3.3 Frequency spectra

For vertical single-liquid filled joints, increasing liquid content results in the increases of spectral amplitude and dominant frequency of transmitted waves, as shown in Figures 5.9a and 5.9c. For horizontal single-liquid filled joints, similar trends of frequency spectra with increasing liquid content are observed only when liquid content is above 50% (Figures 5.9b and 5.9d). When liquid content is lower than 50%, changing liquid content has negligible effects on frequency spectra. Furthermore, the joint orientation has significant effects on spectral contents for single-liquid filled rock joints with a fixed liquid content. For instance, with liquid content of 75%, spectral amplitudes for vertical joints are about three times larger than those for horizontal joints, and the dominant frequency for vertical joints is slightly higher than that for horizontal joints. These findings are consistent with observations from transmission coefficients, which further confirms that the liquid-rock interface on the joint surface determines wave transmission across the joint partially filled with liquid. Figure 5.9 also illustrates that spectral amplitudes are much more sensitive to changing liquid content compared to the dominant frequency regardless of the joint orientation.

For dual-liquid filled rock joints, spectral amplitudes and the dominant frequency slightly increase with increasing water content regardless of joint orientation, as shown in Figure 5.10. This implies that the joint orientation has few influences on spectral contents of transmitted waves across dual-liquid filled joints. It is in accordance with findings on transmission coefficients, which could also be attributed to the fact that dual-liquid filled joints are full of liquids regardless of the joint orientation. It can be concluded that changes in joint surface



conditions caused by different joint orientation have much more significant effects on wave transmission across the joint compared to viscous effects of different filling liquids.

#### 5.3.3.4 $Q$ value

For rock samples with the vertical single-fluid filled joint, a continuously nonlinear increase in  $Q$  value is caused by the growth of liquid content, as shown in Figures 5.11a and 5.11b. This means that wave attenuation could be significantly reduced by filling liquid in vertical joints. By contrast,  $Q$  value for rock samples with the horizontal single-fluid filled joint almost stays constant with liquid content below 50%, while it increases dramatically with increasing liquid content when the liquid content is above 50% (see Figures 5.11c and 5.11d). It indicates that wave attenuation across horizontal joints decreases with increasing liquid content only when the liquid content exceeds a critical value. The above discrepancies in  $Q$  values between vertical and horizontal single-liquid filled joints are consistent with those in transmission coefficients.

By comparison, for rock samples with the dual-liquid filled joint,  $Q$  values consistently increase with water content in the joint regardless of the joint orientation, as illustrated in Figure 5.12. It indicates that the increase of water content in dual-liquid joints gradually reduce wave attenuation no matter what the joint orientation is. Note that variations of  $Q$  values are in accordance with changes of transmission coefficients across the dual-liquid filled rock joints, which could also be attributed to the fact that varying joint orientation leads to minor variations of joint surface conditions when the joint is full of liquids. It is also found that the joint orientation induces relatively less influence on  $Q$  values caused by dual-liquid filled joints rather than single-liquid filled joints.

### 5.3.4 Effects of temperature on wave behaviours across single fluid-filled rock joints

#### 5.3.4.1 Wave velocity

Figure 5.13 shows the wave velocities as a function of temperature. Figure 5.13a indicates that the increasing the temperature (from 10 °C to 80 °C) could result in a nonlinear increase of approximately 3.34% in the wave velocity of the water-filled joint, thereby causing a higher wave velocity in the corresponding jointed rock sample. Furthermore, the temperature dependence of the wave velocity across water-filled rock joints is consistent with that of the

wave velocity in water (Wilson, 1959). This implies that the thermal effect on the wave velocity across an individual water-filled joint is highly affected by that on the wave velocity through the fluid filling the joint.

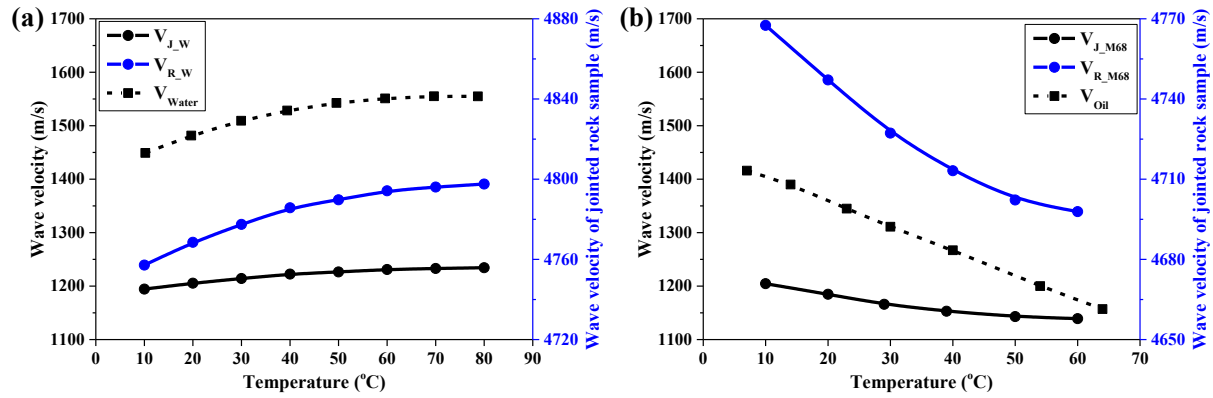


Figure 5.13 Wave velocities versus temperature for: (a) water-filled joint and the corresponding jointed rock sample; and (b) M68-filled joint and the corresponding jointed rock sample. Wave speed of water ( $V_{water}$ ) measured by Wilson (1959) and wave speed of one kind of light oil ( $V_{oil}$ ) measured by Wang and Nur (1991) are also presented in the figure.

In contrast, the wave velocity of the M68-filled rock joint decreases by nearly 5.43% as the temperature increases from 10 °C to 60 °C, as illustrated in Figure 5.13b. More specifically, the rate of decrease in the wave velocity gradually slows with increasing temperature. This finding is approximately consistent with the previous findings on the temperature-dependent wave velocity of light oil (Wang and Nur, 1991). This indicates that the thermal effect on wave velocity across a single M68-filled rock joint is determined by the temperature-dependent properties of the M68 light oil.

### 5.3.4.2 Transmission ratio

Figure 5.14 illustrates the transmission ratios versus temperature. It is shown that the transmission ratio across the water-filled joint sharply increases by approximately 50% with the temperature from 10 °C to 20 °C, after which an increase of approximately 14% is observed as the temperature further increases to 80 °C. This indicates that an increase in temperature could lead to more wave energy transmission through the water-filled rock joint, particularly in the temperature range of 10 °C to 20 °C. On the other hand, as temperature gradually increases from 10 °C to 60 °C, an approximately linear decrease in the transmission ratio is observed for the rock sample with a single M68-filled joint. This means that a higher temperature could result in less wave energy transmission across the M68-filled rock joint.

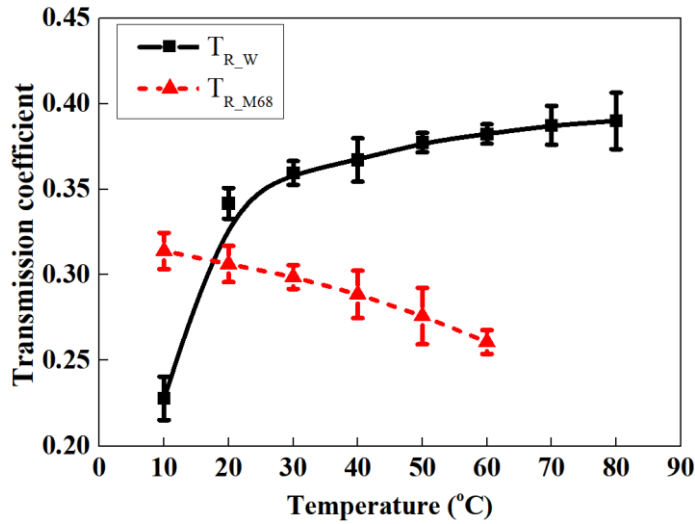


Figure 5.14 Transmission ratios versus temperature for rock samples with different individual fluid-filled joints.  $T_{R\_W}$  and  $T_{R\_M68}$  represent transmission ratios across rock samples with single water-filled and M68-filled joints, respectively.

### 5.3.4.3 Frequency spectra

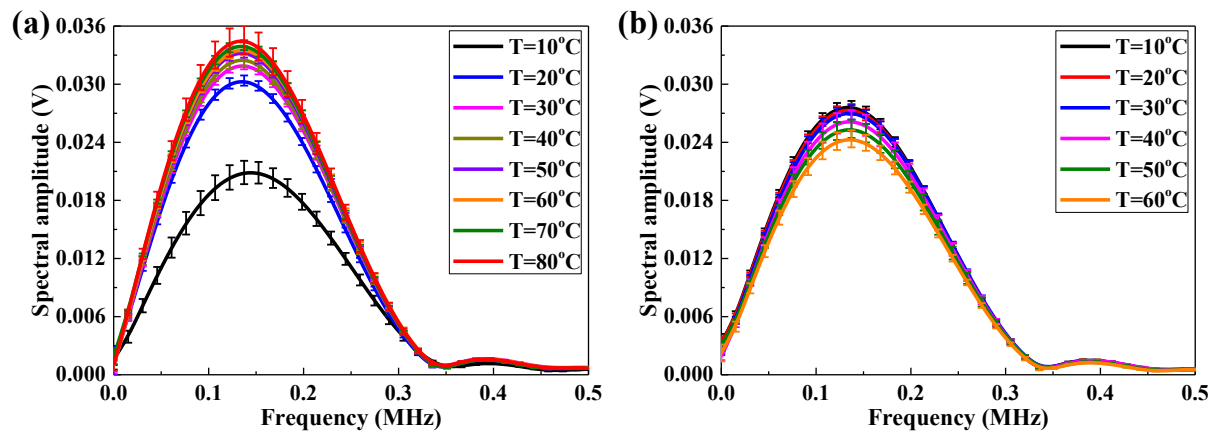


Figure 5.15 Thermal effect on spectral contents of waves transmitted through jointed rock samples with: (a) single water-filled joints; and (b) single M68-filled joints.

Figure 5.15 depicts the frequency spectra for the fluid-filled rock joints under different temperatures. It is shown that, compared with the dominant frequency, the amplitude is more sensitive to the varying temperature. For the rock sample with a water-filled joint (see Figure 5.15a), the spectral amplitude increases with increasing temperature. In particular, the increase in amplitudes is more remarkable at lower temperatures. For instance, the peak amplitude increases by approximately 65.5% when the temperature changes from 10 °C to 20 °C, while

it increases by approximately 13.8% when the temperature further climbs up to 80 °C. This means that, as the temperature increases, the transmitted wave energy through the water-filled joint significantly increases at the low temperature range, followed by a continuous but more gradual increase at higher temperatures. In addition, the dominant frequency slightly increases with increasing temperature. This indicates that more high-frequency wave modes could transmit through the water-filled joint with increasing temperature. By comparison, for the rock sample with an M68-filled joint (see Figure 5.15b), the maximum spectral amplitude slightly decreases by approximately 12% as the temperature increases over the tested temperature range (from 10 °C to 60 °C). Additionally, the dominant frequency decreases slightly with increasing temperature, implying that fewer high-frequency wave modes can transmit across the M68-filled joint at higher temperatures.

#### 5.3.4.4 $Q$ value

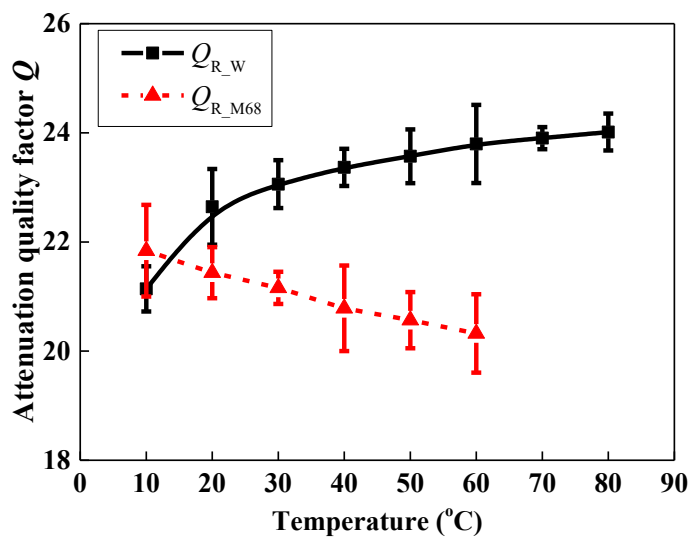


Figure 5.16 The  $Q$  values versus temperature for rock samples with different individual fluid-filled joints.  $Q_{R\_W}$  and  $Q_{R\_M68}$  represent attenuation quality factors across rock samples with single water-filled and M68-filled joints, respectively.

$Q$  values for rock samples with single water-filled and M68 filled joints are calculated and plotted as a function of temperature in Figure 5.16. It is found that rock sample with single water-filled joint,  $Q$  increases at a decreasing rate as temperature goes up. That implies that less wave energy is attenuated by the water-filled rock joint at higher temperature, which is consistent with the former observation regarding the temperature dependence of wave absorption in water (Fox and Rock, 1946, Pinkerton, 1947). This phenomenon could be attributed to the increase in compressibility of water according to Hall's theory (Hall, 1948,

Markham et al., 1951). Besides, the increasing temperature results in the decrease of water viscosity, as observed in Table 5.2. Consequently, viscous loss of wave energy declines when wave propagates through water (Xu et al., 2003), thereby reducing the total attenuation caused by the water-filled joint.

On the other hand, Figure 5.16 illustrates an approximately linear decrease in  $Q$  of rock samples with the M68-filled joint as temperature increases from 10 °C to 60 °C. It means that more wave attenuation occurs when wave propagates through the M68-filled joint at higher temperature. This result could be explained by the temperature dependent properties of the light oil that the relaxation rather than viscosity of M68 may dominate wave attenuation in the M68-filled joint (Litovitz and Davis, 1965, Nur et al., 1984). Specifically, although less wave dissipation might be caused by smaller viscosity as temperature goes up, the relaxation in oil could lead to much more wave absorption, which results in the increase of total wave attenuation in filled M68. Apart from that, the increase of overall wave attenuation induced by increasing temperature may also be attributed to the Darcian resistance mechanism. To be specific, the oscillation of solid and fluid continua gradually becomes out of phase for relatively low fluid viscosity caused by higher temperature, thereby causing more wave energy loss (Eastwood, 1993).

## 5.4 Discussion

### 5.4.1 Comparison with previous studies of fluid effects on wave propagation in fluid-saturated rock masses

In the study, compressional wave behaviours across vertical joints filled with air and liquid are consistent with previous findings (Yang et al., 2019), which further confirms that wave attributes of the rock joint highly depend on weighted volumes of both liquid and air. In addition, for vertical rock joints filled with two types of liquids, wave velocity and wave transmission increase with the increasing volume content of fluid having relatively larger bulk modulus. By comparison, for horizontal joint filled with air and liquid, there is a critical liquid content (i.e., a value between 50% and 75% in this study) for the dependence of compressional wave properties on liquid content in the joint. When liquid content in rock joint is smaller than this critical value, wave behaviours across the joint resemble those through air-filled joint (i.e., open joint), that is, the presence of liquid has few influences on wave attributes of the joint.

The discrepancies between wave behaviours across vertical and horizontal fluid-filled joints are similar with previous findings from rock containing micro-cracks saturated with water-oil (Gist, 1991). These differences could be attributed to that wave responses to the joint depend on conditions of the fluid-rock interface that waves initially impinge on (Gist, 1991).

Furthermore, changes in wave properties of rock samples with individual fluid-filled joints caused by varying fluid composition are in accord with previous findings on rock masses containing fluid-saturated micro-cracks/pore at high saturation degree (O'Connell and Budiansky, 1977, Mavko and Nur, 1979, Winkler and Nur, 1982, Jones, 1986, Knight and Nolen-Hoeksema, 1990). The increase in wave velocity caused by the growth of volume content of the filling liquid with larger bulk modulus in the joint could be attributed to the fact that the increase in effective bulk modulus is much more significant than the increase in overall density of the joint (Cadoret et al., 1995). The decreasing wave attenuation due to larger volume content of the filling liquid might because that filling liquid makes the joint stiffer and the difference in wave impedances between rock matrix and the joint smaller (Stein and Wysession, 2009). Similar with previous studies on rock masses containing fluid-saturated micro-cracks/pore (Wang and Nur, 1990, Gurevich, 2002, Wang, 2001), a strong dependence of wave attributes on the type of filling fluids in the joint is also observed in this study. The larger viscosity of fluid it is, the more wave attenuation caused by fluid-filled joint there is. It is also demonstrated that wave attenuation is much more sensitive to fluid-filled rock joints than wave velocity, which is consistent with observations from rock containing fluid-saturated microcracks/pores (Winkler and Nur, 1979).

#### **5.4.2 Comparison with previous studies of thermal effects on wave propagation in fluids and fluid-saturated geomaterials**

The compressional wave velocity of rock joints filled with water increases with temperature, which agrees well with the thermal effect on the wave speed in water (Wilson, 1959). The thermal effect on wave velocity across single water-filled joints could be attributed to the temperature-dependent water properties. Specifically, as the temperature increases from 10 °C to 80 °C, water density slightly decreases, while the compressibility of water gradually decreases to a minimum at approximately 65 °C before increasing (Eisenberg et al., 2005). In contrast, for the light oil (M68 used in this study), an increase in temperature results in the reduction in the wave speed across the joint, which is in accord with the temperature-dependent wave properties of liquid hydrocarbons (Wang and Nur, 1991). This is likely because the

increase in temperature causes thermal expansion of the M68, weakening intermolecular repulsive forces (Wang and Nur, 1990). Accordingly, the compressibility of the light oil increases, thereby causing lower wave velocity. However, the findings on wave velocity obtained in this study are somewhat different from the results obtained from rock masses containing fluid-saturated micro-cracks/pores (Wang and Nur, 1990). For rock masses with water-saturated micro-cracks/pores, a joint with either water or light oil may decrease the wave speed with increasing temperature, mainly because the decreasing effective bulk moduli of the entire saturated rock dominate the wave velocity in such rock masses (Spencer Jr and Nur, 1976).

Furthermore, the current study reveals that a higher temperature leads to more wave energy transmission through single water-filled joint. This is in accord with findings of water-saturated marine sediments reported by Carbó and Molero (2002). From the perspective of fluid mechanics, the thermal effect on wave transmission through individual water-filled rock joints could be attributed to viscous effects (Kinsler et al., 2000). Specifically, an increase in temperature results in a decrease in the water viscosity (see Table 5.2), thereby reducing the viscous loss of wave energy when waves propagate through the water layer in the joint (Vennard, 2011). Additionally, an increase in temperature leads to an increase in wave velocity but a very small decrease in density. As a result, the acoustic impedance of water gradually increases within the temperature range of 10 °C to 80 °C; hence, more wave energy can transmit at the rock-water interface based on layered medium theory (Zhu et al., 2011, Zhu et al., 2012).

In contrast, an increase in temperature results in a lower wave energy transmission across the light oil-filled rock joint, which somewhat agrees with findings from oil sand (Eastwood, 1993). This observation could be explained by the Darcian resistance mechanism that the oscillation of solid and fluid continua gradually becomes out of phase due to a lower fluid viscosity caused by a higher temperature, thereby causing more wave energy loss (Eastwood, 1993). This may also be because the increase in temperature could reduce the density and wave velocity of M68, thereby decreasing the wave impedance of M68. Consequently, wave transmission at the M68-rock interface decreases according to layered medium theory (Zhu et al., 2011). From the perspective of fluid acoustics, this finding could be explained by the temperature-dependent properties of the light oil causing relaxation, rather than the viscosity of M68 dominating the wave attenuation in the M68 layer (Litovitz and Davis, 1965, Nur et al., 1984). Specifically, as the temperature increases, although the decreasing viscosity causes less wave dissipation (see

Table 5.2), the relaxation in the oil can lead to much more wave absorption, which results in the reduction in the total transmitted wave energy across the M68-filled joint.

### 5.4.3 Interpretation from acoustics in fluids

In this study, the physical mechanisms for wave propagation in fluids, where fluid properties (including bulk modulus, density and viscosity) play significant roles, could be employed to account for wave behaviours across the fluid-filled rock joint. All rock joints tested in the current work are filled with two fluid phases; and hence the effective physical characteristics of those joints depend on the volume fractions and physical properties of two fluids. To be specific, following the Wood's law (Wood and Lindsay, 1956), the effective bulk modulus  $K_{mix}$  of the two-phase fluid layer in the joint can be obtained by

$$\frac{1}{K_{mix}} = \frac{\phi_{F1}}{K_{F1}} + \frac{\phi_{F2}}{K_{F2}} \quad \text{Equation 5.1}$$

where  $K_{F1}$  and  $K_{F2}$  are the bulk moduli of two different fluid phases, respectively;  $\phi_{F1}$  and  $\phi_{F2}$  are volume fractions of these two fluids in the joint, respectively. Based on Equation 5.1, the bulk modulus of the two-phase fluid layer can be expressed in the form (Larock et al., 1999)

$$K_{mix} = \frac{K_{F2}}{1 + \phi_{F1} \left( \frac{K_{F2}}{K_{F1}} - 1 \right)} \quad \text{Equation 5.2}$$

Besides, according to the mass balance, the density of the two-phase fluid layer can be obtained via an arithmetic average of two fluid densities (Batzle and Wang, 1992)

$$\rho_{mix} = \phi_{F1}\rho_{F1} + \phi_{F2}\rho_{F2} = \phi_{F1}\rho_{F1} + (1 - \phi_{F1})\rho_{F2} \quad \text{Equation 5.3}$$

where  $\rho_{F1}$  and  $\rho_{F2}$  are densities of two different fluid phases, respectively. Since the thin fluid-filled rock joint is analogous to a small section of fluid-filled thin-walled pipe, wave velocity across the fluid-filled joint could be expressed in the form (Street et al., 1996)

$$V_{mix} = \frac{\sqrt{K_{F2}/\rho_{mix}}}{\sqrt{1 + K_{F2} \frac{D_t}{E_t e_t} + \phi_{F1} \left( \frac{K_{F2}}{K_{F1}} - 1 \right)}} \quad \text{Equation 5.4}$$



where  $D_t$  and  $e_t$  are outer diameter and wall thickness of the tube, respectively;  $E_t$  is the elastic modulus of the tube material. It is worthy to notice that the formula takes the effect of the PMMA tube used for simulating fluid-filled joints into account. For rock joints filled with water and oil, with the increase of oil volume content (i.e.,  $\phi_{F1}$  in the formula), a more evident decrease in density of the two-phase fluid layer results in a higher wave velocity, which is consistent with observations from Figure 5.5. For rock joints filled with air and liquid, recognizing that  $K_{liq}/K_{air} \gg 1$  and  $\rho_{liq}/\rho_{air} \gg 1$ , wave velocity across the joint can be written as (Wylie et al., 1993)

$$V_{mix} = \frac{\sqrt{K_{liq}/\rho_{mix}}}{\sqrt{1 + K_{liq} \frac{D_t}{E_t e_t} + \phi_{air} \frac{K_{liq}}{K_{air}}}} \quad \text{Equation 5.5}$$

where  $K_{liq}$  and  $K_{air}$  are bulk moduli of the liquid and air, respectively. The formula reveals that the decreasing air volume content, i.e., the increasing liquid volume content, drastically increases the value of  $K_{mix}$ , thereby improving wave velocity across the joint filled with air and liquid (Larock et al., 1999), which is in accord with findings from Figure 5.5.

Moreover, wave attenuation across fluid-filled rock joints is strongly affected by the fluid viscosity according to the mechanisms lying behind acoustics in fluids. Specifically, wave propagation in a fluid leads to a relative motion of adjacent layers of the fluid, causing viscous forces which act against the acoustic pressure due to the wave (Trevena, 1969). To overcome these viscous forces, energy is extracted from the wave, resulting in decrease in wave intensity (i.e., wave energy loss). Theoretically, the relationship between attenuation coefficient in a fluid and its viscosity could be expressed as (Elmore et al., 1985)

$$\alpha = \frac{2\omega^2 \nu}{3\rho c^3} \quad \text{Equation 5.6}$$

where  $\omega$  is angular frequency,  $\rho$  is density of the fluid,  $c$  is the phase velocity, and  $\nu = \eta/\rho$  is the kinematic viscosity while  $\eta$  is the dynamic viscosity. It indicates that viscous loss in fluids is proportional to the fluid viscosity, which is the main reason for that wave attenuation in M68 is higher than that in BL10 and water. Based on the Grunberg-Nissan equation (Teja and Rice, 1981, Rubino and Holliger, 2012), the viscosity of the two-phase fluid layer in the joint can be expressed in the form

$$\eta_{mix} = \eta_{F1} \left( \frac{\eta_{F2}}{\eta_{F1}} \right)^{\phi_{F2}} \quad \text{Equation 5.7}$$

The formula indicates that, as the volume content of the more viscous fluid increases (i.e.,  $\phi_{F2}$  in the formula), the viscosity of two-phase fluid layer becomes larger, causing more wave energy loss. It is consistent with findings of wave attenuation across fluid-filled joints in this work.

#### 5.4.4 Influences of the incident wave frequency

As indicated by Yang et al. (2019), the incident wave frequencies (bandwidth) have influences on wave attributes of individual fluid-filled rock joints. It is further confirmed by the comparison of wave properties between 100-kHz and 1-MHz incident P-waves propagation across various fluid-filled joints in this study. On the one hand, as illustrated in Figs. 4 and 5, wave velocity for 1-MHz incident P-wave is higher than that for 100-kHz incident P-waves. It is likely due to that higher frequency waves tend to find faster paths and diffract around the heterogeneities when propagating through the fluid-filled joint (Louati and Ghidaoui, 2017a). Moreover, the finding is consistent with previous laboratory observations about wave velocity of rock containing fluid-saturated micro-cracks/pores, which could be explained by the local fluid flow theory (Cadoret et al., 1995, Mavko and Vanorio, 2010). To be specific, filling liquids cannot relax immediately when higher frequency waves propagate across the joint, causing a larger bulk modulus and stronger shear effects of the joint.

On the other hand, wave transmission for 100-kHz input waves is slightly greater than that for 1-MHz input waves regardless of joint orientation as well as types and composition of filling liquids (see Figures 5.7 and 5.8). Besides, frequency spectra in Figures 5.9 and 5.10 show that the dominant frequency of 1-MHz P-waves evidently decreases, while it is almost unchanged for 0.1-MHz P-waves propagating across fluid-filled joints. It indicates that, similar with the rock joints having much smaller width than the wavelength, the relatively thicker fluid-filled rock joint could also behave as a low-pass filter. The explanation is that fluid viscosity has greater influences on higher frequency waves than it does lower frequency waves. On the one hand, wave at a higher frequency result in motions of fluid particles at a faster rate, causing stronger molecular vibrations followed by more frictional heat due to the viscosity (Radziuk and Möhwald, 2016). On the other hand, higher frequency waves take longer paths than lower

frequency waves due to the multi-path effects, and hence they dissipate along a longer path length (Louati and Ghidaoui, 2017b).

Furthermore, Figures 5.9 and 5.10 shows that the dominant frequencies for transmitted 100-kHz and 1-MHz waves are about 120 kHz and 0.5 MHz, respectively. Herein, the dominant frequency for transmitted 100-kHz waves through jointed rock is larger than 100-kHz, which seems to violate the fact that the rock joint could act as a low-pass filter. It is presumably because that the real dominant frequencies of signals generated by transducers used in this study are not equivalent to what the manufacturer marks. To support this explanation, an aluminum sample with the same dimensions as the jointed rock sample was tested to examine the exact dominant frequencies of incident pulses generated by ultrasonic transducers. The aluminum is chosen because it has been commonly used to calibrate ultrasonic test systems for its nondispersive and nonattenuative properties (ASTM E127-07). The test results reveal that the real dominant frequency of signals produced by 100-kHz and 1-MHz transducers are about 140 kHz and 0.7 MHz, respectively. It means that the observations in Figs. 8 and 9 are not against the statement that the rock-fluid system could function as a low-pass filter on the propagating wave.

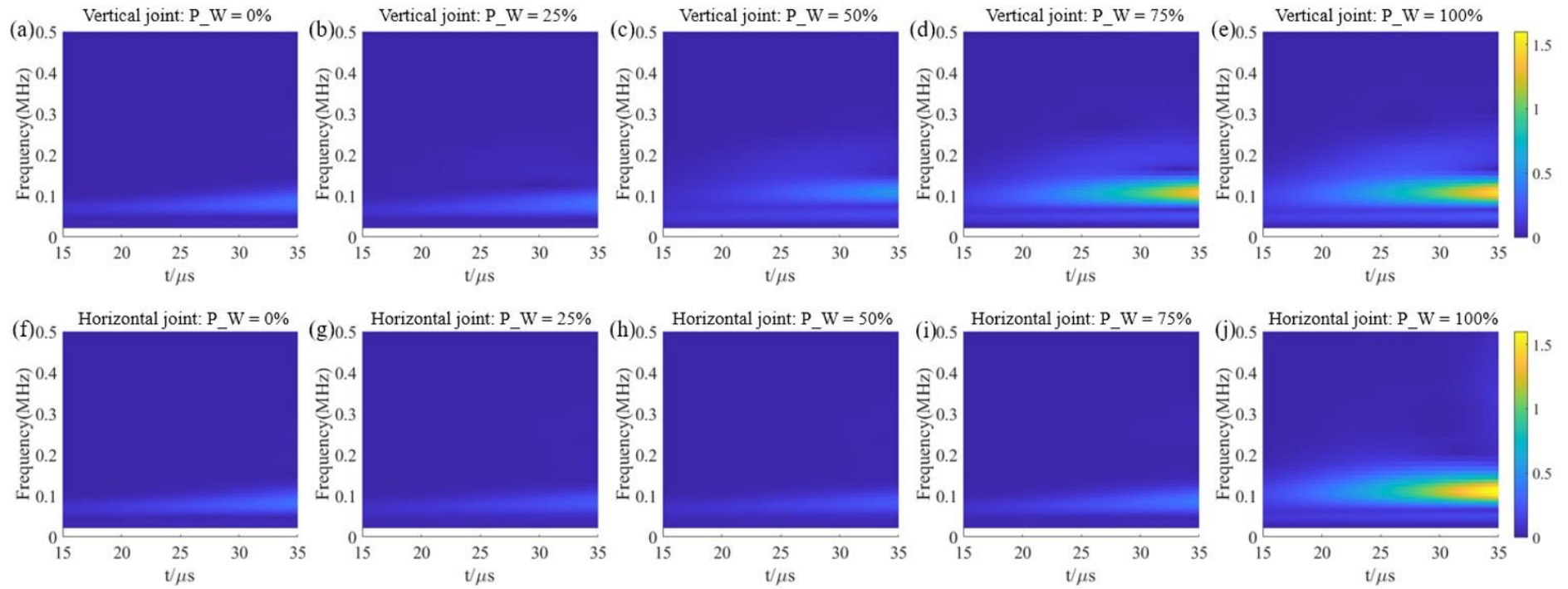


Figure 5.17 Time-frequency maps for 100-kHz P-waves transmitted through air-water filled rock joints with different water contents: (a) - (e) vertical rock joints, (f) - (j) horizontal joints. Herein,  $P_W$  stands for water volume content in the joint.

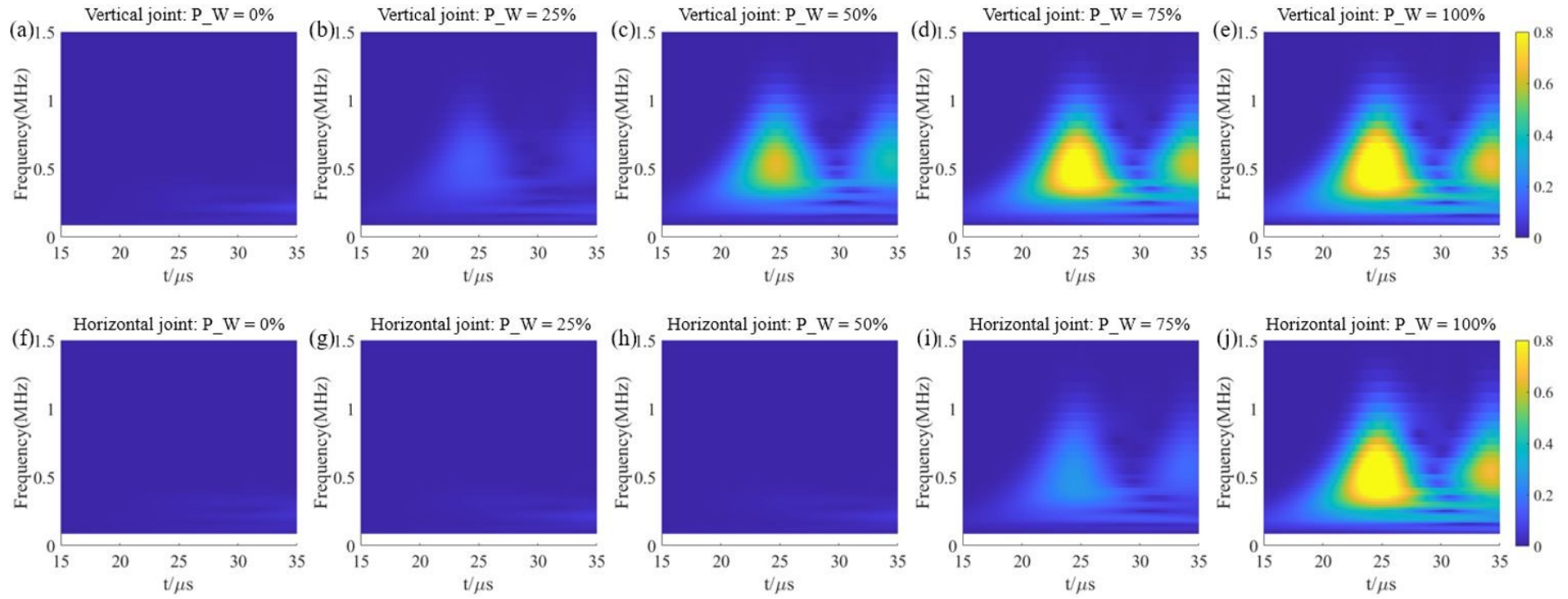


Figure 5.18 Time-frequency maps for 1-MHz P-waves transmitted through air-water filled rock joints with different water contents: (a) - (e) vertical rock joints, (f) - (j) horizontal joints. Herein,  $P_W$  stands for water volume content in the joint

Moreover, to better understand wave behaviours across fluid-filled rock joints in time and frequency domains simultaneously, the time-frequency analysis was performed on received transmitted pulses in this study. Since similar trends of wave velocity and spectral contents have been observed from air-water and air-oil filled joints, the time-frequency analysis on air-water filled joints could be taken as an example to further demonstrated influences of air-liquid on wave propagation. Figures 5.17 and 5.18 provide the typical time-frequency maps of transmitted 100-kHz and 1-MHz P-waves across various air-water filled joints, respectively. It is found that almost no wave energy could transmit across empty joints (i.e., water content of 0%) regardless of the joint orientation, as shown in Figures. 5.17a, 5.17f, 5.18a and 5.18f. For normal wave incidence upon the vertical joints, transmitted wave energy increases with the liquid content regardless of the dominant frequency of input waves. Moreover, Figures 5.17b - 5.17e reveal that transmitted wave energy of 100-kHz input signals concentrates over the frequency range of 80 to 120 kHz, while Figures 5.18b - 5.18e indicate that transmitted wave energy of 1-MHz input signals concentrates in the frequency range from 0.3 to 0.7 MHz. By comparison, for normal wave incidence upon the horizontal joints, little wave energy transmits through the joints with water contents of 25% and 50%, followed by an increase in transmitted wave energy for water content of 75%. Besides, the frequency ranges of energy concentration for horizontal joints with water content of 75% and 100% are similar with those for vertical joints. The above observations from Figures 5.17 and 5.18 are consistent with findings of frequency spectra in Figures 5.9 and 5.10, which means that the spectral analysis could provide comprehensive information for characterizing wave behaviors across fluid-filled rock joints in this work. Furthermore, Figures 5.17 and 5.18 indicate that transmitted wave energy centers on the first arrival pulses, corresponding to the time range from 25  $\mu$ s to 35  $\mu$ s for 100-kHz input signals and the time range from 20  $\mu$ s to 30  $\mu$ s for 1-MHz input signals. The discrepancy between those two types of incident waves could be attributed to that the wave frequency has influences on wave velocity.

## 5.5 Concluding remarks

In this chapter, extensive UPT tests have been performed to obtain deep insights into wave propagation and attenuation across individual fluid-filled rock joints. The results indicate that the type of infill fluids in rock joints plays an important role in seismic responses of jointed rock masses. Specifically, filling water results in faster wave propagation and more wave

transmission compared to light oils. It is attributed to that seismic behaviours across fluid-filled rock joints are mainly dependent on the elastic moduli and viscosity of filling fluids and variation in lumped wave impedance contrast of rock and fluids.

In addition, compositions of fluids in individual rock joints, i.e., volume contents of air and liquid in single-liquid filled joints as well as volume contents of water and oil in dual-liquid filled joints, have significant influences on wave propagation across the joint. In most circumstances, increasing liquid content in a single-liquid filled joint enhances wave velocity and wave transmission. For dual-liquid filled rock joints, both wave velocity and wave transmission increase with increasing water content.

Moreover, joint orientation strongly affects acoustic properties of rock joints partially filled with fluids while it has slight influences on wave propagation across fully fluid-filled joints. For vertical single-liquid filled joints, wave velocity and wave transmission drastically increase with rising liquid content. By comparison, for horizontal single-liquid filled joints, the liquid content could only dominate wave propagation and attenuation when it exceeds a critical value.

Furthermore, wave behaviours across single fluid-filled joints are strongly affected by the thermal condition. Particularly, wave velocity across the water-filled joint nonlinearly increases by approximately 3.34% as the temperature increases from 10 °C to 80 °C, mainly attributed to the slight decrease in the water density and the decrease in the water compressibility. The wave velocity across the M68-filled joint approximately linearly decreases by approximately 5.43% as the temperature increases from 10 °C to 60 °C due to the increase in the compressibility of the light oil. A higher temperature results in more wave energy transmission through the water-filled rock joint because of the less wave absorption induced by the decreasing water viscosity and more wave transmission at the rock-water interface due to the increasing wave impedance of the water. In contrast, wave energy transmission across the M68-filled joint decreases with temperature, which is attributed to less wave transmission at the rock-oil interface resulting from the decreasing wave impedance of the oil and more wave absorption caused by the relaxation in the oil. The thermal effect on the compressional wave attributes of fluid-filled rock joints is highly dependent on the type of fluid because of the differences in thermophysical properties.

Last but not the least, seismic responses of fluid-filled rock joints are affected by the dominant frequency (bandwidth) of the incident waves. Both wave velocity and attenuation increase with the incident wave frequency.



# CHAPTER 6     FLUID EFFECTS ON THE HIGH-INTENSITY STRESS WAVE BEHAVIOURS ACROSS INDIVIDUAL FLUID-FILLED ROCK JOINTS

## 6.1 Introduction

Chapter 5 presents a comprehensive study of fluid effects on low-intensity seismic wave behaviours across individual fluid-filled rock joints, clarifying the role of the fluid composition and spatial distribution, joint orientation, and temperature in ultrasonic compressional wave behaviours across single fluid-filled rock joints. However, the findings in chapter 5 could only provide additional insights into the effects of fluid-filled rock joints on propagation of stress waves with high frequencies and low energy. It should be mentioned that the high-intensity dynamic stresses encountered in many man-induced and natural activities (e.g., earthquakes, fluid injection, drilling, blasting and penetration) commonly exist in the form of stress waves. The presence of high-intensity stress waves could cause varying degrees of dynamic responses of rock joints (Zhang and Zhao, 2014). Understanding the interaction of high-intensity stress waves and rock joints is essential for petroleum, geothermal, earthquake and mining engineering and so on. In this regard, considerable efforts have been devoted to studying dynamic mechanical and high-intensity stress wave behaviours across rock joints, where most of laboratory findings were obtained from the dynamic impacting tests performed by the SHPB technique.

In the literature (see section 2.2.3 in chapter 2), the existing laboratory documents on the interaction of high-intensity stress waves and rock joints have focused mainly on the effects of joint parameters, including the joint thickness, joint orientation, joint roughness, and joint contact area. Note that the joint contact area can be described by the joint matching coefficient (JMC), which is defined as the ratio of the joint contact area to the total area of the joint surface (Zhao 1997a, b). As for the filled rock joints, most of experimental studies have paid attention to the interaction of high-intensity stress waves and rock joints filled with gouge materials, where the effects of the gouge layer thickness, water saturation, mineralogical compositions



and particle size distribution have been well examined. Despite the efforts made in high-intensity stress wave propagation across rock joints, the understanding of the fluid effects on the interaction of high-intensity stress waves with individual fluid-filled rock joints is still at its infancy.

This chapter aims to examine the effects of fluids on the interaction of rock joints and stress waves induced by dynamic impact loading using the SHPB technique. Particularly, emphasis is put on the influences of joint parameters (i.e., the joint thickness and JMC) and filling fluid properties (i.e., volume content and viscosity) on dynamic mechanical and seismic wave behaviours across individual fluid-filled rock joints. The experimental work in this chapter consists of two test programs. In the first set of tests, three groups of jointed rock specimens are utilized to examine the influences of the joint thickness, JMC and filling water volume content on the interaction of high-intensity stress waves with single water-filled rock joints. In the second set of tests, a series of SHPB tests are conducted on five jointed rock specimens to determine the effects of fluid viscosity on the interaction of high-intensity stress waves with single fluid-filled rock joints. Based on the laboratory data, the dynamic mechanical responses, energy evolution and wave behaviours of rock specimens with single fluid-filled rock joints are analysed and elaborated. In addition, the high-speed photography technique is adopted to visually observe the dynamic mechanical and wave responses of single fluid-filled rock joints subjected to the dynamic loading associated with the high-intensity stress waves. Furthermore, the underlying physical mechanisms for the observed mechanical and wave behaviours of single fluid-filled rock joints induced by the high-intensity stress waves are discussed based on the stiffening effect and the wave-induced fluid flow effect.

## **6.2 Experimental procedure**

### **6.2.1 Specimen description**

#### **6.2.1.1 Rock specimens**

Following the method presented in the chapter 4, the jointed rock specimen was generated by assembling two rock cylinders together via a PMMA tube with the help of the epoxy adhesive, as illustrated in Figure 6.1. In detail, the PMMA tube was firstly glued to a rock cylinder using the epoxy adhesive. After the adhesive was totally cured, the other rock cylinder was glued to

the semi-finished product, where a steel block with the weight of 2 kg was put on the upper surface of the whole assembly to guarantee two rock cylinders be tightly contacted during the operating process. It should be mentioned that two rock cylinders included in the jointed rock specimen have the same dimensional size, i.e., approximate 49 mm in diameter and 25 mm in height. Additionally, for a typical jointed rock specimen, one rock cylinder owns two flat and smooth end surfaces while the other has a rough end surface characterized by the spatial distribution of notches. Figure 6.1 shows that the rock joint is simulated by the direct contact of two rock end surface, where one rock surface is smooth and flat while the other is rough because of the existence of asperities. It means that the geometrical properties of synthetic rock joints, such as joint thickness and joint contact area, are determined by the rock cylinder with a rough end surface.

In this experiment, sixty-four rock cylinders with two flat and smooth end surfaces were firstly prepared and then carefully checked using the ultrasonic test system. Those rock cylinders were produced using the same rock material as the former experiments (i.e., black gabbro mined from Shanxi, China). Note that end surfaces of all rock cylinders should be carefully polished to reach the requirements for specimens used in SHPB tests (Zhou et al., 2011). It should be mentioned that, considering the black rock is difficult to capture in a high-speed camera, all rock cylinders were coated with bright yellow spring except for their end surfaces. Then, thirty-two of the prepared rock cylinders were further manufactured into those with single sawed surfaces using the CNC wire-cutting machine, where the cutting notches were symmetrically distributed on the rough surface. In particular, the width and depth of the notches as well as the spacing between two adjacent notches govern the geometrical properties of the synthetic rock joints, i.e., the joint thickness and JMC. More specifically, the joint thickness is thought to be the depth of notches, and the initial joint contact area is identified as the total area of all asperities on the rough joint surface. In light of the definition of JMC (Zhao, 1997, Li et al., 2017), the value of JMC could be computed as the ratio of the joint contact area to the area of the smooth joint surface. The detailed information, including the geometrical sketch and the laboratory photograph, of all rock cylinders with single rough surface is provided in Figure 6.2, where the black regions represent the asperities on the surface.

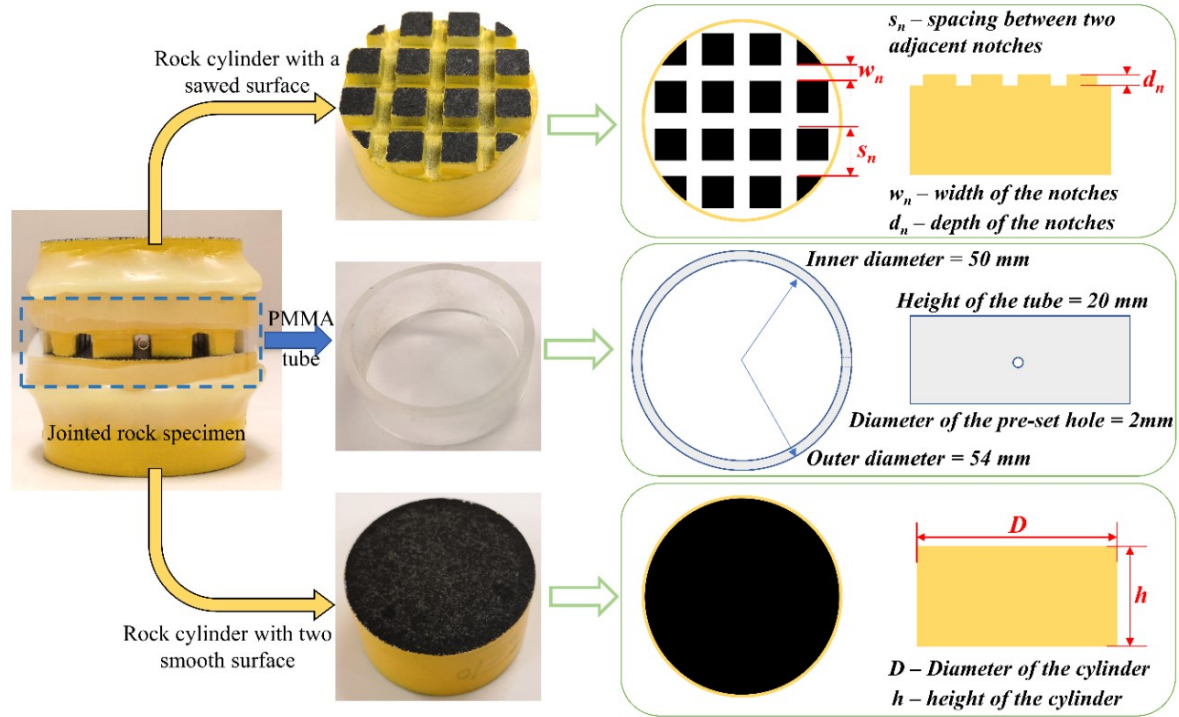


Figure 6.1 The illustration of a typical jointed rock specimen used in this experiment.

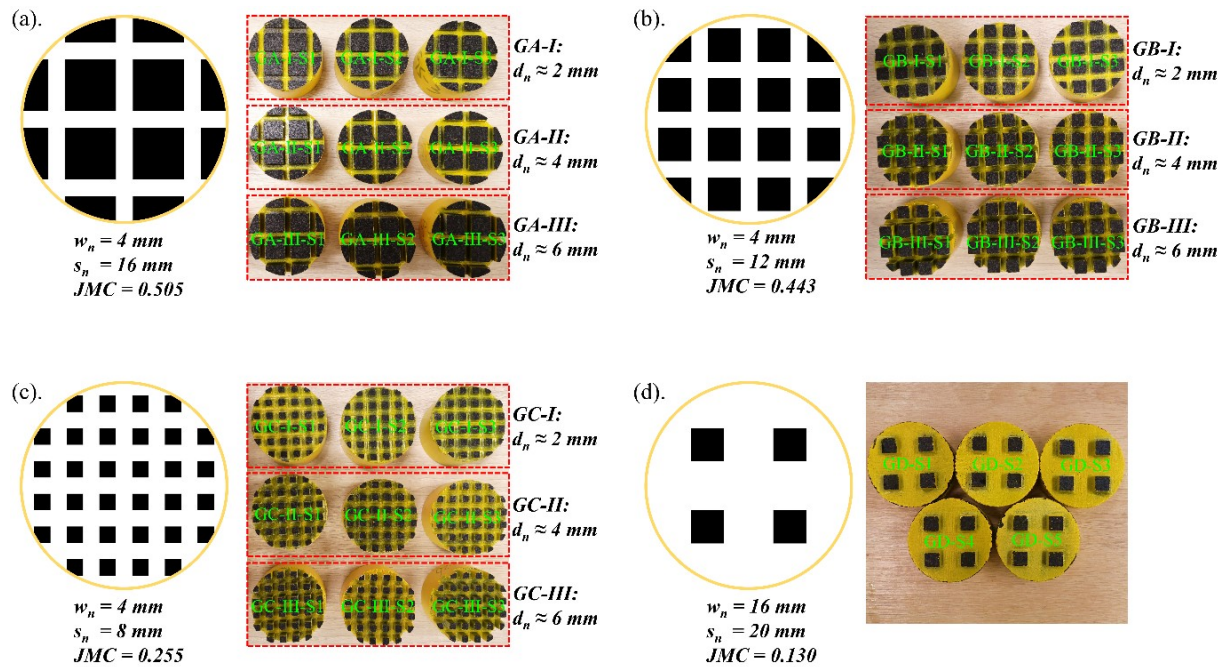


Figure 6.2 The rock cylinders with single rough surface used in this experiment, which were mainly divided into four groups: (a) Group GA, (b) Group GB, (b) Group GC and (b) Group GD according to the geometrical properties of the rough surface.

Table 6.1 The parameters for all jointed rock specimens used in this experiment

Group No.	Set No.	Sample No.	Height (mm)	Diameter (mm)	JMC	Joint thickness (mm)
GA	GA-I	GA-I-S1	50.25	48.87	0.505	1.71
		GA-I-S2	50.28	48.58	0.505	1.80
		GA-I-S3	50.40	48.55	0.505	1.94
	GA-II	GA-II-S1	50.53	48.51	0.505	3.83
		GA-II-S2	50.31	48.85	0.505	3.92
		GA-II-S3	50.49	48.57	0.505	4.00
	GA-III	GA-III-S1	50.20	48.43	0.505	5.84
		GA-III-S2	50.39	48.40	0.505	5.92
		GA-III-S3	50.42	48.44	0.505	5.96
GB	GB-I	GB-I-S1	50.69	48.57	0.443	1.88
		GB-I-S2	50.38	48.40	0.443	1.95
		GB-I-S3	50.60	48.87	0.443	1.98
	GB-II	GB-II-S1	50.04	48.43	0.443	3.80
		GB-II-S2	50.05	48.44	0.443	4.04
		GB-II-S3	50.47	48.27	0.443	4.06
	GB-III	GB-III-S1	50.03	48.55	0.443	6.00
		GB-III-S2	50.24	48.26	0.443	6.05
		GB-III-S3	50.60	48.50	0.443	6.07
GC	GC-I	GC-I-S1	50.59	48.23	0.255	1.84
		GC-I-S2	50.35	48.20	0.255	1.97
		GC-I-S3	50.37	48.29	0.255	1.92
	GC-II	GC-II-S1	50.33	48.42	0.255	3.84
		GC-II-S2	50.60	48.85	0.255	3.95
		GC-II-S3	50.34	48.62	0.255	3.92
	GC-III	GC-III-S1	50.51	48.50	0.255	6.01
		GC-III-S2	50.70	48.81	0.255	6.09
		GC-III-S3	50.42	48.37	0.255	5.86
GD	--	GD-S1	50.14	48.11	0.133	4.09
		GD-S2	50.00	48.28	0.133	4.18
		GD-S3	49.80	48.33	0.133	4.00
		GD-S4	50.02	48.35	0.133	4.04
		GD-S5	50.12	48.28	0.133	4.12

With the prepared sixty-four rock cylinders, there were thirty-two jointed rock specimens produced for the current work. According to the JMC of the rock cylinders with single sawed end surface, jointed rock specimens were divided into four groups, i.e., GA, GB, GC and GD, as illustrated in Figure 6.2. For groups GA, GB and GC, rock specimens in each group were classified into three sets based on the joint thickness, and every set has three specimens with an approximately identical joint thickness. Rock specimens in groups GA, GB and GC were used to study the interaction of high-intensity stress waves and single water-filled rock joints, focusing mainly on the effects of the joint thickness, JMC and filling water content. On the other hand, five rock specimens in group GD have a nearly identical joint thickness, which were employed to examine the effects of fluid viscosity on the interaction of high-intensity stress waves and single fluid-filled rock joints. The parameters for all jointed rock specimens used in this experiment are given in Table 6.1.

### 6.2.1.2 Filling fluid specimens

In this experiment, the deionized water and glycerol (No. 15523, Sigma-Aldrich Chemie GmbH) were mixed at various proportions to prepare five fluid specimens. The basic properties of those fluid specimens at the room temperature ( $\sim 20^\circ\text{C}$ ), including density and viscosity, are provided in Table 6.2. Note that the density was measured using the digital density meter, and viscosity was measured via the rheometer (model MCR 702) in the laboratory (ASTM D4052-18a, ASTM D445-19a).

Table 6.2 The summary of filling fluid specimens used in this study

Filling fluids	The composition of filling fluids (by the percentage of weight)	Density $\rho$ ( $\text{g}/\text{cm}^3$ )	Viscosity $\eta$ ( $\text{mPa}\cdot\text{s}$ )
WG-0	Deionized water: 100% Glycerol: 0%	0.995	1.0
WG-70	Deionized water: 30% Glycerol: 70%	1.188	23.8
WG-80	Deionized water: 20% Glycerol: 80%	1.210	50.5
WG-90	Deionized water: 10% Glycerol: 90%	1.236	157.0
WG-100	Deionized water: 0% Glycerol: 100%	1.252	624.0

Note: The density and viscosity of fluids were measured at a temperature of  $20^\circ\text{C}$ .

## 6.2.2 Test programme

The experiments in this chapter can be divided into two parts. The goal of the first part is to determine the interaction of high-intensity stress waves with single water-filled rock joints, concentrating mainly on the influences of the joint thickness, JMC and filling water content. The second part pays attention to the effects of fluid viscosity on the interaction of high-intensity stress waves with single fluid-filled rock joints.

### 6.2.2.1 The SHPB tests on single water-filled rock joints

This part aims to examine the effects of the joint thickness, JMC and filling water content on the interaction of high-amplitude stress waves with single water-filled rock joints. As mentioned in section 6.2.1, there were twenty-seven jointed rock specimens with various joint thickness and JMC were used in this part. For each jointed rock specimen, various water filling conditions were generated by changing the volume of water injected into the synthetic joint, which includes water volume contents at 0%, 25%, 50%, 75% and 100%. It should be mentioned that the water volume content was defined as the ratio of injecting water volume to the total volume of voids in the joint. To determine the total volume of voids in the rock joint, the relative difference between weights of the dry joint and the joint fully filled with deionized water was measured before performing the SHPB tests. Herein, there were totally 135 SHPB tests were conducted on all jointed rock specimens with varying water contents. It should be mentioned that the driving air pressure for all tests was set to be about 0.035 MPa to guarantee an approximately constant loading rate for all measurements and protect the rock specimen from damage. According to Zhou et al. (2011), the loading rate is defined as the slope of the pre-peak linear portion of the incident stress-time history curve. For all SHPB tests in this part, the loading rate was in the range of  $270 \pm 30$  GPa/s.

### 6.2.2.2 The SHPB tests on single rock joints filled with viscous liquids

The target of this part was to determine the influences of fluid viscosity on the interaction of high-amplitude stress waves with single fluid-filled rock joints. To this end, five different liquids described in Table 6.2 were separately injected into the synthetic rock joints to create a series of fluid-filled rock joints with varying filling liquid content. The test conditions for those synthetic fluid-filled rock joints are summarised in Table 6.3. Under each test condition, three SHPB tests were performed on the jointed rock specimen to ensure the reliability and



repeatability of the observed results. Therefore, there were totally 75 SHPB tests were carried out in this part. Note that the driving gas pressure was controlled to be about 0.035 MPa for all SHPB tests to keep a nearly same the loading rate and to avoid the damage of jointed rock specimen.

**Table 6.3 The summary of test conditions for fluid-filled rock joints used in this part**

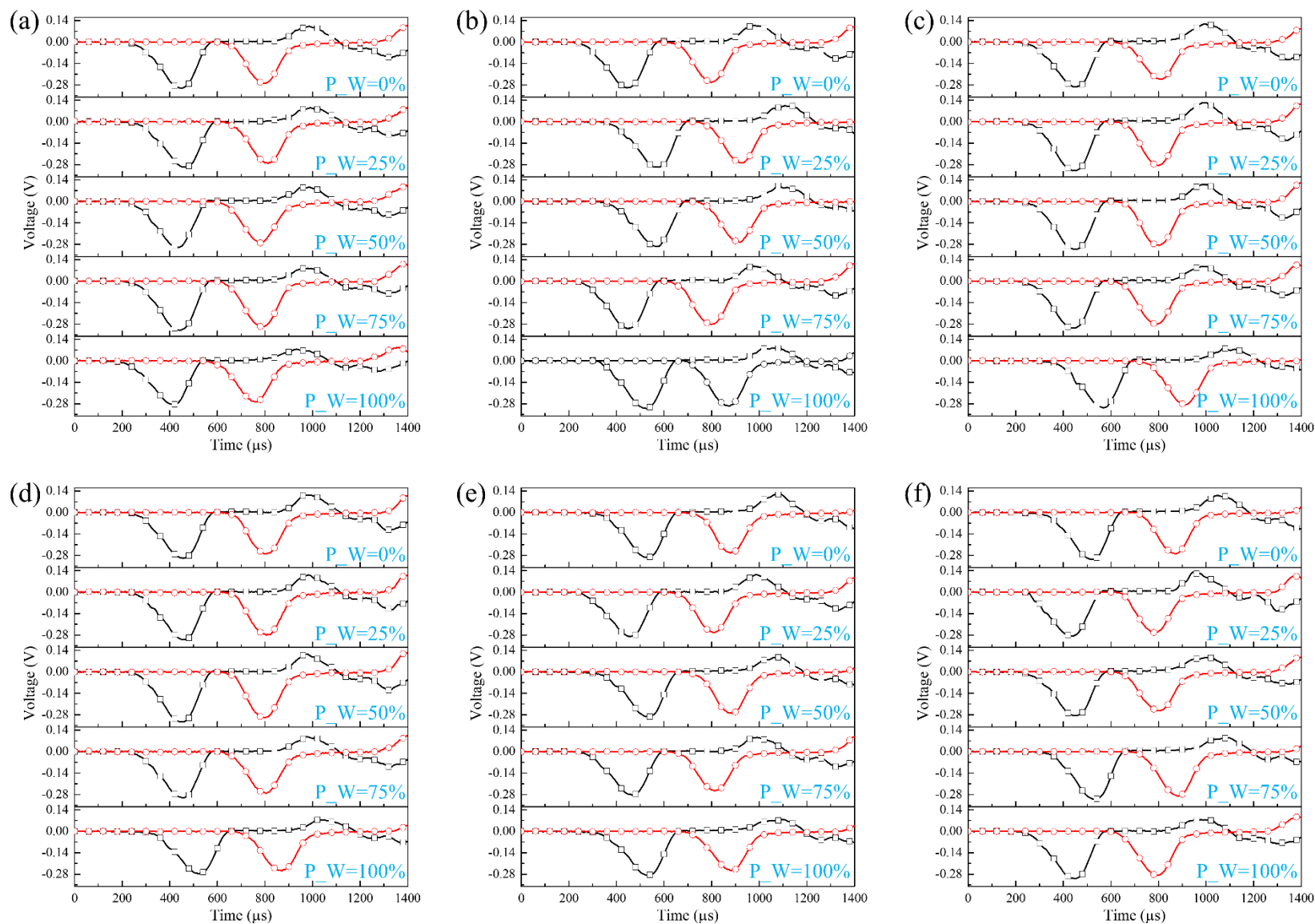
Sample No.	Filling liquid	Liquid content in the joint (by the volume fraction of filling liquid)				
		0%	25%	50%	75%	100%
GD-S1	WG-100	0%	25%	50%	75%	100%
GD-S2	WG-90	0%	25%	50%	75%	100%
GD-S3	WG-80	0%	25%	50%	75%	100%
GD-S4	WG-70	0%	25%	50%	75%	100%
GD-S5	WG-0	0%	25%	50%	75%	100%

## 6.3 Results and analysis

### 6.3.1 The interaction of stress waves with single fluid-filled rock joints

#### 6.3.1.1 Typical signals recorded by the strain gauges

Figure 6.3 presents the smoothed typical signals recorded by strain gauges for various rock specimens with single water-filled joints subjected to dynamic impacting. The approximately identical half-sine waveforms of incident pulses are observed in Figure 6.3, indicating that the applications of an approximately constant driving gas pressure and a proper pulse shaper successfully result in the reliable and repeatable incident waves in this experiment. Meanwhile, the transmitted pulses are almost in the same shape for different water-filled rock joints, indicating that varying joint geometrical properties and filling conditions have negligible influence on the waveform of transmitted signals. Additionally, it is shown that the amplitude of transmitted waves across the fluid-filled joint slightly increases with increasing water content in the joint regardless of the JMC and joint thickness. Besides, under an approximately constant water content, the amplitude of transmitted waves through the fluid-filled joint declines as the JMC decreases, while it increases with the decreasing joint thickness. The above observations suggest that the joint contact area, the joint thickness, and the filling water volume content play an important role in the high-intensity stress wave propagation across single fluid-filled rock joints.



(to be continued)



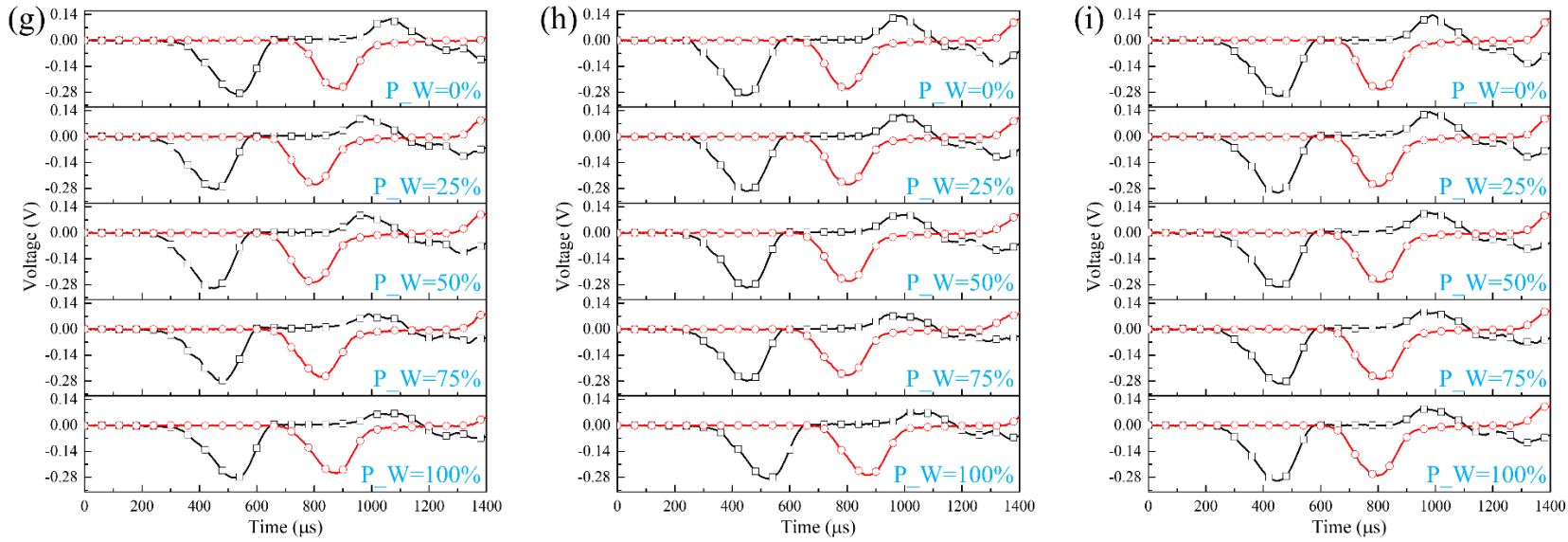


Figure 6.3 Typical waveforms obtained from the SHPB tests for various jointed rock specimens (a) GA-I-S1, (b) GA-II-S1, (c) GA-III-S1, (d) GB-I-S1, (e) GB-II-S1, (f) GB-III-S1, (g) GC-I-S1, (h) GC-II-S1, (i) GC-III-S1 under different filling conditions. Note that the black and red curves represent the signals recorded by the strain gauges mounted on the incident and transmitted bars, respectively. Besides,  $P\_W$  stands for the filling water volume content in the rock joint.

### 6.3.1.2 Stress-deformation relations of single fluid-filled rock joints

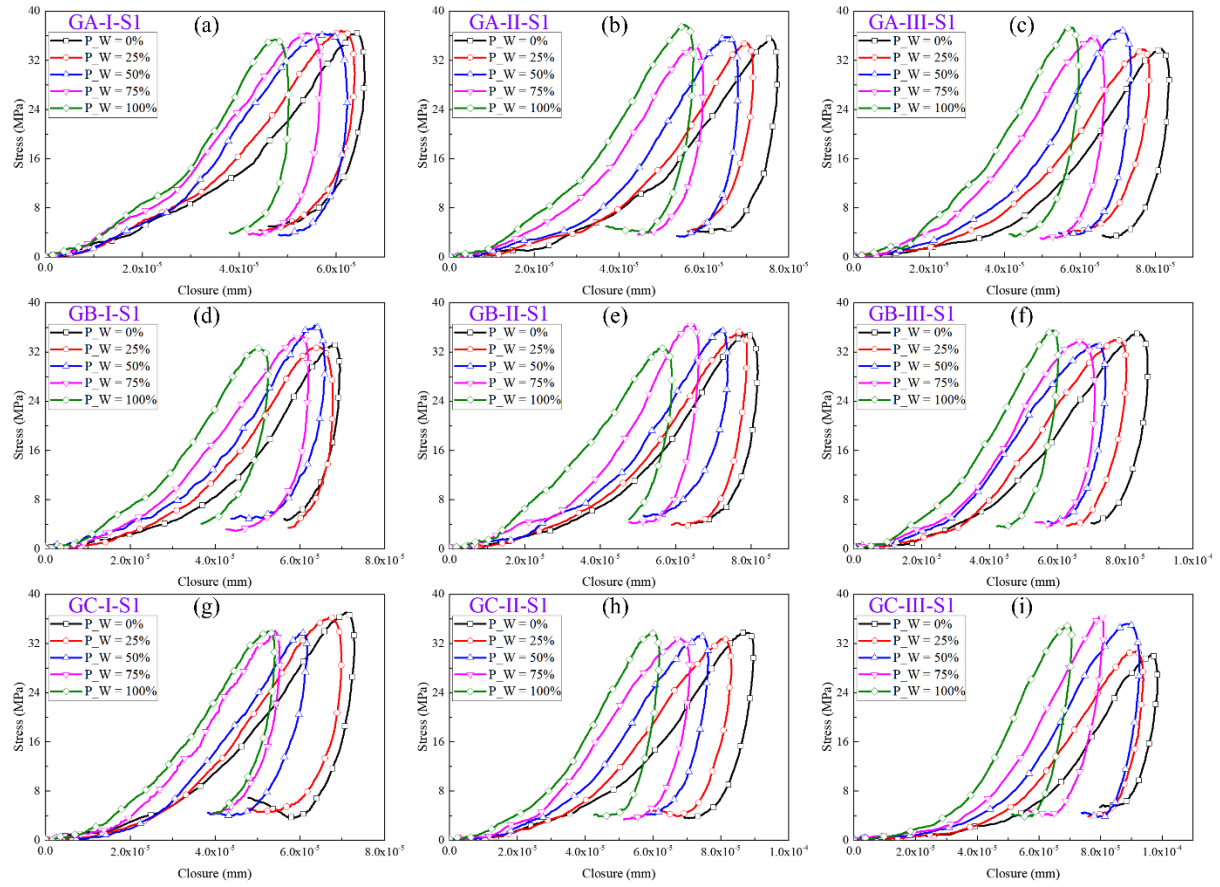


Figure 6.4 The typical stress-deformation curves of single fluid-filled rock joints for different test cases: the effects of water content within the joint.

Figure 6.4 presents the stress-deformation curves of nine representative rock joints under varying water filling conditions. It should be mentioned that the change in the dynamic normal stress produces the deformation of both the contact areas and the joint asperities, leading to a displacement across the joint referred to as the joint closure (Jaeger et al., 2009). In Figure 6.4, three deformation stages, i.e., the compaction, elastic and rebound phases, can be identified from the dynamic stress-closure curves of single fluid-filled rock joints. In the compaction phase, the pre-existing micro-cracks in the asperities as well as the micro-scale voids between the asperities and their connecting joint surface are closed due to the increasing normal stress. Following that, as the normal stress continuously increases to the peak value, the rock joint exhibits an approximately linear deformation in the elastic stage. Note that those two phases constitute the loading process of the joint deformation. It can be concluded from the Figure 6.4 that, during the loading process, the fluid-filled rock joint exhibits a nonlinear stress-closure relation, and the nonlinearity is highly related to the fluid filling condition. In the rebound phase

that refers to the stress-closure curve after reaching the peak stress, the joint closure might increase a little to the maximum deformation and then decrease, indicating the occurrence of an unloading process. At the beginning of the unloading process, the restored elastic energy exceeds the input stress wave energy, causing the release of elastic deformation energy that manifests as a decrease in the joint closure. It is shown that the joint deformation does not fully recover, which is due to the irrecoverable plastic deformation and the wave energy dissipation.

Figure 6.4 reveals that the water content within the rock joint has an apparent effect on the stress-deformation relations of the joint. It is found that the stress-deformation curve for the rock joint with a higher filling water content exhibits a shorter and steeper compaction phase. The compaction of the joint during the initial loading is attributed to the closure of the micro-cracks in the joint asperities as well as the deformation of the micro-scale apertures between joint asperities and the planer surface. Filling water replaces the air in some large voids between joint surfaces and micro-scale apertures between the joint asperities and the contacting surface, reducing the compressibility of those regions and thus causing a decrease in the joint compliance at the macroscopic scale. Regarding the elastic stage, the presence of water in the joint slightly affect the elastic deformation of partially fluid-filled rock joints while it significantly reduces the elastic deformation of the joints full of water. Specifically, with the increasing filling water content, the larger elastic deformation proportion of the pre-peak stress-closure curve is observed, indicating that the more water in the joint, the greater the elastic deformation of the joint. It means that filling water can improve the resistance capacity of the rock joint to deform elastically, particularly at the fully filling condition. Figure 6.4 also shows that the peak joint closure gradually decreases with the increasing filling water content. It is mainly because that filling water is less compressible and thus improve the joint resistance to deform under the normal dynamic stress. Furthermore, as the water content increases, the residual joint closure shows a nearly decreasing tendency, indicating that more reversible deformation of the joint occurs when more water exists in the rock joint.

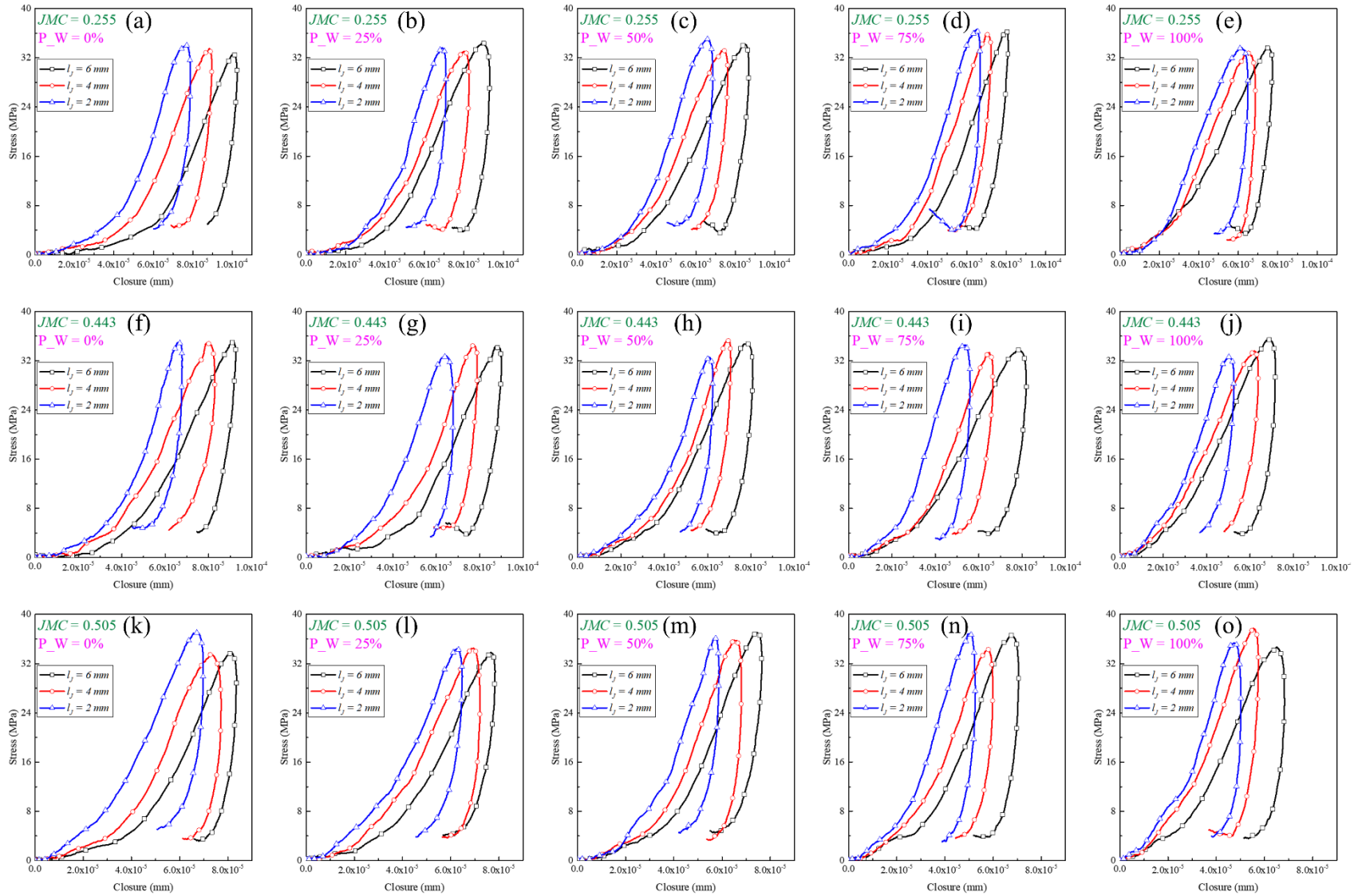


Figure 6.5 The typical stress-deformation curves of single fluid-filled rock joints for different test cases: the effects of the joint thickness.

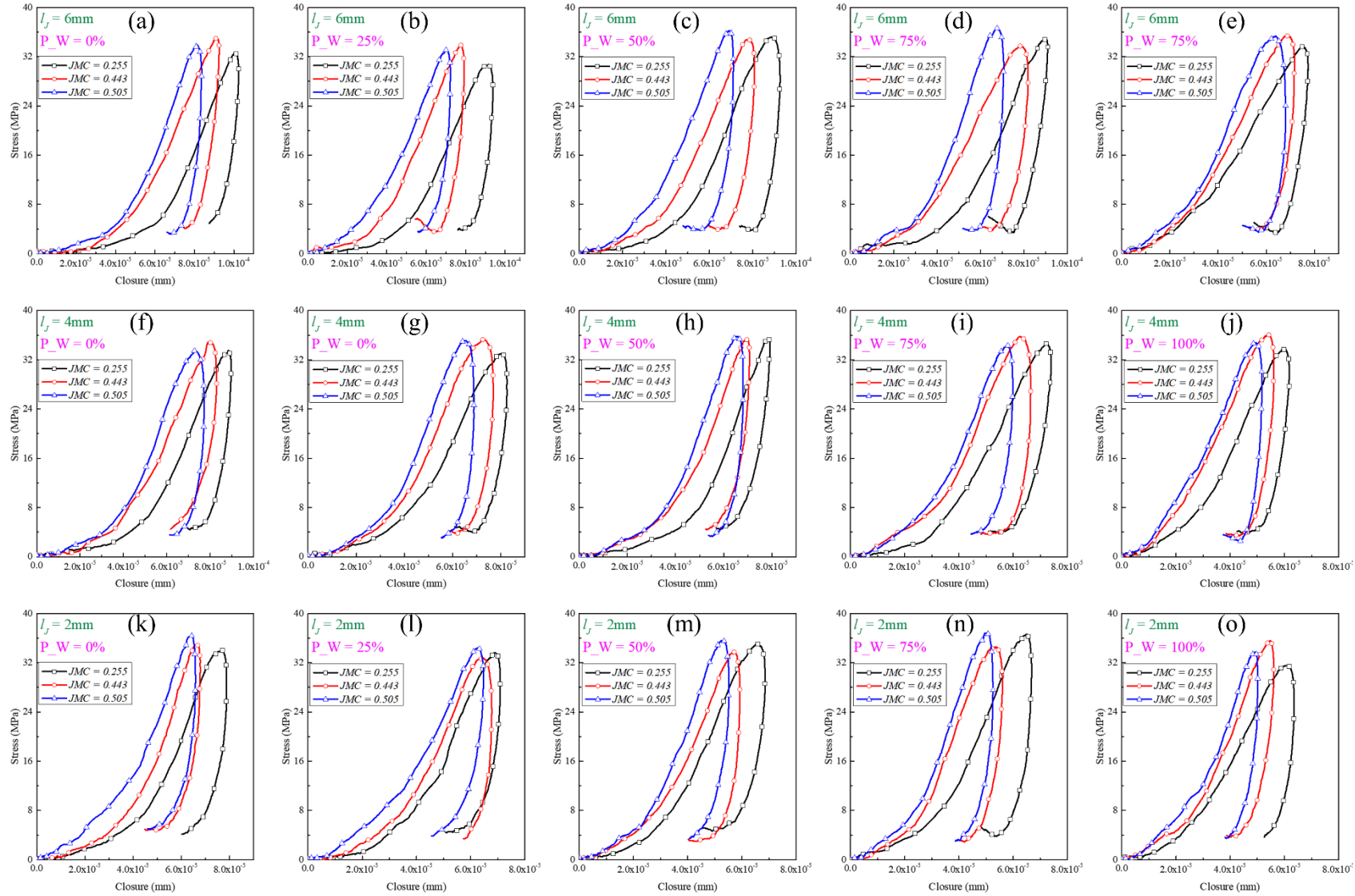


Figure 6.6 The typical stress-deformation curves of single fluid-filled rock joints for different test cases: the effects of the JMC.

Figure 6.5 illustrates the effects of joint thickness on the stress-deformation relations of single rock joints. It is shown that, at a given JMC and an identical water content, the increasing joint thickness leads to an increase in the joint closure. This suggests that the thicker joint is more compressible than the thinner joint under the same condition. Besides, as the joint thickness decreases, the linear portion of the pre-peak stress-deformation curve becomes steeper. It is also found that for the rock joint with the larger thickness, the unloading curve is more open, and the corresponding residual joint closure is greater. The similar phenomena have been observed in previous experimental studies (Hopkins et al., 1990), which suggest that the compliance of fluid-filled rock joint increases with the joint thickness (Lubbe et al., 2008). The explanation is that the joint closure is comprised of the deformation of joint asperities in contact and the deformation of the contacting surface. The joint asperities of the thicker joint own the larger height and thus deform more significantly under the normal stress. Accordingly, the joint closure increases with increasing joint thickness.

Figure 6.6 demonstrates the influences of the JMC on the stress-deformation relations of single fluid-filled rock joints. For rock joints with the approximately same joint thickness and water content, the larger the value of JMC, the smaller joint closure there is, which implies that an increase in the contact area leads to a decrease in joint deformation. It is also found that the nonlinearity is more profound for rock joints with the smaller JMC, indicating that the rock joint owning the smaller contact area is more compliant. Those observations are consistent with the findings reported by Hopkins et al. (1990), which indicate that the increasing contact area results in a decrease in the normal compliance of joint (Lubbe et al., 2008). Furthermore, the comparison between Figure 6.5 and 6.6 reveals that the effects of the contact areas on the mechanical behaviour of the joint are more significant than the effects of the joint thickness, which is consistent with findings in numerical modelling in Lissa et al. (2019).

From Figures 6.4-6.6, it can be concluded that the stress-closure behaviour of single fluid-filled rock joints is concave-shaped under the normal dynamic loading, regardless of the filling water content, the joint thickness and the JMC, which is consistent with findings in previous experimental studies (Barton et al., 1985, Pyrak-Nolte et al., 1987, Cook, 1992). In the compaction stage, the nonlinearity of the joint deformation results from the increasing of joint contact area incurred by the deformation of asperities instead of the linear asperity deformation. More specifically, the plastic, nonlinear joint deformation is largely confined to the tips of joint asperities, which has a limited effect on the overall elastic response of the joint. The elastic



joint deformation indicates that the dynamic normal stress does not exceed the elastic limit of the joint.

### 6.3.1.3 Specific stiffnesses of single fluid-filled rock joints

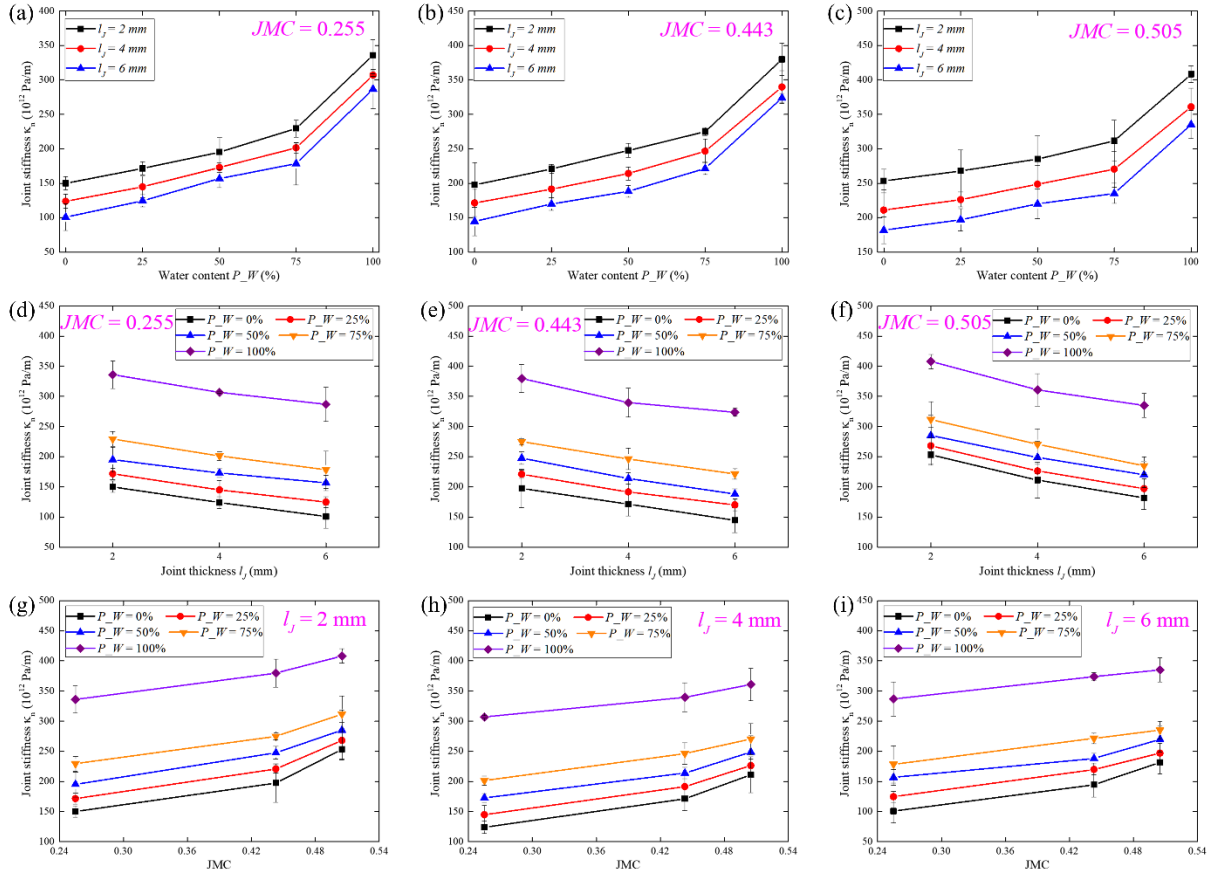


Figure 6.7 The calculated joint normal specific stiffness of individual fluid-filled rock joints: (a) - (c) for the effects of the water content within the joint, (d) - (f) for the effects of the joint thickness, and (g) - (i) for the effects of the JMC.

The normal specific joint stiffnesses of single fluid-filled rock joints are obtained from their stress-closure relations using the method presented in Chapter 3, which are illustrated in Figure 6.7 to further evaluate the effects of the water content, the joint thickness and the JMC on the mechanical response of single fluid-filled joints induced by the passing high-intensity stress wave.

Figures 6.7a-6.7c show that, for fluid-filled rock joints with the approximately identical joint thickness and JMC, the joint stiffness increases with the increasing water content within the joint. It is worthy to noted that a pronounced increase in the joint stiffness at the fully filling

scenario is observed for rock joints, whereas the joint thickness slowly increases with the water content for partially fluid-filled rock joints. For instance, at a joint thickness of about 4mm and JMC of around 0.443, the joint stiffness increases by near 13.5% as water content increases from 50% to 75%, while it increases by about 39.8% as water content rises from 75% to 100%. The distinct discrepancy can also be observed from Figures 6.7d-6.7i. It could be attributed to two reasons. First, in partially filling conditions, there is enough void space for filling water to diffuse; and hence the slight increase in the joint stiffness mainly results from the small increment of compressibility induced by the substitution of air with water (Pyrak-Nolte et al., 1990). Second, for rock joints full of water, there is no space for water to instantaneously response to the normal incidence of the high-intensity stress wave. Given that the dynamic stress wave passes the fully water-filled joint in a short time, the fully filling condition is analogous to the undrained situation in which the compressibility of joint is severely reduced by the less compressible water (Huang et al., 2020). Correspondingly, the anomalously large increase in the joint stiffness occurs at fully water-filled condition.

Figures 6.7d-6.7f reveal that the joint stiffness exhibits an approximately linear decreasing trend with the increasing joint thickness regardless of the water content and the JMC. The similar results have been observed in previous studies (Hopkins et al., 1987, Li et al., 2010, Chen et al., 2015). This is because that the joint thickness proportional to the height of asperities in contact. The shorter joint asperities in contact are less compressible (Hopkins et al., 1987). Consequently, the thinner fluid-filled rock joint is stiffer than the thicker ones. The other explanation is that the increasing joint thickness causes the larger void space and thus increases the volume of water under the same water volume content. Correspondingly, the fluid-filled rock joint becomes more compressible as the joint thickness increases, resulting in a decrease in the joint stiffness (Huang et al., 2020).

Figures 6.7g-6.7i indicate that the increasing JMC results in a nonlinear increase in the joint stiffness regardless of the water content and the joint thickness. This implies that the fluid-filled rock joint becomes stiffer as the contact area increases. It is mainly due to the fact that the contact regions own much larger stiffness than the void space and thus dominate the overall joint stiffness (Zimmerman et al., 1990). Additionally, the increasing rate of joint stiffness becomes greater as the contact area increases. For example, regarding rock joints with the water content of 25% and the joint thickness of 4mm, the joint stiffness increases by 27.9% as the contact area increase by 73.7% (i.e., the JMC from 0.255 to 0.443) while it increases by 10% as the contact area increases by 14% (i.e., the JMC from 0.443 to 0.505). This could be



attributed to the effect of spatial geometry of the joint contact areas. The dispersed contact areas lead to a stiffer joint compared to the cluster contact areas (Hopkins et al., 1987). Correspondingly, the joint surface with the smaller JMC has the more dispersed contact areas (see Figure 6.2), resulting in an additional increment of the joint stiffness. The above-described observations from Figures 6.7g-6.7i agree to some extent with the findings in experimental studies of single rock joints (Myer et al., 1985, Hopkins et al., 1990, Chen et al., 2015, Li et al., 2017).

#### **6.3.1.4 Energy evolution characteristics of the rock specimens with single fluid-filled joints**

With the Equations 3.15-3.18, the energy-time history evolution curves of the incident, transmitted, reflected and absorbed energy for the tested rock specimens with single fluid-filled joints are obtained based on the collected laboratory data. Given that the similar energy evolution characteristics are observed from all the jointed rock specimens, the representative energy-time history curves for the rock specimens with single water-filled joint at an approximately identical JMC of 0.443 are plotted in Figure 6.8 to illustrate the effects of the joint thickness, whereas the typical energy-time history curves for the rock specimens with single water-filled joint at an nearly same joint thickness of 4 mm are presented in Figure 6.9 to demonstrate the influences of the joint contact area. Figures 6.8-6.9 also show that the energy evolution characteristics of the jointed rock specimen are heavily related to the filling water content within the joint.

It can be seen from Figures 6.8 and 6.9 that, as the incident stress wave penetrates a jointed rock specimen, the energy transmitted through the rock specimen occupies the largest proportion of the incident energy, while the reflected energy accounts for the smallest portion of the incident energy. Additionally, the rest of the incident energy is absorbed by the jointed rock specimen mainly for the elastic energy storage and the dynamic responses of the fluid-filled joint. More specifically, the absorbed energy could consist predominantly of three parts, i.e., kinetic energy for filling water flow, inertial friction energy consumed by the filling water, and the deformation energy for the joint closure. Similar to the development of the stress-deformation relation of single rock joints, the process of the energy evolution of the rock specimen with a fluid-filled joint can be briefly divided into three phases:

- 1) The compaction stage: This phase corresponds to the initial compacting associated with the normal wave incidence into the tested rock specimen. It is found that the slopes of the transmitted and absorbed energy curves are very small, whereas the reflected energy rapidly increases as the stress wave passes. The main explanation is that, as the incident wave arrives at the joint interface, a part of the incident energy is reflected by the voids surrounding the contacting joint asperities while the rest is consumed by the deformation of micro-cracks/pores and micro-scale apertures within the fluid-filled joint.
- 2) The elastic stage: During the period, the absorbed energy increases rapidly up to the peak value with the sharply linear increase of the incident energy. It is mainly due to that the passing high-intensity stress wave results in severe flow of filling water within the joint, producing significant kinetic energy and the inertial friction energy, which is manifested as an abrupt increase in the absorbed energy. At the meantime, a linearly fast increase in the transmitted energy occurs while the reflected wave energy increases at a relatively slower rate. It is attributed to that the joint stiffness increases with the increasing applied stress associated with the passing wave (Cook, 1992). According to the existing theories, the stiffer joint allows more wave energy to transmit while it reflects less wave energy (Pyrak-Nolte et al., 1990, Zhu et al., 2011).
- 3) The release stage: In this phase, the incident and transmitted energy continuously increases for a short duration before reaching the peak values, and then the post-peak energy curves remain horizontal, indicating that the dynamic loading associated with the passing wave basically ends. Besides, the reflected energy progressively increases at a slow rate, which could be explained by the multiple reflections and transmissions generated between the bar-specimen interfaces and the joint interfaces during the wave propagation across the tested rock specimen (Li et al., 2017). By contrast, the absorbed energy declines at a gradually decreasing rate, which is mainly attributed to the release of elastic deformation energy. At the end of stage, a part of absorbed energy cannot be recovered, termed as the residual absorbed energy, for that it is largely dissipated by the dynamic response of filling water in the joint.

From Figure 6.8, it is found that, at the given JMC and the water content, the peak absorbed energy increases with the increasing joint thickness. In addition, the slope of the pre-peak portion of the absorbed energy curve becomes steeper as the joint thickness increases. Those phenomena could be mainly explained by that the increasing joint thickness weakens the joint

resistance to deform under the dynamic loading associated with the passing wave. Correspondingly, for the thicker fluid-filled joint, more energy is consumed by the joint deformation induced by the high-intensity stress wave. Another possible reason is that the thicker joint leads to the longer travelling path for the passing wave and thus causes more energy dissipation.

Figure 6.9 shows that, at the approximately identical joint thickness and water content, an increase in the JMC results in the smaller peak absorbed energy, and it causes the absorbed energy to rise at a relatively slower velocity before reaching the maximum value. This implies that the joint with the larger contact area exhibits a more moderate wave absorption tendency. The principal explanation is that an increase in the contact area stiffens the fluid-filled joint. As a result, less energy is consumed by the deformation of the joint, thereby decreasing the total absorbed energy. In addition, as the contact area increases, there are the less interconnected voids and smaller volume of water within the joint. Accordingly, the energy loss caused by the wave-induced water flow declines, reducing the overall energy absorption of the fluid-filled joint.

Regarding the effects of the water content within the joint, it can be observed from Figures 6.8 and 6.9 that the peak absorbed energy decreases with the increasing water content for fluid-filled rock joints with the approximately identical joint thickness and JMC. The main explanation is that the increase in the water content reduces the joint compliance and thus degrades the joint deformation (see Figure 6.4). Accordingly, less energy is consumed by . In addition, it is found that the slope of the pre-peak portion of the absorbed energy evolution curve decreases with the increasing water content, which means that the absorbed energy increases at a faster rate for the joint with the lower water content. This could also be attributed to the reduction in the joint compliance induced by the water addition. The more compressible rock joint consumes more deformation energy as the . Furthermore, the time difference between the moments at which the incident and absorbed energy maximizes becomes larger with the increasing water content, particularly for the higher water content.

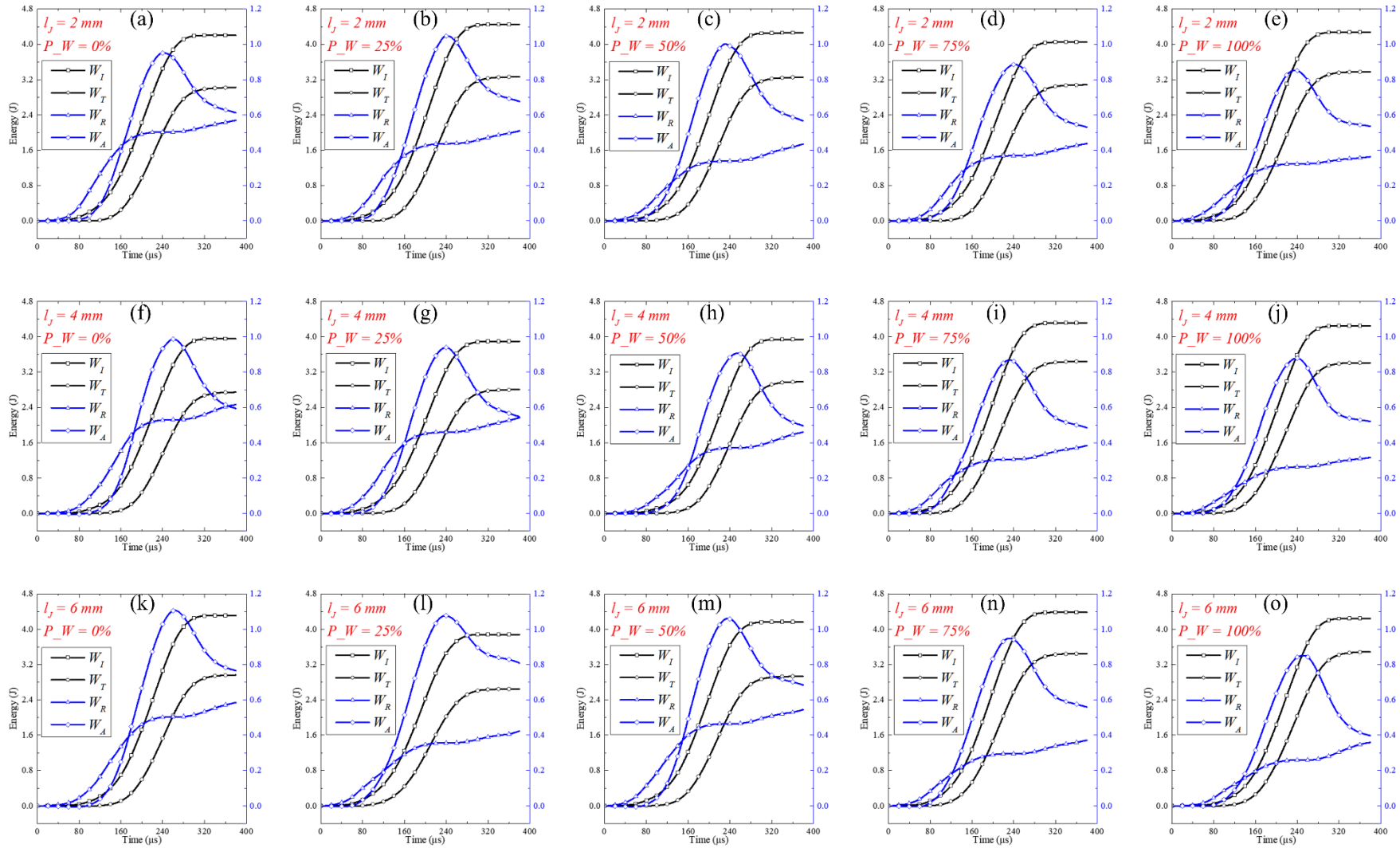


Figure 6.8 The representative energy-time history curves for the tested rock specimens with single fluid-filled joints at an approximately identical JMC of 0.443: (a)-(e) for the joint thickness of 2 mm, (f)-(j) for the joint thickness of 4 mm, (k)-(o) for the joint thickness of 6 mm.

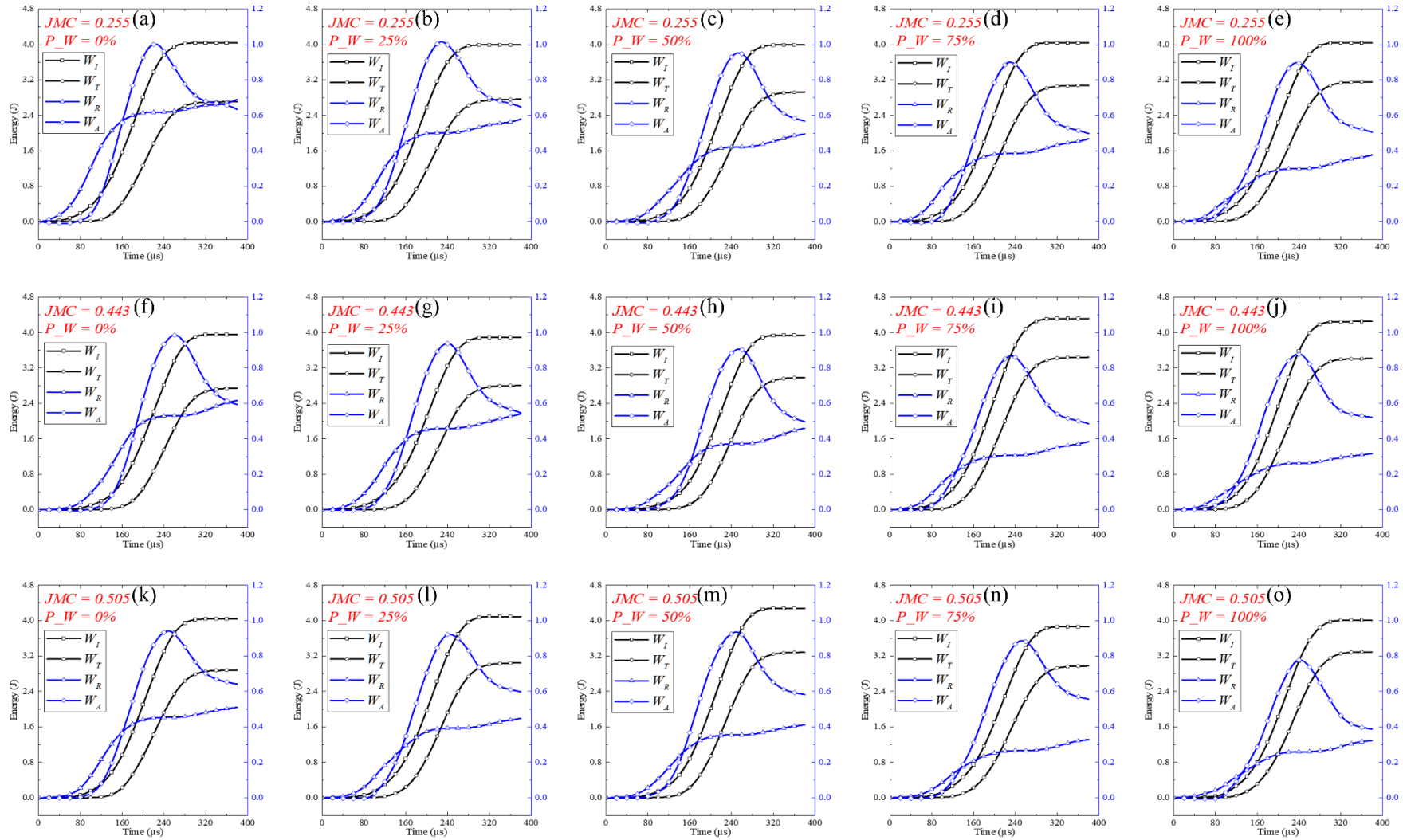


Figure 6.9 The representative energy-time history curves for the tested rock specimens with single fluid-filled joints at an approximately identical joint thickness of 4 mm: (a)-(e) for JMC of 0.255, (f)-(j) for the JMC of 0.443, (k)-(o) for the JMC of 0.505.

### 6.3.1.5 Transmission and reflection coefficients for the rock specimens with single fluid-filled joints

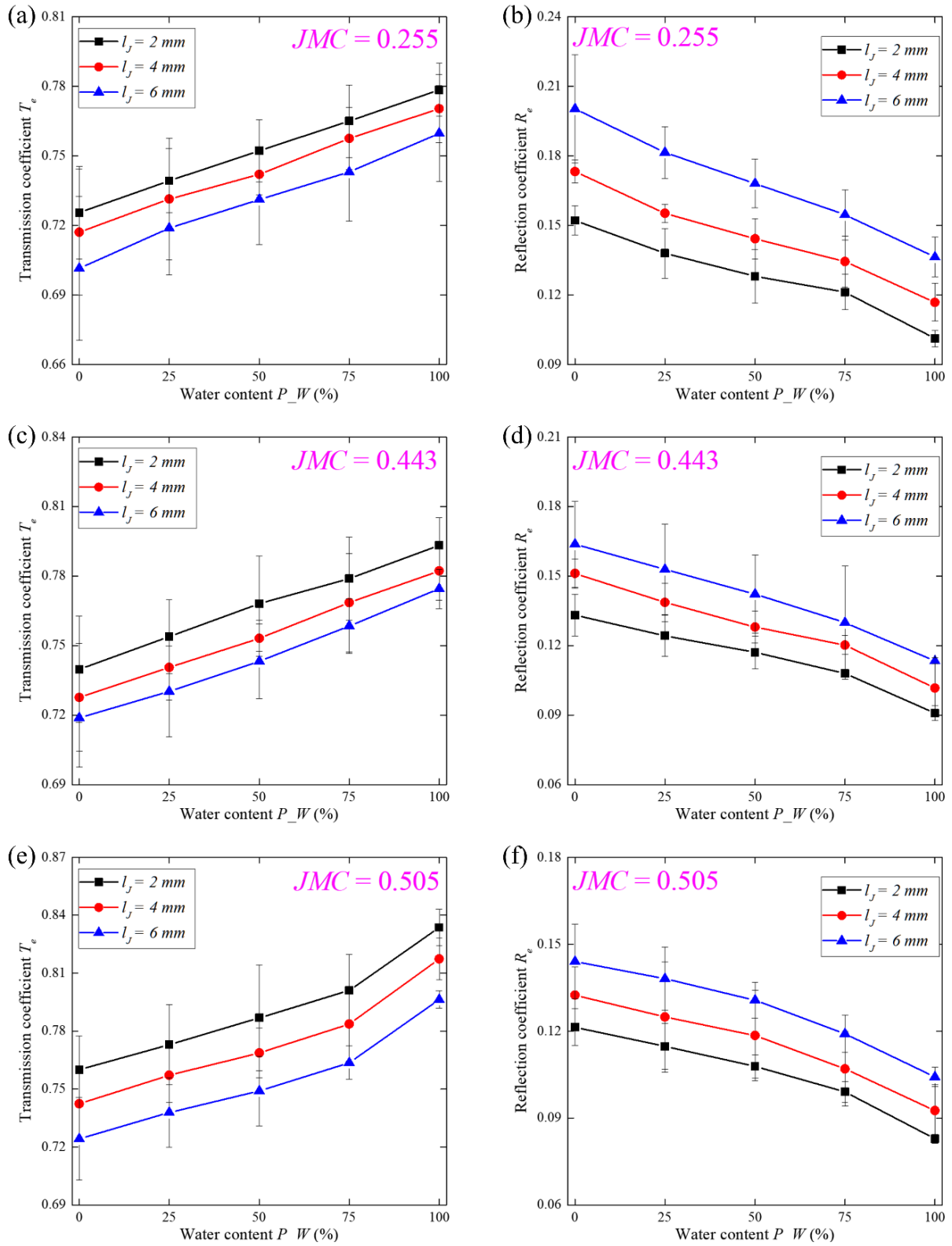


Figure 6.10 The calculated transmission and reflection coefficients for various fluid-filled rock joints: the effects of the water content within the joint.

The transmission and reflection coefficients for the rock specimens with single fluid-filled rock joints are calculated using the Equations 3.19 and 3.20, respectively, which are plotted as a function of the water content in Figure 6.10. It is shown that, at a specific JMC and a nearly constant joint thickness, the transmission coefficient gradually increases with the increasing water content, whereas the reflection coefficient decreases as the water content increases. This is mainly because the addition of water to some extent enhances the normal joint stiffness (see Figure 6.7). Correspondingly, less wave is reflected yet more wave is transmitted at the joint interface for a joint owning higher joint stiffness. Figure 6.10 also shows that the variation in the transmission coefficient is smaller than the change in the reflection coefficient under the same test condition. For example, when the water content within the joint owning the JMC of 0.443 and the joint thickness of 4 mm increases from 25% to 75%, the transmission coefficient increases by nearly 5.5% while the reflection coefficient decreases by about 13.3%. It could be attributed to that the wave reflection is predominantly governed by the joint stiffness while the transmission of wave is also affected by the fluid pressure diffusion within the fluid-filled joint (Barbosa et al., 2016). Specifically, as the incident stress wave impinges upon a single fluid-filled rock joint, the reflection of wave occurs from the moment when the incident stress wave arrives at the joint surface. At the meantime, the rest of the incident stress wave penetrates the joint and causes the wave-induced fluid flow within the joint, which attenuates the wave energy and thus to some extent weakens the transmission of wave.

Figure 6.11 shows the effects of the joint thickness on the transmission and reflection coefficients through single fluid-filled rock joints. It can be observed that, the increasing joint thickness reduces the transmission coefficient but improves the reflection coefficient regardless of the JMC and the fluid filling condition. This is in accordance with the findings reported by previous experimental tests on single rock joints (Li et al., 2010). The principal explanation is that the increasing joint thickness leads to a decrease in the joint stiffness (see Figure 6.7). Consequently, more wave is reflected at the joint surface while less wave can transmit across the joint due to the higher compressibility contrast between the joint and the background rock body (Barbosa et al., 2016). In addition, the increase in the joint thickness results in the higher joint permeability (Zimmerman et al., 1990), and hence more reflection of fast P-wave occurs and more significant slow P-wave (i.e., the wave mode associated with the fluid pressure diffusion) is generated as the high-intensity stress wave passes through the fluid-filled joint (Nakagawa and Schoenberg, 2007). This could be partly responsible for the variations in the transmission coefficient induced by the changing joint thickness.



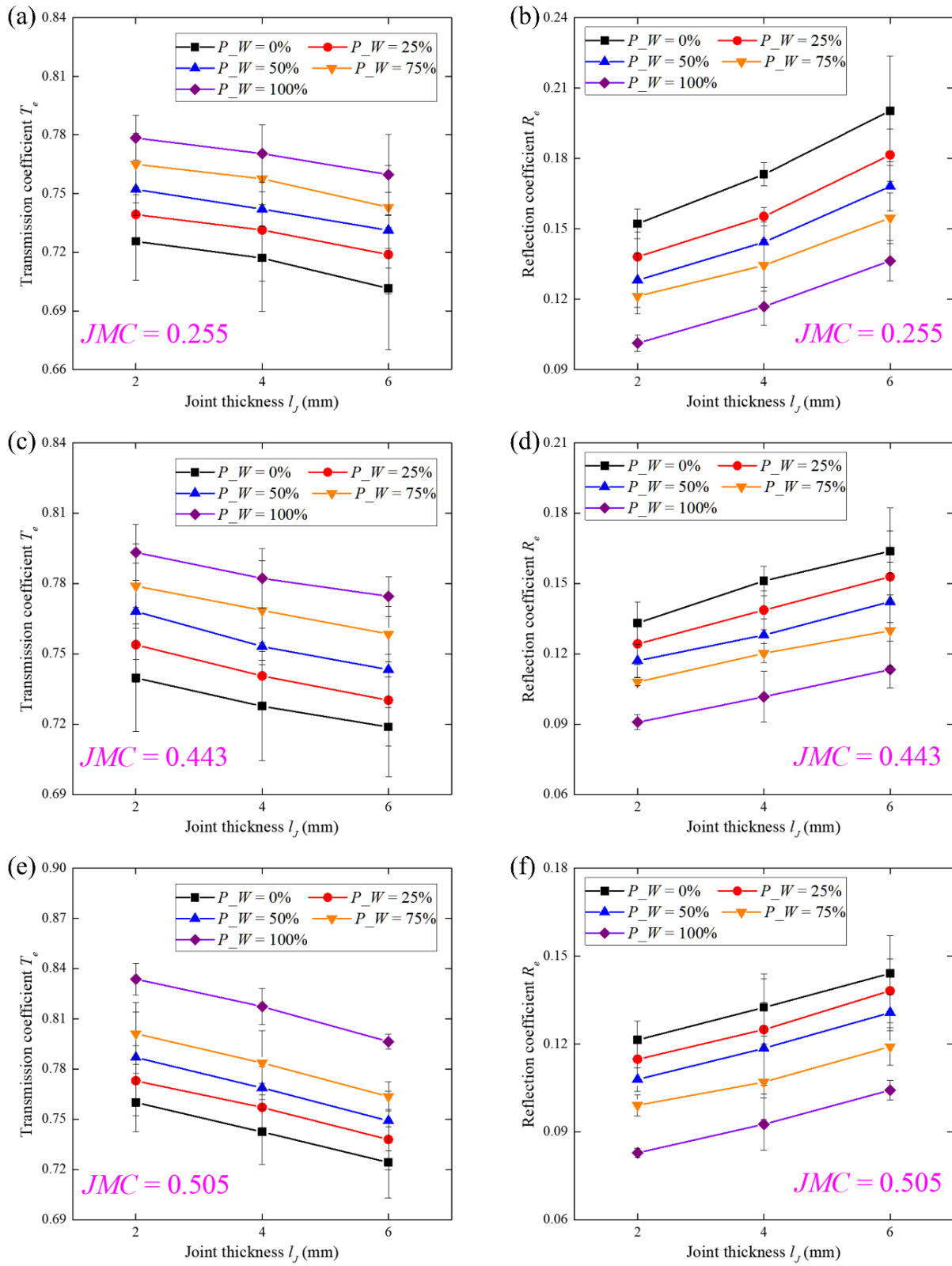


Figure 6.11 The calculated transmission and reflection coefficients for various fluid-filled rock joints: the effects of the joint thickness.

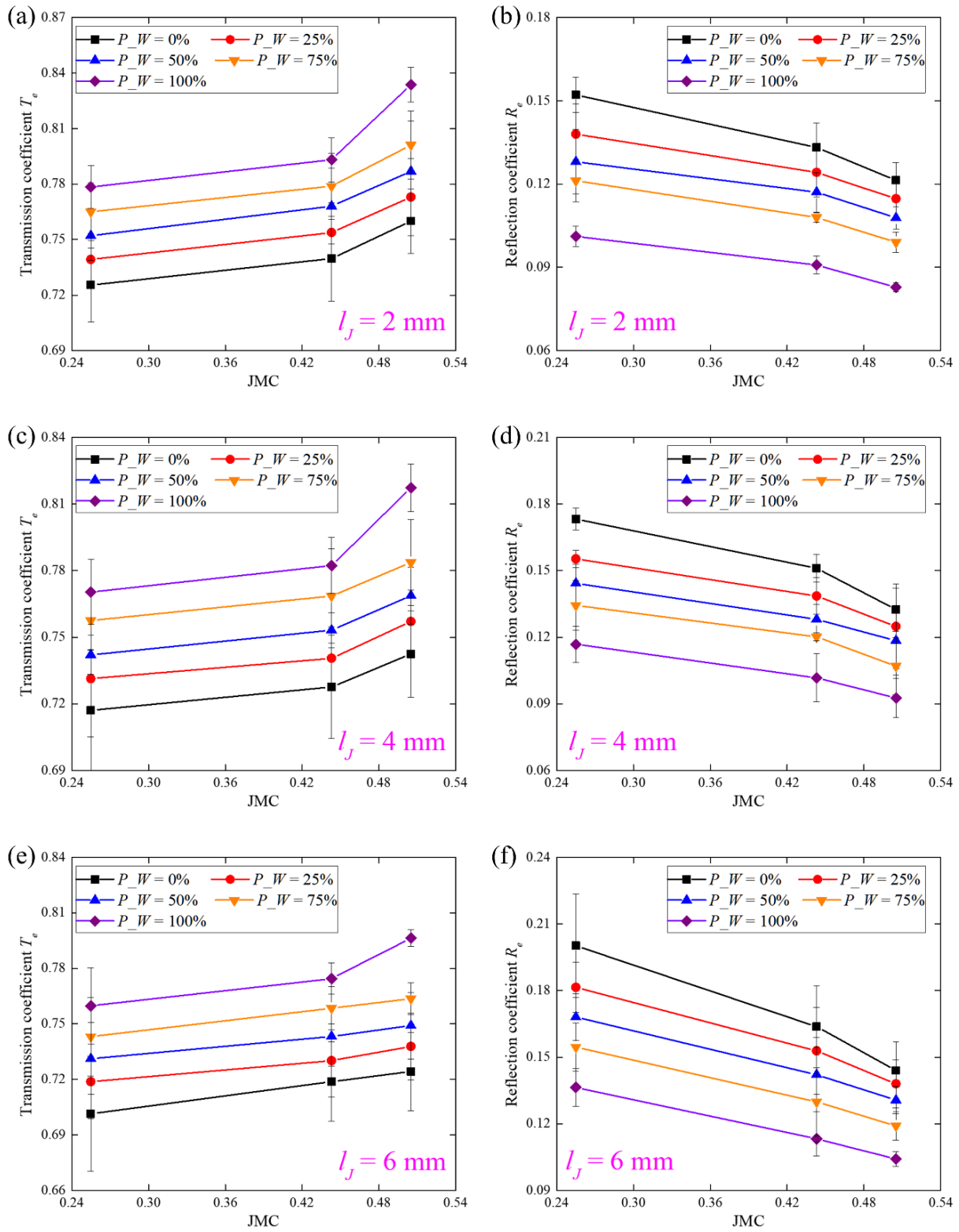


Figure 6.12 The calculated transmission and reflection coefficients for various fluid-filled rock joints: the effects of the JMC.

Figure 6.12 reveals the influences of the contact area on the transmission and reflection coefficients across individual fluid-filled rock joints. It is found that the transmission coefficient increases but the reflection coefficient decreases with the increasing JMC, indicating that the increase in the joint contact area enhances the transmission of wave while it reduces the reflection of wave as the high-intensity stress wave propagates perpendicularly through the fluid-filled rock joint. Similar phenomena were reported by Li et al. (2017), which could be attributed to the enhancement of the joint thickness induced by the increasing contact area (see Figure 6.7). Specifically, the increase in the joint stiffness causes a reduction in the compressibility contrast between the joint and background rock matrix, and hence more wave components can transmit into the joint while less wave reflection occurs at the joint (Barbosa et al., 2016). Moreover, finding in Figure 6.12 could be partly explained by that the increasing contact area reduces the joint permeability (Ishibashi et al., 2018). The joint with higher permeability exhibits a larger reflection of fast P-wave and generates more wave dissipation induced by the wave-induced fluid flow (Nakagawa and Schoenberg, 2007). Correspondingly, the smaller the joint contact area it is, the more the transmission wave and the less the wave reflection occur.

#### 6.3.1.6 Seismic attenuation factor for the rock specimens with single fluid-filled joints

To quantitatively clarify the effects of the filling water content, the joint thickness and the contact area on the wave energy attenuation caused by the water-filled rock joints, the values of the seismic quality attenuation factor  $Q_{sei}$  for all test cases were evaluated through the Equation 3.21. The calculated  $Q_{sei}$  values versus are plotted as functions of the water content, the joint thickness and the JMC, respectively, in Figure 6.13.

In Figures 6.13a-6.13c, there is an inflection point at the water content of 75% for the  $Q_{sei}$  regardless of the joint thickness and JMC. More specifically, the value of  $Q_{sei}$  gradually increases as the water content rises from 0% to 75%, indicating that the overall wave attenuation caused by the rock specimen with single fluid-filled joint slightly decreases with the increasing water content in this range. There are mainly two reasons for this observed result. On one hand, the increasing water content diminishes the compressibility contrast between the joint and the host rock. Consequently, the fluid-filled joint is compressed less and thus the fluid pressure gradients between the air and water regions within the joint are weakened (Hunziker et al., 2018). On the other hand, the generation of the locally shielding zones could to some extent reduce the joint deformation and thus lower the fluid pressure gradients between the

weak and stiff zones within the joint (Kachanov, 1992). As a result, the increasing water content weakens the wave-induced fluid flow within the joint, thereby causing less wave dissipation during the propagation of the high-intensity stress wave. However, for the rock joints at the water content of 100%, the smaller  $Q_{sei}$  values are observed compared to those for the rock joints at the water content of 75%. It means that an unexpected increase in the overall wave attenuation occurs when the water content within the single rock joints increases from 75% to 100%. This could be explained from the standpoint of the fluid dynamics. The rock joint full of water has a significant joint stiffness since it behaves more as almost sealing in the initial phase of the incidence of the stress wave, allowing more wave energy to transmit into the joint. Accordingly, compared to the rock joints in partially filling scenarios, the higher normal dynamic stress is applied to the water within the fully water-filled joint considering that water can support compression. Since only the pre-set small hole can provide the channel for the wave-induced fluid flow, the water within the joint could squirt out at a much higher velocity based on the Bernoulli's principle (Batchelor and Batchelor, 2000). Correspondingly, the kinetic energy associated with the stronger squirt of filling water eventually dissipated at the form of heat loss due to the viscous effect, resulting in more wave attenuation as the high-intensity stress wave penetrates the rock joints full of water.

Figures 6.13g-6.13i shows that the increasing joint thickness results the decreasing  $Q_{sei}$  regardless of the water content and the JMC of the fluid-filled rock joint. Apparent from the continuous decrease in the  $Q_{sei}$  with the joint thickness, the total wave attenuation caused by single fluid-filled rock joints monotonically increases as the joint becomes thicker. It can be attributed to that an increase in the joint thickness reduces the joint stiffness (see Figure 6.7). On one hand, the inelastic deformation related to the joint asperities for the weaker joint is larger and consumes more energy. On the other hand, the propagating wave energy assigned to the filling fluid becomes greater as the joint gets thicker, causing more significant wave-induced fluid flow and thus attenuating more energy. Another possible explanation is that the increase in the joint permeability induced by the increasing joint thickness enhances the wave-induced fluid flow within the joint, causing more wave dissipation. As a consequence, the rock specimen with a thicker fluid-filled joint exhibits the higher overall wave attenuation as the high-intensity stress wave passes across it.

From Figures 6.13d-6.13f, it is observed that, regardless of the water content and the joint thickness, the  $Q_{sei}$  increases with the increasing JMC, implying that wave attenuation becomes less significant as the joint contact area increases. The similar finding has been presented by

Rubino et al. (2014), which can be explained by that the increasing fraction of the contact areas produces a stiffer joint and thus reduces the wave dissipation caused by the wave-induced fluid flow within the joint. In addition, a decrease in the joint permeability induced by the increasing contact area could make some contributions to the declining wave attenuation. Specifically, the smaller the joint permeability it is, the lower level of the wave-induced fluid flow it produces as the high-intensity wave passes through the fluid-filled rock joint. As a result, the increasing contact area leads to a decrease in the overall wave energy dissipation when the high-intensity waves propagate normally across single fluid-filled rock joints.

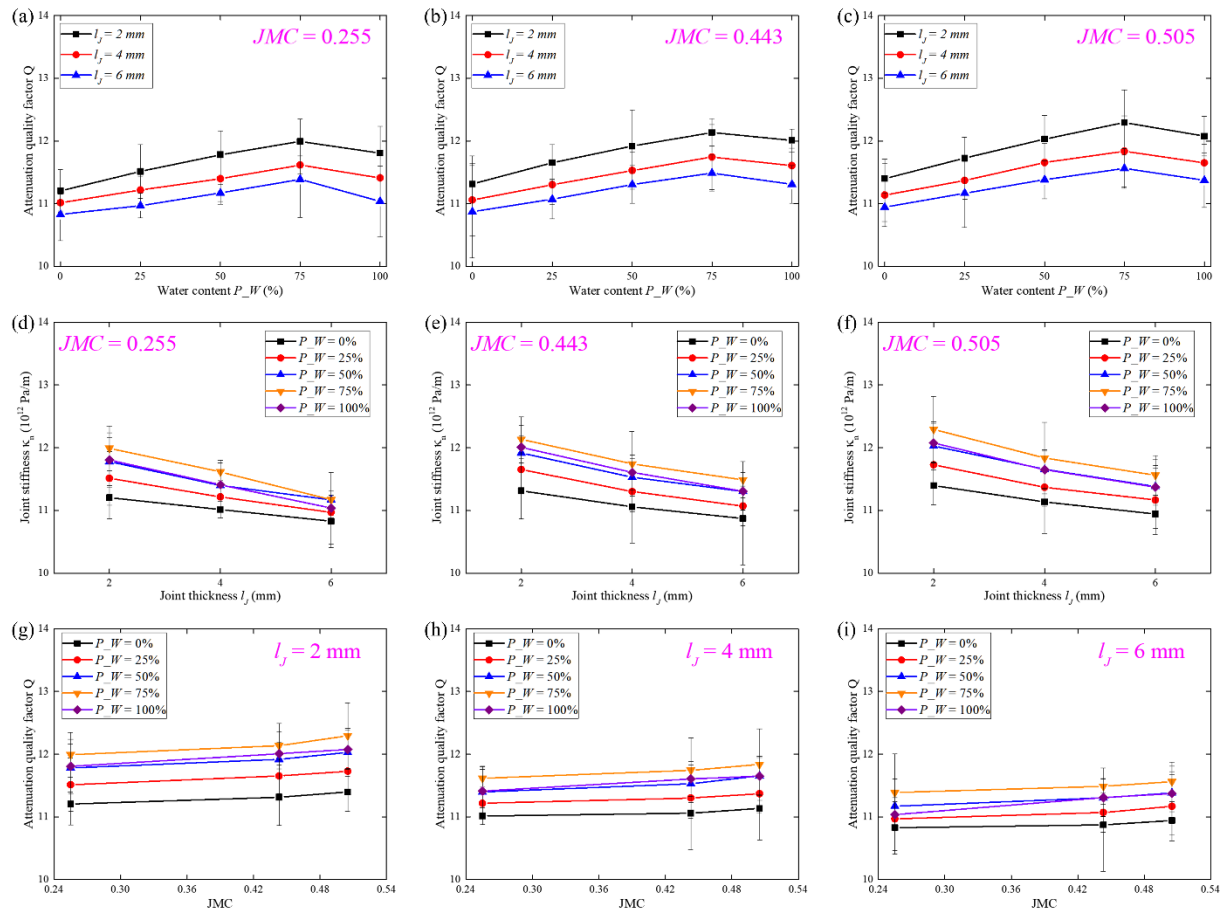


Figure 6.13 The calculated seismic attenuation factor  $Q$  for the tested rock specimens with various single fluid-filled rock joints: (a) - (c) for the effects of the water content within the joint, (d) - (f) for the effects of the joint thickness, and (g) - (i) for the effects of the JMC.

### 6.3.1.7 Frequency spectra for the rock specimens with single fluid-filled joints

Based on the method described in chapter 3, the frequency spectra of the incident, transmitted and reflected signals for all jointed rock specimens tested in this experiment are obtained.

Herein, the representative frequency spectra for the rock specimens with single fluid-filled joints with the approximately same JMC of 0.443 and the rock specimens with single fluid-filled joints at the nearly identical joint thickness of 4 mm are presented in Figure 6.14 and Figure 6.15, respectively, to illustrate the influence of the water content, the joint thickness and the JMC on the wave responses of individual fluid-filled rock joints in the frequency domain. It is shown that, for all test conditions, the energy distribution of the transmitted waves mostly concentrates at the frequencies lower than 7 kHz, while that of the incident wave energy is mainly carried by the frequencies in the 0-8 kHz range. This finding is similar with the observations in previous studies (Pyrak-Nolte et al., 1990, Zhu et al., 2011), which indicating that single fluid-filled joints can act as a low-pass filter that allows wave modes at low frequencies to transmit yet gets rid of the wave components at very higher frequencies when the high-intensity stress waves normally incident on the jointed rock specimens.

According to the difference between the spectral amplitudes of the incident and transmitted waves, the frequency spectra can be divided into three regions, i.e., the low-, intermediate- and the high-frequency parts, as shown in Figures 6.14 and 6.15. In the low-frequency range, the spectral amplitudes of the transmitted waves are evidently smaller than those of the incident waves, indicating that wave modes at those frequencies are significantly attenuated by single rock joints. For the intermediate-frequency part, there is almost no difference between the spectral amplitudes of the transmitted and incident waves, implying that single fluid-filled rock joints allow the wave components within this range to transmit with neglectable attenuation. In the high-frequency band, the spectral amplitudes of both transmitted and incident waves are very smaller and gradually fade away with the increasing frequency. It is clearly identified from Figures 6.14 and 6.15 that the energy of the incident, transmitted and reflected waves are mostly stored within the low- and intermediate-frequency bands. The comparison between the spectral amplitudes of the transmitted and reflected signals unravels that single rock joints owning tightly contacting asperities allows most of incident wave energy to transmit regardless of the water content, the joint thickness, and the contact area. It is due to the fact that the contacting joint asperities controls the joint stiffness and thus dominates the wave responses of the joint.

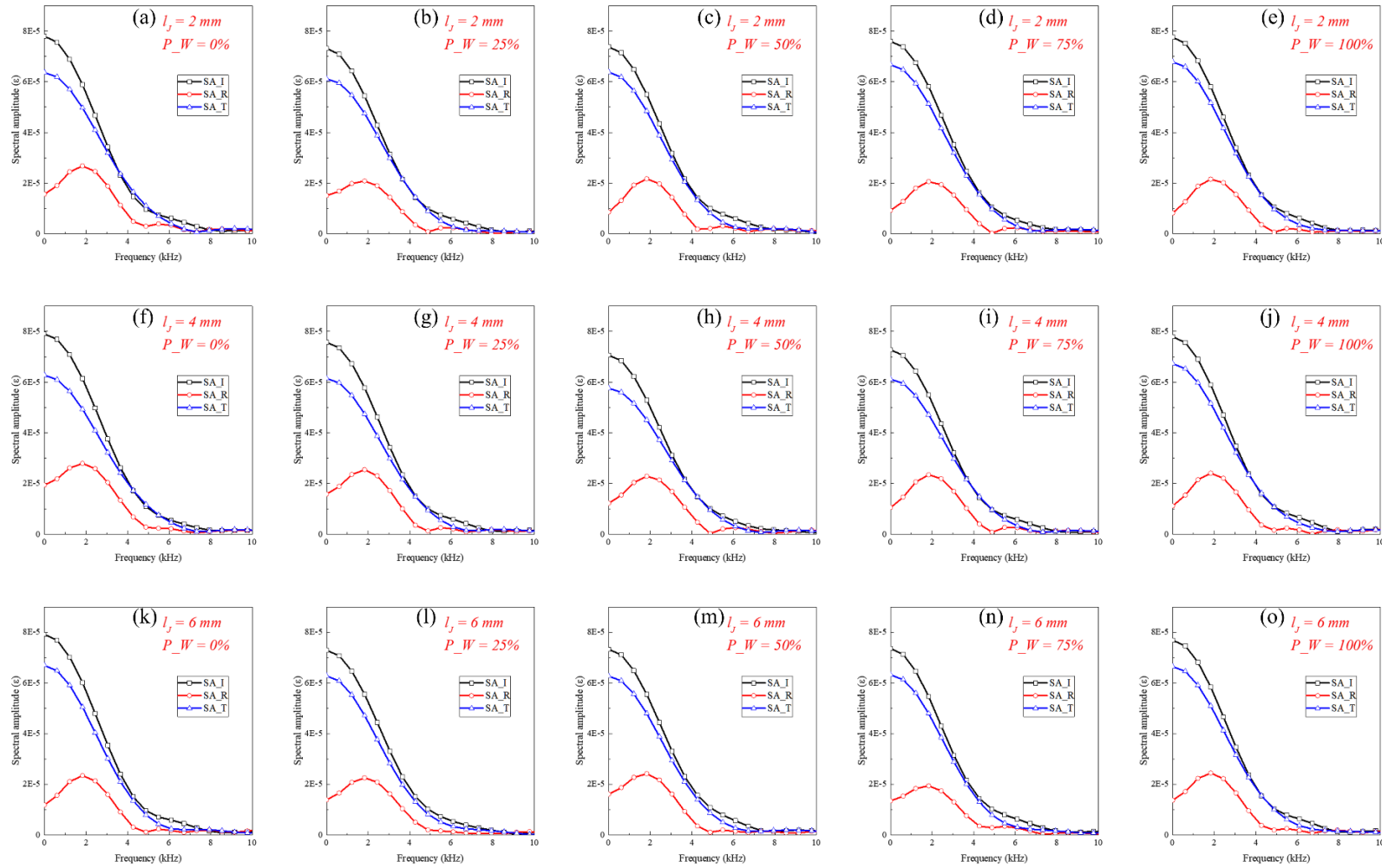


Figure 6.14 The frequency spectra of the incident (SA\_I), transmitted (SA\_T) and reflected waves (SA\_R) for the tested rock specimens with single fluid-filled joints at an approximately identical JMC of 0.443: (a)-(e) for the joint thickness of 2 mm, (f)-(j) for the joint thickness of 4 mm, (k)-(o) for the joint thickness of 6 mm.



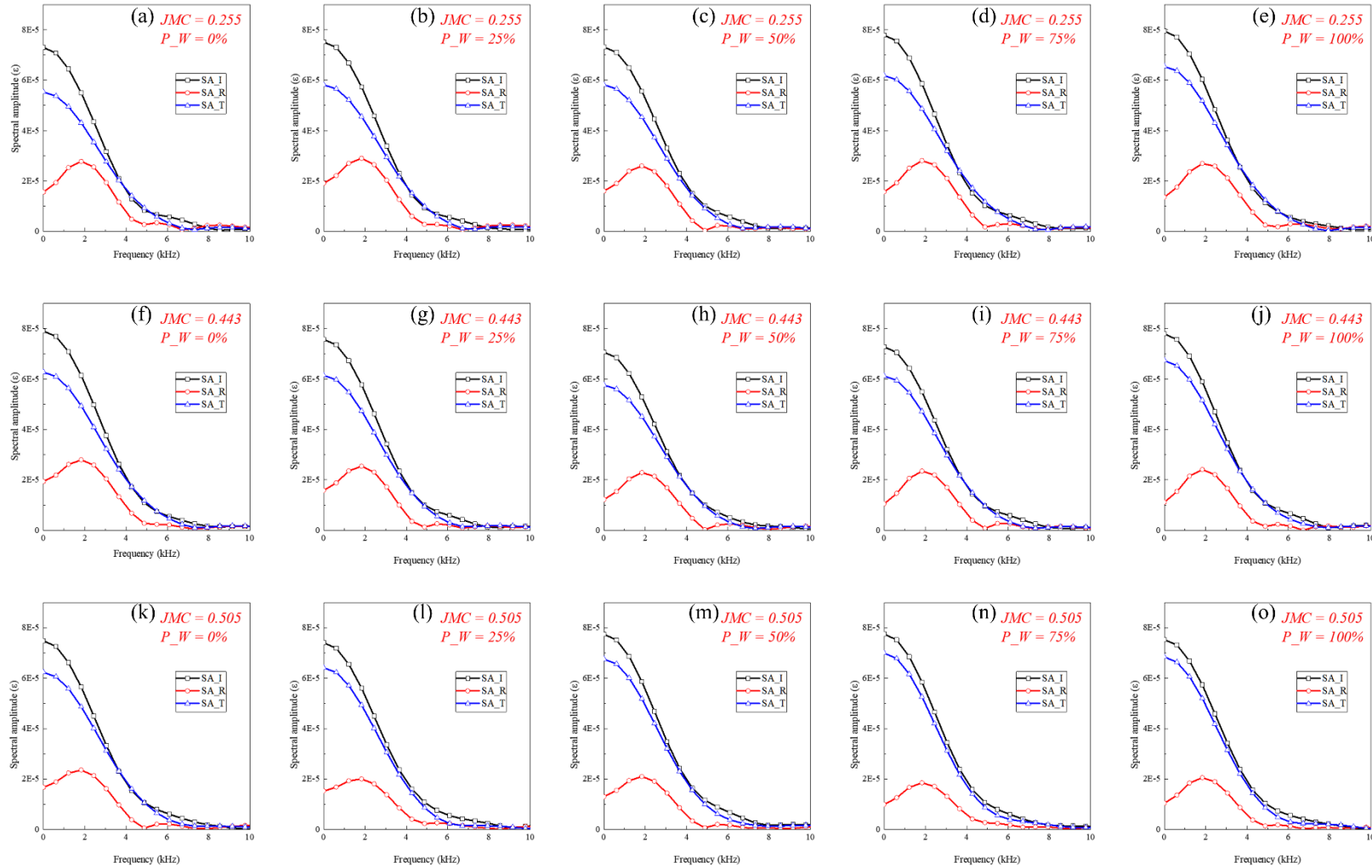


Figure 6.15 The frequency spectra of the incident (SA\_I), transmitted (SA\_T) and reflected waves (SA\_R) for the tested rock specimens with single fluid-filled joints at an approximately identical joint thickness of 4 mm: (a)-(e) for JMC of 0.255, (f)-(j) for the JMC of 0.443, (k)-(o) for the JMC of 0.505.

In Figures 6.14 and 6.15, with the increase of the water content, the low-frequency band gradually becomes narrower while the intermediate-frequency range gets broader. Furthermore, the increasing water content leads to a decrease in the spectral amplitudes of the reflected waves. Those findings are in accordance with the observations from the transmission and reflection coefficients, implying that the substitution of air with water can to some extent enhance wave transmission and weaken wave reflection across a single rock joint regardless of the joint thickness and contact area. Figure 6.14 illustrates that the increasing joint thickness broadens the low-frequency range while it narrows down the intermediate-frequency band. In addition, the spectral amplitudes of the reflected signals increase with the increasing joint thickness. Those phenomena are consistent with the findings of the transmission and reflected coefficients, further clarifying that the thicker the rock joint, the more wave reflection and the lesser the wave transmission no matter what the water content and the joint contact area are. Figure 6.15 shows that the increase in the JMC, i.e., the larger contact area, results in a narrower low-frequency region and a wider intermediate-frequency band. Moreover, the spectral amplitudes of the reflected pulses decrease with the increasing contact area. Those observations agree well with the findings of the transmission and reflection coefficients, indicating that the increasing joint contact area leads to more wave transmission and less wave reflection regardless of the water content and the joint thickness. Besides, in the high-frequency region, the spectral curve of the transmitted wave becomes closer to that of the incident pulse.

### **6.3.2 The effects of the fluid viscosity on the interaction of stress waves with single fluid-filled rock joints**

From the section 6.3.1, it can be concluded that, as the high-intensity stress wave impinges perpendicularly upon a single fluid-filled rock joint, the filling fluid alters the mechanical behaviour of single rock joints with a clear manifestation as the change in joint normal stiffness, which in turn affects the wave responses of the joint manifested as the variations in the transmission and reflection coefficients together with the seismic quality factor. Accordingly, this subsection concentrates mainly on the analyses of the correlations of fluid viscosity with the variations in the joint stiffness, the transmission and reflection coefficients as well as the seismic quality factor, aiming to elaborate the effects of fluid viscosity on the mechanical and seismic wave characteristics of individual fluid-filled rock joints subjected to the passage of the high-intensity stress waves. Particularly, the variation in each parameter is evaluated via the normalized difference ( $P_{NV}$ ) between the measured values for the joint containing a type of

viscous liquid ( $P_{FF}$ ) and the joint in the dry situation ( $P_{Dry}$ ), which can be calculated as the following formula,

$$P_{NV} = \frac{P_{FF} - P_{Dry}}{P_{Dry}} \times 100\% \quad \text{Equation 6.1}$$

where  $P$  could represent the joint stiffness  $\kappa_n$ , the transmission coefficient  $T_e$ , the reflection coefficient  $R_e$ , or the seismic quality factor  $Q_{sei}$ . With the Equation 6.1, the normalized variations in the mechanical and seismic wave responses of single fluid-filled rock joints induced by the changing fluid viscosity are quantitatively evaluated and then clearly illuminated in the following content.

### 6.3.2.1 The influence of fluid viscosity on the specific normal stiffness of single fluid-filled rock joints

The normalized variations in the specific normal stiffness of single fluid-filled rock joints are plotted as functions of the liquid content in the joint and the viscosity of filling liquid, respectively, in Figures 6.16a and 6.16b. It is found from Figure 6.16a that the joint stiffness exhibits an approximately linear increase as the filling liquid content increases from 0% to 75% while it is significantly enhanced at the fully liquid filling condition (i.e.,  $P_L = 100\%$ ) regardless of the liquid viscosity. The observed tendencies are consistent with the results stated in section 6.3.1, which is mainly explained by the compressibility contrast between the air and the liquid. Specifically, in partially liquid filling scenarios, the substitution of the air with the liquid reduces the compressibility of the fluid-filled rock joint because the air is much more compressible than the liquids, which improves the joint resistance ability to deform and thus stiffens the joint. Additionally, the significant increment of joint stiffness induced by the fully liquid filling condition can be attributed to that the filling liquid has no space and sufficient time to instantaneously diffuse at the moment of the normal incidence of the stress waves. As a consequence, the rock joints full of liquids behave as sealing for a short time during the passage of wave, causing a severely reduction in the compressibility of joint and thus resulting in a much larger joint stiffness compared to the partially fluid-filled joints (Huang et al., 2020).

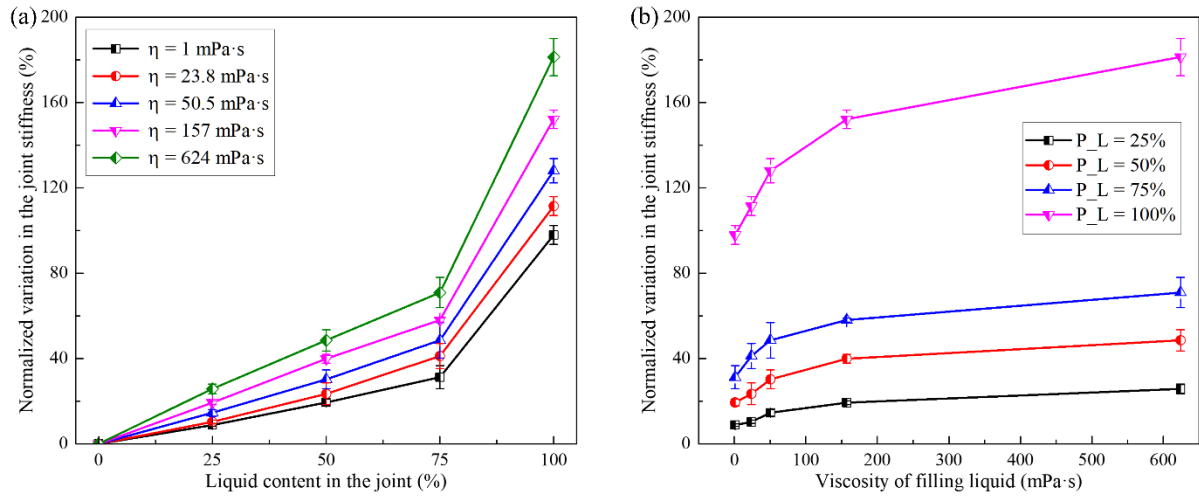


Figure 6.16 The normalized variation in the specific stiffness of single fluid-filled rock joints as functions of (a) the liquid content and (b) the viscosity of filling liquid, respectively.

Figure 6.16b shows that the increment of the joint stiffness induced by the increasing liquid content is more significant for the joint filled with the more viscous liquid. There are mainly two reasons for such phenomenon. First, the increasing viscosity of the filling liquid results in a reduction in the compressibility of the fluid-filled rock joint and thus stiffens the joint. It should be mentioned that the filling liquid used in this experiment is the mixed solvent of the water and the pure glycerol. The laboratory measurements reveals that the viscosity of the filling liquid increases with the increasing fraction of glycerol, as shown in Table 6.2. By comparison, the compressibility of the filling liquid predominantly consisting of the water and the pure glycerol monotonously decreases as the fraction of glycerol increases (Easteal and Woolf, 1985, Egorov and Makarov, 2014). Correspondingly, the more viscous the filling liquid, the less compressible the fluid-filled joint. Second, the larger viscosity of filling liquid leads to the slower mobility and then produces the stiffer joint under the passage of the high-intensity stress waves. The mobility of joint is defined as the ratio of the joint permeability to the viscosity of filling liquid, which determines the pressure distribution as rock is deformed slightly due to the passage of a seismic wave (Batzle et al., 2006). Given that the fluid-filled rock joints tested in this experiment have the approximately identical texture, the permeability almost remains constant for all tested joints, and hence the mobility of the joint is controlled by the viscosity of the filling liquid. The higher the mobility, the shorter time it requires for wave-induced fluid flow to equilibrate (Zhao et al., 2017). It means that the sufficiently high mobility easily allows the fluid pressure equilibration and in turn softens the fluid-filled rock joint. Accordingly, the relaxation associated with the fluid pressure diffusion (FPD) gets

weaker as the liquid viscosity increases, and thus the enhancement of joint stiffness becomes more significant for the higher liquid viscosity (Mavko, 2013).

### 6.3.2.2 The influence of fluid viscosity on transmission and reflection coefficients for the rock specimens with single fluid-filled joints

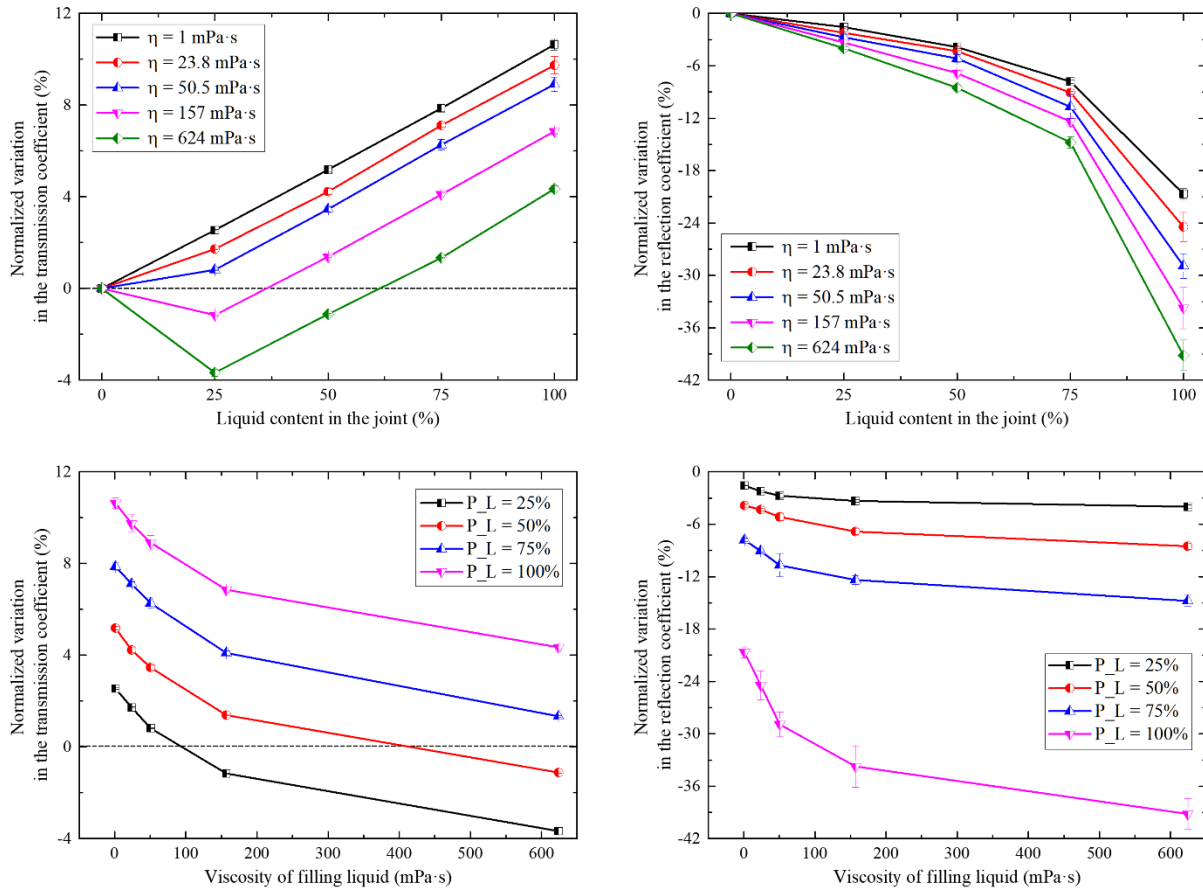


Figure 6.17 The normalized variation in the transmission and reflection coefficients for single fluid-filled rock joints as functions of (a), (b) the liquid content and (c), (d) the viscosity of filling liquid, respectively.

The normalized variations in the transmission and reflection coefficients for single fluid-filled rock joints induced by the varying fluid viscosity are plotted with respect to the filling liquid content and the liquid viscosity in Figure 6.17. It should be mentioned that the negative values suggest the decrement of the transmission/reflection coefficient compared to the corresponding reference data obtained from the dry rock joint.

The effects of filling liquid content are illustrated in Figures 6.17a and 6.17b. It is found from Figure 6.17a that, for rock joints filled with the low-viscosity liquids (i.e.,  $\eta = 1$  mPa·s,  $\eta = 23.8$  mPa·s and  $\eta = 50.5$  mPa·s), the increasing liquid content leads to a continuous increase in

the transmission coefficient. This observation is in accordance with the finding in section 6.3.1, which can be mainly attributed to the increasing joint stiffness induced by the addition of liquid. By comparison, for rock joints filled with the high-viscosity liquids (i.e.,  $\eta = 157 \text{ mPa}\cdot\text{s}$  and  $\eta = 624 \text{ mPa}\cdot\text{s}$ ), the transmission coefficient decreases as the liquid content increases to 25% while it exhibits an increasing trend with the liquid content in the range of 25% - 100%. The transmission loss occurring as filling liquid content increases from 0% to 25% can be attributed to that the viscous energy loss caused by the wave-induced fluid flow (WIFF) within the joint conceal the increase in transmitted wave energy induced by the increasing joint stiffness. For the scenarios where the filling liquid content is higher than 25%, the increment of transmitted wave energy exceeds the growth of energy dissipation within the joint, resulting an increase in the overall wave transmission through the jointed rock specimen. Regarding the role of the liquid content in wave reflection, it is observed that the reflection coefficient decreases with the filling liquid content regardless of the viscosity of filling liquid, as shown in Figure 6.17b. This agrees with the observed correlation of the water content with the reflection coefficient presented in section 6.3.1, which is attributed to that the joint becomes stiffer with the increasing liquid content and thus less wave energy is reflected through at the joint-host rock interface. It is also found that the trend of the reflection coefficient resembles the tendency of the joint thickness induced by the increasing liquid content (see Figure 6.16), which confirms the predominant role of the joint stiffness in wave reflection at the fluid-filled joint.

Figures 6.17c and 6.17d illustrate the influences of liquid viscosity on the transmission and reflection coefficients of single fluid-filled rock joints. It is observed from Figure 6.17c that the increasing liquid viscosity reduces the wave transmission across single fluid-filled rock joints, which is indeed consistent with the theoretical prediction presented by Zhu et al. (2012). This implies that the wave energy transmission declines with the increasing liquid viscosity at a decreasing rate. The explanation for such phenomenon is that wave transmission is controlled by the combined effects of wave attenuation due to the viscous friction and the enhanced stiffening effect induced by the increasing viscosity. With the increase of liquid viscosity, the wave dissipation caused by viscous friction becomes more significant while the increment of wave transmission due to the enhanced joint stiffness gets smaller. Interestingly, Figure 6.17c also shows that, for filling liquids at very higher viscosities (i.e.,  $\eta = 157 \text{ mPa}\cdot\text{s}$  and  $\eta = 624 \text{ mPa}\cdot\text{s}$ ), the wave transmission of the wet rock joint could be smaller than that for the dry joint in some circumstances liquids. The possible explanation is that the viscous effect introduced by the filling liquid is much more significant than the associated stiffening effect in these cases.

In Figure 6.17d, the more viscous the filling liquid, the more the decrement of the reflection coefficient, indicating that the increasing liquid viscosity reduces the wave reflection at individual fluid-filled rock joints. The similar observation has been reported in the theoretical work of Fehler (1982), which is mainly due to that the increase in the joint stiffness (see Figure 6.16). Another possible explanation is that the more viscous liquid causes the lower mobility and thus results in the decrease in the seismic reflectivity (Mavko, 2013).

### 6.3.2.3 The influence of fluid viscosity on seismic quality factor for the rock specimens with single fluid-filled joints

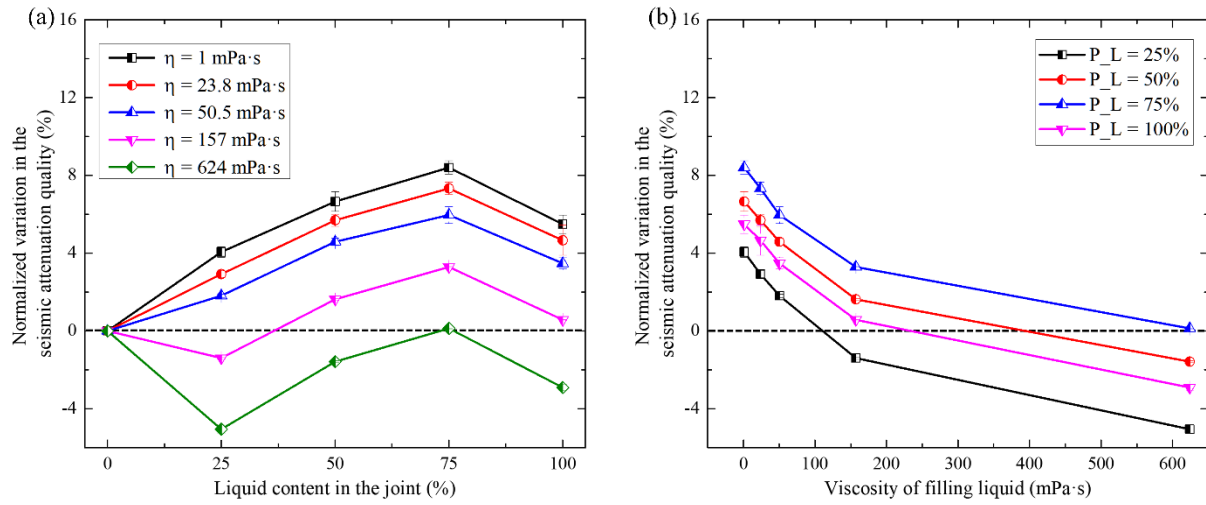


Figure 6.18 The normalized variation in the seismic attenuation quality for single fluid-filled rock joints as functions of (a) the liquid content and (b) the viscosity of filling liquid, respectively.

Figure 6.18 presents the normalized variation in the seismic quality factor  $Q_{sei}$  for individual fluid-filled rock joints filled with different viscous liquids, where the negative values suggest that the  $Q_{sei}$  for such case is smaller than the reference  $Q_{sei}$  corresponding to the dry joint. It can be seen from Figure 6.18a that, within the liquid content range of 25% -100%, the normalized variation in the  $Q_{sei}$  increases with the increasing liquid content and maximizes at the liquid content of 75%, following by a decreasing trend as the liquid content rises to 100%, regardless of the viscosity of filling liquid. Those findings are indeed consistent with the observations in section 6.3.1, which is attributed to that the fluid flow arising within the fluid-filled joint generates significant seismic energy dissipation and dominates the overall wave attenuation through the joint. More specifically, in partially filling conditions, the wave-induced fluid flow is reduced by the increasing liquid content, resulting in less wave energy attenuation across the joint (Kachanov, 1992, Hunziker et al., 2018). For the scenarios where



single rock joints is full of liquid, the overall wave attenuation is more significant because the substantial squirt flow of filling liquid through the pre-set small hole occurs and dissipated much more wave energy. Figure 6.18a also shows that, as the liquid content increases from 0% to 25%, the normalized variation in  $Q_{sei}$  increases for the rock joints filled with low-viscosity liquids (i.e.,  $\eta = 1$  mPa·s,  $\eta = 23.8$  mPa·s and  $\eta = 50.5$  mPa·s) while it exhibits a decreasing tendency for the rock joints filled with high-viscosity liquids (i.e.,  $\eta = 157$  mPa·s and  $\eta = 624$  mPa·s). The main explanation is that the addition of highly viscous liquids causes more viscous friction loss while it has a modest influence on the energy consumption for the inelasticity deformation of the joint. Consequently, single rock joints filled with a small volume of highly viscous liquids dissipate more wave energy compared to the dry rock joints that attenuates seismic energy mainly through the inelastic deformation of the rock frame.

Figure 6.18b shows that, at a given liquid content, the normalized variation in  $Q_{sei}$  for single fluid-filled rock joints decreases with the increasing liquid viscosity. The observed trend is similar with the relationship of liquid viscosity with the  $Q_{sei}$  predicted by the Kelvin-Voigt viscoelastic model (Vasheghani and Lines, 2009), which implying that the more viscous the filling liquid, the greater the wave dissipation in the joint. It is due to that the energy dissipation caused by viscous friction of the filling liquid plays a predominant role in the total wave attenuation across single fluid-filled rock joints. More specifically, the larger viscosity leads to the greater frictional loss associated with the fluid motion triggered by the passing high-intensity stress waves, causing more significant wave dissipation. Moreover, a transition to negative values of the normalized variation in the  $Q_{sei}$  is observed as the liquid viscosity increases, suggesting the dominant role of viscous friction loss in the overall wave attenuation.

### 6.3.3 High-speed images for the dynamic responses of single fluid-filled rock joints under the passage of the high-intensity stress waves

To fully understand the interaction of individual fluid-filled rock joints with the high-intensity stress waves, the high-speed photographing technique is used to record the dynamic responses of single fluid-filled rock joints subjected to the impact loading for each SHPB test, which has been clearly described in chapter 3. In this subsection, Figure 6.19 present the progressive high-speed photos for single fluid-filled rock joints with the JMC of about 0.443 to reveal the effects of the joint thickness, and Figure 6.20 give some selected high-speed images for single fluid-filled rock joints at the joint thickness of nearly 4 mm to illustrate the role of the joint contact area. Besides, the typical high-speed imaging sequences for individual rock joints filled with

different viscous fluids are shown in Figure 6.21 to unravel the influences of fluid viscosity. Note that, for each test case, only 12 photos at the time points of 0, 50, 100, 150, 200, 250, 300, 350, 400, 500, 600, and 700  $\mu\text{s}$ , respectively, are selected to demonstrate the reaction process of single fluid-filled rock joints, where the time zero corresponds to the moment at which the incident wave arrives at the bar-specimen interface.

The high-speed photographic images in Figures 6.19-6.21 show that, in the time range of 0-700  $\mu\text{s}$ , the propagating high-intensity stress waves produce the evident fluid flow within single rock joints. Given that the loading duration of the incident wave is about 380  $\mu\text{s}$  for all SHPB tests in this experiment, significant fluid flow observed from the high-speed images taking after 400  $\mu\text{s}$  indicates that the fluid flow continues after the passage of the high-intensity wave. It is attributed to that the wave-induced fluid flow cannot equilibrate the pressure gradients between the soft and stiff regions during the process of the wave passage. The similar distinct channelling of flow at the submillimetre to several-centimetre scale within single rock joints have been observed by Brown et al. (1998) using the video imaging and nuclear magnetic resonance imaging techniques, which is attributed to the short-range spatial correlation of the apertures of the joint. Specifically, the large aperture regions form the interconnected set of channel-like structures for fluid flow within the joint (Brown et al., 1998).

Furthermore, Figures 6.19-6.21 indicate that there are two modes of fluid-solid interaction simultaneously occurring in the rock joint and affect each other. One mode is the fluid motion parallel to the direction of the propagating compressional wave, which can be explained by that fluid is forced to participate in the motion of rock matrix due to the viscous friction and the inertial coupling. The other is the fluid flow perpendicular to the wave travelling direction, which can be attributed to the compressibility contrast between different void space caused by the layered distribution of air and filling liquid. Specifically, as the intensity-stress waves pressurize the fluid-filled rock joints, the liquid with high compressibility will generate higher pore pressure than that induced by the air with low compressibility. Consequently, the spatial gradient of pore pressure drives the fluid flow between the high-pressure and low-pressure regions. It is found from Figures 6.19-6.21 that, in the initial phase of the wave propagation, the pockets of void space around the contacting joint asperities can provide the continuous flow paths for fluids, which is due to the fact that the contacting joint asperities are not totally closed at the beginning of the dynamic loading (Hopkins, 2000).

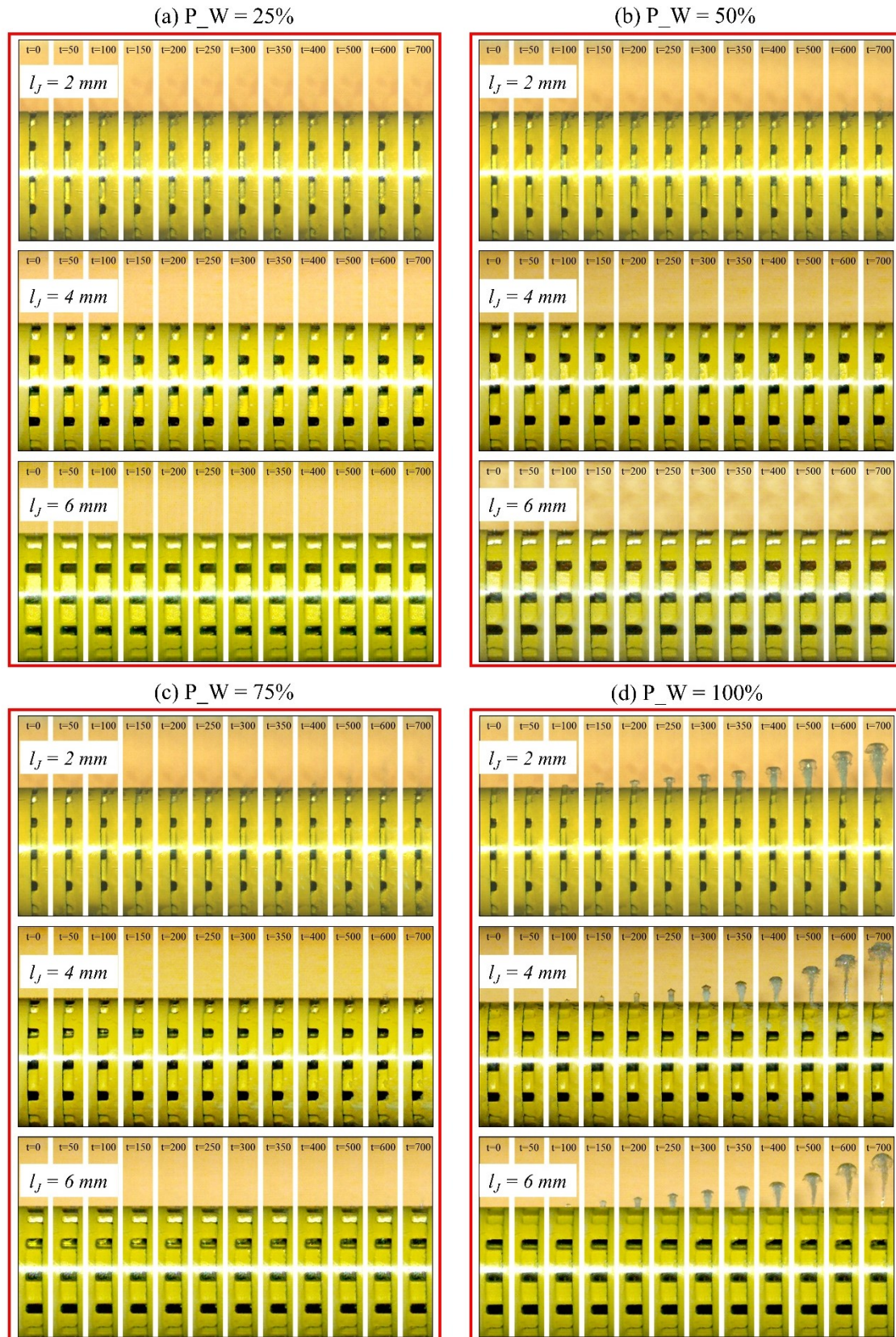


Figure 6.19 The selected high-speed images for the single fluid-filled rock joints at an approximately identical JMC of 0.443 under the impact loading: the effects of the joint thickness.



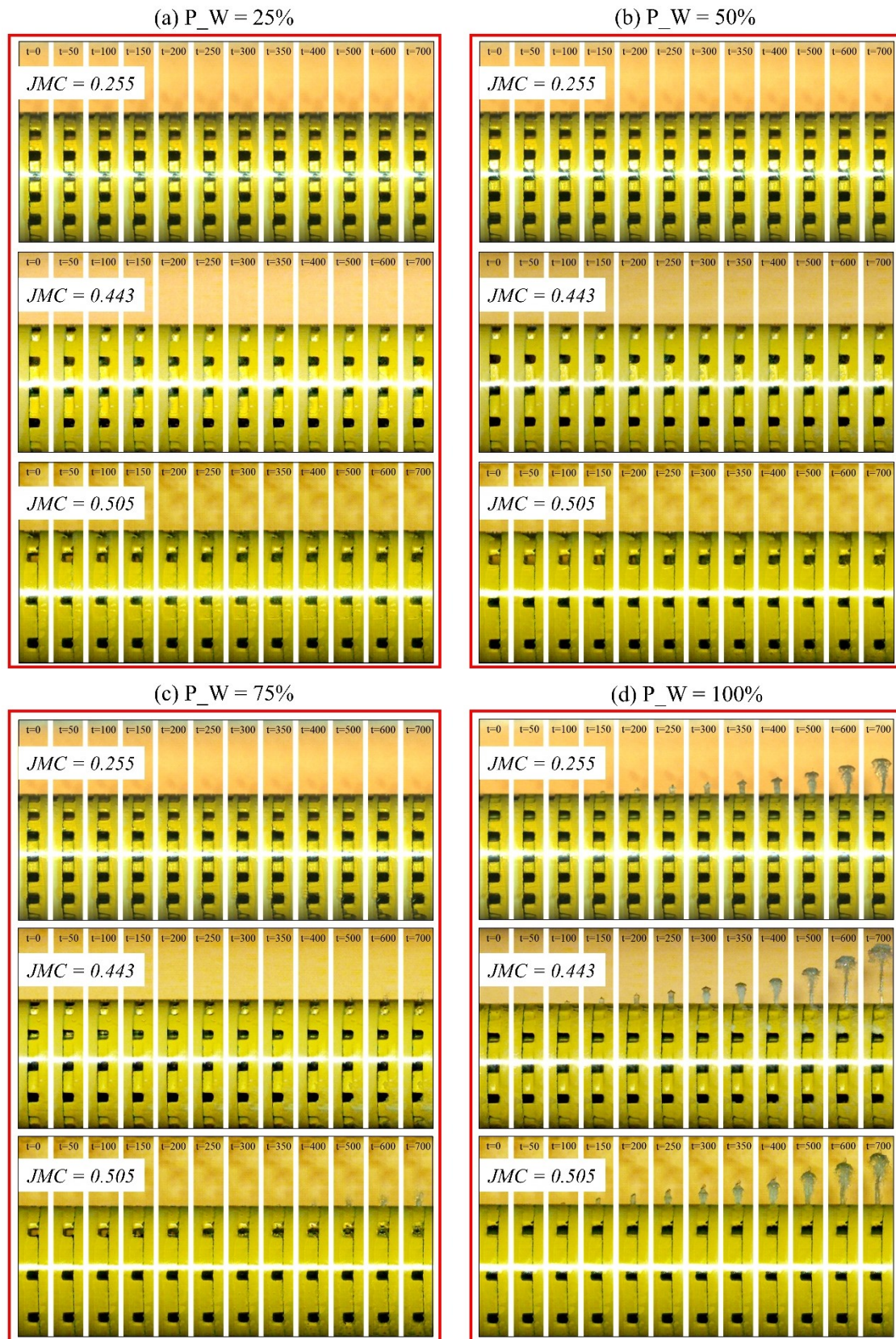
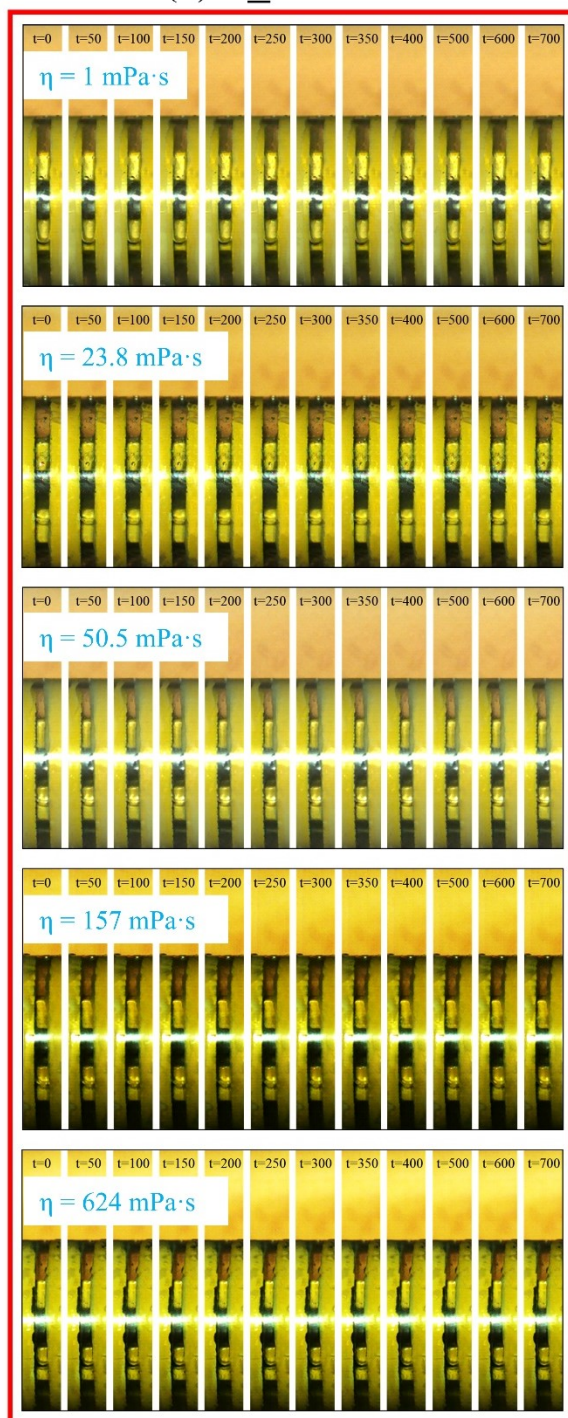
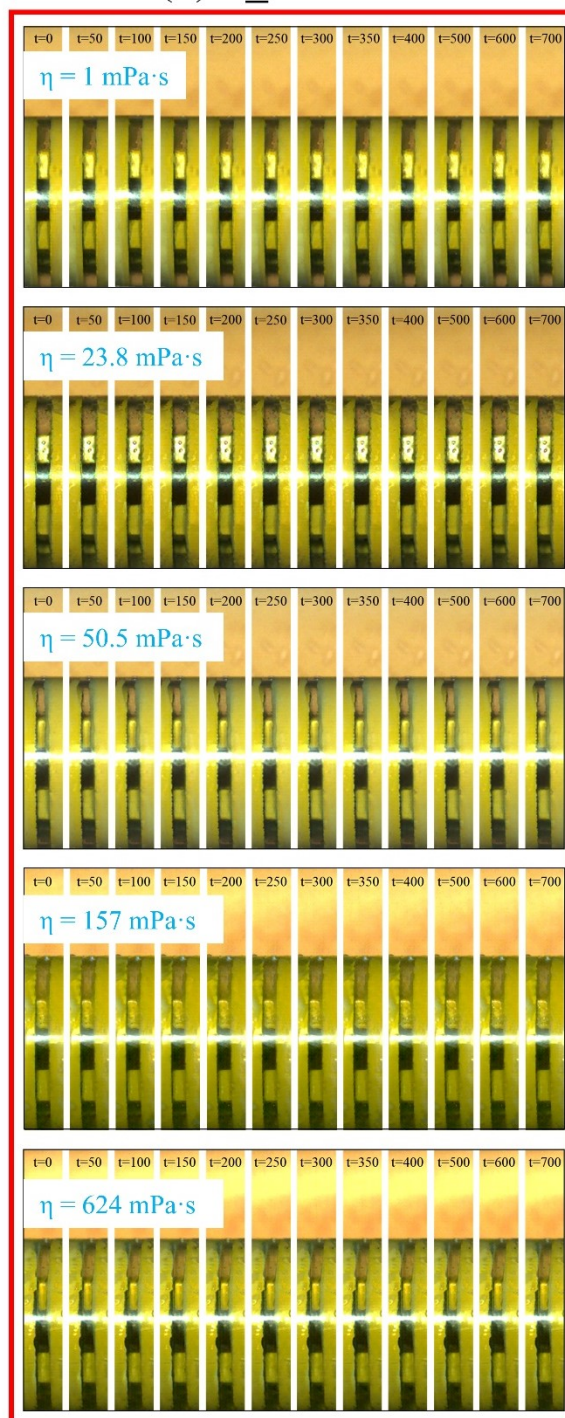


Figure 6.20 The selected high-speed images for the single fluid-filled rock joints at an approximately identical JMC of 0.443 during the passage of the high-intensity stress waves: the effects of the joint thickness.



(a)  $P_L = 25\%$ (b)  $P_L = 50\%$ 

(to be continued)



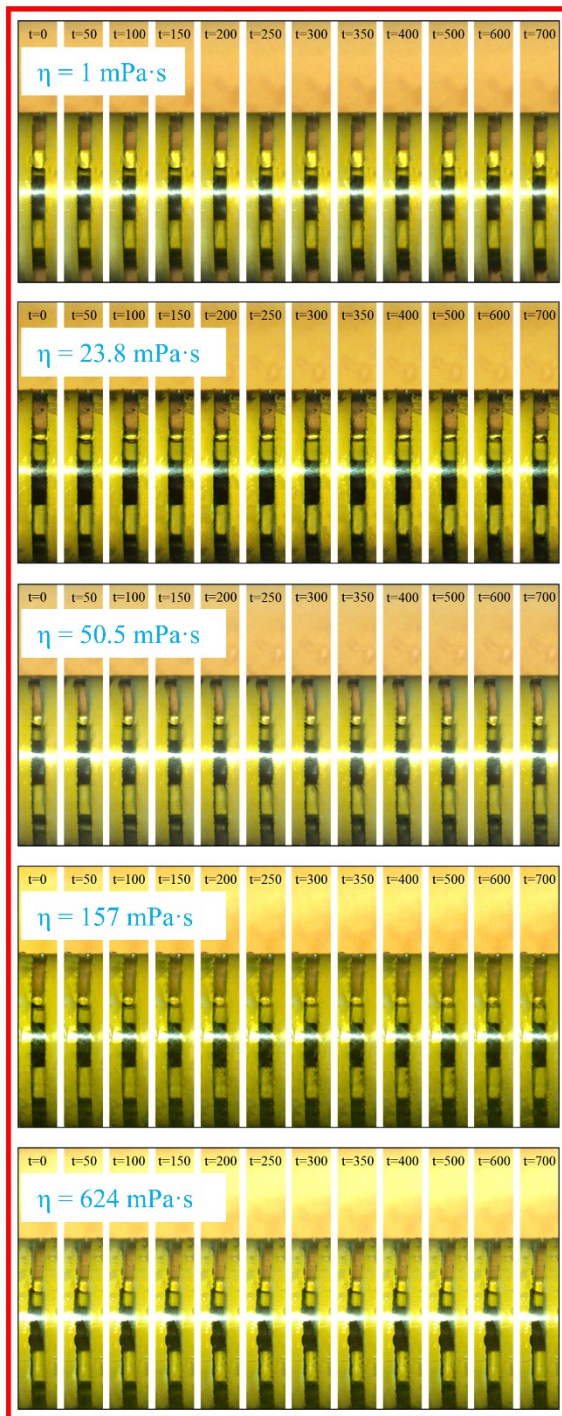
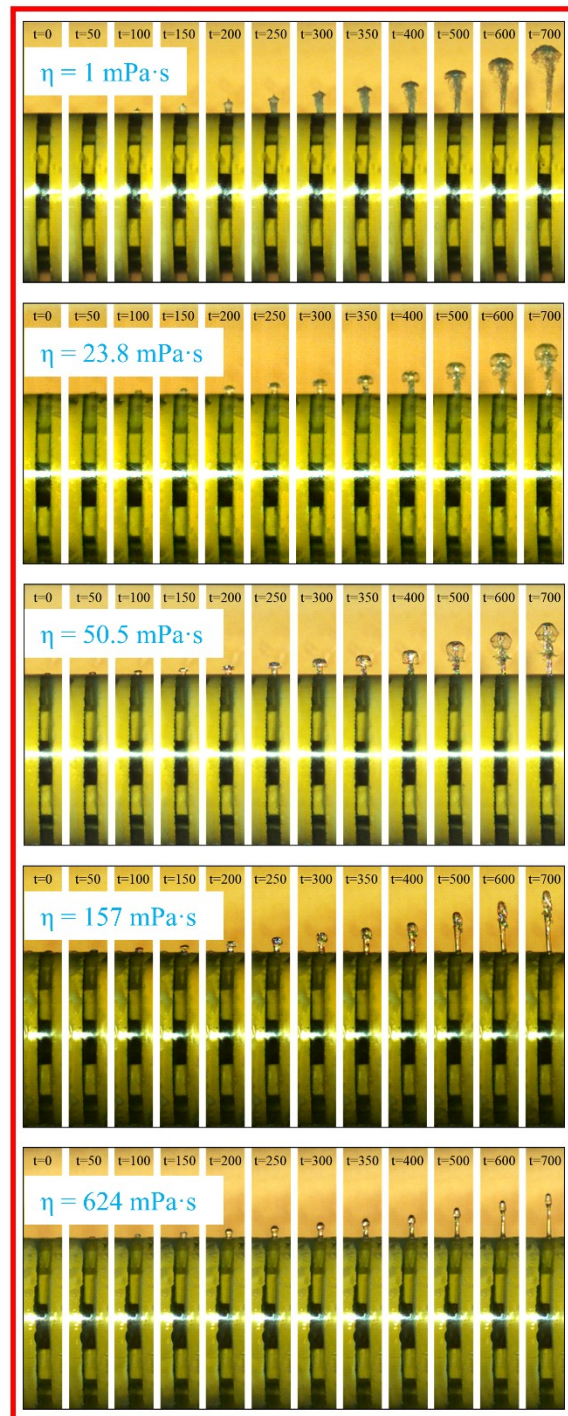
(c)  $P_L = 75\%$ (d)  $P_L = 100\%$ 

Figure 6.21 The selected high-speed images for individual rock joints filled with different viscous liquids.

As shown in Figure 6.19, the increasing joint thickness weakens the wave-induced fluid flow. It is because that the thinner joint is much stiffer and allows more wave energy to transmit into the joint. Accordingly, more wave energy is assigned to the fluid and leads to more significant fluid flow in the thinner joint. Figure 6.20 reveal that the larger JMC leads to the severer fluid motion within the joint. It means that the larger the joint contact area, the more significant the wave-induced fluid flow, which could also be attributed to the enhancement of joint stiffness. Furthermore, Figures 6.19 and 6.20 show that, at the given joint thickness and JMC, the increasing water content has a modest effect on the wave-induced fluid flow when rock joint is partially filled with water. The possible explanation is that the addition of water slightly changes the pressure gradients within the partially water-filled joints. By comparison, for rock joints full of water, much more significant squirt flow of water through the pre-set small hole is observed. It is because that, for fully filling scenarios, the joint is almost in the undrained state during the initial stage of the passage of the wave, as show in high-speed images before 150  $\mu\text{s}$ , which results in a remarkable increase in the joint stiffness.

Figures 6.21a-6.21c show that, for single rock joints partially filled with different viscous liquids, the fluid motion induced by the passing wave is insignificant, particularly within the duration of the wave propagation (i.e., 0-400  $\mu\text{s}$ ). The main reason is that the low joint stiffness caused by the small contact area allows less wave energy to transmit into the fluid-filled joint. Consequently, the pressure gradients induced by the wave energy assigned to the filling liquid is not enough to overcome the viscous drags in the liquid, and hence the liquid is very difficult to move within the joint. For single rock joints full of a liquid, the transition from the turbulent jet to the laminar jet is observed as the liquid viscosity increases, as shown in Figure 6.21d. It suggests that the liquid viscosity have an important influence on the flow patterns of the filling liquid within the rock joints subjected to the dynamic loading associated with the high-intensity stress waves.

## 6.4 Discussion

### 6.4.1 Discussion on the possible mechanisms lying behind the laboratory observations

The experimental results show that the dynamic mechanical behaviour of single fluid-filled rock joints is affected by the passing high-intensity stress waves. This, in turn, affects the wave



behaviours across those joints. The dominant physical mechanisms responsible for the lab-scale interaction of the high-intensity stress waves with single fluid-filled rock joints reported by the current work are discussed in this section. More specifically, there are mainly two mechanisms, i.e., the stiffening effect and the wave-induced fluid flow (WIFF), adopted to interpret the observations in present laboratory study. It should be mentioned that, in this experiment, the wavelength is at the scale of meter, which is much larger than the size of the tested fluid-filled rock joints, and thus the scattering attenuation caused by the joints could be negligible and thus excluded in this discussion (Müller et al., 2010).

When the high-intensity stress waves associated with the dynamic impacting propagate through single fluid-filled rock joint, the fluid pressure diffusion occurs between the compliant region (i.e., air voids) and the stiffer region (i.e., liquid voids). The resultant fluid pressure gradient drives the fluid to flow between the high-pressure and low-pressure regions. Within the short duration of the passage of the high-intensity stress waves, the liquid in the joint has insufficient space and time to reach the equilibrium and be entirely relaxed, as observed in the high-speed images. Consequently, the filling liquid could enhance the joint resistance ability to compression and thus improves the joint stiffness. This suggests that the stiffening effect induced by the filling liquid is a manifestation of the nonrelaxation of fluid pressure gradient during the passage of the high-intensity stress waves (Müller et al., 2010). The observed mechanical behaviours of single fluid-filled rock joints confirm that the stiffening effect of the filling liquid could effectively reduce the wave-induced fracture deformation and the resultant nonlinear joint behaviour (Nakagawa et al., 2019).

Furthermore, the high-speed images show that two modes of WIFF could simultaneously occur in the individual fluid-filled rock joints as the high-intensity stress waves penetrate the joints. On one hand, the WIFF perpendicularly to the wave propagating direction observed in this experiment is similar with the WIFF in the presence of fracture connectivity identified by Rubino et al. (2013), indicating that the wave-induced mesoscopic fluid flow mechanism could be responsible for the wave dissipation caused by single fluid-filled rock joints (Pride et al., 2004, Müller et al., 2010). Specifically, the individual fluid-filled rock joints tested in this experiment could be regarded as the mesoscopic analogy of the fracture network that consisting of interconnected vertical and horizontal fractures (Rubino et al., 2013). According to Rubino et al. (2013), the fluid pressure diffusion in single fluid-filled rock joints could manifest in two ways, i.e., fracture-to-background wave-induced fluid flow (FB-WIFF) and fracture-to-fracture wave-induced fluid flow (FF-WIFF), which are induced by the compressibility contrasts

between the joint and host rock as well as between intersecting channels within the joint upon the passage of the stress waves. It should be mentioned that the characteristic time scale for the FB-WIFF is governed by the hydraulic diffusivity of the host rock while that for the FF-WIFF depends on the effective hydraulic diffusivity of the joint and the host rock together with the distance between the tip of a fracture and its intersection with an adjacent fracture (Caspari et al., 2019). Herein, single rock joints can be hydraulically isolated from the surrounding rock matrix because that the background rock owns a very small porosity compared to the synthetic rock joints owning the large hydraulic connectivity between the vertical and horizontal voids. Accordingly, the wave-induced pressure gradients diffusing inside the joint are much more significant than those diffusing toward the embedding background rock. It indicates that the contribution of the FB-WIFF to energy attenuation is negligible while the FF-WIFF generates significant seismic energy dissipation as the high-intensity stress waves propagates across single fluid-filled rock joints (Germán Rubino et al., 2013). On the other hand, the observed WIFF along the direction of the propagating wave suggests that the global flow could make contributions to the overall wave attenuation caused by single fluid-filled rock joints. Physically, the global flow is driven by the inertial forces when the rock joint frame is accelerated by the passing wave, resulting in the relative fluid displacements with respect to the joint walls. Since the global flow caused by the inertial friction is only significant at high frequencies, it could play a secondary role in the wave dissipation caused by the WIFF within single rock joints compared with the wave-induced mesoscopic fluid flow effect (Müller et al., 2010).

Based on the experimental results, it can be inferred that the overall wave dissipation caused by single fluid-filled rock joints is governed by the superposition of the frame-related attenuation and fluid-related attenuation. Particularly, the fluid-related attenuation is mainly caused by the WIFF within the joint, and the frame-related attenuation is due to the inelasticity of the joint frame that predominantly governed by the stiffening effect. For partially fluid-filled rock joints, the frame-related attenuation dominates the overall wave dissipation, and thus the changes in the joint thickness and joint contact area have more significant influences on the values of the  $Q_{sei}$  compared to the addition of liquid. By comparison, for rock joints full of a liquid, even though the stiffening effect is also maximal in such condition, the squirt flow occurs and causes an unexpected decrease in the  $Q_{sei}$  values. It indicates the fluid-related attenuation play a crucial role in the overall wave dissipation caused by the fluid-filled rock joints when the evident WIFF is induced by the high-intensity stress waves.

### 6.4.2 Comparison with the findings of the low-intensity wave behaviours across single fluid-filled rock joints

In chapter 5, the fluid-filled rock joint is analogous to the simple model of single fractures that are conceptualized as a pair of parallel interfaces separated by a constant distance referred to as the aperture. Accordingly, the findings in chapter 5 are only valid for the joint with smooth surfaces under sufficiently low normal stress with respect to the fracture plane (Liu, 2005). For this scenario, when the ultrasonic wave propagates through the fluid-filled joint, the wave dissipation is caused by the wave scattering. More specifically, for the fluid-filled rock joints in chapter 5, the wave attenuation caused by the joints monotonously decreases with the increase liquid content, which is attributed to that the wavelength of the ultrasonic wave is comparable to the joint thickness and length. As a result, the overall wave attenuation is mainly due to the wave scattering at the joint surface predominantly comprised of the air-rock interface and the liquid-rock interface. Additionally, the propagating low-intensity ultrasonic wave is insufficient to induce the WIFF within the joint, indicating that the frictional loss caused by the WIFF can be negligible for the overall wave attenuation.

By comparison, the synthetic fluid-filled rock joint in this chapter can be regarded as an analogy of the conceptual simplification of the natural rock joints considering the fact that nature joints tend to be rough-welded with the surfaces being in contact with each other at certain locations (Pyrak-Nolte and Morris, 2000). The test results show that the overall wave dissipation slightly decreases with the increasing liquid content in the partially filling conditions while it increases in the fully filling case, which is different from the findings of wave attenuation in chapter 5. This is because that, for rock joints partially filled with liquids, the overall wave dissipation is dominated by the inelastic joint deformation caused by the dynamic stress associated with the high-intensity stress waves, whereas the WIFF induced by the passing high-intensity stress waves also exerts important effects on the total wave attenuation for rock joints full of liquids. More specifically, the addition of liquid slightly improves the stiffness of the joint partially filled with liquids and thus reduces the energy consumption by the inelastic joint deformation, while the substantial WIFF occurs for rock joints full of liquids and causes significant viscous dissipation of wave energy.

For both fluid-filled joints in chapter 5 and this chapter, the transmission coefficient monotonously increases with the liquid content, suggesting the predominant role of the stiffening effect induced by the liquid in the wave transmission across single fluid-filled rock

joints. However, it is found that the increment of the transmission coefficient caused by the increasing liquid content in this chapter is much smaller than that reported in chapter 5, indicating that the stiffening effect induced by the filling liquid play a more significant role in the low-intensity wave propagation across single fluid-filled rock joints tested in chapter 5. Besides, the measured large values of the transmission coefficient for the dry rock joints tested in this chapter indicates that the contacting joint asperities contributes greatly to the joint stiffness and thus the stiffening effect due to the addition of liquid have a modest effect on the fluid-filled rock joints, particularly for partially filling scenarios. Furthermore, the test results in this chapter unravels that the overall wave attenuation across single fluid-filled rock joints increases with the filling liquid viscosity, which is in accordance with the findings in chapter 5. It is mainly due to that the liquid at a higher viscosity causes more viscous loss as the seismic waves penetrate individual fluid-filled rock joints and thus more wave energy is dissipated.

## 6.5 Concluding remarks

The present study in this chapter investigates the effects of joint parameters (i.e., the joint thickness and JMC) and filling fluid properties (i.e., fluid viscosity and volume content in the joint) on the interaction of high-intensity stress waves with single fluid-filled rock joints via the SHPB technique. Based on the laboratory data, the dynamic mechanical properties, energy evolution characteristics and wave responses of rock specimens with single fluid-filled joints were analysed and elaborated using the data processing techniques described in Chapter 3. The experimental results show that the mechanical behaviours of single fluid-filled rock joints are highly affected by the joint thickness, the joint contact area, the components and viscosity of filling fluids when the high-intensity stress wave travel through the joints, which in turn alter the wave propagation and attenuation across single fluid-filled joints.

Specifically, the increasing joint thickness enhances the inelasticity of the joints and thus reduce the joint stiffness when the high-intensity stress waves pass through single fluid-filled rock joints. Accordingly, the wave transmission decreases while the wave reflection and wave attenuation increase with the joint thickness. By comparison, the increasing joint contact area weakens the inelastic behaviour of the joints and stiffens the joint as the high-intensity stress waves propagates across individual fluid-filled rock joints. As a result, an increase in the wave transmission and decreases in the wave reflection and wave dissipation occurs when the joint contact area gradually increases.

On the other hand, the components of filling fluids have more complex influences on the interaction of single fluid-filled rock joints and the high-intensity stress waves. Particularly, for the partially liquid filling scenarios, the higher liquid content improves the elasticity of the joint to some extent and results in a slight increase in the joint stiffness. Consequently, the more the liquid content within the joint, the more the wave transmission and the less the wave reflection and the wave attenuation. On the other hand, for rock joints full of liquid, the increase in joint stiffness is significantly larger than that for partially fluid-filled rock joints. Meanwhile, the sudden jet of filling liquid is thrown high into the air through the pre-set hole as the high-intensity stress waves impinges upon the joint. In this condition, both the wave transmission and wave dissipation are larger than those for rock joints at a liquid content of 75%. The unexpected increase in wave attenuation can be attributed to the squirt flow of filling liquid. The above-mentioned liquid content-dependent wave responses of single fluid-filled rock joints indicate that the high-intensity stress wave behaviours across individual rock joints are dominated by a combination of the wave-induced fluid flow and stiffening effect. The competition between the increment of transmission increment due to the stiffening effect and the wave dissipation caused by wave-induced fluid flow illustrates the important role of filling fluid in stress wave propagation across single rock joints.

Furthermore, the liquid content-dependent mechanical and wave behaviours of the joint is highly related to the viscosity of filling fluids when the high-intensity stress waves propagate normally across individual fluid-filled rock joints. Specifically, the joint stiffness increases with the liquid viscosity regardless of the liquid content because that the liquid owning a higher viscosity is less compressible and thus strengthen the stiffening effect. Additionally, at a given liquid content, the increasing liquid viscosity results in more wave attenuation and therefore reduce the wave transmission across single fluid-filled rock joints, indicating that the viscous loss makes great contributions to the overall wave dissipation. The test results also show that, for rock joints partially filled with highly viscous liquids, wave attenuation for lower liquid contents is greater than that for the dry condition, implying that the increase in viscous loss conceal the enhanced stiffening effect for such cases. For rock joints partially filled with lowly viscous liquids, wave attenuation decreases with the liquid content, indicating that the addition of liquid makes more contributions to the stiffening effect compared to the viscous effect. Besides, for rock joints full of liquid, the pattern of the squirt flow changes from the turbulent state to the laminar state with the increasing viscosity of liquid.

Importantly, the concurrent high-speed camera imaging adopted in this chapter directly records the interaction of single fluid-filled rock joints with the high-intensity stress waves. The wave-induced fluid flow can be visually observed in high-speed camera images of the fluid-filled rock joints subjected to dynamic impacting associated with the high-intensity stress waves, which confirms the role of wave-induced fluid flow in the overall wave attenuation caused by the joint. Moreover, the high-speed camera images firstly provide the concrete evidence for the mesoscopic wave-induced fluid flow between voids within single rock joints. And the measured wave properties provide the indications of the role of wave-induced flow in the high-intensity wave responses of individual fluid-filled rock joints.

# CHAPTER 7 SUMMARY AND FUTURE WORK

## 7.1 Summary of the thesis work

The thesis research aims to determine the role of fluids in the interaction of waves with individual rock joints. To this end, the ultrasonic pulse-transmission method and the split Hopkinson pressure bar (SHPB) technique have been developed and applied to systematically and quantitatively investigate the effects of fluids on wave behaviours across single rock joints in the laboratory. Based on the experimental results and discussion in the preceding chapters, the main conclusions are summarized as follows.

### *(1) Fluid effects on the low-intensity wave behaviours across individual clay-rich rock joints*

The results obtained from a series of ultrasonic tests in chapter 4 show that water plays a crucial role in low-intensity wave behaviours across individual rock joints filled with clay-rich gouges. The key outcomes of this subject include:

- a) The increasing water saturation enhances P-wave velocity and attenuation across single kaolinite-rich rock joints while an approximately opposite trend is found for individual bentonite-rich rock joints. It is mainly attributed to the difference in the saturation distribution caused by the clay hydration. Specifically, the weak hydration of kaolinite results in heterogeneously distributed patchy saturation within the kaolinite-rich gouge layer. As a result, the increasing water saturation strengthens the local flow effect, stiffening some regions of the kaolinite-rich joint and thus causing faster P-wave velocity. Meanwhile, the enhanced fluid-solid motion results in more frictional loss and then causes more P-wave energy attenuation. By contrast, the strong hydration of bentonite results in a homogenous saturation distribution and most water exists in the form of bound water in the bentonite-rich rock joint. Accordingly, the local flow effect is insignificant, and the weakening stiffness of skeleton caused by water absorption dominates and causes a decrease in P-wave velocity across single bentonite-rich rock joints.
- b) With the increase of water saturation, an approximately nonlinear decrease trend is observed for the wave velocity while a concave trend (down first and then up) is revealed for wave energy attenuation when S-waves pass across both kaolinite- and



bentonite-rich rock joints. The decrease in S-wave velocity is mainly explained by that the addition of water weakens the grain contacts and thus reducing the bulk modulus of clay skeleton. Additionally, the concave trend of the overall S-wave attenuation could be the result from the trade-off of the decreasing viscosity and weakening stiffness induced by water addition. At low water saturation degrees, the viscous friction is the dominant mechanistic for wave attenuation across single clay-rich rock joints. In detail, the decreasing viscosity caused by water addition results in less frictional loss of passing wave energy and thus reduces the overall wave attenuation. For high-saturation cases, the contrast in stiffness between the joint and host rock plays a controlling on the total wave attenuation across single clay-rich rock joints. More specifically, the decreasing stiffness of clay-rich joint causes more wave reflection and less wave transmission into the joint, and thus the overall wave attenuation to some extent increases as S-waves pass through the clay-rich rock joint.

***(2) Fluid effects on the low-intensity wave behaviours across individual fluid-filled rock joints***

The massive ultrasonic tests in chapter 5 reveal that the low-intensity compressional wave propagation and attenuation across single fluid-filled rock joints are strongly affected by the temperature, the joint orientation as well as the compositions and spatial distribution of filling fluids within the joint. The main findings of this topic include:

- a) The joint orientation has a modest influence on wave behaviours across individual rock joints full of liquids (i.e., dual-liquid filled joints) while it strongly affects wave attributes of rock joints partially filled with a liquid (i.e., single-liquid filled joints). For single-liquid filled rock joints, the increasing liquid content results in the faster wave velocity and the more wave energy transmission across, especially for the vertical rock joints. For dual-liquid filled rock joints, the increasing water content leads to increases in wave velocity and wave energy transmission, where the joint orientation affects the pattern of the curves for water content-wave properties relations. The variations in wave behaviours induced by the joint orientation could be attributed to that it affects the spatial distribution of fluids within the joint and the coupling conditions of the rock-fluid-rock of the joint. In addition, the changes in wave properties caused by the varying fluid compositions could be explained by the differences in bulk modulus, density and viscosity of those fluids.

- b) Compared to the light oils, water leads to much more enhancement of the wave velocity and wave transmission across individual fluid-filled rock joints. It is mainly due to the fact that the bulk modulus of water is larger than that of the light oil. In this regard, water leads to a greater increment of joint stiffness compared to the light oils, thereby exerting more positive influences on wave velocity and transmission across individual fluid-filled rock joints.
- c) The wave velocity across single water-filled joint nonlinearly increases as the temperature increases from 10 °C to 80 °C, whereas the wave velocity across the light oil-filled joint approximately linearly decreases as the temperature increases from 10 °C to 60 °C. The variations in P-wave velocity of individual fluid-filled rock joints caused by the varying temperature are in accordance with the temperature-induced tendency of bulk moduli of filling fluid. It suggests that the temperature dependence of bulk moduli of filling fluids is responsible for the temperature dependent P-wave velocity across the fluid-filled rock joint. On the other hand, the higher the temperature, the more the wave energy transmitted through the water-filled rock joint. In contrast, less wave energy can transmit across the light oil-filled rock joint as temperature rises. The temperature dependence of wave energy transmission is to some extent consistent with that of bulk moduli of fluids, indicating that the temperature-induced variations in bulk moduli of filling fluids plays a dominant role in wave energy transmission across single fluid-filled rock joints. More specifically, the bulk modulus of a liquid dominates the stiffness of joint fully filled with the liquid, and thus controls wave reflection and transmission at the joint surface.

### ***(3) Fluid effects on the high-intensity wave behaviours across individual fluid-filled rock joints***

The laboratory observations from the substantial SHPB tests in chapter 6 indicate that the interaction of the high-intensity compressional stress waves with single fluid-filled rock joints is dependent on the joint thickness, the joint contact area, the content and viscosity of filling liquid. The important outcomes of this subject include:

- a) Independent of the fluid filling condition, the decrease in the joint thickness and the increase in the joint contact area improves the stiffness of single fluid-filled rock joints, resulting in more wave transmission, minor wave reflection and less wave dissipation. It indicates that joint asperities play a dominant role in wave behaviours

across single rock joints. This is because joint asperities cannot only determine the joint stiffness but also controls porosity and permeability of the joint.

- b) Regardless of the viscosity of filling liquid, the increasing liquid content slightly reduce the nonlinearity of single fluid-filled rock joints and thus improves the joint stiffness to some extent, which is pronounced for rock joints full of liquid. It could be explained by that a liquid has the much larger bulk modulus than air. The substitution of air with liquid results in an increase in the bulk modulus of the joint and thus stiffens the joint.
- c) In general, the higher the liquid content within single fluid-filled rock joint, the less the wave reflection and the more the wave transmission across the joint. For rock joints partially filled with liquids, wave attenuation decreases with the liquid content. By comparison, the rock joints full of liquid exhibit more wave dissipation due to the occurrence of squirt flow. These observations indicate that the squirt flow plays a more important role in wave behaviours across rock joints full of liquids. For fully liquid-filled rock joints, the significant squirt flow causes a remarkable increase in the joint stiffness and consumes much more wave energy for the fluid motion relative to the host rock. Therefore, although less wave reflection and more wave transmission occur at the rock-joint interface, less overall wave transmission is observed due to the energy dissipation caused by the squirt flow.
- d) The influences of the liquid content on wave attributes are dependent on the viscosity of liquid. Interestingly, wave transmission across rock joints filled with low-viscosity liquids is always larger than that across the corresponding dry joints, whereas wave transmission across rock joints filled with high-viscosity liquids could be smaller than that across the corresponding dry joints. Compared to the dry condition, the presence of liquid leads to less wave reflection at rock joints. These findings could be explained by that the variations in wave attributes of single fluid-filled rock joints results from the combined effects of bulk modulus and viscosity of filling fluids.
- e) The higher the liquid viscosity, the smaller the increment of wave transmission and the greater the decrement of wave reflection there are for high-intensity wave propagation across single fluid-filled rock joints. It can be explained by that wave energy dissipation caused by the liquid-rock matrix interaction gradually becomes stronger with the increasing liquid viscosity.

- f) The high-speed images unravel that passage of the high-intensity stress waves can cause the wave-induced fluid flow in single fluid-filled rock joints. The flow pattern is highly related to the liquid viscosity.

The findings in this research make a great contribution to the understanding of the fluid effects on the interaction of waves with individual fluid-filled rock joints from the laboratory perspective. Additionally, the results could serve as a guide for the interpretation of field acoustic data when employing the wave-based geophysical techniques to identify, monitor and characterize rock joints containing fluids. Furthermore, the thesis work could provide additional insights into the physical mechanisms lying behind the interaction of fluid-filled rock joints and waves.

## 7.2 Future work

The predominant lab-scale findings of the fluid effects on the wave propagation and attenuation across single rock joints obtained from this research have been summarized and presented in the previous section. Although the research topics covered in this thesis is only a small part of the rich and profound issues in the research field of the interaction of waves with rock discontinuities. We believe that this study could shed a little light on the unveiled area of this research field. Due to the limitations of the experiments in this research work, there are still some important issues need to be investigated in future work. Herein, the following projects are proposed with the intention to extend this thesis research.

### ***(1) Shear wave propagation and attenuation across the fluid-filled rock joints***

The thesis work focuses only on the compressional wave behaviours across single fluid-filled rock joints. It should be mentioned that the viscous fluids can also transmit shear waves. Given the fact that both the shear and compressional waves are used by some seismic methods in a complementary way for characterizing rock discontinuities, the understanding of the shear wave propagation and attenuation through the fluid-filled rock joints is important for many practical applications.

### ***(2) Further research on the fluid-dependent wave responses of individual gouge-filled rock joints***

This research only pays attention to the water saturation-dependent wave behaviours across individual rock joints filled with two kinds of clay-rich gouges (i.e., kaolinite and bentonite).

To ascertain a comprehensive understanding of the fluid effects on the interaction of waves with gouge-filled rock joints, it is necessary to perform more laboratory tests on rock joints filled with other representative fluids (brines and hydrocarbons) and minerals (e.g., illite and chlorite). In addition, the scanning electron microscope (SEM) is recommended to access the micro-scale structures of the fluid-saturated gouge materials within rock joints to provide more insights into the fluid effects on the interaction of waves with gouge-filled rock joints from a microscopic perspective.

***(3) Fluid effects on wave propagation and attenuation across the rock joints containing fluids at different flow conditions***

In this research, the fluids within the tested rock joints are limited to the static state. Although the fluid flow in single rock joints has been extensively studied in the laboratory because of its fundamental importance to the earth sciences, how the fluid movement affects wave behaviours across single rock joints is still poorly understood. In this regard, it is suggested to further study the role of the fluid flow conditions (e.g., the speed and direction of fluid motion) in wave propagation and attenuation across individual rock joints.

***(4) Fluid effects on wave propagation and attenuation across the fluid-filled rock joints at sub-zero temperatures***

In nature, fluids commonly exist in the form of gas, liquid, and solid (i.e., ice) phases within rock joints, where the ice is usually encountered at sub-zero temperatures. It has been recognized that the presence of ice in rock joints has important influences on rock collapses and avalanches in some cold regions (e.g., Tibet and Norway). In this context, the future work will be extended to the effects of ice on wave propagation and attenuation across single rock joints.

***(5) Fluid effects on wave propagation and attenuation across the fluid-filled rock joints at various stress states***

As mentioned in the literature review, the stress states surrounding the rock joints highly affect the interaction of waves with individual fluid-filled rock joints. However, all experiments in the current research are performed without applying external stresses. The fluid effects on wave responses to individual rock joints subjected to various stress states (including the compressional, shear and tensile loading) will be one of the subjects of our forthcoming studies.

***(6) Fluid effects on the joint specific viscosity that is introduced in the existing theories for characterizing wave behaviours across viscoelastic rock joints***

According to existing theories, the joint specific viscosity is an important factor affecting wave propagation and attenuation across individual rock joints, particularly for those with viscoelastic behaviours. However, the effects of the filling fluids within the joint on the joint specific viscosity remain enigmatic. In our future work, the correlations between the dynamic joint viscosity and the properties (i.e., density, bulk modulus, and viscosity) of the filling fluids measured in the lab will be investigated based on the obtained laboratory data to determine the role of fluids in the joint specific viscosity.

## REFERENCES

- ACHENBACH, J. 2012. *Wave propagation in elastic solids*, Elsevier.
- ACOSTA-COLON, A., OLANDER, M. & PYRAK-NOLTE, L. 2009. Seismic wave propagation across partially in-filled fractures. In *Proceedings of the Project Review, Geo-mathematical Imaging Group*, 193-204.
- ADAM, L., BATZLE, M., LEWALLEN, K. & VAN WIJK, K. 2009. Seismic wave attenuation in carbonates. *Journal of Geophysical Research: Solid Earth*, 114.
- AKSU, I., BAZILEVSKAYA, E. & KARPYN, Z. 2015. Swelling of clay minerals in unconsolidated porous media and its impact on permeability. *GeoResJ*, 7, 1-13.
- ALBERS, B. 2011. Linear elastic wave propagation in unsaturated sands, silts, loams and clays. *Transport in Porous Media*, 86, 537-557.
- AMALOKWU, K., BEST, A. I., SOTHCOTT, J., CHAPMAN, M., MINSHULL, T. & LI, X.-Y. 2014. Water saturation effects on elastic wave attenuation in porous rocks with aligned fractures. *Geophysical Journal International*, 197, 943-947.
- AMIR-FARYAR, B. & AGGOUR, M. S. 2016. Effect of fibre inclusion on dynamic properties of clay. *Geomechanics and Geoengineering*, 11, 104-113.
- ASTM D-18 on Soil and Rock. 2008. *Standard Test Method for Laboratory Determination of Pulse Velocities and Ultrasonic Elastic Constants of Rock*. ASTM International, West Conshohocken, PA.
- ASTM International. ASTM D4052-18a. 2018. *Standard Test Method for Density, Relative Density, and API Gravity of Liquids by Digital Density Meter*. ASTM International, West Conshohocken, PA.
- ASTM D445-19a. 2019. *Standard Test Method for Kinematic Viscosity of Transparent and Opaque Liquids (and Calculation of Dynamic Viscosity)*. ASTM International, West Conshohocken, PA.



- ATKINSON, B. K. 1984. Subcritical crack growth in geological materials. *Journal of Geophysical Research: Solid Earth*, 89, 4077-4114.
- AULD, B. A. 1973. *Acoustic fields and waves in solids*. Wiley Interscience Pub.
- AYDIN, A. 2013. Upgraded ISRM suggested method for determining sound velocity by ultrasonic pulse transmission technique. In *The ISRM Suggested Methods for Rock Characterization, Testing and Monitoring: 2007-2014*. Springer.
- BANDIS, S., LUMSDEN, A. & BARTON, N. 1983. Fundamentals of rock joint deformation. *International Journal of Rock Mechanics and Mining Sciences & Geomechanics Abstracts*, 249-268.
- BARBOSA, N. D., RUBINO, J. G., CASPARI, E., MILANI, M. & HOLLIGER, K. 2016. Fluid pressure diffusion effects on the seismic reflectivity of a single fracture. *The Journal of the Acoustical Society of America*, 140, 2554-2570.
- BARBOSA, N. D., RUBINO, J. G., CASPARI, E. & HOLLIGER, K. 2017. Extension of the classical linear slip model for fluid-saturated fractures: Accounting for fluid pressure diffusion effects. *Journal of Geophysical Research: Solid Earth*, 122, 1302-1323.
- BARBOSA, N. D., RUBINO, J. G., CASPARI, E., MILANI, M. & HOLLIGER, K. 2016. Fluid pressure diffusion effects on the seismic reflectivity of a single fracture. *The Journal of the Acoustical Society of America*, 140, 2554-2570.
- BARLA, G., MONACIS, G., PERINO, A. & HATZOR, Y. 2010. Distinct element modelling in static and dynamic conditions with application to an underground archaeological site. *Rock Mechanics and Rock Engineering*, 43, 877-890.
- BARTON, N. 1978. Suggested methods for the quantitative description of discontinuities in rock masses. *ISRM, International Journal of Rock Mechanics and Mining Sciences & Geomechanics Abstracts*, 15, 319-368.
- BARTON, N., BANDIS, S. & BAKHTAR, K. 1985. Strength, deformation and conductivity coupling of rock joints. *International Journal Of Rock Mechanics and Mining Sciences & Geomechanics Abstracts*, 121-140.

- BARTON, N. & CHOUBEY, V. 1977. The shear strength of rock joints in theory and practice. *Rock mechanics*, 10, 1-54.
- BATCHELOR, C. K. & BATCHELOR, G. 2000. *An introduction to fluid dynamics*, Cambridge university press.
- BATHIJA, A. P., LIANG, H., LU, N., PRASAD, M. & BATZLE, M. L. 2009. Stressed swelling clay. *Geophysics*, 74, A47-A52.
- BATZLE, M. L., HAN, D.-H. & HOFMANN, R. 2006. Fluid mobility and frequency-dependent seismic velocity—Direct measurements. *Geophysics*, 71, N1-N9.
- BATZLE, M. & WANG, Z. 1992. Seismic properties of pore fluids. *Geophysics*, 57, 1396-1408.
- BAUMGARTEN, W., DÖRNER, J. & HORN, R. 2013. Microstructural development in volcanic ash soils from South Chile. *Soil and Tillage Research*, 129, 48-60.
- BASU, A. & AYDIN, A. 2006. Evaluation of ultrasonic testing in rock material characterization. *Geotechnical Testing Journal*, 29, 117-125.
- BERTA, G. 1994. Blasting-induced vibration in tunnelling. *Tunnelling and Underground Space Technology*, 9, 175-187.
- BIRCH, F. 1960. The velocity of compressional waves in rocks to 10 kilobars: Part 1. *Journal of Geophysical Research*, 65, 1083-1102.
- BIRCH, F. 1961. The velocity of compressional waves in rocks to 10 kilobars: Part 2. *Journal of Geophysical Research*, 66, 2199-2224.
- BISWAS, A. 1967. The transmission of waves through a layered Voigt solid sandwiched between isotropic homogeneous elastic media of same nature. *Pure and Applied Geophysics*, 66, 25-29.
- BRADY, B. H. & BROWN, E. T. 1993. *Rock mechanics: for underground mining*, Springer science & business media.

- BREKHOVSKIKH, L. 2012. *Waves in layered media*, Elsevier.
- BROSSIER, R., OPERTO, S. & VIRIEUX, J. 2009. Seismic imaging of complex onshore structures by 2D elastic frequency-domain full-waveform inversion. *Geophysics*, 74, WCC105-WCC118.
- BROWN, S., CAPRIHAN, A. & HARDY, R. 1998. Experimental observation of fluid flow channels in a single fracture. *Journal of Geophysical Research: Solid Earth*, 103, 5125-5132.
- BUTT, S. 2001. Experimental measurement of P-wave attenuation due to fractures over the 100 to 300 kHz bandwidth. *Pure and Applied Geophysics*, 158, 1783-1796.
- CADORET, T., MARION, D. & ZINSZNER, B. 1995. Influence of frequency and fluid distribution on elastic wave velocities in partially saturated limestones. *Journal of Geophysical Research: Solid Earth*, 100, 9789-9803.
- CAI, J. G., 2001. *Effects of Parallel Fractures on Wave Attenuation in Rock Masses*. Ph. D. thesis. Nanyang Technological University, Singapore.
- CARBÓ, R. & MOLERO, A. 2002. Temperature dependence of high frequency sound attenuation in porous marine sediments. *Acta Acustica United With Acustica*, 88, 190-194.
- CARRIER, B., VANDAMME, M., PELLENQ, R. J.-M. & VAN DAMME, H. 2014. Elastic properties of swelling clay particles at finite temperature upon hydration. *The Journal of Physical Chemistry C*, 118, 8933-8943.
- CASCANTE, G., SANTAMARINA, C. & YASSIR, N. 1998. Flexural excitation in a standard torsional-resonant column device. *Canadian Geotechnical Journal*, 35, 478-490.
- CASPARI, E., NOVIKOV, M., LISITSA, V., BARBOSA, N. D., QUINTAL, B., RUBINO, J. G. & HOLLIGER, K. 2019. Attenuation mechanisms in fractured fluid-saturated porous rocks: a numerical modelling study. *Geophysical Prospecting*, 67, 935-955.
- CENGEL, Y. A. & BOLES, M. A. 2007. *Thermodynamics: An Engineering Approach 6th Edition (SI Units)*, The McGraw-Hill Companies, Inc., New York.

- CHA, M., CHO, G.-C. & SANTAMARINA, J. C. 2009. Long-wavelength P-wave and S-wave propagation in jointed rock masses. *Geophysics*, 74, E205-E214.
- CHA, M. S., SIM, Y. J., CHO, G. C. & LEE, S. W. 2006. The effect of joint conditions on the longitudinal and flexural wave velocities of a rock mass. *Key Engineering Materials*, 321, 306-309.
- CHEN, B. & EVANS, J. R. 2006. Elastic moduli of clay platelets. *Scripta Materialia*, 54, 1581-1585.
- CHEN, R., XIA, K., DAI, F., LU, F. & LUO, S. 2009. Determination of dynamic fracture parameters using a semi-circular bend technique in split Hopkinson pressure bar testing. *Engineering Fracture Mechanics*, 76, 1268-1276.
- CHEN, W. W. & SONG, B. 2010. *Split Hopkinson (Kolsky) bar: design, testing and applications*, Springer Science & Business Media.
- CHEN, X., LI, J., CAI, M., ZOU, Y. & ZHAO, J. 2015. Experimental study on wave propagation across a rock joint with rough surface. *Rock Mechanics and Rock Engineering*, 48, 2225-2234.
- CHEN, X., LI, J. C., CAI, M., ZOU, Y. & ZHAO, J. 2016. A further study on wave propagation across a single joint with different roughness. *Rock Mechanics and Rock Engineering*, 49, 2701-2709.
- CHENU, C. 1995. Low temperature scanning electron microscopy of clay and organic constituents and their relevance to soil microstructures. *Scanning Microscopy*, 9, 989-1010.
- CHO, G. C. & SANTAMARINA, J. C. 2001. Unsaturated particulate materials—particle-level studies. *Journal of Geotechnical and Geoenvironmental Engineering*, 127, 84-96.
- CHOPRA, S. & MARFURT, K. J. 2016. Spectral decomposition and spectral balancing of seismic data. *The Leading Edge*, 35, 176-179.
- CLARIÁ, J. J. & RINALDI, V. A. 2007. Shear wave velocity of a compacted clayey silt. *Geotechnical Testing Journal*, 30, 399-408.

- COOK, N. G. 1992. Natural joints in rock: mechanical, hydraulic and seismic behaviour and properties under normal stress. *International Journal of Rock Mechanics and Mining Sciences & Geomechanics Abstracts*, 29, 3 198-223.
- COSENZA, P. & TABBAGH, A. 2004. Electromagnetic determination of clay water content: role of the microporosity. *Applied Clay Science*, 26, 21-36.
- CUI, Z., SHENG, Q. & LENG, X. 2017. Analysis of S wave propagation through a nonlinear joint with the continuously yielding model. *Rock Mechanics and Rock Engineering*, 50, 113-123.
- DAI, F., HUANG, S., XIA, K. & TAN, Z. 2010. Some fundamental issues in dynamic compression and tension tests of rocks using split Hopkinson pressure bar. *Rock Mechanics and Rock Engineering*, 43, 657-666.
- DIMRI, V., SRIVASTAVA, R. & VEDANTI, N. 2012. Reservoir geophysics: some basic concepts. *Handbook of Geophysical Exploration: Seismic Exploration*. Elsevier.
- EASTEAL, A. J. & WOOLF, L. A. 1985. (p, V<sub>m</sub>, T, x) measurements for [(1-x) H<sub>2</sub>O + xCH<sub>3</sub>OH] in the range 278 to 323 K and 0.1 to 280 MPa I. Experimental results, isothermal compressibilities, thermal expansivities, and partial molar volumes. *The Journal of Chemical Thermodynamics*, 17, 49-62.
- EASTWOOD, J. 1993. Temperature-dependent propagation of P-and S-waves in Cold Lake oil sands; comparison of theory and experiment. *Geophysics*, 58, 863-872.
- EBRAHIMI, D., PELLENQ, R. J.-M. & WHITTLE, A. J. 2012. Nanoscale elastic properties of montmorillonite upon water adsorption. *Langmuir*, 28, 16855-16863.
- EGOROV, G. I. & MAKAROV, D. M. 2014. Volumetric properties of binary liquid-phase mixture of (water+ glycerol) at temperatures of (278.15 to 323.15) K and pressures of (0.1 to 100) MPa. *The Journal of Chemical Thermodynamics*, 79, 135-158.
- EISENBERG, D., KAUZMANN, W. & KAUZMANN, W. 2005. *The structure and properties of water*, Oxford University Press on Demand.

- EL AZHARI, H. & EL HASSANI, I.-E. E. A. 2013. Effect of the number and orientation of fractures on the P-wave velocity diminution: application on the building stones of the Rabat area (Morocco). *Geomaterials*, 3, 3, 71-81.
- ELMORE, W. C., ELMORE, W. C. & HEALD, M. A. 1985. *Physics of waves*, Courier Corporation.
- ELSWORTH, D., SPIERS, C. J. & NIEMEIJER, A. R. 2016. Understanding induced seismicity. *Science*, 354, 1380-1381.
- EWING, W. M., JARDETZKY, W. S., PRESS, F. & BEISER, A. 1957. Elastic waves in layered media. *Physics Today*, 10, 27.
- FANG, Y., ELSWORTH, D., WANG, C., ISHIBASHI, T. & FITTS, J. P. 2017. Frictional stability-permeability relationships for fractures in shales. *Journal of Geophysical Research: Solid Earth*, 122, 1760-1776.
- FATHOLLAHY, M., UROMEIEHY, A., RIAHI, M. A. & ZAREI, Y. 2021. P-Wave Velocity Calculation (PVC) in Rock Mass Without Geophysical-Seismic Field Measurements. *Rock Mechanics and Rock Engineering*, 1-15.
- FARAGHER, R. 2012. Understanding the basis of the kalman filter via a simple and intuitive derivation [lecture notes]. *IEEE Signal processing magazine*, 29, 128-132.
- FEHLER, M. 1982. Interaction of seismic waves with a viscous liquid layer. *Bulletin of the Seismological Society of America*, 72, 55-72.
- FOX, F. E. & ROCK, G. D. 1946. Compressional viscosity and sound absorption in water at different temperatures. *Physical Review*, 70, 68.
- FRATTA, D. & SANTAMARINA, J. 2002. Shear wave propagation in jointed rock: State of stress. *Géotechnique*, 52, 495-505.
- FREW, D., FORRESTAL, M. J. & CHEN, W. 2001. A split Hopkinson pressure bar technique to determine compressive stress-strain data for rock materials. *Experimental Mechanics*, 41, 40-46.

- FREW, D. J., FORRESTAL, M. J. & CHEN, W. 2002. Pulse shaping techniques for testing brittle materials with a split Hopkinson pressure bar. *Experimental Mechanics*, 42, 93-106.
- GIST, G. A. 1991. Fluid effects on velocity and attenuation in sandstones. *The Journal of the Acoustical Society of America*, 90, 2370-2371.
- GOODMAN, R. E. 1989. *Introduction to rock mechanics*, Wiley New York.
- GRAY, G. T., III 2000. Classic Split-Hopkinson Pressure Bar Testing. In: KUHN, H. & MEDLIN, D. (eds.) *Mechanical Testing and Evaluation*. ASM International.
- GROENENBOOM, J. & FOKKEMA, J. T. 1998. Monitoring the width of hydraulic fractures with acoustic waves. *Geophysics*, 63, 139-148.
- GU, B., SUÁREZ-RIVERA, R., NIHEI, K. T. & MYER, L. R. 1996. Incidence of plane waves upon a fracture. *Journal of Geophysical Research: Solid Earth*, 101, 25337-25346.
- GUREVICH, B. 2002. Effect of fluid viscosity on elastic wave attenuation in porous rocks. *Geophysics*, 67, 264-270.
- HALL, L. 1948. The origin of ultrasonic absorption in water. *Physical Review*, 73, 775.
- HEDAYAT, A. 2013. *Mechanical and geophysical characterization of damage in rocks*. Ph.D. thesis. Purdue University West Lafayette, IN.
- HEDAYAT, A., HAERI, H., HINTON, J., MASOUMI, H. & SPAGNOLI, G. 2018. Geophysical signatures of shear-induced damage and frictional processes on rock joints. *Journal of Geophysical Research: Solid Earth*, 123, 1143-1160.
- HEDAYAT, A., PYRAK-NOLTE, L. J. & BOBET, A. 2014. Precursors to the shear failure of rock discontinuities. *Geophysical Research Letters*, 41, 5467-5475.
- HOLTHUSEN, D., PETH, S. & HORN, R. 2010. Impact of potassium concentration and matric potential on soil stability derived from rheological parameters. *Soil and Tillage Research*, 111, 75-85.



- HOPKINS, D. L. 1991. *The effect of surface roughness on joint stiffness, aperture, and acoustic wave propagation*. Ph.D. thesis. University of California, Berkeley.
- HOPKINS, D. 2000. The implications of joint deformation in analyzing the properties and behavior of fractured rock masses, underground excavations, and faults. *International Journal of Rock Mechanics and Mining Sciences*, 37, 175-202.
- HOPKINS, D., COOK, N. & MYER, L. 1990. Normal joint stiffness as a function of spatial geometry and surface roughness. In *International symposium on rock joints*, 203-210.
- HOPKINS, D. L., COOK, N. G. & MYER, L. R. 1987. Fracture stiffness and aperture as a function of applied stress and contact geometry. In *The 28th US Symposium on Rock Mechanics (USRMS)*. American Rock Mechanics Association.
- HOPKINSON, J. 1872. On the rupture of iron wire by a blow. *Proc. Literary and Philosophical Society of Manchester*, 1, 40-45.
- HORN, R. & PETH, S. 2011. Mechanics of unsaturated soils for agricultural applications. *Handbook of soil sciences*, 2, 1-30.
- HUANG, J., LIU, X., ZHAO, J., WANG, E. & WANG, S. 2020. Propagation of Stress Waves Through Fully Saturated Rock Joint Under Undrained Conditions and Dynamic Response Characteristics of Filling Liquid. *Rock Mechanics and Rock Engineering*, 53(8), 3637-3655.
- HUANG, X., QI, S., GUO, S. & DONG, W. 2014. Experimental study of ultrasonic waves propagating through a rock mass with a single joint and multiple parallel joints. *Rock Mechanics and Rock Engineering*, 47, 549-559.
- HUANG, X., QI, S., XIA, K. & SHI, X. 2018a. Particle crushing of a filled fracture during compression and its effect on stress wave propagation. *Journal of Geophysical Research: Solid Earth*, 123, 5559-5587.
- HUANG, X., QI, S., XIA, K., ZHENG, H. & ZHENG, B. 2016. Propagation of high amplitude stress waves through a filled artificial joint: An experimental study. *Journal of Applied Geophysics*, 130, 1-7.

- HUANG, X., QI, S., YAO, W. & XIA, K. 2018b. Effect of Filling Humidity on the Propagation of High-Amplitude Stress Waves through an Artificial Joint. *Geotechnical Testing Journal*, 42, 30-42.
- HUNZIKER, J., FAVINO, M., CASPARI, E., QUINTAL, B., RUBINO, J. G., KRAUSE, R. & HOLLIGER, K. 2018. Seismic attenuation and stiffness modulus dispersion in porous rocks containing stochastic fracture networks. *Journal of Geophysical Research: Solid Earth*, 123, 125-143.
- INDRARATNA, B., PREMADASA, W., BROWN, E. T., GENS, A. & HEITOR, A. 2014. Shear strength of rock joints influenced by compacted infill. *International Journal of Rock Mechanics and Mining Sciences*, 70, 296-307.
- IWASA, K. & YOSHIOKA, N. 1998. An experimental trial to detect precursory slips by transmission waves across a fault. *Geophysical Research Letters*, 25, 3907-3910.
- ISHIBASHI, T., ELSWORTH, D., FANG, Y., RIVIERE, J., MADARA, B., ASANUMA, H., WATANABE, N. & MARONE, C. 2018. Friction-stability-permeability evolution of a fracture in granite. *Water Resources Research*, 54, 9901-9918.
- JAEGER, J. C., COOK, N. G. & ZIMMERMAN, R. 2009. *Fundamentals of rock mechanics*, John Wiley & Sons.
- JOHN, K. 1969. Engineering methods to determine the strength and deformability of regularly jointed rock. In *The 11th US Symposium on Rock Mechanics (USRMS)*. American Rock Mechanics Association.
- JOHNSTON, D. H., TOKSÖZ, M. & TIMUR, A. 1979. Attenuation of seismic waves in dry and saturated rocks: II. Mechanisms. *Geophysics*, 44, 691-711.
- JONES, T. D. 1986. Pore fluids and frequency-dependent wave propagation in rocks. *Geophysics*, 51, 1939-1953.
- JU, Y., SUDAK, L. & XIE, H. 2007. Study on stress wave propagation in fractured rocks with fractal joint surfaces. *International Journal of Solids and Structures*, 44, 4256-4271.

- JUNG, G., CULL, J. P. & COX, S. 1995. Spectral acoustic techniques for joint and fracture characterization. *Exploration Geophysics*, 26, 374-378.
- KACHANOV, M. 1992. Effective elastic properties of cracked solids: critical review of some basic concepts. *Applied Mechanics Reviews*, 45, 8, 304-335.
- KAHRAMAN, S. 2001. A correlation between P-wave velocity, number of joints and Schmidt hammer rebound number. *International Journal of Rock Mechanics and Mining Sciences*, 38, 729-733.
- KAHRAMAN, S. 2002. The effects of fracture roughness on P-wave velocity. *Engineering Geology*, 63, 347-350.
- KALMAN, R. E. 1960. A new approach to linear filtering and prediction problems. *Journal of Basic Engineering*, 82, 1, 35-45.
- KAMALI-ASL, A., KC, B., GHAZANFARI, E. & HEDAYAT, A. 2019. Flow-induced alterations of ultrasonic signatures and fracture aperture under constant state of stress in a single-fractured rock. *Geophysics*, 84, WA115-WA125.
- KAPROTH, B. M. & MARONE, C. 2014. Evolution of elastic wave speed during shear-induced damage and healing within laboratory fault zones. *Journal of Geophysical Research: Solid Earth*, 119, 4821-4840.
- KARABORNI, S., SMIT, B., HEIDUG, W., URAI, J. & VAN OORT, E. 1996. The swelling of clays: molecular simulations of the hydration of montmorillonite. *Science*, 271, 1102-1104.
- KENIGSBERG, A. R., RIVIÈRE, J., MARONE, C. & SAFFER, D. M. 2019. The effects of shear strain, fabric, and porosity evolution on elastic and mechanical properties of clay-rich fault gouge. *Journal of Geophysical Research: Solid Earth*, 124, 10968-10982.
- KHANDELWAL, M. & SINGH, T. 2007. Evaluation of blast-induced ground vibration predictors. *Soil Dynamics and Earthquake Engineering*, 27, 116-125.
- KHAZANEHDARI, J. & SOTHCOTT, J. 2003. Variation in dynamic elastic shear modulus of sandstone upon fluid saturation and substitution. *Geophysics*, 68, 472-481.

- KING, M. 2002. Elastic wave propagation in and permeability for rocks with multiple parallel fractures. *International Journal of Rock Mechanics and Mining Sciences*, 39, 8, 1033-1043.
- KING, M., MARSDEN, J. & DENNIS, J. 2000. Biot dispersion for P-and S-wave velocities in partially and fully saturated sandstones. *Geophysical Prospecting*, 48, 1075-1089.
- KINSLER, L. E., FREY, A. R., COPPENS, A. B. & SANDERS, J. V. 2000. *Fundamentals of Acoustics*. John Wiley & Sons. Inc, New York.
- KNIGHT, R., DVORKIN, J. & NUR, A. 1998. Acoustic signatures of partial saturation. *Geophysics*, 63, 132-138.
- KNIGHT, R. & NOLEN-HOEKSEMA, R. 1990. A laboratory study of the dependence of elastic wave velocities on pore scale fluid distribution. *Geophysical Research Letters*, 17, 1529-1532.
- KNOPOFF, L. 1964. Department of Physics and Institute of Geophysics and Planetary Physics University of California, Los Angeles. *Reviews of Geophysics*, 2, 625-660.
- KNUTH, M. W., TOBIN, H. J. & MARONE, C. 2013. Evolution of ultrasonic velocity and dynamic elastic moduli with shear strain in granular layers. *Granular Matter*, 15, 499-515.
- KOLSKY, H. 1949. An investigation of the mechanical properties of materials at very high rates of loading. In *Proceedings of the physical society. Section B*, 62, 676.
- KOLSKY, H. 1963. *Stress waves in solids*, Courier Corporation.
- LAROCK, B. E., JEPPSON, R. W. & WATTERS, G. Z. 1999. *Hydraulics of pipeline systems*, CRC press.
- LEONG, E.-C., YEO, S.-H. & RAHARDJO, H. 2004. Measurement of wave velocities and attenuation using an ultrasonic test system. *Canadian Geotechnical Journal*, 41, 844-860.

- LEURER, K. C. 1997. Attenuation in fine-grained marine sediments: Extension of the Biot-Stoll model by the “effective grain model”(EGM). *Geophysics*, 62, 1465-1479.
- LI, D., HAN, Z., ZHU, Q., ZHANG, Y. & RANJITH, P. 2019a. Stress wave propagation and dynamic behavior of red sandstone with single bonded planar joint at various angles. *International Journal of Rock Mechanics and Mining Sciences*, 117, 162-170.
- LI, D., WEI, J., DI, B., DING, P. & SHUAI, D. 2017. The effect of fluid saturation on the dynamic shear modulus of tight sandstones. *Journal of Geophysics and Engineering*, 14, 1072-1086.
- LI, D., WEI, J., DI, B., SHUAI, D., TIAN, L. & DING, P. 2020. Effect of fluid saturation on the shear modulus of artificial clay-rich tight sandstones. *Geophysical Journal International*, 222, 15-26.
- LI, J., LI, H., JIAO, Y., LIU, Y., XIA, X. & YU, C. 2014. Analysis for oblique wave propagation across filled joints based on thin-layer interface model. *Journal of Applied Geophysics*, 102, 39-46.
- LI, J., LI, H., MA, G. & ZHAO, J. 2012. A time-domain recursive method to analyse transient wave propagation across rock joints. *Geophysical Journal International*, 188, 631-644.
- LI, J., LI, N., LI, H. & ZHAO, J. 2017. An SHPB test study on wave propagation across rock masses with different contact area ratios of joint. *International Journal of Impact Engineering*, 105, 109-116.
- LI, J. & MA, G. 2009. Experimental study of stress wave propagation across a filled rock joint. *International Journal of Rock Mechanics and Mining Sciences*, 46, 471-478.
- LI, J. & MA, G. 2010. Analysis of blast wave interaction with a rock joint. *Rock Mechanics and Rock Engineering*, 43, 777-787.
- LI, J., MA, G. & HUANG, X. 2010. Analysis of wave propagation through a filled rock joint. *Rock Mechanics and Rock Engineering*, 43, 789-798.
- LI, J., MA, G. & ZHAO, J. 2011a. Analysis of stochastic seismic wave interaction with a slippery rock fault. *Rock mechanics and rock engineering*, 44, 85-92.

- LI, J., MA, G. & ZHAO, J. 2010. An equivalent viscoelastic model for rock mass with parallel joints. *Journal of Geophysical Research: Solid Earth*, 115.
- LI, J., RONG, L., LI, H. & HONG, S. 2019b. An SHPB test study on stress wave energy attenuation in jointed rock masses. *Rock Mechanics and Rock Engineering*, 52, 403-420.
- LI, J. C., WU, W., LI, H., ZHU, J. & ZHAO, J. 2013. A thin-layer interface model for wave propagation through filled rock joints. *Journal of Applied Geophysics*, 91, 31-38.
- LI, X., LI, H., LI, J. & ZHAO, J. 2018. Effect of joint thickness on seismic response across a filled rock fracture. *Géotechnique Letters*, 8, 190-194.
- LI, X., LOK, T. & ZHAO, J. 2005. Dynamic characteristics of granite subjected to intermediate loading rate. *Rock Mechanics and Rock Engineering*, 38, 21-39.
- LI, X., LOK, T., ZHAO, J. & ZHAO, P. 2000. Oscillation elimination in the Hopkinson bar apparatus and resultant complete dynamic stress–strain curves for rocks. *International Journal of Rock Mechanics and Mining Sciences*, 37, 1055-1060.
- LI, X., ZHONG, L. & PYRAK-NOLTE, L. J. 2001. Physics of partially saturated porous media: Residual saturation and seismic-wave propagation. *Annual Review of Earth and Planetary Sciences*, 29, 419-460.
- LI, X., ZHOU, Z., LOK, T.-S., HONG, L. & YIN, T. 2008. Innovative testing technique of rock subjected to coupled static and dynamic loads. *International Journal of Rock Mechanics and Mining Sciences*, 45, 739-748.
- LI, Y. & ZHU, Z. 2012. Study on the velocity of P waves across a single joint based on fractal and damage theory. *Engineering Geology*, 151, 82-88.
- LI, Y., ZHU, Z., LI, B., DENG, J. & XIE, H. 2011b. Study on the transmission and reflection of stress waves across joints. *International Journal of Rock Mechanics and Mining Sciences*, 48, 364-371.

- LINDHOLM, U., YEAKLEY, L. & NAGY, A. 1974. The dynamic strength and fracture properties of dresser basalt. *International Journal of Rock Mechanics and Mining Sciences & Geomechanics Abstracts*, 181-191.
- LISSA, S., BARBOSA, N. D., RUBINO, J. & QUINTAL, B. 2019. Seismic attenuation and dispersion in poroelastic media with fractures of variable aperture distributions. *Solid Earth*, 10, 1321-1336.
- LITOVITZ, T. & DAVIS, C. 1965. *Structural and shear relaxation in liquids*. Physical acoustics. Elsevier.
- LIU, E. 2005. Effects of fracture aperture and roughness on hydraulic and mechanical properties of rocks: implication of seismic characterization of fractured reservoirs. *Journal of Geophysics and Engineering*, 2, 38-47.
- LIU, E., HUDSON, J. A. & POINTER, T. 2000. Equivalent medium representation of fractured rock. *Journal of Geophysical Research: Solid Earth*, 105, 2981-3000.
- LIU, T., LI, J., LI, H., LI, X., ZHENG, Y. & LIU, H. 2017. Experimental study of s-wave propagation through a filled rock joint. *Rock Mechanics and Rock Engineering*, 50, 2645-2657.
- LIU, T., LI, X., ZHENG, Y., MENG, F. & SONG, D. 2020. Analysis of Seismic Waves Propagating through an In Situ Stressed Rock Mass Using a Nonlinear Model. *International Journal of Geomechanics*, 20, 04020002.
- LO, W.-C., YEH, C.-L. & TSAI, C.-T. 2007. Effect of soil texture on the propagation and attenuation of acoustic wave at unsaturated conditions. *Journal of Hydrology*, 338, 273-284.
- LOUATI, M. & GHIDAOU, M. S. 2017a. High-frequency acoustic wave properties in a water-filled pipe. Part 1: dispersion and multi-path behaviour. *Journal of Hydraulic Research*, 55, 613-631.



- LOUATI, M. & GHIDAOU, M. S. 2017b. High-frequency acoustic wave properties in a water-filled pipe. Part 2: range of propagation. *Journal of Hydraulic Research*, 55, 632-646.
- LU, N. & KHORSHIDI, M. 2015. Mechanisms for soil-water retention and hysteresis at high suction range. *Journal of Geotechnical and Geoenvironmental Engineering*, 141, 04015032.
- LUBBE, R., SOTHCOTT, J., WORTHINGTON, M. & MCCANN, C. 2008. Laboratory estimates of normal and shear fracture compliance. *Geophysical Prospecting*, 56, 239-247.
- LUCET, N. & ZINSZNER, B. 1992. Effects of heterogeneities and anisotropy on sonic and ultrasonic attenuation in rocks. *Geophysics*, 57, 1018-1026.
- LUNDBERG, B. A split Hopkinson bar study of energy absorption in dynamic rock fragmentation. 1976. *International Journal of Rock Mechanics and Mining Sciences & Geomechanics Abstracts*, 187-197.
- MARKHAM, J. J., BEYER, R. T. & LINDSAY, R. 1951. Absorption of sound in fluids. *Reviews of Modern Physics*, 23, 353.
- MARKGRAF, W. & HORN, R. 2006. Rheological-stiffness analysis of K<sup>+</sup>-treated and CaCO<sub>3</sub>-rich soils. *Journal of Plant Nutrition and Soil Science*, 169, 411-419.
- MARKGRAF, W., HORN, R. & PETH, S. 2006. An approach to rheometry in soil mechanics—structural changes in bentonite, clayey and silty soils. *Soil and Tillage Research*, 91, 1-14.
- MAVKO, G. 2013. Relaxation shift in rocks containing viscoelastic pore fluids. *Geophysics*, 78, M19-M28.
- MAVKO, G. & JIZBA, D. 1994. The relation between seismic P-and S-wave velocity dispersion in saturated rocks. *Geophysics*, 59, 87-92.
- MAVKO, G., MUKERJI, T. & DVORKIN, J. 2020. *The rock physics handbook*, Cambridge university press.

- MAVKO, G. & NOLEN-HOEKSEMA, R. 1994. Estimating seismic velocities at ultrasonic frequencies in partially saturated rocks. *Geophysics*, 59, 252-258.
- MAVKO, G. M. & NUR, A. 1979. Wave attenuation in partially saturated rocks. *Geophysics*, 44, 161-178.
- MAVKO, G. & VANORIO, T. 2010. The influence of pore fluids and frequency on apparent effective stress behavior of seismic velocities. *Geophysics*, 75, N1-N7.
- MEZGER, T. G. 2006. *The rheology handbook: for users of rotational and oscillatory rheometers*, Vincentz Network GmbH & Co KG.
- MILLER, R. 1977. An approximate method of analysis of the transmission of elastic waves through a frictional boundary. *Journal of Applied Mechanics*, 44, 4, 652-656.
- MILLER, R. K. 1978. The effects of boundary friction on the propagation of elastic waves. *Bulletin of the Seismological Society of America*, 68, 987-998.
- MINDLIN, R. 1960. Waves and vibrations in isotropic, elastic plates. *Structure Mechanics*, 199-232.
- MITCHELL, J. K. & SOGA, K. 2005. *Fundamentals of soil behavior*, John Wiley & Sons New York.
- MOHD-NORDIN, M. M., SONG, K.-I., CHO, G.-C. & MOHAMED, Z. 2014. Long-wavelength elastic wave propagation across naturally fractured rock masses. *Rock Mechanics and Rock Engineering*, 47, 561-573.
- MOHD-NORDIN, M. M., SONG, K.-I., KIM, D. & CHANG, I. 2016. Evolution of joint roughness degradation from cyclic loading and its effect on the elastic wave velocity. *Rock Mechanics and Rock Engineering*, 49, 3363-3370.
- MONTONE, P. & MARIUCCI, M. T. 2015. P-wave velocity, density, and vertical stress magnitude along the crustal Po Plain (Northern Italy) from sonic log drilling data. *Pure and Applied Geophysics*, 172, 1547-1561.

- MORLET, J., ARENS, G., FOURGEAU, E. & GLARD, D. 1982. Wave propagation and sampling theory—Part I: Complex signal and scattering in multilayered media. *Geophysics*, 47, 203-221.
- MÜLLER, T. M., GUREVICH, B. & LEBEDEV, M. 2010. Seismic wave attenuation and dispersion resulting from wave-induced flow in porous rocks—A review. *Geophysics*, 75, 75A147-75A164.
- MUNSON, B. R., OKIISHI, T. H., HUEBSCH, W. W. & ROTHMAYER, A. P. 2013. *Fluid mechanics*, Wiley Singapore.
- MYER, L., HOPKINS, D. & COOK, N. 1995. Effects of contact area of an interface on acoustic wave transmission characteristics. In *The 26th US Symposium on Rock Mechanics (USRMS)*, American Rock Mechanics Association.
- MYER, L. R., PYRAK-NOLTE, L. J. & COOK, N. G. 1990. Effects of single fractures on seismic wave propagation. In *International symposium on rock joints*, 467-473.
- NAGATA, K., KILGORE, B., BEELER, N. & NAKATANI, M. 2014. High-frequency imaging of elastic contrast and contact area with implications for naturally observed changes in fault properties. *Journal of Geophysical Research: Solid Earth*, 119, 5855-5875.
- NAGATA, K., NAKATANI, M. & YOSHIDA, S. 2008. Monitoring frictional strength with acoustic wave transmission. *Geophysical Research Letters*, 35.
- NAKAGAWA, S. 1998. *Acoustic resonance characteristics of rock and concrete containing fractures*. Ph.D. Thesis. Lawrence Berkeley National Lab.(LBNL), Berkeley, CA (United States).
- NAKAGAWA, S., NIHEI, K. & MYER, L. 2000. Shear-induced conversion of seismic waves across single fractures. *International Journal of Rock Mechanics and Mining Sciences*, 37, 203-218.

- NAKAGAWA, S., PRIDE, S. R. & NIHEI, K. T. 2019. Interaction of a normally-incident plane wave with a nonlinear poroelastic fracture. *The Journal of the Acoustical Society of America*, 146, 1705-1720.
- NAKAGAWA, S. & SCHOENBERG, M. A. 2007. Poroelastic modeling of seismic boundary conditions across a fracture. *The Journal of the Acoustical Society of America*, 122, 831-847.
- NOURIFARD, N., MASHINSKII, E. & LEBEDEV, M. 2019. The effect of wave amplitude on S-wave velocity in porous media: an experimental study by Laser Doppler Interferometry. *Exploration Geophysics*, 50, 683-691.
- NUR, A., TOSAYA, C. & VO-THANH, D. 1984. Seismic monitoring of thermal enhanced oil recovery processes. In *SEG Technical Program Expanded Abstracts 1984*. Society of Exploration Geophysicists.
- O'CONNELL, R. J. & BUDIANSKY, B. 1977. Viscoelastic properties of fluid-saturated cracked solids. *Journal of Geophysical Research*, 82, 5719-5735.
- OELKE, A., ALEXANDROV, D., ABAKUMOV, I., GLUBOKOVSKIY, S., SHIGAPOV, R., KRÜGER, O., KASHTAN, B., TROYAN, V. & SHAPIRO, S. 2013. Seismic reflectivity of hydraulic fractures approximated by thin fluid layers. *Geophysics*, 78, T79-T87.
- PERINO, A. & BARLA, G. 2015. Resonant column apparatus tests on intact and jointed rock specimens with numerical modelling validation. *Rock Mechanics and Rock Engineering*, 48, 197-211.
- PÉRTILE, P., HOLTHUSEN, D., GUBIANI, P. I. & REICHERT, J. M. 2018. Microstructural strength of four subtropical soils evaluated by rheometry: properties, difficulties and opportunities. *Scientia Agricola*, 75, 154-162.
- PÉRTILE, P., REICHERT, J. M., GUBIANI, P. I., HOLTHUSEN, D. & COSTA, A. D. 2016. Rheological parameters as affected by water tension in subtropical soils. *Revista Brasileira de ciência do solo*, 40.

- PESELNICK, L., DIETERICH, J., MJACHKIN, V. & SOBOLEV, G. 1976. Variation of compressional velocities in simulated fault gouge under normal and direct shear stress. *Geophysical Research Letters*, 3, 369-372.
- PETROVITCH, C., PYRAK-NOLTE, L. & NOLTE, D. 2014. Combined scaling of fluid flow and seismic stiffness in single fractures. *Rock Mechanics and Rock Engineering*, 47, 1613-1623.
- PHAM, N. H., CARCIONE, J. M., HELLE, H. B. & URSIN, B. 2008. Wave velocities and attenuation of shaley sandstones as a function of pore pressure and partial saturation. *Geophysical Prospecting*, 50, 615-627.
- PINKERTON, J. 1947. A pulse method for the measurement of ultrasonic absorption in liquids: results for water. *Nature*, 160, 128-129.
- PLACE, J., GHAFAR, A. N., MALEHMIR, A., DRAGANOVIC, A. & LARSSON, S. 2016. On using the thin fluid-layer approach at ultrasonic frequencies for characterising grout propagation in an artificial fracture. *International Journal of Rock Mechanics and Mining Sciences*, 89, 68-74.
- POLLARD, D. D. & AYDIN, A. 1988. Progress in understanding jointing over the past century. *Geological Society of America Bulletin*, 100, 8, 1181-1204.
- PRIDE, S. R., BERRYMAN, J. G. & HARRIS, J. M. 2004. Seismic attenuation due to wave-induced flow. *Journal of Geophysical Research: Solid Earth*, 109.
- PYRAK-NOLTE, L. 1988. *Seismic visibility of fractures*. Ph. D. Thesis. University of California at Berkeley, 160p.
- PYRAK-NOLTE, L. The seismic response of fractures and the interrelations among fracture properties. 1996. *International Journal of Rock Mechanics and Mining Sciences & Geomechanics Abstracts*, 33, 8, 787-802.
- PYRAK-NOLTE, L. J., MYER, L. & COOK, N. 1987. Seismic visibility of fractures. In *US symposium on rock mechanics*, 28, 47-56.

- PYRAK-NOLTE, L. J., MYER, L. R. & COOK, N. G. 1990. Transmission of seismic waves across single natural fractures. *Journal of Geophysical Research: Solid Earth*, 95, 8617-8638.
- PYRAK-NOLTE, L. J. & NOLTE, D. D. 1995. Wavelet analysis of velocity dispersion of elastic interface waves propagating along a fracture. *Geophysical Research Letters*, 22, 1329-1332.
- RADZIUK, D. & MÖHWALD, H. 2016. Ultrasonically treated liquid interfaces for progress in cleaning and separation processes. *Physical Chemistry Chemical Physics*, 18, 21-46.
- REISER, F., SCHMELZBACH, C., SOLLBERGER, D., MAURER, H., GREENHALGH, S., PLANKE, S., KÄSTNER, F., FLÓVENZ, Ó., GIESE, R. & HALLDÓRSDÓTTIR, S. 2020. Imaging the high-temperature geothermal field at Krafla using vertical seismic profiling. *Journal of Volcanology and Geothermal Research*, 391, 106474.
- RESENDE, J. R. P. 2010. *An investigation of stress wave propagation through rock joints and rock masses*. Ph. D. Thesis. Universidade do Porto (Portugal), Ann Arbor.
- RICHART, F. E., HALL, J. R. & WOODS, R. D. 1970. *Vibrations of soils and foundations*. Printed in the United States of America.
- RIENSTRA, S. W. & HIRSCHBERG, A. 2004. An introduction to acoustics. Eindhoven University of Technology, *IWDE report 9206*, 18, 19.
- ROKHLIN, S. & WANG, Y. 1991. Analysis of boundary conditions for elastic wave interaction with an interface between two solids. *The Journal of the Acoustical Society of America*, 89, 503-515.
- ROY, S. & PYRAK-NOLTE, L. J. 1995. Interface waves propagating along tensile fractures in dolomite. *Geophysical Research Letters*, 22, 2773-2776.
- ROY, S. & PYRAK-NOLTE, L. J. 1997. Observation of a distinct compressional-mode interface wave on a single fracture. *Geophysical Research Letters*, 24, 173-176.

- RUBINO, J. G., CASTROMÁN, G. A., MÜLLER, T. M., MONACHESI, L. B., ZYSERMAN, F. I. & HOLLIGER, K. 2015. Including poroelastic effects in the linear slip theory. *Geophysics*, 80, A51-A56.
- RUBINO, J. G., GUARRACINO, L., MÜLLER, T. M. & HOLLIGER, K. 2013. Do seismic waves sense fracture connectivity? *Geophysical Research Letters*, 40, 692-696.
- RUBINO, J. G. & HOLLIGER, K. 2012. Seismic attenuation and velocity dispersion in heterogeneous partially saturated porous rocks. *Geophysical Journal International*, 188, 1088-1102.
- RUBINO, J. G., MÜLLER, T. M., MILANI, M. & HOLLIGER, K. 2014. Seismic attenuation and velocity dispersion in fractured rocks: The role played by fracture contact areas. *Geophysical Prospecting*, 62, 1278-1296.
- SCHOENBERG, M. 1980. Elastic wave behavior across linear slip interfaces. *The Journal of the Acoustical Society of America*, 68, 1516-1521.
- SCHOEN, M., RHYKERD, C. L., DIESTLER, D. J. & CUSHMAN, J. H. 1989. Shear forces in molecularly thin films. *Science*, 245, 1223-1225.
- SEBASTIAN, R. & SITHARAM, T. 2015. Long wavelength propagation of elastic waves across frictional and filled rock joints with different orientations: experimental results. *Geotechnical and Geological Engineering*, 33, 923-934.
- SEBASTIAN, R. & SITHARAM, T. 2016. Long-wavelength propagation of waves in jointed rocks-study using resonant column experiments and model material. *Geomechanics and Geoengineering*, 11, 281-296.
- SEBASTIAN, R. & SITHARAM, T. 2018. Resonant Column Tests and Nonlinear Elasticity in Simulated Rocks. *Rock Mechanics and Rock Engineering*, 51, 155-172.
- SENFT, L. E. & STEWART, S. T. 2009. Dynamic fault weakening and the formation of large impact craters. *Earth and Planetary Science Letters*, 287, 471-482.
- SHERIFF, R. E. & GELDART, L. P. 1995. *Exploration seismology*, Cambridge University Press.



- SINGH, P. 2002. Blast vibration damage to underground coal mines from adjacent open-pit blasting. *International Journal of Rock Mechanics and Mining Sciences*, 39, 959-973.
- SINHA, S., ROUTH, P. S., ANNO, P. D. & CASTAGNA, J. P. 2005. Spectral decomposition of seismic data with continuous-wavelet transform. *Geophysics*, 70, P19-P25.
- SONG, K.-I. & CHO, G.-C. 2010. Numerical study on the evaluation of tunnel shotcrete using the Impact-Echo method coupled with Fourier transform and short-time Fourier transform. *International Journal of Rock Mechanics and Mining Sciences*, 47, 1274-1288.
- SPENCER JR, J. W. & NUR, A. M. 1976. The effects of pressure, temperature, and pore water on velocities in Westerly granite. *Journal of Geophysical Research*, 81, 899-904.
- STEIN, S. & WYSS, M. 2009. *An introduction to seismology, earthquakes, and earth structure*, John Wiley & Sons.
- STOICA, P. & MOSES, R. L. 2005. *Spectral analysis of signals*. J Wiley&Sons.
- STREET, R. L., WATTERS, G. Z. & VENNARD, J. K. 1996. *Elementary fluid mechanics*. J Wiley&Sons.
- SUÁREZ-RIVERA, F. R., COOK, N. G. & MYER, L. R. 1992. Influence of rheology on shear-wave propagation across thin layers of clay. *In SEG Technical Program Expanded Abstracts*, 670-673. Society of Exploration Geophysicists.
- SUÁREZ-RIVERA, R. 1994. *The influence of thin clay layers containing liquids on the propagation of shear waves*. Ph.D. Thesis. University of California, Berkeley
- SUKOLRAT, J. 2007. *Structure and deconstruction of Bothkennar clay*. Ph.D. Thesis. University of Bristol.
- SUN, Y., LIN, H. & LOW, P. 1986. The nonspecific interaction of water with the surfaces of clay minerals. *Journal of Colloid and Interface Science*, 112, 556-564.
- TEJA, A. & RICE, P. 1981. Generalized corresponding states method for the viscosities of liquid mixtures. *Industrial & Engineering Chemistry Fundamentals*, 20, 77-81.

- THOMSON, W. T. 1950. Transmission of elastic waves through a stratified solid medium. *Journal of Applied Physics*, 21, 89-93.
- TINTI, E., SCUDERI, M., SCOGNAMIGLIO, L., DI STEFANO, G., MARONE, C. & COLLETTINI, C. 2016. On the evolution of elastic properties during laboratory stick-slip experiments spanning the transition from slow slip to dynamic rupture. *Journal of Geophysical Research: Solid Earth*, 121, 8569-8594.
- TOKSÖZ, M., JOHNSTON, D. H. & TIMUR, A. 1979. Attenuation of seismic waves in dry and saturated rocks: I. Laboratory measurements. *Geophysics*, 44, 681-690.
- TREVENA, D. 1969. Ultrasonic waves in liquids. *Contemporary Physics*, 10, 601-614.
- TUTUNCU, A. N., PODIO, A. L. & SHARMA, M. M. 1998. Nonlinear viscoelastic behavior of sedimentary rocks, Part II: Hysteresis effects and influence of type of fluid on elastic moduli. *Geophysics*, 63, 195-203.
- VANORIO, T., PRASAD, M. & NUR, A. 2003. Elastic properties of dry clay mineral aggregates, suspensions and sandstones. *Geophysical Journal International*, 155, 319-326.
- VASHEGHANI, F. & LINES, L. R. 2009. Viscosity and Q in heavy-oil reservoir characterization. *The Leading Edge*, 28, 856-860.
- VENNARD, J. K. 2011. *Elementary fluid mechanics*, Read Books Ltd.
- VIDALE, J. E. & LI, Y.-G. 2003. Damage to the shallow Landers fault from the nearby Hector Mine earthquake. *Nature*, 421, 524.
- VIGGIANI, G. & ATKINSON, J. 1995. Interpretation of bender element tests. *Geotechnique*, 45, 149-154.
- WANG, C. Y., GOODMAN, R. E. & SUNDARAM, P. 1975. Variations of VP and VS in granite premonitory to shear rupture and stick-slip sliding: Application to earthquake prediction. *Geophysical Research Letters*, 2, 309-311.

- WANG, R., HU, Z. & WANG, Q. 2019. A time-domain recursive method of SH-wave propagation through the filled fracture with linear viscoelastic deformation behavior. *Waves in Random and Complex Media*, 1-14.
- WANG, R., HU, Z., ZHANG, D. & WANG, Q. 2017. Propagation of the stress wave through the filled joint with linear viscoelastic deformation behavior using time-domain recursive method. *Rock Mechanics and Rock Engineering*, 50, 3197-3207.
- WANG, Z., DI, H., SHAFIQ, M. A., ALAUDAH, Y. & ALREGIB, G. 2018. Successful leveraging of image processing and machine learning in seismic structural interpretation: A review. *The Leading Edge*, 37, 451-461.
- WANG, Z. & NUR, A. 1990. Wave velocities in hydrocarbon-saturated rocks: Experimental results. *Geophysics*, 55, 723-733.
- WANG, Z. & NUR, A. 1991. Ultrasonic velocities in pure hydrocarbons and mixtures. *The Journal of the Acoustical Society of America*, 89, 2725-2730.
- WILSON, W. D. 1959. Speed of sound in distilled water as a function of temperature and pressure. *The Journal of the Acoustical Society of America*, 31, 1067-1072.
- WINKLER, K. & NUR, A. 1979. Pore fluids and seismic attenuation in rocks. *Geophysical Research Letters*, 6, 1-4.
- WINKLER, K. W. & MURPHY III, W. F. 1995. Acoustic velocity and attenuation in porous rocks. *Rock physics and phase relations. A Handbook of physical constants*, 20-34.
- WINKLER, K. W. & NUR, A. 1982. Seismic attenuation: Effects of pore fluids and frictional-sliding. *Geophysics*, 47, 1-15.
- WOOD, A. B. & LINDSAY, R. 1956. A textbook of sound. *Physics Today*, 9, 11, 37.
- WU, W., LI, H. & ZHAO, J. 2015. Dynamic responses of non-welded and welded rock fractures and implications for P-wave attenuation in a rock mass. *International Journal of Rock Mechanics and Mining Sciences*, 100, 174-181.

- WU, W., LI, J. & ZHAO, J. 2012a. Loading rate dependency of dynamic responses of rock joints at low loading rate. *Rock Mechanics and Rock Engineering*, 45, 421-426.
- WU, W., LI, J. & ZHAO, J. 2013a. Seismic response of adjacent filled parallel rock fractures with dissimilar properties. *Journal of Applied Geophysics*, 96, 33-37.
- WU, W., LI, J. & ZHAO, J. 2014. Role of filling materials in a P-wave interaction with a rock fracture. *Engineering Geology*, 172, 77-84.
- WU, W. & ZHAO, J. 2015. Effect of water content on P-wave attenuation across a rock fracture filled with granular materials. *Rock Mechanics and Rock Engineering*, 48, 867-871.
- WU, W., ZHU, J. & ZHAO, J. 2012b. A further study on seismic response of a set of parallel rock fractures filled with viscoelastic materials. *Geophysical Journal International*, 192, 671-675.
- WU, W., ZHU, J. & ZHAO, J. 2013b. Dynamic response of a rock fracture filled with viscoelastic materials. *Engineering Geology*, 160, 1-7.
- WYLLIE, M. R. J., GREGORY, A. R. & GARDNER, L. W. 1956. Elastic wave velocities in heterogeneous and porous media. *Geophysics*, 21, 41-70.
- WYLIE, E. B., STREETER, V. L. & SUO, L. 1993. *Fluid transients in systems*, Prentice Hall Englewood Cliffs, NJ.
- XIA, K., NASSERI, M., MOHANTY, B., LU, F., CHEN, R. & LUO, S. 2008. Effects of microstructures on dynamic compression of Barre granite. *International Journal of Rock Mechanics and Mining Sciences*, 45, 879-887.
- XIA, K. & YAO, W. 2015. Dynamic rock tests using split Hopkinson (Kolsky) bar system—A review. *Journal of Rock Mechanics and Geotechnical Engineering*, 7, 27-59.
- XIE, H., WANG, J.-A. & STEIN, E. 1998. Direct fractal measurement and multifractal properties of fracture surfaces. *Physics Letters A*, 242, 41-50.

- XU, Y., LI, J., DUAN, J., SONG, S., JIANG, R. & YANG, Z. 2020. Soil water content detection based on acoustic method and improved Brutsaert's model. *Geoderma*, 359, 114003.
- XU, J., REN, X., GONG, W., DAI, R. & LIU, D. 2003. Measurement of the bulk viscosity of liquid by Brillouin scattering. *Applied Optics*, 42, 6704-6709.
- YANG, H., DUAN, H. & ZHU, J. 2019. Ultrasonic P-wave propagation through water-filled rock joint: an experimental investigation. *Journal of Applied Geophysics*, 169, 1-14.
- YANG, H., DUAN, H.-F. & ZHU, J. 2020. Effects of filling fluid type and composition and joint orientation on acoustic wave propagation across individual fluid-filled rock joints. *International Journal of Rock Mechanics and Mining Sciences*, 128, 104248.
- YOSHIOKA, N. & IWASA, K. 2006. A laboratory experiment to monitor the contact state of a fault by transmission waves. *Tectonophysics*, 413, 221-238.
- ZHANG, Q. 2014. *Mechanical behaviour of rock materials under dynamic loading*. Ph.D. Thesis. École Polytechnique Fédérale de Lausanne (EPFL), Lausanne, Switzerland.
- ZHANG, Q. B. & ZHAO, J. 2014. A review of dynamic experimental techniques and mechanical behaviour of rock materials. *Rock Mechanics and Rock Engineering*, 47, 1411-1478.
- ZHAO, J. 1997a. Joint surface matching and shear strength part A: joint matching coefficient (JMC). *International Journal of Rock Mechanics and Mining Sciences*, 34, 173-178.
- ZHAO, J. 1997b. Joint surface matching and shear strength part B: JRC-JMC shear strength criterion. *International Journal of Rock Mechanics and Mining Sciences*, 34, 179-185.
- ZHAO, J. & BROWN, E. 1992. Hydro-thermo-mechanical properties of joints in the Carnmenellis granite. *Quarterly Journal of Engineering Geology and Hydrogeology*, 25, 279-290.
- ZHAO, J. & CAI, J. 2001. Transmission of elastic P-waves across single fractures with a nonlinear normal deformational behavior. *Rock Mechanics and Rock Engineering*, 34, 3-22.

- ZHAO, J., CAI, J., ZHAO, X. & LI, H. 2006. Experimental study of ultrasonic wave attenuation across parallel fractures. *Geomechanics and Geoengineering: An International Journal*, 1, 87-103.
- ZHAO, J., ZHOU, Y., HEFNY, A., CAI, J., CHEN, S., LI, H., LIU, J., JAIN, M., FOO, S. & SEAH, C. 1999. Rock dynamics research related to cavern development for ammunition storage. *Tunnelling and Underground Space Technology*, 14, 513-526.
- ZHAO, L., YUAN, H., YANG, J., HAN, D. H., GENG, J., ZHOU, R., LI, H. & YAO, Q. 2017. Mobility effect on poroelastic seismic signatures in partially saturated rocks with applications in time-lapse monitoring of a heavy oil reservoir. *Journal of Geophysical Research: Solid Earth*, 122, 8872-8891.
- ZHAO, X. 2004. *Theoretical and numerical studies of wave attenuation across parallel fractures*. Ph.D. Thesis. Nanyang Technological University.
- ZHENG, Y. & ZAOUI, A. 2018. Mechanical behavior in hydrated Na-montmorillonite clay. *Physica A: Statistical Mechanics and its Applications*, 505, 582-590.
- ZHOU, Y., XIA, K.-W., LI, X., LI, H., MA, G., ZHAO, J., ZHOU, Z. & DAI, F. 2011. Suggested methods for determining the dynamic strength parameters and mode-I fracture toughness of rock materials. In *The ISRM Suggested Methods for Rock Characterization, Testing and Monitoring: 2007-2014*. Springer.
- ZHOU, Z., LI, X., ZOU, Y., JIANG, Y. & LI, G. 2014. Dynamic Brazilian tests of granite under coupled static and dynamic loads. *Rock Mechanics and Rock Engineering*, 47, 495-505.
- ZHU, J. 2011. *Theoretical and numerical analysis of wave propagation in jointed rock masses*. Ph.D. Thesis, École Polytechnique Fédérale de Lausanne (EPFL), Lausanne, Switzerland.
- ZHU, J., PERINO, A., ZHAO, G., BARLA, G., LI, J., MA, G. & ZHAO, J. 2011. Seismic response of a single and a set of filled joints of viscoelastic deformational behaviour. *Geophysical Journal International*, 186, 1315-1330.

- ZHU, J., ZHAO, X., WU, W. & ZHAO, J. 2012. Wave propagation across rock joints filled with viscoelastic medium using modified recursive method. *Journal of Applied Geophysics*, 86, 82-87.
- ZIMMERMAN, R. W. & BODVARSSON, G. S. 1996. Hydraulic conductivity of rock fractures. *Transport in Porous Media*, 23, 1-30.
- ZIMMERMAN, R., CHEN, D., LONG, J. & COOK, N. 1990. Hydromechanical coupling between stress, stiffness, and hydraulic conductivity of rock joints and fractures. In *International symposium on rock joints*, 571-577.
- ZOU, Y., LI, J. & ZHAO, J. 2019. A Novel Experimental Method to Investigate the Seismic Response of Rock Joints Under Obliquely Incident Wave. *Rock Mechanics and Rock Engineering*, 1-8.